UNIVERSITAT DE BARCELONA

Exploring the Ligand Chemical Space with Computational Tools and its Effect on the Electronic Structure of Spin-Crossover of Different Complexity

Laia Navarro i Maestro

Exploring the Ligand Chemical Space with Computational Tools and its Effect on the Electronic Structure of Spin-Crossover Systems of Different Complexity

Laia Navarro i Maestro

UNIVERSITAT DE BARCELONA

Memòria presentada per

Laia Navarro i Maestro

Per optar al grau de Doctor per la
Universitat de Barcelona

Programa de doctorat en Química Teòrica i
Modelització Computacional

Exploring the Ligand Chemical Space with Computational Tools and its Effect on the Electronic Structure of Spin-Crossover Systems of Different Complexity

Explorant l'Espai Químic de Lligands amb Eines Computacionals i el seu Efecte sobre l'Estructura Electrònica de Sistemes amb Transició d'Spin de Diferent Complexitat

Dirigida per:

Dr. Jordi Cirera Fernandez
Universitat de Barcelona

Prof. Eliseo Ruiz Sabín
Universitat de Barcelona

Tutor:
Prof. Gabriel Aullón López
Universitat de Barcelona

UNIVERSITAT DE BARCELONA

Barcelona, 2025

The work presented in this doctoral thesis has been carried out at the Departament de Química Inorgànica i Orgànica, Secció de Química Inorgànica of Universitat de Barcelona (UB), within the research facilities of the Institut de Química Teòrica i Computacional (IQTC).

Laia Navarro i Maestro acknowledges Universitat de Barcelona for funding four-year predoctoral contract through the “Predocs-UB 2019” and “Predocs-UB 2022”.

ACKNOWLEDGEMENTS

M’agradaria expressar el meu agraïment al Dr. Jordi Cirera per tots els anys que hem treballat junts, des del Treball Final de Grau, passant pel Treball Final de Màster fins a aquests últims quatre anys amb la Tesi Doctoral. Jordi, ets el millor director que es pot tenir. Gràcies per la teva paciència, la teva dedicació i passió per la teva feina, per ensenyar-me que un no s’ha de posar nerviós, que es pot arribar a tot. Gràcies per transmetre’m la teva manera de fer ciència i l’entusiasme per la vida, no només per la química. Gràcies per recolzar-me, per haver-me deixat fer, per confiar en mi i per fer-me veure que el que importa és fer el que a una mateixa li agrada i ser feliç amb allò al que una es dedica. Gràcies per haver-me guiat tots aquests anys i haver estat tan bon mentor i, per haver-me donat, també, l’espai i la comprensió per poder parlar del que fos. Gràcies per ser tan empàtic i sempre intentar tenir un bon ambient de treball i comunicació. Em falten paraules per expressar com te n’estic d’agraïda.

Gràcies al Dr. Jesús Jover i al Dr. Jorge Echeverría pels bons moments viscuts i per l’ajuda que m’han ofert quan l’he necessitat. És un plaer compartir espai amb bons científics i bones persones.

Gràcies als companys de despatx que he tingut durant tots aquests anys. Gràcies per l’increïble suport que heu estat per mi, per escoltar-me, per cuidar-me, per fer-me riure, per haver-me fet feliç, per ser tan divertits, i per sempre estar disposats a ajudar. Gràcies Adriana, Aïda, Álex, Àlex, Arnau, Carlota, Frank, Joan, Juan Diego, Mauri, Oliver, Pablo i Patri.

Gràcies també al Prof. Eliseo Ruiz, al Prof. Gabriel Aullón i a la resta del grup d’Estructura Electrònica.

I would love to thank Prof. John E. McGrady for being my supervisor while I was doing my internship at University of Oxford. Thank you for showing me new computational methods and for the interesting discussions we have had. I would also like to thank my colleagues at Physical and Theoretical Chemistry Laboratory for making my stay more enjoyable and funnier, especially Jim, Aidan, Sourav and Zisheng. Thank you very much.

Hablando de mi estancia en Oxford, sin duda me gustaría agradecerles a Mónica, Marcos y Raúl los momentos que vivimos juntos. Me sentí muy comprendida, que hacía equipo con cada uno, y los recuerdos que me llevé de Oxford con vosotros los guardaré para siempre. Siempre os llevaré en el corazón.

Ines, thank you so much for everything you have done for me and for sharing with me one of the best years of my life. Thank you for making me happy. I keep looking at the moon.

També vull agrair a les amigues que m'han fet costat durant tots aquests anys, les que em vaig endur del grau, les que tinc des de petita, la gent de l'esplai, i la gent nova que he anat coneixent i que s'hi ha quedat. Moltes gràcies a la gent que he conegut a través del món de la música, especialment a la Paula i a N'Clauvocal. Heu fet que agafi empenta amb els meus propis projectes musicals i que confiï en mi mateixa. Gema, Helena, Marina, Roc, sou els meus àngels de la guarda, gràcies per formar part de la meva vida i deixar-me formar part de la vostra.

I per últim, però no menys important, gràcies Mama, Papa, Pau i Miquel. No sé què hagués estat de mi si no haguéssiu estat al meu costat sempre. Gràcies pel vostre suport i amor incondicional. Gràcies també als meus avis, que han estat uns grans referents per a mi, per haver-me transmès el seu esperit lluitador. Gràcies Àvia, per sempre tenir un plat de sopa per reconfortar-me el cor. Abuelo, Yaya, Yayo, sé que no habéis vivido este proceso a mi lado, pero estoy segura que os habría gustado ver la persona en la que me he convertido. Os mando muchos besos y abrazos.

Nothing in life is to be feared, it is only to be understood.
Now is the time to understand more, so that we may fear less.

Marie Curie

But music, don't you know, is a dream from which the veils have been lifted.
It's not even the expression of a feeling, it's the feeling itself.

Claude Debussy

ABSTRACT

Spin-crossover (SCO) compounds are a fascinating class of molecular systems containing first-row transition metal ions with d^4 to d^7 electronic configurations, capable of alternate between two electronic states that are close in energy. Originally described by Cambi and co-workers in 1931 on some tris(*N*,*N*-dialkyldithiocarbamato)iron(III) complexes, this phenomenon has since grown into a vibrant field of research due to its potential applications as sensors, molecular level based switches, nanodevices, energy storage, and self-healing materials, among others.

The SCO transition is triggered by an external stimulus, commonly temperature but also pressure or electromagnetic radiation, and is accompanied by significant changes in the physical properties of the system since the spin state of the metal centre is changed, including changes in the magnetic moment, colour, or structural distortions. The temperature at which the two spin states are equally populated, is defined as the transition temperature ($T_{1/2}$), and is a key parameter in the physical characterization of such systems.

Research into SCO compounds has predominantly focused on d^6-Fe(II) coordination complexes, with numerous examples spanning mononuclear, polynuclear, and extended systems, including coordination polymers. While these systems dominate the field, other 3d metal ions capable of exhibiting SCO behaviour remain comparatively underexplored.

In this thesis, some unusual systems exhibiting SCO have been studied computationally, such as Cr(II)-based, or anionic Fe(II)-based complexes. The level of complexity has also been increased, studying dinuclear Fe(II)-based metal-organic cages (MOCs) that can undergo SCO showing different types of transitions depending on the nature of the guest molecules that the cages can encapsulate. In all cases, ligand functionalization has been studied to understand how these changes affect the transitions, with the aim of design new materials with tailored properties.

Different levels of computation have been used, from density functional theory (DFT) to higher-level multireference methods, like Complete Active Space Self-Consistent Field (CASSCF)/N-Electron Valence Perturbation Theory (NEVPT2) and *Ab initio* Ligand Field Theory (AILFT). In this thesis also a new methodology that develops density functional theories that use multiconfigurational reference wave functions, like Multiconfiguration Pair-Density Functional Theory (MC-PDFT) was used, for a Fe(II)-based SCO system that is well described both experimentally and computationally. MC-PDFT, in principle, allows a

description of static and dynamic correlation with affordable computational costs and with an accuracy comparable to multireference perturbation theory methods.

The results outlined in this thesis help in understanding the versatility and unique properties of SCO systems, which continue to drive interest in their applications expanding the scope of functional materials in advanced technologies.

Keywords: computational chemistry, computational modelling, computational studies, coordination complexes, density functional theory, electronic structure, host-guest chemistry, inorganic chemistry, ligand functionalization, metal-organic cage, new materials, organometallic compounds, spin-crossover, spin-state energy gap, theoretical chemistry, thermochemistry, TPSSh functional, transition metal ions, transition temperature.

RESUM

Els compostos de transició d'spin (SCO) són una classe fascinant de sistemes moleculars amb ions de metalls de la primera sèrie de transició amb configuracions electròniques d^4–d^7 capaços d'alternar entre dos estats electrònics d'energies similars. Descrits per primera vegada el 1931 per Cambi i els seus col·laboradors en complexos tris(*N*,*N*-dialquilditiocarbamato)ferro(III), aquests sistemes han esdevingut un camp de recerca destacat gràcies a les seves aplicacions potencials com a sensors, interruptors moleculars, nanodispositius, emmagatzematge d'energia i materials autoreparables, entre altres.

La transició té lloc per mitjà d'estímuls externs, com ara la temperatura, la pressió o la radiació electromagnètica, i implica canvis significatius en les propietats físiques del sistema, incloent canvis del moment magnètic, del color o distorsions estructurals. La temperatura a la qual les poblacions dels dos estats de spin són iguals es defineix com a temperatura de transició ($T_{1/2}$) i és un paràmetre clau en la caracterització física d'aquests sistemes.

La recerca en aquest camp s'ha centrat majoritàriament en complexos de coordinació d^6-Fe(II), incloent-hi sistemes mononuclears, polinuclears i polímers de coordinació. Malgrat això, altres ions metàl·lics 3d amb capacitat SCO han estat menys explorats.

En aquesta tesi, s'han estudiat computacionalment sistemes SCO inusuals, com complexos basats en Cr(II) i complexos aniònics de Fe(II). També s'han analitzat gàbies metàl·lo-orgàniques (MOCs) dinuclears de Fe(II) que poden mostrar diferents tipus de transicions en funció de l'hoste que encapsulin. En tots els casos, s'han modificat els lligands per comprendre com afecta a les transicions, amb l'objectiu de dissenyar materials amb propietats fetes mida.

S'han utilitzat diversos mètodes computacionals, des de la teoria del funcional de la densitat (DFT) fins a mètodes multirreferencials com Complete Active Space Self-Consistent Field (CASSCF)/N-Electron Valence Perturbation Theory (NEVPT2) i *Ab initio* Ligand Field Theory (AILFT). També s'ha aplicat una nova metodologia, la Multiconfiguration Pair-Density Functional Theory (MC-PDFT), en un sistema SCO basat en Fe(II) ben descrit experimentalment i computacionalment. Aquesta metodologia descriu, en principi, la correlació estàtica i dinàmica amb costos computacionals assequibles i una precisió comparable als mètodes multirreferencials basats en la teoria de pertorbacions.

En conjunt, les propietats úniques i la versatilitat dels sistemes SCO continuen impulsant el seu estudi, ampliant les aplicacions de materials funcionals en tecnologies avançades.

Paraules clau: complexos de coordinació, compostos organometàl·lics, química computacional, química hoste-amfitrió, química inorgànica, química teòrica, diferència d'energia d'estat d'spin, estudis computacionals, estructura electrònica, funcionalització de lligands, funcional TPSSh, gàbia metàl·lo-orgànica, ions de metalls de transició, modelatge computacional, nous materials, temperatura de transició, termoquímica, teoria del funcional de la densitat, transició d'spin.

ABBREVIATIONS

AILFT	*Ab Initio* Ligand Field Theory
AI	Artificial Intelligence
AO	Atomic Orbital
B3LYP	Becke Three Parameter exchange functional and Lee-Yang-Parr correlation functional with 20% Hartree-Fock exchange
B3LYP*	Becke Three Parameter exchange functional and Lee-Yang-Parr correlation functional with 15% Hartree-Fock exchange
BGR	24-bit representation where the lower-addressed 8 bits are blue, the next-addressed 8 are green and higher-addressed 8 are red
BLYP	Becke exchange functional and Lee-Yang-Parr correlation functional
bpp	2,6-di(pyrazol-1-yl-)pyridine
bpy	2,2'-bipyridine
bpym	2,2'-bipyrimidine
BS	Basis Set
BSSE	Basis Set Superposition Error
bt	2,2'-bi-2-thiazoline
Bu	Butyl
CAS	Complete Active Space
CASPT2	Complete Active Space Second-Order Perturbation Theory
CASSCF	Complete Active Space Self-Consistent Field
CC	Coupled Cluster
CD	Circular Dichroism
CFT	Crystal Field Theory
CI	Configuration Interaction
Cp	Cyclopentadienyl
CSD	Cambridge Structural Database
CSF	Configuration State Function
CShM	Continuous Shape Measures
CTIST	Charge-Transfer-Induced Spin Transition
ddpd	*N,N'*-dimethyl-*N,N'*-dipyridine-2-yl-pyridine-2,6-diamine
depe	1,2-bis(diethylphosphino)ethane

DFT	Density Functional Theory
EC	Electron Correlation
EDG	Electron-Donating Group
en	ethylenediamine
EPR	Electron Paramagnetic Resonance
ESR	Electron Spin Resonance
Et	Ethyl
EWG	Electron-Withdrawing Group
GD3BJ	Grimme's D3 dispersion scheme with Becke–Johnson damping
GGA	Generalized Gradient Approximation
GPU	Graphical Process Units
H-GGA	Hybrid Generalized Gradient Approximation
HF	Hartree-Fock
HK	Hohenberg–Kohn
HOMO	Highest Occupied Molecular Orbital
HS	High-Spin
Ind	Indenyl
IR	Infrared
KS	Kohn–Sham
LCAO	Linear Combination of Atomic Orbitals
LD-LISC	Ligand-Driven Light-Induced Spin Change
LDA	Local Density Approximation
LFT	Ligand Field Theory
LIESST	Light-Induced Excited-Spin-State-Trapping
LS	Low-Spin
LSDA	Local Spin Density Approximation
LUMO	Lowest Unoccupied Molecular Orbital
M06L	Functional of Zhao and Truhlar
MC-PDFT	Multiconfiguration Pair-Density Functional Theory
MCSCF	Multi-Configurational Self-Consistent Field
Me	Methyl
MEMS	Micro-Electromechanical Systems
MO	Molecular Orbital

MOF	Metal-Organic Framework
MP	Møller–Plesset
MR-PT2	Multi-Reference Perturbation Theory
MRI	Magnetic Resonance Image
NBO	Natural Bond Orbital
NCI	Non-Covalent Interaction
NEVPT2	N-Electron Valence State Perturbation Theory
NIS	Nuclear Inelastic Scattering
NMR	Nuclear Magnetic Resonance
O_h	Octahedral point group
OLYP	Handy's OPTX modification of Becke's exchange functional and Lee, Yang, and Parr correlation functional
OPBE	Handy's OPTX modification of Becke's exchange functional and Perdew, Burke and Ernzerhof correlation functional
ox	oxalate
PCP	Porous Coordination Polymer
pDOS	Partial Density of Vibrational States
PES	Potential Energy Surface
phen	1,10-phenantroline
Pr	Propyl
ptz	1-propyltetrazole
py	pyridine
py_4C	tetrakis(2-pyridyl)methane
QM	Quantum Mechanics
QQ	Quintet-Quintet
QZV	Quadruple-ζ Valence basis set
QZVP	Quadruple-ζ Valence basis set with Polarization functions
RMSD	Root Mean Square Deviation
SCF	Self-Consistent Field
SCO	Spin-Crossover
SQ	Singlet-Quintet
SS	Singlet-Singlet
SV	Split-Valence basis set

SVP	Split-Valence basis set with Polarization functions
SVWN	Slater exchange functional and Vosko, Wilk, and Nusair correlation functional
thio-pybox	2,6-bis(4,4-dimethyl-4,5-dihydrothiazol-2-yl)pyridine
TPSS	Tao-Perdew-Staroverov-Scuseria functional
TPSSh	Hybrid Tao-Perdew-Staroverov-Scuseria with 10% of Hartree–Fock exchange functional
TZV	Triple-ζ Valence basis set
TZVP	Triple-ζ Valence basis set with Polarization functions
TZVPP	Triple-ζ Valence basis set with double Polarization functions
VMD	Visual Molecular Dynamics
WFT	Wave Function Theory
ZPE	Zero-Point Energy

CONTENTS

CHAPTER 1

The Spin-Crossover Phenomena

1.1. Introduction

Spin-crossover (SCO) phenomena was discovered by Cambi and co-workers in 1931 upon observing drastic changes in the magnetic susceptibility of iron(III) based tris-dithiocarbamate complexes when subjected to continuous temperature variations.[1] This led to the first recognition of temperature-dependent interconversion between two spin-states.[2] Research progressed on investigating the magnetism of diverse heme derivatives of both iron(II)[3] and iron(III), revealing that in these naturally existing systems, along with associated porphyrin derivatives, the spin-state exhibited remarkable sensitivity to the nature of the axial ligands. In some cases, intermediate magnetic moments were observed, suggesting a partially ionic and partially covalent bonding nature.[4] Orgel later proposed that there was an equilibrium between iron(III) species with one unpaired electron and iron(III) species with five unpaired electrons to explain these observations.[5]

The 1960-1980 period was the renaissance in mononuclear SCO compounds and there was great activity around the world in many research groups coinciding with the growing acceptance of ligand field theory among coordination chemists. This theory offered valuable insights into the stability, reactivity, structure, and spectroscopic and magnetic properties of transition metal complexes.[6–9]

The early work in the field of SCO quickly focussed primarily on iron(II) systems aiming to establish the conditions for SCO, its dependence on chemical and physical perturbations and the bases for its theoretical interpretation. The first examples of synthetic iron(II) d^6 based monomeric SCO complexes were reported by König and Madeja in 1967.[10] This discovery ignited a continuing exploration of N-donor ligand combinations that can induce spin transitions. Sorai and co-workers[11] developed important thermodynamic studies that demonstrated that a spin transition is an entropy driven process (Section 1.5). Furthermore, Beattie and co-workers[12,13] led the studies of the dynamics of the spin interconversion processes in solution that probed the mechanisms underlying spin changes.

Since 1980, the study of SCO complexes had a renewed interest in polynuclear transition metal ions (mostly iron(II), iron(III) and cobalt(II)) complexes since they represent an interesting challenge due to its possible applications as display, sensor and memory devices.[14–17]

In the next sections the most common descriptions of the bonds in coordination complexes will be explained in order to gain insight into the explanation of spin-crossover compounds. After, the SCO phenomena will be explained: the possible applications of SCO compounds,

the external stimuli that trigger the transition, the mechanism and the thermochemistry of the phenomena as well as several experimental techniques to measure such behaviour. Finally, the objectives of the thesis will be outlined.

1.2. Crystal Field Theory

Crystal field theory (CFT) is a bonding model that explains many important properties of transition metal complexes, including their colours, magnetism, structures, stability, and reactivity. CFT considers a complex as an entity formed by a central cation surrounded by anionic or polar (δ^-) ligands that are electrostatically attracted to the cation. The bond is essentially electrostatic: there is cation–ligand attraction but, at the same time, there is repulsion between the ligands and the electrons of the central cation. This theory elucidates the breaking of degeneracy of the metal's orbitals induced by a static electric field generated by the surrounding charge distribution, that is, the surrounding ligands.[18] The energy levels of the free ion, before subjecting it to the effect of the crystalline field (electrostatic field that exists in the crystal), are degenerate. In the 1930s Bethe[6] and Van Vleck[7,8,19,20] demonstrated that, depending on the symmetry of the crystalline field, this degeneracy is lost, developing a theory that they applied only to 3D ionic solids.

The essential idea of the model applied to coordination complexes is to assume that the coordination sphere of the anions or ligands around a metal ion behaves as a set of negative point charges that interact repulsively with the electrons of the central metal cation. The lone pair of electrons of a ligand is like a negative point charge (or like the partial negative charge of an electric dipole) that suffers a repulsion effect with respect to the electrons of the d orbitals of the central metal ion. The theory correctly identifies the importance of the symmetry of the orbitals of a complex, however, CFT has limitations: it assumes no overlap or interaction between the ligand electrons and the metal electrons. While ligands can be polarized by the metal ion, their electron movement is considered independent of the metal's electron state (excited or not). In essence, CFT treats ligands as providers of a constant electric potential (based on ligand arrangement) within which the metal's electrons move.[6,21]

The d orbitals split energetically under the effects of octahedral or tetrahedral fields, whereas p orbitals do not (if the symmetry is decreased, they split). Logically the s orbital never splits regardless of symmetry. With group theory, we can obtain the irreducible representations for any value of the quantum number *l*. For the octahedral point group, O_h, the irreducible representations are those shown in Table 1.1.

Table 1.1. Splitting of atomic orbitals in O_h symmetry, indicating the symmetry labels for the orbitals.

Orbital	Irreducible Representation
s	a_{1g}
p	t_{1u}
d	$e_g + t_{2g}$
f	$a_{2g} + t_{1u} + t_{2g}$

In an octahedral (O_h) complex, the six ligands are located on the Cartesian axes, whose origin is the metal ion. Consequently, the ligands are close to the d_{z^2} and $d_{x^2-y^2}$ orbitals whose symmetry label in the O_h point group is e_g. The other three d orbitals (d_{xy}, d_{xz}, d_{yz}) are further away from the ligands and its symmetry label on the point group O_h is t_{2g}. The orbital degeneracy of the d electrons is broken, as they tend to avoid areas with the highest electronic density of the ligands. If we consider the repulsions between the d orbitals and the electrons of the ligands, such repulsions will be greater between the ligands and the e_g orbitals than between the same ligands and the t_{2g} orbitals (directed towards the bisectors of the *xy*, *xz*, and *yz* planes). Consequently, the five d orbitals split into two groups: e_g and t_{2g} (Figure 1.1). This allows us to say that the potential energy of the three degenerate orbitals t_{2g} is lower than the energy of the two degenerate orbitals e_g.

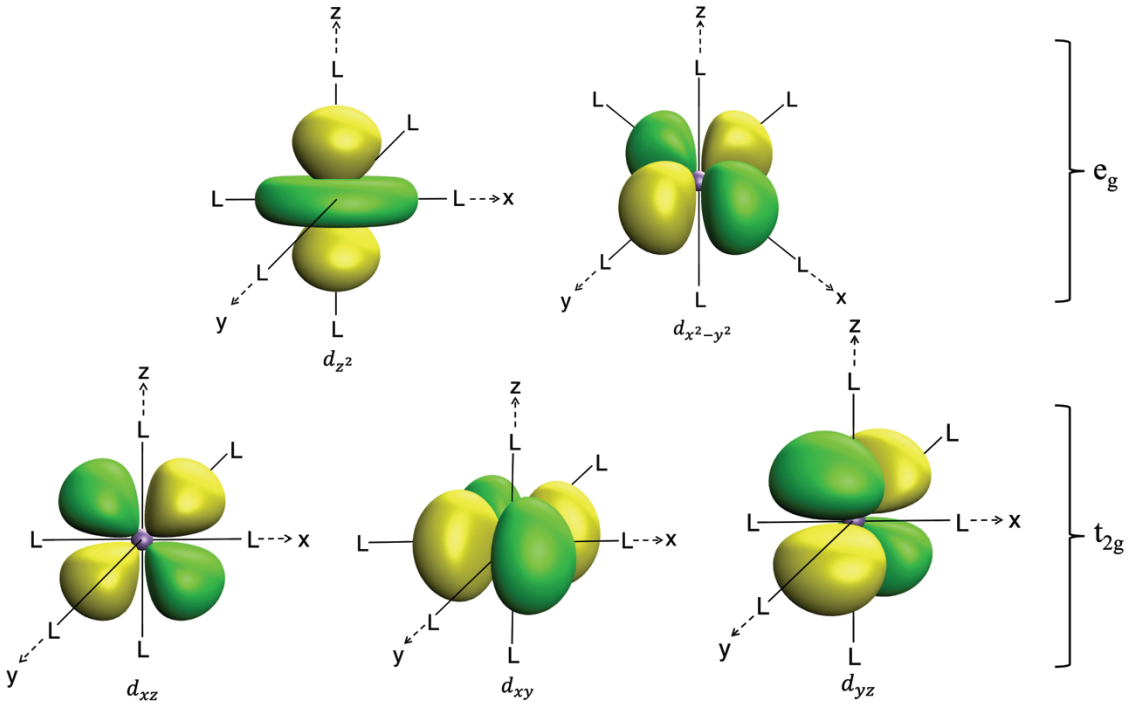

Figure 1.1. d orbitals in an octahedral complex ML_6 (M = metal, L = ligand).

The situation is shown in Figure 1.2. The fivefold degenerate d orbitals are split up by the inclusion of the octahedral field. The energies of the t_{2g} and e_g levels are divided into two contributions: a spherical part that shifts the electronic levels of the free ion and another contribution related to the symmetry lowering, resulting in a degeneracy partial splitting. The energy difference $10Dq$ is the crystal field splitting, and Dq corresponds to a semi-empirical parameter related to the crystal force field[22] and it is a function of the effective charge, Z_{eff}, of the metal ion, the bond distance between the metal and the ligands and the value of formal charges, dipoles, etc., found upon the ligands.[21] By selecting appropriate values of these new parameters, it is possible to obtain a reasonable value for Dq. However, it is evident that this procedure only tries to avoid the issue: the calculation of Dq based on the molecule's complete Hamiltonian. This task is difficult, yet it has been successfully accomplished by Shulman and Sugano.[23] The performance of the integration of Dq holds minimal importance for the practical application of the CFT since Dq is always determined semi-empirically.

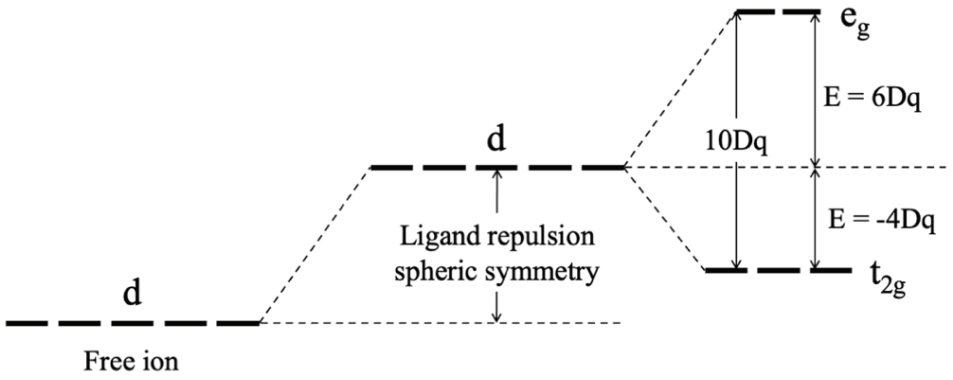

Figure 1.2. Splitting of the d orbitals in an octahedral field.

$10Dq$ varies depending on the type of ligands and the central ion. Empirical observations, often from electronic spectra, have grouped ligands into a spectrochemical series[24,25] based on the strength of the crystalline field they create, ranging from lowest to highest energy. While there are minor variations based on the specific central ion used in combination with these ligands, the overall trend of the ligands appears to be almost independent of the central ion. For d^4 to d^7 configurations, the electrons can be placed in two different set of orbitals: in the t_{2g} orbitals pairing with already existing electrons, which represents a price in terms of energy destabilization due to the pairing energy of the electrons, P, or jump to the e_g free orbitals, so the electrons will not have to pair but will have to overcome the positive energy $10Dq$. This will depend on the relative values of $10Dq$ and P. If $10Dq >> P$, the electrons will tend to pair

up in the t_{2g} orbitals, and this is called strong field (low-spin, LS). If $10Dq << P$, the electrons will tend to move to the e_g orbitals, and this is called weak field (high-spin, HS). The field can be of intermediate strength when the splitting of the orbitals is close to P (and thus, spin-crossover may occur). This will be further explained in Section 1.4.

The ordering in the spectrochemical series is as follows:

$$I^- < Br^- < S^{2-} < SCN^- < Cl^- < NO_3^- < N_3^- < F^- < OH^- < ox < O^{2-} < H_2O < NCS^- < CH_3CN < NH_3 \approx py < en < bpy < phen < NO_2^- < PPh_3 < CN^- < CO$$

(ox = oxalate; py = pyridine; en = ethylenediamine; bpy = 2,2'-bipyridine; phen = 1,10-phenantroline; PPh_3 = triphenylphosphine)

The values of $10Dq$ also depend on the metallic ion. $10Dq$ increases with oxidation number and when moving down a group. In general, it increases by 50% when going from the first to the second transition series, and by 25% when going from the second to the third series.[18] The complexes of the second and third transition series generally adopt the LS (strong field) configuration because even with ligands that create a weak field, the field created by the ion is sufficiently strong.

In octahedral complexes an increasing d-orbital splitting is associated with an increasingly strong metal–ligand interaction. From the CFT's point of view, the relationship $I^- < Br^- < Cl^- < F^-$ makes sense because the smaller anion has more repulsion energy (q_1q_2/r) since r is lower and that causes a larger split of the orbitals. However, experimentally the octahedral splitting is not always directly proportional to the ligand charge, the theory cannot explain why an anionic ligand like OH^- creates a smaller field than H_2O or why CN^- or CO are among the strongest field ligands. Fluoride complexes which according to CFT should show large splittings, actually show smaller splittings than complexes with neutral ligands. The reason behind the failure of the electrostatic model is attributed to covalency. Consequently, the ionic crystal field model was modified to incorporate a more covalent molecular orbital (MO) picture.[26] Several experiments[27,28] strongly suggested that the magnetic electrons move in a molecular orbital extending across the entire complex and therefore a molecular orbital approach provides a description closer to the truth compared to the crystalline field description. This idea evolved into ligand field theory, as will be outlined in the next section.

The presence of the nephelauxetic effect also highlights the disadvantages of the crystal field theory, since it has to do with the covalent character in the metal–ligand interaction. This

effect consists of a decrease in the Racah interelectronic repulsion parameter, *B*, that occurs when a free transition metal ion forms a complex with ligands. The decrease in the Racah *B* parameter indicates that in a complex there is less repulsion between the two electrons in a doubly occupied metallic d orbital than in the respective gaseous metal ion M^{n+}, which in turn implies that the size of the orbital is larger in the complex. This cloud expansion effect can occur for two reasons:

1. Because the positive charge of the metal has decreased. As the positive charge of the metal is reduced for any negative charge of the ligands, the d orbitals can expand slightly.
2. Because overlapping with the orbitals of the ligands and forming covalent bonds increases the size of the orbital since the resulting molecular orbital is formed from two atomic orbitals.

The reduction of *B* with respect to its value in the free ion normally occurs with the nephelauxetic parameter β.

$$\beta = \frac{B_{complex}}{B_{gaseous\ free\ ion}} \tag{1.1}$$

With all of this, it exists the nephelauxetic series[29] corresponding to increasing tendency of partly covalent bonding, which differs from the spectrochemical series. The nephelauxetic series in order of smaller values of β in the series of metals is:

$$Mn(II) > Ni(II) > Cr(III) > Co(III) > Rh(III) > Ir(III)$$

and in the series of ligands is:

$$F^- > H_2O > NH_3 > en > ox > SCN^- > Cl^- > CN^- > Br^-$$

(en = ethylenediamine; ox = oxalate)

Despite this limitation, CFT remains a valuable tool for chemists. It provides a good starting point for understanding many properties of transition metal complexes and it has been applied to explain diverse spectroscopic phenomena observed in transition metal coordination complexes.

1.3. Molecular Orbital Theory and Ligand Field Theory

In the molecular orbital (MO) theory it is assumed that the bond between the central ion and the ligands is essentially covalent, produced by the overlap of the s, p and d orbitals of the central ion and the group orbitals of the ligands of the appropriate symmetry.

The most useful tool for dealing with coordination complexes is the ligand field theory (LFT), which incorporates the best features of both the pure crystal field theory (Bethe[6] and Van Vleck[7,8]) and the molecular orbital theory (Mulliken[9]). We have to point out though, that nearly all the results of the crystal field theory are also valid in the ligand field theory.

Unlike the crystalline field procedure, which focuses on the wave function of the single central atom, the ligand field method considers the entire complex ion as the structural unit. To build suitable wave functions, this approach needs to use the linear combination of atomic orbitals (LCAO) method. The group orbitals of the ligands are constructed through their projection operators, and they are combined with the orbitals of the central ion. This is valid for both σ and π bond types.

Let us now focus on the molecular orbitals of an octahedral complex, specifically the σ and π molecular orbitals.

1.3.1. σ-Type Molecular Orbitals

The symmetry labels of the s, p and d orbitals are known and shown in Table 1.1. Then it is possible to simply calculate the group orbitals from the ligands' orbitals that can combine properly with the metal ion's orbitals. If each ligand provides a σ-type bond, in the O_h point group, the six σ orbitals of the ligands can be grouped according to the symmetry group orbitals $a_{1g} + e_g + t_{1u}$ (Figure 1.3). By applying the projection operators, the group orbitals are obtained as combinations of these six orbitals, and their adaptation to the symmetry of the central ion's orbitals can be correlated. The t_{2g} orbitals of the metallic central ion (d_{xy}, d_{xz} and d_{yz}) are not involved in this type of bond since they do not have the proper symmetry to combine with the group orbitals coming from the ligands, therefore, they remain as non-bonding orbitals. With all this information, the MO diagram can be built (Figure 1.3).

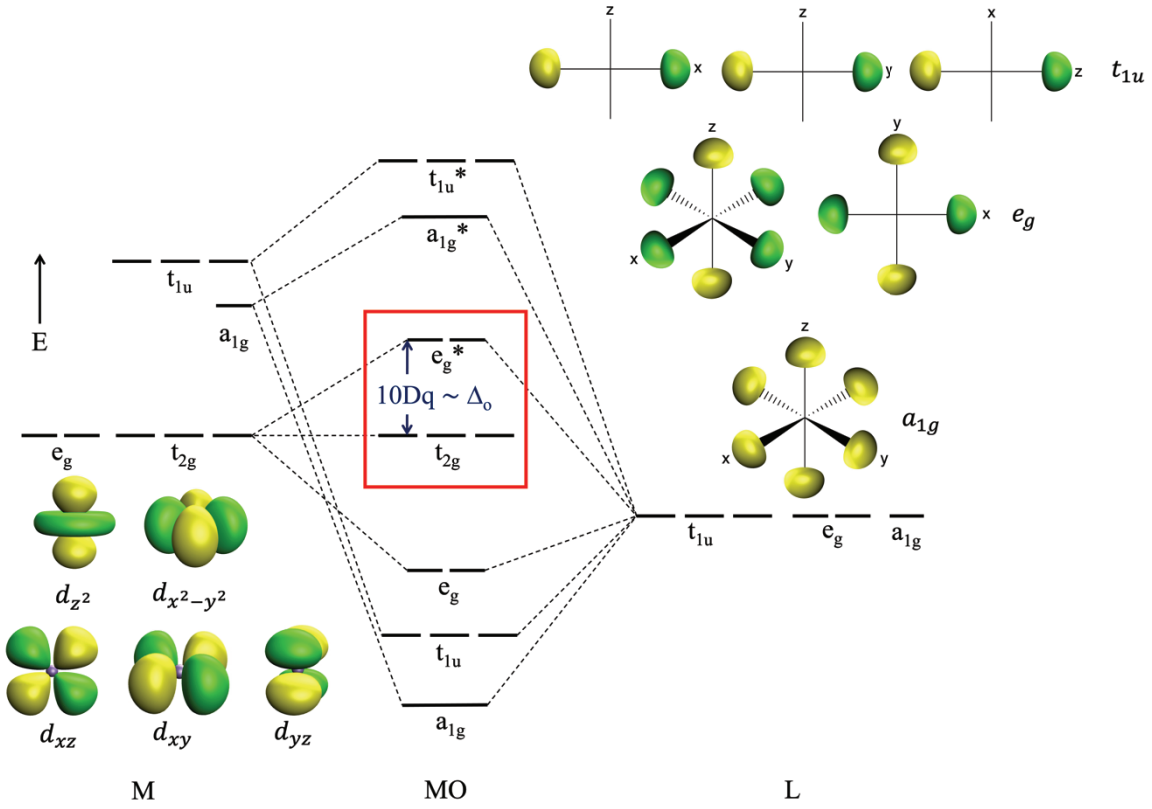

Figure 1.3. Molecular orbital diagram of an octahedral complex with six pure σ–donor ligands (this diagram has been built without considering any quantitative scale).

Each of the σ orbital of the ligands contains two electrons, hence, there will be always twelve electrons in this type of diagram plus the electrons coming from the central metal ion. Therefore, the key orbitals from the complex's point of view are the t_{2g} (non-bonding) and the e_g* (antibonding) orbitals.

In the CFT the energy difference between the e_g and t_{2g} orbitals corresponds to 10*Dq*. In the LFT, 10*Dq* becomes Δ_o and is the energy difference between the antibonding e_g* orbitals and the non-bonding t_{2g} orbitals. CFT does not contemplate that since it considers the complex is formed by the electrostatic interaction between the metal ion and the ligands, and the splitting of the orbitals is a measure of the field's strength. In LFT, this splitting depends on the degree of overlap between the orbitals of the metal and the ligands. Formally, the LFT scenario is not distinguishable from the "ionic" bonding pattern of the CFT. However, the LFT theory offers a better description of the bonding, and the value of 10*Dq* in this theory depends on how strong the bonding is. If π bonding is present, the t_{2g} orbitals will participate in the bonding and therefore the value of 10*Dq* will be further modified. This implies that 10*Dq* is highly sensitive to changes in the bonding situation.

1.3.2. π-Type Molecular Orbitals

There are 12 p orbitals that can form π bonds perpendicular to the σ bonds. The symmetry of these orbitals is $t_{2g} + t_{1u} + t_{2u} + t_{1g}$. By applying the projection operators, the group orbitals of the ligands that can form π-type bonds with the metal are obtained. From twelve atomic orbitals we obtained twelve group orbitals. The only orbitals of the central metal ion with the appropriate symmetry to bond with the ligand's group orbitals are t_{2g} and t_{1u} (the t_{1u} orbitals have already interacted with other ligand's σ group orbitals of the same symmetry, so we will not consider them in this explanation). The t_{2g} group orbitals of the ligands can interact with the t_{2g} (non-bonding) orbitals of the metal ion and form π bonds.

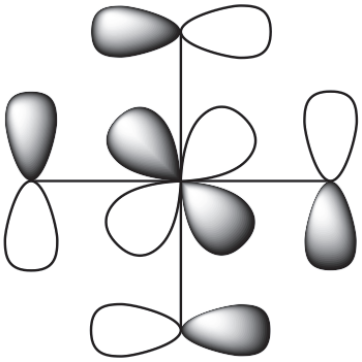

Figure 1.4. π-bonding interactions between the metal t_{2g} orbitals (d_{xy}, d_{xz} or d_{yz}) and the group orbitals of the ligands in a O_h symmetry.

The influence of these π interactions will be different depending on the energy of the t_{2g} group orbitals. We could have two situations:

1. Filled orbitals, such as the p orbitals of a Cl^- ion. These orbitals are very stable and will be lower on the energy scale of the molecular orbitals. These are the so-called π-basic ligands because in addition to the σ bond L→M, they can form a π bond in the same direction. They stabilize metals with high oxidation states.
2. High energy empty orbitals, such as the π-antibonding molecular orbital of carbonyls, nitrosyls, cyanides or isocyanides groups. These are the so-called π-acid ligands since they get electronic density from the metal forming a π bond L←M. They stabilize metal ions with high electronic densities. This phenomenon is called back bonding and olefines and phosphines can also form this type of bonds. In the case of phosphines, the

π back bond is formed between the metal and σ-antibonding molecular orbitals that have π symmetry.

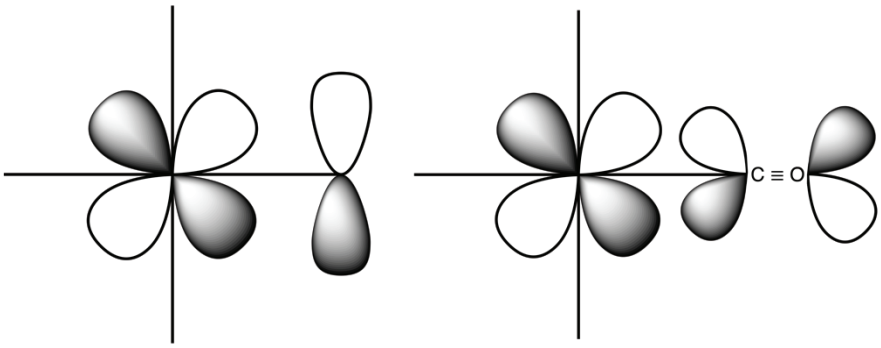

Figure 1.5. Types of π MO. Left: dπ–pπ; right: dπ–π*.

As it can be seen in Figure 1.6, the contribution of the two types of π bond causes a variation in the value of Δ_o (or $10Dq$): the π-basic ligands decrease the value of Δ_o (or $10Dq$) and correspond to the first ligands of the spectrochemical series, and the π-acid ligands increase the value of Δ_o (or $10Dq$) and correspond to the last ligands of the spectrochemical series.

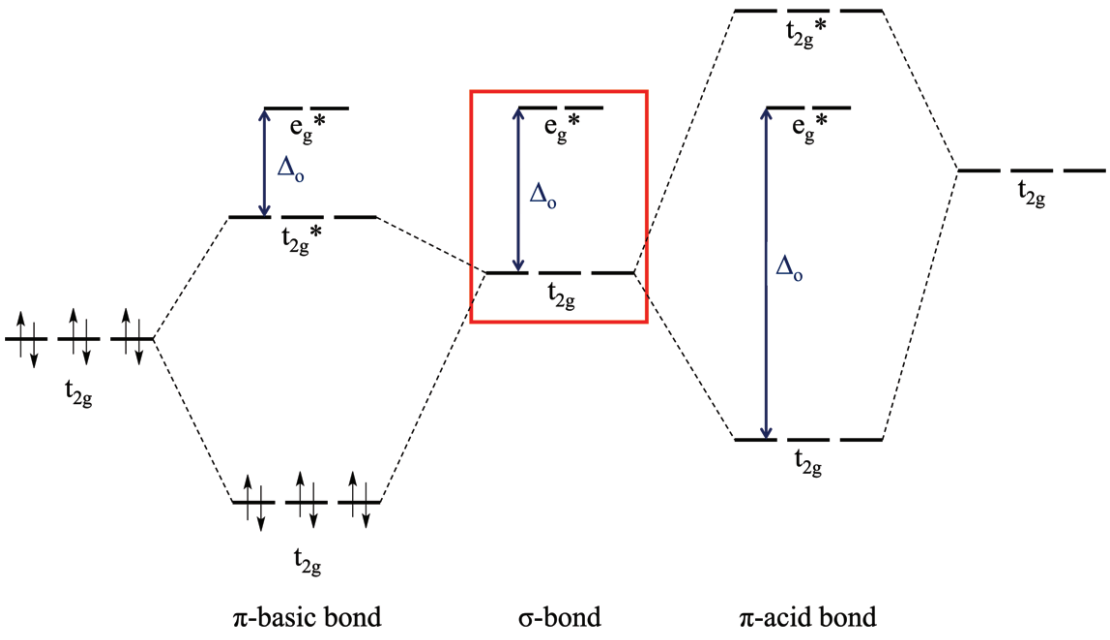

Figure 1.6. MO diagram in O_h symmetry starting from the σ-type model (centre), including π-basic ligands (left) and π-acid ligands (right). This diagram has been built without considering any quantitative scale.

1.4. Spin-Crossover Phenomena

Spin-crossover phenomena appears when two different electronic states that are close in energy are accessible in transition metal ions from the first row in which the splitting of the orbitals is close to the interelectronic repulsion (mostly d^4 to d^7 electronic configurations). In such cases, it is possible to crossover from one state to another *via* external stimuli, usually temperature.[30] Nevertheless, other external stimuli can induce spin-state changes in SCO-active metal complexes, such as pressure,[31–33] an external magnetic field,[34] light[35–37] and light driven ligand isomerization,[38–40] as well as the presence or absence of solvent molecules.[41]

When a transition metal ion with configuration d^4 to d^7 is in octahedral symmetry (O_h) coordination environment, its ground state can be low-spin (LS) or high-spin (HS), depending on the energy gap between the t_{2g} and e_g* orbitals ($10Dq$ or Δ_o) caused by the interaction of the metal with the ligands, in relation to the mean spin pairing energy (P), which is the energy penalty for having two paired electrons in the same orbital. As previously explained, the octahedral symmetry induces a partial degeneracy splitting of the metal ion's 3d energy level: a lower energy subset t_{2g} (d_{xy}, d_{xz}, d_{yz}) and a higher energy subset e_g* (d_{z^2} and $d_{x^2-y^2}$). The energy gap between these levels can be described in terms of ligand field force or crystal field splitting being $10Dq$ (or Δ_o), where Dq corresponds to a semi-empirical parameter related to the crystal force field.

A complex will be a LS ground state when $\Delta_o >> P$ (strong ligand field), that is, when overcoming Δ_o ligand-field splitting energy requires more energy than pairing the electrons. On the other hand, when $\Delta_o << P$ (weak ligand field), the complex will be a HS ground state, obeying the Hund's rule. In both cases, there is no spin transition. However, the SCO behaviour may appear when $|\Delta_o - P| \approx k_B T$. We need to point out that although the electron pairing energy is almost insensitive to the spin-state, Δ_o depends on the electronic state, and that Δ_o(LS) and Δ_o(HS) are not the same.[42] The SCO is related to LS and HS potential energy curves (Figure 1.7). In a configurational coordinate diagram along the totally symmetric stretch vibration, the minima (including the zero-point energy correction (ZPE)) of the potential wells of both LS and HS states are displaced relative to each other, both vertically and horizontally. ZPE is the lowest energy a quantum mechanical system may have, is the ground state energy of the system and it corresponds to the sum of electronic and vibrational contributions since, even at absolute zero, atoms and molecules retain some vibrational motion. Therefore, the condition for the thermal spin transition phenomenon becomes evident: in order to thermal populate the HS state,

the zero-point energy difference between the two states has to be of the order of thermally accessible energies, $k_B T$.

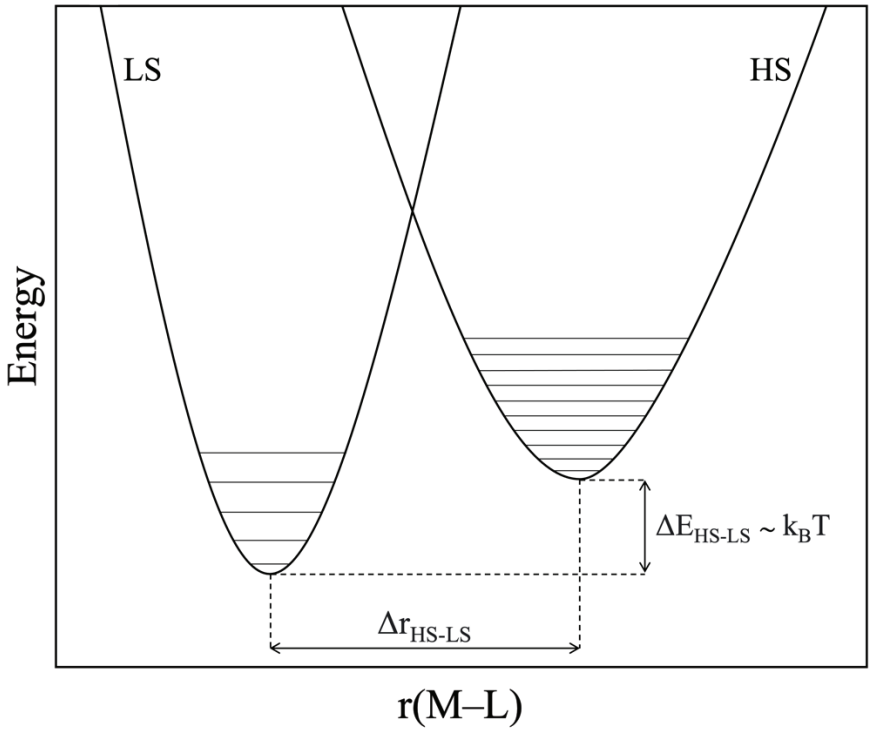

Figure 1.7. Low-spin and High-spin potential energy curves for a spin-crossover compound in the adiabatic approximation (T = 0 K).

Table 1.2. Nature of the ground state of first row transition metal ions from d^4 to d^7 in octahedral environment.

	$\Delta_o >> P$ **(LS)**	$\Delta_o << P$ **(HS)**
d^4	$^3T_{1g}$	^5E_g
d^5	$^2T_{2g}$	$^6A_{1g}$
d^6	$^1A_{1g}$	$^5T_{2g}$
d^7	^2E_g	$^4T_{1g}$

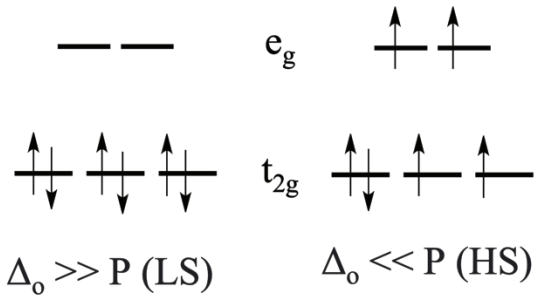

Figure 1.8. Electron configurations of the two possible ground states for a d^6 metal ion in an octahedral coordination environment. Left: low-spin state, right: high-spin state.

The change in the spin-state is an electron rearrangement that has profound changes in the physical properties of the system. We can see in Figure 1.8 that in d^6 metal ions in O_h symmetry these changes are clearly observed, since they go from diamagnetic systems (LS) to paramagnetic ones (HS).[43,44] Other changes in SCO compounds are change in its optical[30,43,45,46] and dielectric properties,[47–49] changes in colour,[50–56] among others. A clear example for the change in colour due to the spin-state is the $[Fe(ptz)_6](BF_4)_2$ (ptz = 1-propyltetrazole) compound, which is colourless/white at 293 K in its HS state, and deep purple at 20 K in its LS state.[30,57,58]

1.4.1. Applications of Spin-Crossover Compounds

This rearrangement of electrons, which causes changes in the properties of the system, confers switching properties that can have several practical potential applications in futuristic electronic devices.[14–17,47,59–62]

By spot-heating or cooling, it is possible to switch the colour or dielectric constant of pixels made of SCO materials, useful for memory and display devices.[47] It has also been demonstrated significant potential in the development of micro-electromechanical systems (MEMS)[63] and electronic elements,[64] which use such variation of corresponding mechanic and electric properties of these materials upon the spin change. There are even bending molecular artificial muscles based on spin-crossover molecules, so they have potential applications as actuators.[63,65]

These materials also have interest as photonic materials for the development of optical switches,[66] protective elements[67] and microthermometers.[68]

It is also possible to detect changes in the electrical resistance of SCO thin films and these changes can also be used to quench light emission, useful for electrical and electroluminescent

devices.[68] As mentioned, it is possible to crossover from a diamagnetic system to a paramagnetic one by changing the spin-state, for example in d^6 metal ions, useful for a temperature-sensitive magnetic resonance image (MRI) contrast agent.[69–71] Also, it has been achieved switchable liquid crystals,[72] nanoparticles[73] and thin films of SCO materials.[74,75]

For these reasons, SCO materials have raised a lot of attention from the chemistry and physics community over the last years.

1.4.2. External Stimuli

As previously said, this phenomenon has to be triggered by an external stimulus, such as temperature[30] but also pressure,[76] light irradiation,[35,77–80] magnetic[81,82] and electric fields,[83] or guest molecules,[84–86] among others.

1.4.2.1. Ligand Substitution, Anions and Solvate Effects

Replacing the ligands of the coordination complexes can modify their spin-state, generating or altering the SCO characteristics, since the electronic structure of the system is modified. This, in itself, would not be an external perturbation like changes in temperature, however, it can be useful. There are several examples in which by modifying the ligands a LS or a HS system can be obtained. For example, the species $[Fe(phen)(py)_2(NCS)_2]$ and $[Fe(phen)_2(NCS)_2]$ do present SCO behaviour. If the two thiocyanate groups are replaced by phenanthrolines, a LS complex, $[Fe(phen)_3]^{2+}$, is obtained. If the thiocyanates are replaced by strong-field ligands such as cyanides, a purely LS complex, $[Fe(phen)_2(CN)_2]$, is also obtained. On the other hand, a purely HS complex can be obtained by changing the thiocyanates for weak-field ligands such as chlorides, obtaining $[Fe(phen)_2(Cl)_2]$.[87] Another example is the $[Fe(py)_4(NCS)_2]$ complex, which is HS at room temperature, therefore, does not show a thermal spin transition. If two pyridines of the complex are replaced by a phenanthroline, the complex $[Fe(phen)(py)_2(NCS)_2]$ is obtained, which does present a spin transition, as previously mentioned.[88] These examples illustrate the different strength of the pyridine *versus* phenanthroline across the spectrochemical series.

Substitution within a ligand is not either an external perturbation *per se*, but can also significantly alter the spin-state of a system, as showed by the effects observed in LS $[Fe(phen)_3]^{2+}$. For instance, introducing a methyl group at the 2-position of phenanthroline induces spin-crossover behaviour. The approach of the N_{methyl} donor to the metal atom is

hindered due to steric effects. Methyl groups also introduce inter-ligand repulsions, destabilizing the singlet state of the complex.[89,90] In contrast, the bulkiness and electron-withdrawing nature of a chloro substituent make the singlet state inaccessible.[91,92] A more subtle chemical influence involves changing the anion associated with a cationic SCO system or altering the nature and extent of solvation in salts or neutral species. These variations can shift the transition temperature, potentially eliminating SCO observations altogether, or they may fundamentally change the nature of the transition, such as from abrupt to gradual.[93–97] All of this represents a form of electronic fine-tuning that could be further explored and extended.

1.4.2.2. Pressure

Now focusing on external perturbations, changes in pressure can cause SCO to occur. The ligand-field strength can be modified by applying pressure. Given that HS to LS transformations typically involve a decrease in metal–ligand distances and consequently a reduction in crystal unit-cell volume, pressure can serve as an external perturbation triggering this spin change. Applying pressure to a HS complex is anticipated to initially decrease the unit cell volume, leading to shorter intermolecular spacing and increased lattice strain. As the strain reaches a critical threshold, a structural rearrangement occurs, stabilizing the LS state due to its lower volume, resulting in a HS to LS conversion. Many researchers have studied pressure-induced spin-crossover compounds for iron(II) and cobalt(II) complexes, among others.[76,98–100] Thus, in general pressure tends to stabilise the LS state since the molecular volume is smaller than the one of the HS, and shifts the transition to higher temperatures.[31,32] König pointed out that there is a strong dependence of the ligand-field strength on the metal–donor atom bond lengths.[101] This leads to large differences in metal–ligand bond lengths between the two spin-states, and both effects cause a change in entropy that drives the transition.[32] An interesting application for pressure-induced spin conversion effects could be in the design of pressure sensors.[102]

1.4.2.3. Light Irradiation

Photochemically-induced perturbation of the equilibrium between low-spin $^1A_{1g}$ state and high-spin $^5T_{2g}$ spin-state of some iron (II) complexes in solution can be achieved by laser pulse irradiation. Rapid perturbation of this equilibrium in several iron(II) complexes occurs in the metal-to-ligand charge-transfer absorption region of the low spin-state, indicating the

formation of a ^{5}T state from the initially populated charge-transfer state. This allows for the investigation of spin change dynamics across a wide range of solvents.[35] Additionally, other experiments have demonstrated a trapped light-induced metastable high-spin state even at low temperatures, known as the light-induced excited-spin-state-trapping (LIESST) effect.[79,103] There are other effects such as ligand-driven light-induced spin change[38–40] (LD-LISC) based on the change of the ligand-field strength of a SCO complex by means of a photochemical reaction on the ligand,[40] and the charge-transfer-induced spin transition (CTIST), among others (CTIST can occur also due to thermal or pressure stimuli in addition to light).[104–106]

1.4.2.4. Temperature

Thermal perturbation is the most common feature to induce SCO, and it originates changes in the magnetic, structural and optical properties of the system, which makes the transition more perceptible and easier to follow. As mentioned in Section 1.4, the condition for the thermal spin transition is that the ZPE difference between the HS and the LS states must be approximately of the same order of magnitude as the thermal energy, $k_B T$. The lowest ZPE is the LS state, generally, and therefore the ground state is the LS state at 0 K or low temperatures. At elevated temperatures, the HS state is the thermodynamic stable one. This change is due to the entropic contributions which are more important in the HS state than in the LS state, it is accepted that the SCO can be seen as an entropy-driven phase conversion. The entropy difference between two states arises from basically two contributions:

1. Electronic contribution due to the higher spin multiplicity of the HS state.
2. Vibrational contribution due to lower vibrational frequencies in the HS state since metal–ligand bond lengths are longer than in the LS state due to the occupation of the antibonding e_g* orbitals.

It exists a temperature in which the population of both spin-states is equal ($\gamma_{HS} = \gamma_{LS} = 0.5$), that is, the two spin-states are present in a 1:1 ratio. This temperature is defined as the transition temperature, $T_{1/2}$ (Figure 1.9), and is a key parameter for the physical characterization of such systems.

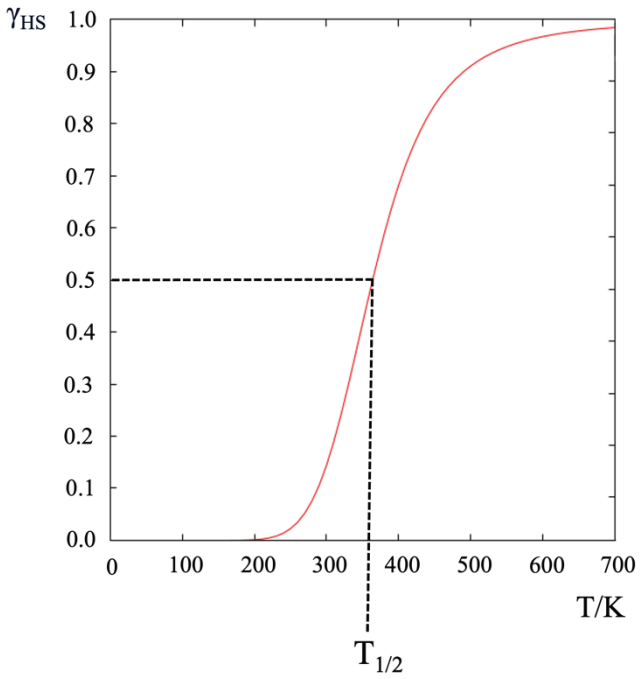

Figure 1.9. High-spin state molar fraction depending on temperature in Kelvin. The temperature at which $\gamma_{HS} = \gamma_{LS} = 0.5$ is the transition temperature, $T_{1/2}$.

1.5. Thermochemistry of the Spin-Crossover Phenomena

Temperature-induced spin transitions are the most studied ones owing to the adaptability of the techniques commonly used for the characterization of SCO-active complexes to its variation. Because of that, we will focus now on them to explain the thermodynamics behind this phenomenon. We will start with a thermodynamic approach to the spin transition at the molecular level, which will later be expanded to account for cooperative effects that can, in some cases, play an important role.

1.5.1. Mechanism of the Spin-Crossover

To explain the process, we will focus on octahedral iron(II) complexes, which are by far the most studied systems, and the central ones in this thesis.

At the molecular scale, the spin transition is an electron rearrangement and is characterized by a $\gamma_{HS} = f(T)$ curve. The sum of both spin populations is 1, therefore, $\gamma_{LS} = 1 - \gamma_{HS}$. Taking an octahedral complex:

Table 1.3. Change on the total spin angular momentum, *S*, depending on the metal ion.

Metal ion	*S* (LS)	*S* (HS)	ΔS ($S_{HS} - S_{LS}$)	Number of electrons transferred
d^4	1	2	1	1
d^5	1/2	5/2	2	2
d^6	0	2	2	2
d^7	1/2	3/2	1	1

As mentioned, the metal–ligand bond lengths are longer in the HS state than in the LS state due to the occupation of the antibonding e_g* orbitals. The difference typically is about between 0.14–0.24 Å for iron(II), 0.11–0.15 Å for iron(III), and 0.09–0.11 Å for cobalt(II).[42] As a general guideline, the LS bond lengths for Fe–N coordination are between 1.95–2.00 Å, for instance. In contrast, the HS bond lengths are normally ~0.2 Å longer than for the LS, ranging between 2.12 and 2.18 Å for Fe–N or Fe–O coordination.[107–109] The increase of the metal–ligand bond lengths in iron(II) compounds when transitioning from LS to HS is of about 10–15%, corresponding to an increase in the octahedron volume of about 25%.

One could think that the transition is more likely to occur when the energies of both spin-states are closer, which is a necessary condition but not sufficient. We need to consider a set of *N* noninteracting (isolated) SCO molecules in contact with a thermal bath *T* with a control of the external pressure *P*, that is, an isothermal and isobaric ensemble (*N*,*P*,*T*), and that it exists a thermodynamic equilibrium between the LS and HS states. Thus, the important state function for such conditions is the Gibbs free energy *G* (*G* = *H* – *TS*), which considers the entropy factor *S* in addition to the enthalpy factor *H*. At constant pressure, the change in the Gibbs free energy that leads the LS ⇄ HS transition is:[22]

$$G_{HS} - G_{LS} = (H_{HS} - H_{LS}) - T(S_{HS} - S_{lS}) \tag{1.2}$$

$$\Delta G = \Delta H - T\Delta S \tag{1.3}$$

When $T < T_{1/2}$ the enthalpic term is dominant favouring the LS state, whereas when $T > T_{1/2}$ the entropic term is dominant, favouring the HS state (entropy-driven phase transition).

Now let us examine the contributions to enthalpy and entropy changes. The enthalpy change consists of a temperature-independent electronic part (ΔH_{el}) and a vibrational part (ΔH_{vib}):

$$\Delta H = \Delta H_{el} + \Delta H_{vib} \tag{1.4}$$

ΔH_{el} is defined as the energy difference between the minima of the LS and HS potential energy curves. Strictly speaking, ΔH is the energy difference between the lowest vibrational states associated with the LS and HS electronic states, respectively (Figure 1.7).[42] That is, the vibrational part of the enthalpy can be obtained from the normal modes of vibration and the standard harmonic-oscillator approximations used in statistical thermodynamics:[110]

$$H_{vib} = \sum_{\lambda} \left(\frac{1}{2} h\nu_{\lambda} + \frac{h\nu_{\lambda} e^{-\frac{h\nu_{\lambda}}{k_B T}}}{1 - e^{-\frac{h\nu_{\lambda}}{k_B T}}} \right) \tag{1.5}$$

The sum runs over all the vibration modes λ.

ΔS can be divided into different contributions to the statistical disorder:

$$\Delta S = \Delta S_{el} + \Delta S_{vib} + \Delta S_{trans} + \Delta S_{rot} \tag{1.6}$$

ΔS_{trans} and ΔS_{rot} correspond to the entropy variation due to translation and rotation respectively, and can be neglected most of the time in the solid state.[22] ΔS_{el} is the electronic entropy variation, favors the HS state, is temperature independent and originates from the orbital and spin momenta difference between the HS and the LS states:

$$\Delta S_{el} = \Delta S_{orb} + \Delta S_{spin} \tag{1.7}$$

$$\Delta S_{orb} = R \ln \left(\frac{2L_{HS} + 1}{2L_{LS} + 1} \right) \tag{1.8}$$

$$\Delta S_{spin} = R \ln \left(\frac{2S_{HS} + 1}{2S_{LS} + 1} \right) \tag{1.9}$$

where R is the universal gas constant, L_i and S_i (i = HS, LS) are the total orbital and total spin momenta of the spin-state i, respectively. For a real case SCO Fe(II) complex, the local symmetry of the iron is usually lower than a perfect octahedral and the orbital contribution to the entropy change can be neglected since $L = 0$. In such case, $\Delta S_{el} = \Delta S_{spin} > 0$.

ΔS_{vib} corresponds to the vibrational entropy change, depends on the system and can be estimated using the harmonic vibrations. For isolated systems it only depends on the variation of the intramolecular modes between the HS and LS states. In the solid state the intermolecular vibrations need to be added even if they are considered less important than the intramolecular

ones, because both vibrations are coupled, and it is difficult to distinguish their own contributions.[22]

$$S_{vib}(T) = R\sum_{\lambda}\left(-\ln\left[1-e^{-\frac{h\nu_\lambda}{k_BT}}\right]+\frac{h\nu_\lambda}{k_BT}\frac{1}{e^{\frac{h\nu_\lambda}{k_BT}}}\right) \tag{1.10}$$

The sum runs over all the vibration modes λ. Assuming the low frequency approximation in which $h\nu << k_BT$, S_{vib} can be expressed as:

$$S_{vib} = -R\sum_{\lambda}\ln\left(\frac{h\nu_\lambda}{k_BT}\right) \tag{1.11}$$

Thus, the vibrational entropy change results in:

$$\Delta S_{vib} = S_{vib}^{HS} - S_{vib}^{LS} = R\sum_{\lambda=1}^{15}\ln\left(\frac{\nu_\lambda^{LS}}{\nu_\lambda^{HS}}\right) = 15R\ln\left(\frac{\langle\nu^{LS}\rangle}{\langle\nu^{HS}\rangle}\right) \tag{1.12}$$

In which λ = 15 molecular vibrational modes for a perfect iron(II) octahedral compound. The number of normal modes of vibration in a non-linear molecule is $3N - 6$, being N the number of "atoms". Thus, considering 6 ligands bonded to the iron(II), we would have $3\cdot7 - 6 = 15$ normal modes of vibration.

As a conclusion, vibrations in the SCO phenomena have an important role, more than the electronic entropy variation. Vibrational entropy is higher for the HS: the vibrational disorder is more pronounced in the HS state due to the longer metal–ligand bond lengths. Thus, HS state is favored at high temperatures as both ΔS and ΔH are positive. Hence, in order to observe a spin transition, the minimum of the LS potential energy curve must be slightly lower than the HS one. At low temperatures, below $T_{1/2}$, the enthalpy factor dominates, ΔG is positive and the LS state is the most stable. At high temperatures, above $T_{1/2}$, the entropy factor dominates, ΔG is negative and the HS state is the most stable.

The Gibbs free energy can be related to the equilibrium constant, K_{eq}, which can be expressed in terms of the molar fraction of each spin-state as follows:

$$\Delta G(T) = -RT\ln K_{eq} = -RT\ ln\left(\frac{\gamma_{HS}}{\gamma_{LS}}\right) = -RT\ ln\left(\frac{\gamma_{HS}}{1-\gamma_{HS}}\right) \tag{1.13}$$

Eq. 1.13 shows that when the molar fractions of both spin-states are the same, $\gamma_{HS} = \gamma_{LS}$, the ratio within the natural logarithm becomes 1, which implies that $\Delta G(T) = 0$. Therefore, Eq. 1.3 is satisfied and defines $T_{1/2}$ as

$$T_{1/2} = \frac{\Delta H}{\Delta S} \tag{1.14}$$

under equilibrium conditions. It is noteworthy that both ΔH and ΔS exhibit some temperature dependence (specially at low temperature values, Figure 1.10) that can be, in principle, neglected without sacrificing accuracy.

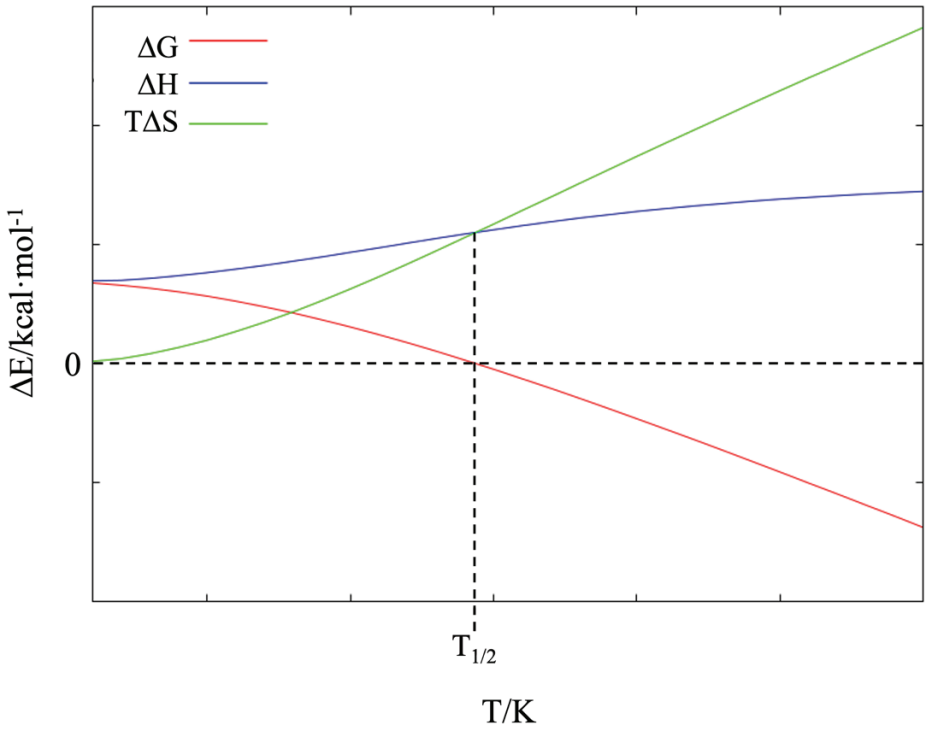

Figure 1.10. Gibbs free energy, enthalpy, and entropy dependence on temperature in an SCO complex.

1.5.2. Spin-Crossover and Cooperativity

Let us define the HS fraction, γ_{HS}, as the ratio of HS molecules (N_{HS}) to the total number of molecules (N) in a system of N noninteracting molecules undergoing an LS ⇌ HS transition. That is, $\gamma_{HS} = N_{HS}/N$. Consequently, the fraction of LS molecules, γ_{LS}, can be expressed as $\gamma_{LS} = N_{LS}/N = 1 - \gamma_{HS}$. An additional entropy term known as mixing entropy, S_{mix}, must be included

in the Gibbs free energy. Therefore, we can express the molar Gibbs free energy of an SCO system as follows:

$$G = \gamma_{HS} G_{HS} + (1 - \gamma_{HS}) G_{LS} - TS_{mix} \tag{1.15}$$

in which the mixing entropy, S_{mix}, reflects the loss of statistical information related to the fact that there are many possibilities of distributing N_{HS} molecules and N_{LS} molecules within the assembly of N molecules. In the thermodynamic limit, the mixing entropy is given by

$$S_{mix} = -k_B N[\gamma_{HS} \ln(\gamma_{HS}) + (1 - \gamma_{HS}) \ln(1 - \gamma_{HS})] \tag{1.16}$$

where $k_B N = R$ and is the gas constant. S_{mix} is maximum when $\gamma_{HS} = 0.5$ and vanishes when $\gamma_{HS} = 0$ or 1.

$$\left(\frac{\partial G}{\partial \gamma_{HS}}\right) = \Delta G + RT \ln\left(\frac{\gamma_{HS}}{1 - \gamma_{HS}}\right) \tag{1.17}$$

The equilibrium condition is the following one:

$$\left(\frac{\partial G}{\partial \gamma_{HS}}\right)_{T,P} = 0 \tag{1.18}$$

$$\Delta G = -RT \ln\left(\frac{\gamma_{HS}}{1 - \gamma_{HS}}\right) \tag{1.19}$$

$$\ln\left(\frac{\gamma_{HS}}{1 - \gamma_{HS}}\right) = \frac{\Delta G}{RT} = \frac{\Delta H}{RT} - \frac{\Delta S}{R} \tag{1.20}$$

With the equilibrium condition (Eq. 1.18) is then possible to follow up the thermal evolution of γ_{HS} (Figure 1.9), from which we can find the transition temperature value knowing that is the temperature in which $\gamma_{HS} = \gamma_{LS} = 0.5$.

$$ln\left(\frac{1 - \gamma_{HS}}{\gamma_{HS}}\right) = \frac{\Delta H}{RT} - \frac{\Delta S}{R} \tag{1.21}$$

Considering Eq. 1.14 and 1.21, γ_{HS} is expressed as:

$$\gamma_{HS} = \frac{1}{1 + e^{\frac{\Delta H}{R}\left(\frac{1}{T} - \frac{1}{T_{1/2}}\right)}} \tag{1.22}$$

and $T_{1/2}$ becomes:

$$T_{1/2} = \frac{\Delta H}{R \ln\left(\frac{1 - \gamma_{HS}}{\gamma_{HS}}\right) + \Delta S} \tag{1.23}$$

At $T = 0$ K, $\gamma_{HS} = 0$, that is, all the molecules are in the LS state. At high temperatures, γ_{HS} will tend to $\left(1 + e^{-\frac{\Delta H}{T_{1/2}}}\right)^{-1}$, instead of unity.[42] Furthermore, this transformation occurs smoothly over a large temperature range. Such transitions are typically seen in solution but are quite rare in the solid state. The abrupt first-order transition observed in SCO compounds are directly related to the emission or absorption of latent heat, which is entirely governed by interactions between SCO compounds. Unlike basic thermodynamic models that describe SCO in isolated molecules, understanding the complex interaction mechanisms among SCO molecules often requires introducing phenomenological parameters, and establishing the links between these parameters and experimentally measurable quantities is not straightforward. These parameters involve significant simplifications of collective behavior mechanisms in the solid state. Therefore, it is not valid to ignore intermolecular interactions. If the origin of the spin transition is essentially molecular, it is due to a delicate balance between enthalpy and entropy factors. The manifestation of this phenomenon is heavily influenced by the cooperativity within the assembly of molecules.[22,42]

There are two main thermodynamic models to account for this cooperative character: the regular solution model or Slichter and Drickamer[111] model and the domain model[11] based on the formation of domains within the assembly. From these models, even more refined models have been obtained. We will not explain these models since the studies carried out in this thesis are for isolated single molecules.

1.6. Types of Spin-Crossover Transitions

High-spin fraction (γ_{HS}) against temperature curves gives valuable information and exhibit various forms for solid-state systems (Figure 1.11). Among other factors, the degree of cooperativity is the most significant for the diversity of transitions behaviour. Cooperativity is determined by lattice properties and refers to the extent to which spin changes, particularly changes in metal–donor atom distances, propagate throughout the solid. This distance changes imply the molecules experience a change in volume because metal–ligand bond lengths enlarge when the e_g* antibonding orbitals are occupied.

With noninteracting SCO molecules, a gradual LS to HS transition can only be contemplated by increasing the temperature. Other types of transition such as abrupt, stepwise, with hysteresis or even incomplete occur due to the emission or absorption of a latent heat governed by interactions between SCO compounds and the degree of cooperativity between molecules associated with the transition.[22] Therefore, the more cooperativity, the more abrupt is the transition. In contrast to a gradual transition, which is a molecular property and is observed when cooperativity is relatively weak, abrupt hysteretic transitions are more likely to occur in systems which are highly cooperative. The SCO at one centre is communicated effectively to others, either through covalent bridges or strong intermolecular interactions.[112] The presence of hysteresis associated with a spin transition is often accompanied by a crystallographic phase change, and is one of the most important features of the whole spin-crossover phenomenon.

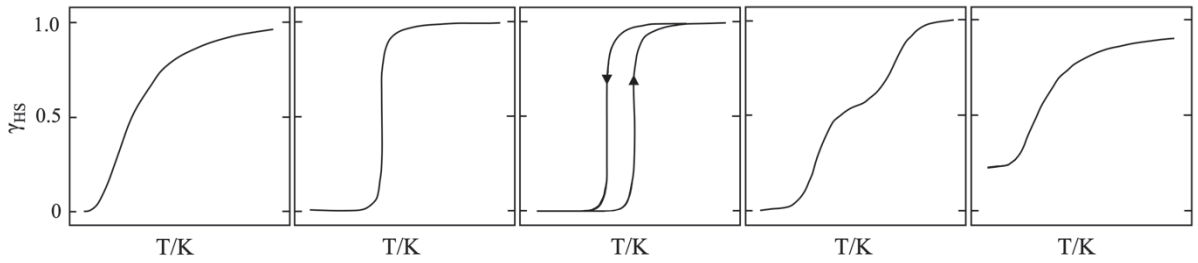

Figure 1.11. Type of transitions. From left to right: gradual, abrupt, with hysteresis, stepwise and incomplete. Figure adapted from Ref.[34]

SCO systems are bistable due to the fact that they can have two different spin-states, although many authors only mention their bistability when there is hysteresis. SCO systems are bistable by definition since they can be observed in two different electronic states in a certain range of some external stimuli, that is, two accessible electronic states that are minimum

in energy. The fact that many authors only mention bistability when there is hysteresis is due to the potential applications that this behaviour confers to the systems. Hysteresis potentiates the bistability and confers the system a memory effect, among others. Kahn and Martinez[47] highlighted the potential applications of this aspect of SCO in storage, memory and display devices.

This different type of transitions can be useful for molecular-based memory devices and displays, specially the abrupt ones involving large thermal hysteresis with an associated thermochromic effect.[113] To be used in memory devices, the bistability must be associated with a response function, for instance, optical or magnetic, which reveals the state of the system.[47] Thermal hysteresis favours the bistability of SCO complexes, since consists in a lag in the magnetic response on changing the temperature, resulting in a loop of the magnetic susceptibility vs temperature (multi-stability is possible in multi-step SCO compounds). Therefore, there are two transition temperatures, one obtained in the warming process $T_{1/2}\uparrow$, and another obtained during the cooling one $T_{1/2}\downarrow$. The spin-state depends on its immediate history, that is, when the compound enters the high temperature side, it retains the HS state whereas when it enters the low temperature region, it retains the LS state. These two states can be understood as a binary code, on/off, 0/1, therefore, represent a memory component since after the perturbation, the compound returns to ambient temperature (as long as it is within the temperature range of the loop) retaining that spin-state. To switch from HS to LS we need to cool to temperatures below $T_{1/2}\downarrow$, whereas from LS to HS we need to warm above $T_{1/2}\uparrow$, before allowing it to relax back to ambient temperature (retaining the new spin-state).

The key difference between a compound that undergoes SCO with thermal hysteresis (memory) and one that does not, is that the latter can only be used as a switch, because it cannot exist in two different spin-states at the same temperature, therefore, it does not have memory.

The pursuit of stable systems exhibiting a well-defined, broad hysteresis loop that encompass room temperature, as well as comprehension of the factors contributing to such behaviour remains ongoing.

1.7. Experimental Measurement of Spin-Crossover with Spectroscopic Techniques

SCO behaviour is observable by many characterization techniques because the changes in the spin-state produce variations in the microscopic and macroscopic properties such as the electron density of states, magnetic moment, metal–ligand bond lengths, vibrational properties, magnetization, unit cell volume, etc. These techniques must be adequate to monitor the

evolution of the different spin-states as a function of external stimulus such as temperature, pressure or electromagnetic radiation, and can be used in solution, solid state, thin films or even in nanoparticles, depending on the method of choice.[114]

As previously said, a thermally induced LS ⇄ HS transition is characterized by a $\gamma_{HS} = f(T)$ curve, and several techniques can be used to obtain such plot. The simplest method is to measure the temperature dependence of the molar magnetic susceptibility, χ_M, in which $\chi_M T$ is constant in the temperature range where all the molecules are in the same spin-state, with $(\chi_M T)_{LS}$ and $(\chi_M T)_{HS}$ values, respectively. Therefore, the $\gamma_{HS} = f(T)$ curve can be deduced in a straightforward manner from the experimental $\chi_M T = f(T)$ curve according to:[42]

$$\gamma_{HS} = \frac{\chi_M T - (\chi_M T)_{LS}}{(\chi_M T)_{HS} - (\chi_M T)_{LS}} \tag{1.24}$$

1.7.1. Vibrational Spectroscopy

Vibrational spectroscopic methods have been used to detect spin marker bands indicative of different spin-states within a sample. The key phenomenon followed by this type of spectroscopy is the shift in molecular vibrational frequencies upon spin-state switching.

In an SCO complex, metal–ligand bond lengths are enlarged when changing from LS to HS state due to the population of the antibonding orbitals, e_g*. In the HS state, then, the longer metal–ligand bonds are weaker compared to those in the LS state, resulting in increased elasticity and decreased force constants, especially those with stretching character. This leads to a softening of the metal–ligand stretching vibrations in the HS state compared to those in the LS state. These metal–ligand covalent stretching vibrations appear in the IR area under 1000 cm^{-1}, usually are below 500 cm^{-1}.

This effect is very pronounced for d^6 Fe(II) octahedral systems. For instance, in a Fe(II) complex with N-ligands, the Fe–N stretching vibrations may shift downward by up to 200 cm^{-1} during a LS to HS transition,[114–116] where all the Fe–ligand bonds are elongated by approximately 10-15%.

Some of these techniques are infrared spectroscopy (IR), Raman spectroscopy, nuclear inelastic scattering (NIS) or nuclear resonance vibrational spectroscopy.

1.7.2. Optical Spectroscopy

Switching the spin-state of an SCO complex brings changes in the spectral properties observed with optical spectroscopy. The change on the spin-state causes a change on the ground state term and multiplicity and thus, selection rules change. SCO systems often show changes in colour with the transition, which makes them interesting materials for temperature, pressure and solvent sensors.[117]

In terms of ligand-field theory, the spin switching corresponds to a shift along the $10Dq/B$ axis of the Tanabe-Sugano diagram. The ligand-field strength decreases with the elongation of the metal–ligand bonds due to the LS-HS transition. $10Dq$ and B (that barely changes on spin transition), could be derived from optical absorption spectra of single crystals.[58,118]

Optical spectroscopy, similar to vibrational spectroscopy, tracks spin-crossover processes across various mediums: solution, solid state *via* transmission and/or reflection techniques, thin films, and nanoparticles. Acclaimed for its quickness, it is fundamental in studying fast and ultrafast photoinduced relaxation processes in SCO complexes, following McGarvey and coworkers' approach.[35] In addition to solution studies, single crystals reveal notable insights into corresponding HS to LS relaxation rates.[119] The emergence of luminescent SCO materials[14] prompts the utilization of emission spectroscopy. By modifying SCO complexes with fluorescent moieties, fluorescence is measured against temperature changes, reflecting the spin-state of the crossover centre. Chirality integration in SCO complexes/materials enables circular dichroism (CD) spectroscopy. Despite limited examples, Guralskiy *et al.*[120] highlighted a memory effect in the chiro-optical properties linked with spin transition hysteresis.

1.7.3. Nuclear Magnetic Resonance

The Nuclear Magnetic Resonance (NMR) pattern of diamagnetic molecules differ from the paramagnetic ones. In fact, NMR spectra of SCO complexes are necessarily the ones of the paramagnetic molecules.[114] The ^{1}H-NMR measurements offer a direct method to track spin-crossover phenomena in solution.

Paramagnetic NMR techniques were initially applied to study spin equilibria. Subsequent research focused on octahedral Fe(III) dithiocarbamate SCO systems. Key findings from NMR spectra for spin switching include magnetic susceptibility measurements *via* the Evans method[121,122] or the more modern ideal solution model, and deviations from Curie behaviour

indicating spin equilibria. Recently, Hogue *et al*. proposed an improved method for measuring magnetic susceptibility using NMR, analysing the spectra of SCO systems and their diamagnetic zinc analogue.[123] Additionally, variable temperature ^{1}H-NMR spectroscopy has been employed to deduce thermodynamics and kinetics for SCO in kinetically robust Fe(II) complexes, as demonstrated years ago.[124]

1.7.3.1. Evans Method

The Evans method is a technique for calculating the number of unpaired electrons in solution-state metal complexes, which can be determined from the magnetic moment of the given molecule. The magnetic moments of fist row transition metal complexes can be approximated from the contributions of unpaired electrons, called the spin-only magnetic moment. μ_{eff} is, to a first approximation, a simple function of the number of unpaired electrons. For the second and third row transition metal complexes, both the spin and orbital contributions must be considered. In general, spin-orbit coupling causes μ_{eff} to deviate from the spin-only formula.

Assuming a spin-only situation:

$$\mu = g\mu_B\sqrt{S(S+1)} \tag{1.25}$$

$$\mu_{eff} = \frac{\mu}{\mu_B} \tag{1.26}$$

The magnetic moment reflects the degree of magnetization of a complex in an applied magnetic field, as indicated by its magnetic susceptibility.

$$\chi_M T = \frac{\mu_{eff}^2}{8} \tag{1.27}$$

$$\mu_{eff} = 2.83\sqrt{\chi_M T} \tag{1.28}$$

If there is no orbital contribution, we can determine the μ_{eff} and χ_M calculated for n unpaired electrons (g ≈ 2.00 for the free electron) as:

$$\mu_{eff} = g\sqrt{S(S+1)} = 2\sqrt{S(S+1)} = \sqrt{n(n+2)} \tag{1.29}$$

Table 1.4. Spin, number of unpaired electrons, effective magnetic moment, and magnetic susceptibility (spin-only approach):

S	n	μ_{eff}	$\chi_M T$
1/2	1	$3^{1/2} = 1.73$	0.37
1	2	$8^{1/2} = 2.83$	1.00
3/2	3	$15^{1/2} = 3.87$	1.87
2	4	$24^{1/2} = 4.90$	3.00
5/2	5	$35^{1/2} = 5.92$	4.38
3	6	$48^{1/2} = 6.92$	6.00
7/2	7	$63^{1/2} = 7.93$	7.87

In NMR spectroscopy, the chemical shift of a species is influenced by the overall magnetic susceptibility of the sample solution. Thus, the chemical shift of a solvent alters when a paramagnetic solute is present. The Evans method exploits this relationship to derive the magnetic susceptibility and subsequently the magnetic moment of the paramagnetic solute.

Data is obtained collecting a ^{1}H-NMR spectrum of a sample comprising a capillary filled with pure solvent, placed within an NMR tube containing the paramagnetic solution. The resulting NMR spectrum displays two solvent peaks: one for the solvent interacting with the compound and another for the solvent in the capillary. The magnetic susceptibility is determined from the frequency difference and concentration of the paramagnetic compound in the sample (subtracting the diamagnetic correction). Then, the magnetic moment is calculated in terms of the Bohr magneton unit, allowing for comparison with theoretical spin-only values to estimate the number of unpaired electrons in the sample.

This analysis of magnetic data provides valuable thermodynamic parameters for the spin transition, treating it as a thermal equilibrium process between two spin-states. The difference between states is categorized in terms of magnetic moment (μ_{eff}) or HS molar fraction (γ_{HS}) as a function of temperature. The magnetic moment is frequently employed due to the change in the number of unpaired electrons between both states, giving magnetic moment values around 4.90 μ_B. for the HS and 0.00 μ_B for the LS (applying the spin-only approximation) in a Fe(II) octahedral compound.

1.7.4. Mössbauer Spectroscopy

Mössbauer spectroscopy relies on the Mössbauer effect, first observed by Rudolf Mössbauer in 1958. This effect involves the nearly recoil-free emission and absorption of nuclear gamma rays in solids. As a result, Mössbauer spectroscopy is highly sensitive to subtle alterations in the chemical surroundings of specific nuclei.

^{57}Fe Mössbauer spectroscopy has emerged as a powerful technique for investigating the oxidation and spin-states of iron in coordination compounds.[30,125,126]. Key parameters extracted from Mössbauer spectra, such as the isomer shift (δ) and quadrupole splitting (ΔE_Q), exhibit notable variations between iron(II)-HS and iron(II)-LS states. The resonance signal area fractions correlate with the concentrations of coexisting spin-states, often allowing for the derivation of the spin transition curve, $\gamma_{HS}(T)$. Typically, plotting the area fraction of the dominant spin-state, typically the HS state, against temperature yields the spin transition curve. It shows two well resolved quadrupole doublets with variable intensity as a function of temperature. One of these doublets is associated with LS molecules and the other with HS molecules. The HS molar fraction may then be deduced from the relative intensities of these quadrupole doublets.[42] This method allows to obtain the magnitude and the symmetry for the electron density as well as the magnetic field at the corresponding Mössbauer nuclide. The application of ^{57}Fe Mössbauer spectroscopy has been one of the most powerful quantitative probes of the spin-state because it is so sensitive to the contribution of the 3d electrons in iron compounds. The variation in the electron density and oxidation state of the iron ions when transitioning from LS to HS is observed in a change of the isomer shift. Changes in the asymmetry of the electron cloud can be detected by variations in the quadrupole splitting.[114]

1.7.5. X-Ray Spectroscopy

X-ray spectroscopy encompasses various methods where spectroscopic data is derived from the creation of a core hole by an X-ray photon. These techniques offer valuable insights into electronic and molecular structures, often combined with element-, spin-, orbital-, and orientational sensitivity.[127–129] In the context of SCO systems, X-ray spectroscopy becomes crucial for accurately identifying spin and oxidation states, especially in heteronuclear or charge transfer systems like, for instance, Prussian-blue analogues. In transition metal complexes, the metal centre is usually the absorbing atom, although in principle, the donor atom of the ligand can also be examined.

It exists the X-ray absorption spectroscopy and also the X-ray emission spectroscopy technique.

1.7.6. Electron Paramagnetic Resonance Spectroscopy

Electron paramagnetic resonance (EPR), also known as electron spin resonance (ESR) spectroscopy, is employed to investigate chemical species containing one or more unpaired electrons, including organic and inorganic free radicals, as well as inorganic complexes featuring transition metal ions. While the fundamental principles of EPR resemble those of NMR, EPR measures the relaxation of excited electron spins rather than excited nuclear spins. Although less prevalent than NMR, EPR's specificity to paramagnetic species makes it highly valuable.

For iron(II) compounds, the EPR is silent, so the lattice is doped with an EPR active ion such as copper(II). The HS-LS transition in an iron compound can be detected by analysing the EPR spectrum of a doped species, serving as a "spy" to obtain insights of the spin-state of the host lattice.[130]

1.7.7. Comments on Computational Methods to Study Spin-Crossover Phenomena

The interpretation of vibrational band patterns from various methods benefits greatly from quantum chemistry calculations, notably density functional theory (DFT), known for its accuracy in predicting molecular geometry and vibrational frequencies.[131,132] DFT allows precise calculations of molecular vibrations with an accuracy of 20 to 30 cm^{-1},[115] helping in the assignment of spin-state marker bands to specific vibrational modes. Both IR spectra and pDOS (partial density of vibrational states) derived from NIS (nuclear inelastic scattering) are well reproduced with DFT, as are vibrational frequencies observed in Raman spectra, although calculating Raman intensities is more complex.[115] DFT analysis also provides crucial parameters like zero-point correction, total vibrational energy, and vibrational entropy contribution, complementing experimental data. However, DFT calculations, typically performed for isolated molecules in vacuum, may overlook or inaccurately represent soft vibrations crucial for entropy. While solid-state calculations have shown effectiveness in predicting spin transition energetics,[133] computational demands and limitations persist, particularly for soft transitions. Despite these challenges, methods like molecular dynamics[132]

offer promising avenues for advancing understanding in this field, yet classical isotope substitution remains a potent tool for bands assignment.[134]

In general, standard DFT methods may not accurately predict electronic spectra compared to their performance in geometry and vibrational frequency calculations. However, time-dependent DFT serves as a standard procedure and offers a reasonable estimation of the electronic structure and UV-vis spectra of SCO complexes.[131,135–137] For more precise calculations, wave function-based methods are recommended.[131]

1.8. Importance of Spin-Crossover Materials

SCO systems are significant due to their fascinating physical properties and wide-ranging applications in materials science, chemistry, and technology. As previously mentioned, SCO materials exhibit bistability, which offers many applications such as display, sensor, storage and memory devices, and the change in their magnetic and optical properties can also make them useful to act as switches.[14–17,47,59–62,64,66–75] There are also bilayer actuator devices that use molecular SCO devices.[63,65]

Most SCO-active complexes studied have been either monometallic or polymeric (metal-organic frameworks, MOFs, also known as porous coordination polymers, PCPs).[138,139] However, relatively recently, chemists focused their attention on linking multiple metal centres together within a discrete molecule to enhance the SCO properties and obtain abrupt and hysteretic transitions, and multistep switching. Ligand design have led to self-assembly of discrete polynuclear iron(II) complexes, forming structures such as helicates, cages, cubes and other supramolecular architectures with rich SCO activity. These supramolecular structures enhance the chemistry related to host-guest interactions.[140]

The majority of SCO Fe(II) complexes are either mononuclear or polymeric, with discrete di- to polynuclear systems being significantly much rarer.[14,141–146] This also extends to other metals such as Fe(III), Co(II), and Mn(II), for which only a limited number of polynuclear SCO systems have been reported.[14] Discrete polynuclear complexes, where multiple metal centres are covalently bridged to enhance cooperativity, offer distinct advantages over polymeric alternatives. These include greater control in design and synthesis and more straightforward characterization.[14,143,147,148] Furthermore, polynuclear systems, whether discrete or polymeric, provide the possibility of multistep SCO behaviour, enabling access to multiple spin states and facilitating polynary information storage instead of traditional binary.[17,47,149]

Computational studies can help in the rational design of SCO systems, either mononuclear or polynuclear, with tailored properties. New SCO systems with tailored properties are an important target towards the rational design of multifunctional materials that can be operated at specific temperatures. In this thesis, several computational tools are used to help in gaining insights into how to modulate the transition temperatures in several systems, going from mononuclear Fe(II) and Cr(II) compounds to dinuclear Fe(II) metal-organic cages.

1.9. Objectives

The main objective of this thesis is to explore the theoretical and computational modelling of several compounds that show spin-crossover behaviour. To do so, it is necessary to accurately predict their electronic structure, as well as to understand how the transition temperatures can be tuned, so we can obtain new materials with tailored properties. Thus, several steps need to be accomplished:

1. Evaluate the performance of several DFT functionals in predicting the energies of the different spin-states for the systems of study.
2. Correct such energies at the DFT level with the harmonic approximation in order to compute the thermodynamics of the systems and therefore, compute the transition temperatures.
3. Calculate the d orbitals energy gap at a higher level of computation such as N-Electron Valence State Perturbation Theory (NEVPT2) level followed by the *Ab Initio* Ligand Field Theory (AILFT) approximation, to obtain information about the orbitals and the Δ_o parameter.
4. Compare the results with available experimental data to ensure the methods used are sufficient to study such properties.
5. Study several possible modifications on the systems that can tune the transition temperatures in order to find correlations that can help in the prediction of new compounds with tailored properties without the need of synthesise them or even to perform calculations.

The thesis is organised first with introductory chapters (current chapter: **Chapter 1**, and **Chapter 2**) to put some context on the field of this thesis, and secondly with the studies that were carried out and their results (**Chapter 3**, **Chapter 4** and **Chapter 5**).

In **Chapter 1**, we have delved into several theories to describe the transition metal complexes: the crystal field theory, the molecular orbital theory and the ligand field theory.

After that, an introduction to the spin-crossover phenomena has been presented in which it is explained, in a general way, the characteristics of such phenomena, the mechanisms that take place, the potential applications of the systems that can undergo SCO as well as some of the experimental measurement techniques for such systems. **Chapter 2** provides an overview of the theoretical methods used in this thesis, starting from the Schrödinger equation, through density functional theory to post-HF methods such as Multireference Methods and *Ab Initio* Ligand Field Theory.

Chapter 3 introduces the study of two unusual SCO complexes, using DFT methods. This uncommon SCO systems are chromium(II)-based and anionic iron(II)-based complexes. These studies provide models that can help in the design of new systems exhibiting SCO behaviour. **Chapter 4** is the work developed during the thesis' internship at University of Oxford under the supervision of Prof. John E. McGrady, and consists in the application of a new methodology, the Multiconfiguration Pair-Density Functional Theory, which in principle can give energy results comparable with second order perturbation theory accuracy but involving less computational cost.

Until now, the systems studied in this thesis were mononuclear. **Chapter 5** increases the complexity by introducing dinuclear Fe(II)-based SCO metal-organic cages. Using DFT methods and an adaptation of the Slichter and Drickamer model applied to dinuclear systems, we were able to model and understand the tuning in the spin transition properties, not only through the functionalization of the ligands, but also through the introduction of different guests into the cavity of the metal-organic cage.

Finally, the general conclusions of the thesis are presented in **Chapter 6**, including the key findings, the implications to the SCO materials field, and suggestions for future research.

1.10. References

1. L. Cambi and L. Szegö, *Ber. Dtsch. Chem. Ges. (A and B Series)*, 1931, **64**, 2591–2598.
2. L. Cambi and L. Malatesta, *Ber. Dtsch. Chem. Ges. (A and B Series)*, 1937, **70**, 2067–2078.
3. L. Pauling and C. D. Coryell, *PNAS*, 1936, **22**, 210–216.
4. L. Pauling, C. D. Coryell and F. Stitt, *J. Am. Chem. Soc.*, 1937, **59**, 633–642.
5. L. E. Orgel, Bruxelles, 1956.
6. V. H. Bethe, *Ann. Phys.*, 1929, **395**, 133–208.
7. J. H. Van Vleck, *J. Chem. Phys.*, 1935, **3**, 807–813.

8. J. H. Van Vleck, *J. Chem. Phys.*, 1935, **3**, 803–806.
9. R. S. Mulliken, *Phys. Rev.*, 1932, **40**, 55–62.
10. E. König and K. Madeja, *Inorg. Chem.*, 1967, **6**, 48–55.
11. M. Sorai and S. Seki, *J. Phys. Chem. Solids*, 1974, **35**, 555–570.
12. J. K. Beattie, N. Sutin, D. H. Turner and G. W. Flynn, *J. Am. Chem. Soc.*, 1973, **95**, 2052–2054.
13. J. K. Beattie, R. A. Binstead and R. J. West, *J. Am. Chem. Soc.*, 1978, **100**, 3044–3050.
14. M. A. Halcrow, *Spin-Crossover Materials: Properties and Applications*, John Wiley & Sons, Ltd., 2013.
15. A. Real, J. Zarembowitch, O. Kahn and X. Solans, *Inorg. Chem.*, 1987, **26**, 2939–2943.
16. K. S. Murray and C. J. Kepert, in *Spin Crossover in Transition Metal Compounds I*, eds. P. Gütlich and H. A. Goodwin, 2004, vol. 233, pp. 195–228.
17. J.-F. Létard, P. Guionneau and L. Goux-Capes, in *Spin Crossover in Transition Metal Compounds III*, eds. P. Gütlich and H. A. Goodwin, 2004, vol. 235, pp. 221–249.
18. J. Ribas, *Coord. Chem.*, Wiley-VCH, 2008.
19. J. H. Van Vleck, *Phys. Rev.*, 1932, **41**, 208–215.
20. J. H. Van Vleck and A. Sherman, *Rev. Mod. Phys.*, 1935, **7**, 167–228.
21. C. J. Ballhausen, *Introduction to Ligand Field Theory*, McGraw-Hill, First Edition., 1962.
22. W. Nicolazzi and A. Bousseksou, *C. R. Chimie*, 2018, **21**, 1060–1074.
23. R. G. Shulman and S. Sugano, *Phys. Rev. Lett.*, 1961, **7**, 175–159.
24. V. K. Fajans, *Die Naturwissenschaften*, 1923, **11**, 165–172.
25. T. Ryutaro, *Bull. Chem. Soc. Jpn.*, 1938, **13**, 436–450.
26. L. E. Orgel, *An Introduction to Transition-Metal Chemistry: Ligand Field Theory*, 2nd edn., 1966.
27. J. Owen and K. W. H. Stevens, *Nature*, 1953, **171**, 836.
28. M. Tinkham, *Proc. R. Soc. Lond. A. Math. Phys. Sci.*, 1956, **236**, 535–548.
29. C. E. Schäffer and K. C. Jørgensen, *J. Inorg. Nucl. Chem.*, 1958, **8**, 143–148.
30. P. Gütlich, A. B. Gaspar and Y. Garcia, *Beilstein J. Org. Chem.*, 2013, **9**, 342–391.
31. H. A. Ewald, R. L. Martin, I. G. Ross and A. H. White, *The Royal Society*, 1964, **280**, 235–257.
32. P. Gütlich, V. Ksenofontov and A. B. Gaspar, *Coord. Chem. Rev.*, 2005, **249**, 1811–1829.
33. G. G. Levchenko, A. V. Khristov and V. N. Varyukhin, *Low Temp. Phys.*, 2014, **40**, 571–585.

34. P. Gütlich and H. A. Goodwin, in *Spin Crossover in Transition Metal Compounds I*, eds. P. Gütlich and H. A. Goodwin, 2004, vol. 233, pp. 1–47.
35. J. J. Mcgarvey and I. Lawthers, *J. Chem. Soc., Chem. Commun.*, 1982, **16**, 906–907.
36. J.-F. Létard, *J. Mater. Chem.*, 2006, **16**, 2550–2559.
37. G. Chastanet, C. Desplanches, C. Baldé, P. Rosa, M. Marchivie and P. Guionneau, *Chemistry Squared*, 2018, **2**, 1–18.
38. M.-L. Boillot, S. Chantraine, J. Zarembowitch, J.-Y. Lallemand and J. Prunet, *New J. Chem.*, 1999, **23**, 179–184.
39. B. Brachňaková and I. Šalitroš, *Chemical Papers*, 2018, **72**, 773–798.
40. M.-L. Boillot, J. Zarembowitch and A. Sour, in *Spin Crossover in Transition Metal Compounds II*, 2004, vol. 234, pp. 261–276.
41. R. G. Miller and S. Brooker, *Chem. Sci.*, 2016, **7**, 2501–2505.
42. O. Kahn, *Molecular Magnetism*, VCH Publishers, Inc., New York, 1993.
43. J. A. Real, A. B. Gaspar and M. Carmen Muñoz, *Dalton Trans.*, 2005, 2062–2079.
44. G. Aromí, L. A. Barrios, O. Roubeau and P. Gamez, *Coord. Chem. Rev.*, 2011, **255**, 485–546.
45. C. Bartual-Murgui, A. Akou, C. Thibault, G. Molnár, C. Vieu, L. Salmon and A. Bousseksou, *J. Mater. Chem. C*, 2015, **3**, 1277–1285.
46. O. Roubeau, *Chem. Eur. J.*, 2012, **18**, 15230–15244.
47. O. Kahn and C. J. Martinez, *Science*, 1998, **279**, 44–48.
48. C.-F. Wang, R.-F. Li, X.-Y. Chen, R.-J. Wei, L.-S. Zheng and J. Tao, *Angew. Chem. Int. Ed.*, 2015, **54**, 1574–1577.
49. S. Bonhommeau, T. Guillon, L. M. Lawson Daku, P. Demont, J. S. Costa, J.-F. Létard, G. Molnár and A. Bousseksou, *Angew. Chem. Int. Ed.*, 2006, **45**, 1625–1629.
50. T. Houari, E. Cuza, D. Pinkowicz, M. Marchivie, S. Yefsah and S. Triki, *Crystals*, 2018, **8**, 401.
51. B. Gallois, J. A. Real, C. Hauw and J. Zarembowitch, *Inorg. Chem.*, 1990, **29**, 1152–1158.
52. P. Ganguli, P. Gütlich and E. W. Müller, *J. Chem. Soc., Dalton Trans.*, 1981, 441–446.
53. A. Tissot, X. Kesse, S. Giannopoulou, I. Stenger, L. Binet, E. Rivière and C. Serre, *Chem. Commun.*, 2019, **55**, 194–197.
54. K. Kagesawa, Y. Ichikawa, H. Iguchi, B. K. Breedlove, Z. Li, M. Yamashita, A. Okazawa, W. Kosaka and H. Miyasaka, *Chem. Lett.*, 2019, **48**, 1221–1224.

55. K. A. Zenere, S. G. Duyker, E. Trzop, E. Collet, B. Chan, P. W. Doheny, C. J. Kepert and S. M. Neville, *Chem. Sci.*, 2018, **9**, 5623–5629.
56. L. Sun, A. Rotaru, K. Robeyns and Y. Garcia, *Ind. Eng. Chem. Res.*, 2021, **60**, 8788–8798.
57. A. Hauser, *Chem. Phys. Lett.*, 1986, **124**, 543–548.
58. A. Hauser, *J. Chem. Phys.*, 1991, **94**, 2741–2748.
59. E. Coronado, *Nat. Rev. Mater.*, 2020, **5**, 87–104.
60. A. Bousseksou, G. Molnár, L. Salmon and W. Nicolazzi, *Chem. Soc. Rev.*, 2011, **40**, 3313–3335.
61. G. Molnár, L. Salmon, W. Nicolazzi, F. Terki and A. Bousseksou, *J. Mater. Chem. C*, 2014, **2**, 1360–1366.
62. G. Molnár, S. Rat, L. Salmon, W. Nicolazzi and A. Bousseksou, *Adv. Mater.*, 2018, **30**, 1703862.
63. H. J. Shepherd, I. A. Gural'skiy, C. M. Quintero, S. Tricard, L. Salmon, G. Molnár and A. Bousseksou, *Nat. Commun.*, 2013, **4**, 2607.
64. A. Rotaru, J. Dugay, R. P. Tan, I. A. Gural'skiy, L. Salmon, P. Demont, J. Carrey, G. Molnár, M. Respaud and A. Bousseksou, *Adv. Mater.*, 2013, **25**, 1745–1749.
65. B. Tondu, M. Piedrahita-Bello, L. Salmon, G. Molnár and A. Bousseksou, *Sens. Actuators A Phys.*, 2022, **335**, 113359.
66. I. A. Gural'skiy, C. M. Quintero, K. Abdul-Kader, M. Lopes, C. Bartual-Murgui, L. Salmon, P. Zhao, G. Molnár, D. Astruc and A. Bousseksou, *J. Nanophotonics*, 2012, **6**, 063517.
67. V. Nagy, K. Halász, M.-T. Carayon, I. A. Gural'skiy, S. Tricard, G. Molnár, A. Bousseksou, L. Salmon and L. Csóka, *Colloids Surf A: Physicochem. Eng. Aspects*, 2014, **456**, 35–40.
68. L. Salmon, G. Molnár, D. Zitouni, C. Quintero, C. Bergaud, J.-C. Micheau and A. Bousseksou, *J. Mater. Chem.*, 2010, **20**, 5499–5503.
69. A. Tsukiashi, K. S. Min, H. Kitayama, H. Terasawa, S. Yoshinaga, M. Takeda, L. F. Lindoy and S. Hayami, *Sci. Rep.*, 2018, **8**, 14911.
70. I.-R. Jeon, J. G. Park, C. R. Haney and T. D. Harris, *Chem. Sci.*, 2014, **5**, 2461–2465.
71. S. Venkataramani, U. Jana, M. Dommaschk, F. D. Sönnichsen, F. Tuczek and R. Herges, *Science*, 2011, **331**, 445–448.
72. A. B. Gaspar and M. Seredyuk, *Coord. Chem. Rev.*, 2014, **268**, 41–58.

73. D. J. Harding, in *Novel Magnetic Nanostructures: Unique Properties and Applications*, Elsevier, 2018, pp. 401–426.
74. M. Cavallini, *Phys. Chem. Chem. Phys.*, 2012, **14**, 11867–11876.
75. T. Mallah and M. Cavallini, *C. R. Chimie*, 2018, **21**, 1270–1286.
76. V. Ksenofontov, G. Levchenko, H. Spiering, P. Gütlich, J.-F. Letard, Y. Bouhedja and O. Kahn, *Chem. Phys. Lett.*, 1998, **294**, 545–553.
77. I. Lawthers and J. J. McGarvey, *J. Am. Chem. Soc.*, 1984, **106**, 4280–4282.
78. J. K. McCusker, K. N. Walda, R. C. Dunn, J. D. Simon, D. Magde and D. N. Hendrickson, *J. Am. Chem. Soc.*, 1992, **114**, 6919–6920.
79. S. Decurtins, P. Gütlich, C. P. Köhler, H. Spiering and A. Hauser, *Chem. Phys. Lett.*, 1984, **105**, 1–4.
80. S. Bedoui, M. Lopes, W. Nicolazzi, S. Bonnet, S. Zheng, G. Molnár and A. Bousseksou, *Phys. Rev. Lett.*, 2012, **109**, 135702.
81. Y. Qi, E. W. Müller, H. Spiering and P. Gütlich, *Chem. Phys. Lett.*, 1983, **101**, 503–505.
82. S. Bonhommeau, G. Molnár, M. Goiran, K. Boukheddaden and A. Bousseksou, *Phys. Rev. B*, 2006, **74**, 064424.
83. C. Lefter, V. Davesne, L. Salmon, G. Molnár, P. Demont, A. Rotaru and A. Bousseksou, *Magnetochemistry*, 2016, **2**, 18.
84. G. J. Halder, C. J. Kepert, B. Moubaraki, K. S. Murray and J. D. Cashion, *Science*, 2002, **298**, 1762–1765.
85. S. Cobo, G. Molnár, J. A. Real and A. Bousseksou, *Angew. Chem. Int. Ed.*, 2006, **45**, 5786–5789.
86. M. Ohba, K. Yoneda, G. Agustí, M. C. Muñoz, A. B. Gaspar, J. A. Real, M. Yamasaki, H. Ando, Y. Nakao, S. Sakaki and S. Kitagawa, *Angew. Chem. Int. Ed.*, 2009, **121**, 4767–4771.
87. K. Madeja and E. König, *J. Inorg. Nucl. Chem.*, 1963, **25**, 377–385.
88. R. Claude, J. A. Real, J. Zarembowitch, O. Khan, O. Lahcène, D. Grandjean, K. Boukheddaden, F. Varret and A. Dworkin, *Inorg. Chem*, 1990, **29**, 4442–4448.
89. H. A. Goodwin and R. N. Sylva, *Aust. J. Chem.*, 1968, **21**, 83–90.
90. H. A. Goodwin, E. S. Kucharski and A. H. White, *Aust. J. Chem.*, 1983, **36**, 1115–1124.
91. W. M. Reiff and G. J. Long, *Inorg. Chem.*, 1974, **13**, 2150–2153.
92. J. Fleisch, P. Gütlich and K. M. Hasselbach, *Inorganica Chim. Acta*, 1976, **17**, 51–54.
93. G. A. Renovitch and W. A. Baker, *J. Am. Chem. Soc.*, 1967, **89**, 6377–6378.

94. M. Sorai, Y. Yumoto, D. M. Halepoto and L. F. Larkworthy, *J. Phys. Chem. Sol.*, 1993, **54**, 421–430.
95. H. Spiering, E. Meissner, H. Köppen, E. W. Müller and P. Gütlich, *Chem. Phys.*, 1982, **68**, 65–71.
96. R. Hogg and R. G. Wilkins, *J. Chem. Soc.*, 1962, 341–350.
97. R. N. Sylva and H. A. Goodwin, *Aust. J. Chem.*, 1967, **20**, 479–496.
98. J. Zarembowitch, C. Roux, M. L. Boillot, R. Claude, J. P. Itie, A. Polian and M. Bolte, *Mol. Cryst. Liq. Cryst.*, 1993, **234**, 247–254.
99. J. Jeftić and A. Hauser, *Chem. Phys. Lett.*, 1996, **248**, 458–463.
100. J. Jeftić, R. Hinek, S. C. Capelli and A. Hauser, *Inorg. Chem.*, 1997, **36**, 3080–3087.
101. E. König, *Ber. Bunsenges. Phys. Chem.*, 1972, **76**, 975–990.
102. D. Gao, Y. Liu, B. Miao, C. Wei, J.-G. Ma, P. Cheng and G.-M. Yang, *Inorg. Chem.*, 2018, **57**, 12475–12479.
103. P. Gütlich, S. Decurtins, K. M. Hasselbach, H. Spiering and A. Hauser, *Inorg. Chem.*, 1985, **24**, 2174–2178.
104. O. Sato, T. lyoda, A. Fujishima and K. Hashimoto, *Science*, 1996, **271**, 49–51.
105. O. Sato, Y. Einaga, A. Fujishima and K. Hashimoto, *Inorg. Chem.*, 1999, **38**, 4405–4412.
106. N. Shimamoto, S. Ohkoshi, O. Sato and K. Hashimoto, *Inorg. Chem.*, 2002, **41**, 678–684.
107. A. G. Orpen, L. Brammer, F. H. Allen, O. Kennard, D. G. Watson and R. Taylor, *J. Chem. Soc. Dalton Trans.*, 1989, **Suppl 171**, S1.
108. H. Montgomery, R. V. Chastain, J. J. Natt, A. M. Witkowska and E. C. Lingafelter, *Acta Cryst.*, 1967, **22**, 775.
109. S. Dick, *Z. Kristallogr. - New Cryst. Struct.*, 1998, **213**, 356.
110. D. A. McQuarrie and J. D. Simon, *Physical Chemistry: A Molecular Approach*, University Science Books, Sausalito, 1997.
111. C. P. Slichter and H. G. Drickamer, *J. Chem. Phys.*, 1972, **56**, 2142–2160.
112. S. Brooker, *Chem. Soc. Rev.*, 2015, **44**, 2880–2892.
113. Y. Garcia, *J. Mater. Chem.*, 1997, **7**, 857–858.
114. J. A. Wolny, V. Schünemann, Z. Németh and G. Vankó, *C. R. Chimie*, 2018, **21**, 1152–1169.
115. J. A. Wolny, R. Diller and V. Schünemann, *Eur. J. Inorg. Chem.*, 2012, 2635–2648.

116. J.-P. Tuchagues, A. Bousseksou, G. Molnár, J. J. McGarvey and F. Varret, in *Spin Crossover in Transition Metal Compounds III*, eds. P. Gütlich and H. A. Goodwin, Springer-Verlag, 2004, vol. 235, pp. 85–103.
117. J. Linares, E. Codjovi and Y. Garcia, *Sensors*, 2012, **12**, 4479–4492.
118. A. Hauser, in *Spin Crossover in Transition Metal Compounds I*, eds. P. Gütlich and H. A. Goodwin, Springer-Verlag, 2004, vol. 233, pp. 49–58.
119. I. Krivokapic, P. Chakraborty, R. Bronisz, C. Enachescu and A. Hauser, *Angew. Chem. Int. Ed.*, 2010, **49**, 8509–8512.
120. I. A. Gural'Skiy, V. A. Reshetnikov, A. Szebesczyk, E. Gumienna-Kontecka, A. I. Marynin, S. I. Shylin, V. Ksenofontov and I. O. Fritsky, *J. Mater. Chem. C*, 2015, **3**, 4737–4741.
121. D. F. Evans, *J. Chem. Soc.*, 1959, 2003–2005.
122. D. F. Evans and T. A. James, *J. Chem. Soc., Dalton Trans.*, 1979, 723–726.
123. R. W. Hogue, C. P. Lepper, G. B. Jameson and S. Brooker, *Chem. Commun.*, 2018, **54**, 172–175.
124. H. Petzold, P. Djomgoue, G. Hörner, J. M. Speck, T. Rüffer and D. Schaarschmidt, *Dalton Trans.*, 2016, **45**, 13798–13809.
125. P. Gütlich, B. Eckhard and A. X. Trautwein, *Mössbauer Spectroscopy and Transition Metal Chemistry: Fundamentals and Applications*, Springer, 1st edn., 2011.
126. P. Gütlich, *Z. Anorg. Allg. Chem.*, 2012, **638**, 15–43.
127. P. Glatzel and U. Bergmann, *Coord. Chem. Rev.*, 2005, **249**, 65–95.
128. F. M. F. de Groot and A. Kotani, *Core Level Spectroscopy of Solids*, Taylor & Francis Group, 2008.
129. L. J. P. Ament, M. Van Veenendaal, T. P. Devereaux, J. P. Hill and J. Van Den Brink, *Rev. Mod. Phys.*, 2011, **83**, 705–767.
130. W. Vreugdenhil, J. G. Haasnoot, O. Kahn, P. Thuéry and J. Reedijk, *J. Am. Chem. Soc.*, 1987, **109**, 5272–5273.
131. D. C. Ashley and E. Jakubikova, *Coord. Chem. Rev.*, 2017, **337**, 97–111.
132. H. Paulsen, V. Schünemann and J. A. Wolny, *Eur. J. Inorg. Chem.*, 2013, 628–641.
133. S. Vela and H. Paulsen, *Inorg. Chem.*, 2018, **57**, 9478–9488.
134. J. H. Takemoto and B. Hutchinson, *Chem. Letters*, 1972, **8**, 769–772.
135. T. Petrenko and F. Neese, *J. Chem. Phys.*, 2007, **127**, 164319.

136. I. Y. Barskaya, S. L. Veber, E. A. Suturina, P. S. Sherin, K. Y. Maryunina, N. A. Artiukhova, E. V. Tretyakov, R. Z. Sagdeev, V. I. Ovcharenko, N. P. Gritsan and M. V. Fedin, *Dalton Trans.*, 2017, **46**, 13108–13117.
137. J. A. Wolny, H. Paulsen, J. J. McGarvey, R. Diller, V. Schünemann and H. Toftlund, *Phys. Chem. Chem. Phys.*, 2009, **11**, 7562–7575.
138. Z.-P. Ni, J.-L. Liu, Md. N. Hoque, W. Liu, J.-Y. Li, Y.-C. Chen and M.-L. Tong, *Coord. Chem. Rev.*, 2017, **335**, 28–43.
139. J. Cirera, *Rev. Inorg. Chem.*, 2014, **34**, 199–216.
140. R. W. Hogue, S. Singh and S. Brooker, *Chem. Soc. Rev.*, 2018, **47**, 7303–7338.
141. K. Senthil Kumar and M. Ruben, *Coord. Chem. Rev.*, 2017, **346**, 176–205.
142. J. A. Real, A. B. Gaspar, V. Niel and M. C. Muñoz, *Coord. Chem. Rev.*, 2003, **236**, 121–141.
143. K. S. Murray, *Eur. J. Inorg. Chem.*, 2008, 3101–3121.
144. M. Ruben, J. Rojo, F. J. Romero-Salguero, L. H. Uppadine and J.-M. Lehn, *Angew. Chem. Int. Ed.*, 2004, **43**, 3644–3662.
145. J. G. Hardy, *Chem. Soc. Rev.*, 2013, **42**, 7881–7899.
146. A. B. Gaspar, M. C. Muñoz and J. A. Real, *J Mater. Chem.*, 2006, **16**, 2522–2533.
147. J. A. Real, A. B. Gaspar, M. C. Muñoz, P. Gütlich, V. Ksenofontov and H. Spiering, in *Spin Crossover in Transition Metal Compounds I*, eds. P. Gütlich and H. Goodwin, Springer, 2004, vol. 233, pp. 167–193.
148. Y. Garcia, V. Niel, M. Carmen Muñoz and J. A. Real, in *Spin Crossover in Transition Metal Compounds I*, eds. P. Gütlich and H. Goodwin, Springer, 2004, vol. 233, pp. 229–257.
149. J.A. Real, H. Bolvin, A. Bousseksou, A. Dworkin, O. Kahn, F. Varret and J. Zarembowitch, *J. Am. Chem. Soc*, 1992, **114**, 4650–4658.

CHAPTER 2

Theoretical Methods

2.1. Schrödinger Equation

The fundamental postulates of quantum mechanics (QM) stablish that the state of a system is described, at each instant, by a wave function that completely characterises all the physical properties of such system. For each physical observable, there are quantum mechanical operators that, when applied to the wave function, enable the prediction of the probability of finding the system exhibiting a specific value or range of values for that observable.[1,2]

The properties of any chemical system are governed by the many-body Schrödinger equation[3] through its wave function, which depends on the positions of the nuclei and the electrons. Hence, the main goal of *ab initio* wave function methods is to solve the Schrödinger equation, which, to understand chemistry at the microscopic level, it suffices to consider the non-relativistic time-independent Schrödinger equation:

$$\hat{H}\Psi(\boldsymbol{r}_i, \boldsymbol{R}_A) = E\Psi(\boldsymbol{r}_i, \boldsymbol{R}_A) \tag{2.1}$$

where $\hat{H}$ is the Hamiltonian operator that returns the energy, E, of the system, and $\Psi(\boldsymbol{r}_i,\boldsymbol{R}_A)$ (i = 1 to N, A = 1 to M) is the eigenfunction called wave function, that depends on the positions of the nuclei ($\boldsymbol{R}_A$) and the electrons ($\boldsymbol{r}_i$).

The Hamiltonian operator takes into account five contributions to the total energy of a system: kinetic energy of the electrons ($\hat{T}_e$), kinetic energy of the nuclei ($\hat{T}_N$), attraction of the electrons to the nuclei ($\hat{V}_{Ne}$), interelectronic repulsions ($\hat{V}_{ee}$) and internuclear repulsions ($\hat{V}_{NN}$). In more complicated situations (in the presence of an external electric or magnetic field, considering relativistic effects, etc.) other terms need to be added, but we will focus on the non-relativistic time-independent Schrödinger equation:

$$\hat{H} = \hat{T} + \hat{V} = \left(\hat{T}_e + \hat{T}_N\right) + \left(\hat{V}_{Ne} + \hat{V}_{ee} + \hat{V}_{NN}\right) =$$

$$= -\sum_{i=1}^{N} \frac{\hbar^2}{2m_e}\nabla_i^2 - \sum_{A=1}^{M} \frac{\hbar^2}{2M_A}\nabla_A^2 - \sum_{i=1}^{N}\sum_{A=1}^{M} \frac{e^2 Z_A}{r_{iA}} + \sum_{i=1}^{N}\sum_{j>i}^{N} \frac{e^2}{r_{ij}} + \sum_{A=1}^{M}\sum_{B>A}^{M} \frac{e^2 Z_A Z_B}{R_{AB}} \tag{2.2}$$

where i and j run over electrons, A and B run over nuclei, $\hbar$ is the Planck's constant divided by 2π, m_e is the mass of the electron, M_A is the mass of the nucleus A, ∇^2 is the Laplacian operator, e is the charge of the electron, Z is the atomic number and r and R are the distances between particles. Hence, Ψ is a function of $3n$ coordinates where n is the total number of particles

(nuclei and electrons), for example, the *x*, *y*, and *z* Cartesian coordinates specific to each particle. In Cartesian coordinates, the Laplacian is:

$$\nabla_i{}^2 = \frac{\partial^2}{\partial x_i^2} + \frac{\partial^2}{\partial y_i^2} + \frac{\partial^2}{\partial z_i^2} \tag{2.3}$$

The kinetic energy for a QM particle is expressed as the eigenvalue of the kinetic energy operator:

$$\hat{T} = -\frac{\hbar^2}{2m}\nabla^2 \tag{2.4}$$

Most of the constants are equal to 1 when atomic units are chosen:

$$\hat{H} = -\frac{1}{2}\sum_{i=1}^{N}\nabla_i^2 - \frac{1}{2}\sum_{A=1}^{M}\frac{1}{M_A}\nabla_A^2 - \sum_{i=1}^{N}\sum_{A=1}^{M}\frac{Z_A}{r_{iA}} + \sum_{i=1}^{N-1}\sum_{j>i}^{N}\frac{1}{r_{ij}} + \sum_{A=1}^{M-1}\sum_{B>A}^{M}\frac{Z_A Z_B}{R_{AB}} \tag{2.5}$$

However, this equation is unsolvable because of the correlated motions of particles. The Hamiltonian contains pairwise attraction and repulsion terms, implying that no particle is moving independently of all the others, therefore, we need some sort of approximation.

2.2. The Born–Oppenheimer Approximation

To solve the Schrödinger equation, the Born–Oppenheimer[4] approximation is used, which enables the separation of nuclear motion from electronic motion and serves as the foundation for most electronic structure methods.

Neutrons are approximately 1800 times more massive than electrons. As a result, under typical physical conditions, the nuclei in molecular systems move significantly slower than electrons. This disparity in motion allows for the convenient decoupling of nuclear and electronic motions, and is considered that the electrons move within the field of "fixed" nuclei. Consequently, electronic energies can be calculated for "fixed" nuclear positions. In this framework, the nuclear kinetic energy term can be neglected, and the repulsive nuclear-nuclear potential energy term becomes a constant for a given geometry. Hence, the electronic Hamiltonian is:

$$\hat{H}_{el} = -\frac{1}{2}\sum_{i=1}^{N}\nabla_i^2 - \sum_{i=1}^{N}\sum_{A=1}^{M}\frac{Z_A}{r_{iA}} + \sum_{i=1}^{N-1}\sum_{j>i}^{N}\frac{1}{r_{ij}} \tag{2.6}$$

and the electronic Schrödinger equation:

$$\hat{H}_{el}\Psi_{el}(\boldsymbol{r}_i;\boldsymbol{R}_A) = E_{el}(\boldsymbol{R}_A)\Psi_{el}(\boldsymbol{r}_i;\boldsymbol{R}_A) \tag{2.7}$$

we can rewrite the expression for the wavefunction as:

$$\Psi_{tot}(\boldsymbol{r}_i;\boldsymbol{R}_A) = \Psi_{el}(\boldsymbol{r}_i;\boldsymbol{R}_A)\Psi_N(\boldsymbol{R}_A) \tag{2.8}$$

where Ψ_{el} and Ψ_N are the electronic and the nuclear wave functions, respectively. The electronic wave function describes the motion of the electrons and explicitly depends on the electronic coordinates but parametrically on the nuclear coordinates, as does the electronic energy. The total energy for fixed nuclei includes the constant nuclear repulsion V_{NN}:

$$\hat{H}_{tot} = \hat{H}_{el} + \hat{V}_{NN} = \hat{H}_{el} + \sum_{A=1}^{M-1}\sum_{B>A}^{M}\frac{Z_A Z_B}{R_{AB}} \tag{2.9}$$

Once the electronic problem has been solved, the motion of the nuclei can be tackled under the same premises used for the electronic problem. Given that electrons move significantly faster than nuclei, it is a reasonable approximation in Eq. 2.5 to replace the electronic coordinates with their average values, averaged over the electronic wave function. This results in the formulation of a nuclear Hamiltonian that describes the motion of the nuclei within the average field of the electrons.

$$\hat{H}_N = -\frac{1}{2}\sum_{A=1}^{M}\frac{1}{M_A}\nabla_A^2 + \left\langle -\frac{1}{2}\sum_{i=1}^{N}\nabla_i^2 - \sum_{i=1}^{N}\sum_{A=1}^{M}\frac{Z_A}{r_{iA}} + \sum_{i=1}^{N-1}\sum_{j>i}^{N}\frac{1}{r_{ij}}\right\rangle + \sum_{A=1}^{M-1}\sum_{B>A}^{M}\frac{Z_A Z_B}{R_{AB}}$$

$$= -\frac{1}{2}\sum_{A=1}^{M}\frac{1}{M_A}\nabla_A^2 + E_{el}(\boldsymbol{R}_A) + \sum_{A=1}^{M-1}\sum_{B>A}^{M}\frac{Z_A Z_B}{R_{AB}}$$

$$= \frac{1}{2}\sum_{A=1}^{M}\frac{1}{M_A}\nabla_A^2 + E_{tot}(\boldsymbol{R}_A) \tag{2.10}$$

The total energy $E_{tot}(\boldsymbol{R}_A)$ serves as a potential for nuclear motion, forming what is known as a potential energy surface (PES) (Figure 2.1). Within the Born–Oppenheimer approximation, the nuclei move on this PES, which is derived from solving the electronic problem. The solutions to the nuclear Schrödinger equation then describe the vibration, rotation, and translation of a molecule.

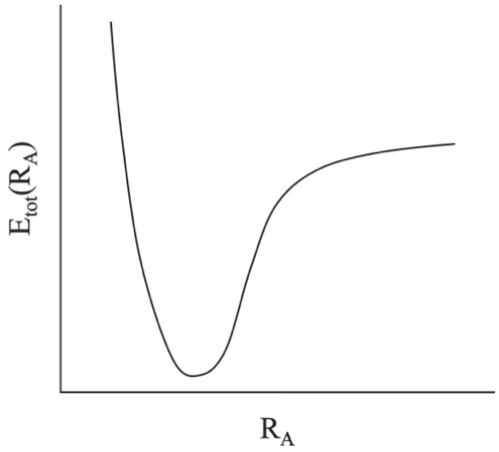

Figure 2.1. Schematic representation of a potential energy surface.

The Born–Oppenheimer approximation provides numerous benefits. As mentioned, this approximation enables the concept of the PES. It also establishes the concepts of equilibrium and transition state geometries, as they represent critical points on the PES. Without this approximation, we would need to discuss high-probability regions of the nuclear wave functions instead. However, even with the advantages offered by the Born–Oppenheimer approximation, finding the exact solution of the electronic Schrödinger equation remains highly challenging due to the difficulty in evaluating interelectronic repulsion. Eq. 2.7 only has an analytical solution for very small systems ($N_{particles} \leq 2$), and the high dimensionality of the wave function Ψ_{el} makes solving the equation numerically extremely challenging. Consequently, additional approximations must be considered to obtain an approximate solution of the Schrödinger equation. Various approximate methods have been developed to address this problem, such as Hartree–Fock (HF) theory.[1,5–7]

HF is a wave function-based method that approximates the many-electron wave function of a system by using a mean-field approximation in which each electron moves in the average field generated by all other electrons. This includes the exchange interaction which arises due to the Pauli exclusion principle, but does not account for electron correlation (E_C^{HF}), defined as the difference between the exact energy of the system (E_0) and the HF energy (E_{HF}), and is always negative due to the variational principle.

$$E_C^{HF} = E_0 - E_{HF} \tag{2.11}$$

This can be enhanced at the expense of computational cost adding the electron correlation through post-HF methods such as Møller–Plesset (MP) perturbation theory,[8] coupled cluster (CC) approach[9] and quantum Monte Carlo,[10] all of them wave function-based methods.

Another approximation that includes electron correlation is the density functional theory (DFT), [1,5,6,11–13] based on the electron density rather than the wave function. This method includes electron correlation *via* an exchange-correlation functional, which is a mathematical expression that depends on the electron density, to approximate the energy of a system. However, the exact form of this functional is unknown and several approximations are used.

When selecting an appropriate method for a target study, one must consider the nature and size of the system, the computational cost, and the accuracy. DFT currently stands out as the most widely used electronic structure method in computational chemistry because it offers a better balance between computational cost and accuracy compared to wave function-based methods, across a broad range of systems, making it particularly suitable for large systems.

2.3. Density Functional Theory

Density functional theory is a method that works with the electron density, $\rho(\boldsymbol{r})$, as the basic variable instead of the wave function $\Psi(\boldsymbol{r}_1, s_1, \boldsymbol{r}_2, s_2 \cdots, \boldsymbol{r}_n, s_n)$.

The idea of using the electron density dates back to the Thomas–Fermi model,[11,14] and later on by Slater.[15] Modern DFT as we know it today has its foundations in the Hohenberg and Kohn theorems,[12] and the Kohn–Sham approach.[13]

2.3.1. Electron Density

The number of electrons per unit volume in a given state is the electron density for that state. It is designed as $\rho(\boldsymbol{r})$, and is a function that gives the probability of finding an electron in an infinitesimal volume of space. Its formula in terms of Ψ is:

$$\rho(\boldsymbol{r}_1) = N \int \cdots \int |\Psi(\boldsymbol{x}_1, \boldsymbol{x}_2, \cdots, \boldsymbol{x}_N)|^2 ds_1 d\boldsymbol{x}_2 \cdots d\boldsymbol{x}_N \tag{2.12}$$

i.e is a multiple integral over the spin coordinates of all electrons and over all but one of the spatial variables. The electron density integrated over all space gives the total number of electrons, *N*:

$$N = \int \rho(\boldsymbol{r}) d\boldsymbol{r} \qquad \rho(\boldsymbol{r}) \geq 0 \tag{2.13}$$

2.3.1.1. Electron Density-Based Methods in Contrast with Wave Function-Based Methods

Wave function methods, such as Hartree–Fock, use the wave function Ψ as the central quantity. Ψ holds all the information about a particular state of our system. The problem is that the wave function is a complicated quantity that cannot be obtained experimentally and that depends on 4*N* variables (three spatial and one spin variable for each of the *N* electrons). Since the systems we are interested in contain many atoms and electrons, wave function methods quickly reach an unmanageable size, which makes a computational treatment very difficult, but also reduces the possibility of a descriptive understanding. In contrast, the Hamiltonian operator $\widehat{H}$ only contains operators acting on one ($\hat{T}$ and $\hat{V}_{Ne}$) or at most two ($\hat{V}_{ee}$) particles at a time, independent of system size. This raises the question of whether the intricate wave function is necessary for obtaining the energy and other properties, or whether it contains redundant and irrelevant information. Indeed, a simpler quantity, the electron density $\rho(\boldsymbol{r})$, which depends only on the three spatial variables and is therefore an object in the three-dimensional physical space, can be used to reach a solution to the Schrödinger equation. The electron density already provides all essential elements for constructing the system specific Hamiltonian and it seems at least very plausible that in fact $\rho(\boldsymbol{r})$ can determinate completely all

molecular properties, although this does not eliminate the need to solve the corresponding Schrödinger equation and all the difficulties related to this.

2.3.2. The Hohenberg–Kohn Theorems

2.3.2.1. The First Theorem: Proof of Existence

The first theorem of Hohenberg and Kohn states that "*The external potential* $V_{ext}(\mathbf{r})$ *is (to within a constant) a unique functional of* $\rho(\mathbf{r})$*; since, in turn* $V_{ext}(\mathbf{r})$ *fixes* $\hat{H}$ *we see that the full many particle ground state is a unique functional of* $\rho(\mathbf{r})$".[12] That means that for an *N*-electron system, the external potential $V_{ext}(\boldsymbol{r})$ completely fixes the Hamiltonian. Thus, *N* and $V_{ext}(\boldsymbol{r})$ determine all properties for the ground state. Since $\rho(\boldsymbol{r})$ determines *N*, it follows that it also determines the ground state wave function, Ψ_0, and all other electronic properties of the system.

$$\Psi_0 = \Psi_0[\rho_0]$$

Hence, the ground state energy, E_0, is also a functional of the ground state density, ρ_0. Since E_0 is a functional of ρ_0, so must be its individual terms ("*Ne*" subscript specifies the kind of external potential present in this case, defined by the attraction due to the nuclei):

$$E_0 = E_0[\rho_0] = T[\rho_0] + E_{ee}[\rho_0] + E_{Ne}[\rho_0] \tag{2.14}$$

This energy expression can be separated into a universal part (its form is independent of *N*, R_A, and Z_A), and a system-dependent part. That is:

$$E_0[\rho_0] = \underbrace{T[\rho_0] + E_{ee}[\rho_0]}_{\text{universally valid}} + \underbrace{\int \rho_0(\boldsymbol{r}) V_{Ne} d\boldsymbol{r}}_{\text{system-dependent}} \tag{2.15}$$

We can define the Hohenberg–Kohn functional by grouping the independent parts:

$$E_0[\rho_0] = F_{HK}[\rho_0] + \int \rho_0(\boldsymbol{r}) V_{Ne} d\boldsymbol{r} \tag{2.16}$$

If $F_{HK}[\rho]$ is made to act on an arbitrary density $\rho(\mathbf{r})$, it generates the expectation value of the kinetic and electron-electron repulsion energies of the ground state wave function related to this density:

$$F_{HK}[\rho] = T[\rho] + E_{ee}[\rho] = \langle \Psi | \hat{T} + \hat{V}_{ee} | \Psi \rangle \tag{2.17}$$

If the exact form of the universal functional were known, the Schrödinger equation would be solved exactly, rather than approximately. The problem is that the explicit form of $T[\rho]$ and $E_{ee}[\rho]$ functionals is unknown. However, we can extract the classical Coulomb part $J[\rho]$ from $E_{ee}[\rho]$:

$$E_{ee}[\rho] = \frac{1}{2} \iint \frac{\rho(\boldsymbol{r}_1)\rho(\boldsymbol{r}_2)}{r_{12}} d\boldsymbol{r}_1 d\boldsymbol{r}_2 + E_{ncl}[\rho] = J[\rho] + E_{ncl}[\rho] \tag{2.18}$$

Therefore, we can rewrite Eq. 2.14 as:

$$E_0[\rho_0] = T[\rho_0] + J[\rho_0] + E_{ncl}[\rho_0] + \int \rho_0(\boldsymbol{r}) V_{Ne} d\boldsymbol{r} \tag{2.19}$$

where $E_{ncl}[\rho]$ is the non-classical contribution to the electron-electron interaction, and includes the self-interaction correction, exchange and Coulomb correlation. It is important to note that ρ_0 determines the Hamiltonian, so it will also determine all the properties of all states of the system. However, the functional for this would be different than that of Eq. 2.19, constructed to deliver E_0.

2.3.2.2. The Second Theorem: Variational Principle

In the first theorem we have stablished that the ground state density of a system is enough to obtain all properties. But how one can assure that a certain density is the truly ground state density? The second Hohenberg–Kohn theorem states that the functional ($F_{HK}[\rho]$) that delivers the ground state energy of the system (E_0), delivers the lowest energy if and only if the input density is the true ground state density, ρ_0. This is the variational principle.

$$E_0 \leq E[\tilde{\rho}] = T[\tilde{\rho}] + E_{ee}[\tilde{\rho}] + E_{Ne}[\tilde{\rho}] \tag{2.20}$$

For any trial density $\tilde{\rho}$ which fulfil the appropriate boundary conditions:

$$\int \tilde{\rho}\,(\boldsymbol{r})d\boldsymbol{r} = N \qquad \tilde{\rho} \geq 0 \tag{2.21}$$

and which is associated with some external potential $\tilde{V}_{\text{ext}}$, yields to an upper bound for the true ground state energy, E_0. Any trial density $\tilde{\rho}$ will define its own trial Hamiltonian, $\widetilde{H}$ and, as a result, its own trial wave function, $\widetilde{\Psi}$. This wave function can be taken as the trial wave function for the Hamiltonian generated from the true external potential V_{ext}:

$$\langle\widetilde{\Psi}|\widetilde{H}|\widetilde{\Psi}\rangle = T[\tilde{\rho}] + V_{ee}[\tilde{\rho}] + \int \tilde{\rho}(\boldsymbol{r})V_{ext}d\boldsymbol{r} = E[\tilde{\rho}] \geq E_0[\rho_0] = \langle\Psi_0|\widehat{H}|\Psi_0\rangle \tag{2.22}$$

The densities under consideration must be V_{ext} representable, that is, associated to an antisymmetric wave function and a Hamiltonian operator with some kind of external potential. This condition can be replaced by a weaker condition: the *N*-representability, which ask for the density to arise from an antisymmetric wave function.

$$E_0 = \min_{\Psi\to N}\langle\Psi|\hat{T} + \hat{V}_{ee} + \hat{V}_{Ne}|\Psi\rangle \tag{2.23}$$

The wave function, in the set of *N*-representable functions, which leads to the lowest expectation value of the Hamiltonian, is the ground state wave function. This can be applied to DFT by dividing this search into two steps:

1. We look at all allowed antisymmetric functions Ψ^{X} that yield a certain density ρ_{X} (which integrates to *N*). As a result, we get $\Psi^{\text{X}}_{\text{min}}$, which gives the lowest energy of set.
2. We look not just at ρ_{X} but all possible densities ρ_Γ with $\Gamma = A, B, X, \ldots$ The density ρ_Γ with the associated $\Psi^{\text{X}}_{\text{min}}$ that provides with the lowest energy of all is the ground state density of the system.

This was introduced by Levy[16] and it is known as the Levy constrained-search formulation, and it can be expressed as:

$$E_0 = \underbrace{\min_{\rho \to N} \underbrace{\left(\min_{\Psi \to \rho} \langle \Psi | \hat{T} + \hat{V}_{ee} + \hat{V}_{Ne} | \Psi \rangle \right)}_{\text{first step}}}_{\text{second step}} \tag{2.24}$$

The energy due to the external potential is determined simply by the density and is then independent of the wave function generating that density, which means that it is the same for all wave functions integrating to a particular density and we can separate it from the kinetic and electron-electron repulsion contributions:

$$E_0 = \min_{\rho \to N} \left(\min_{\Psi \to \rho} \langle \Psi | \hat{T} + \hat{V}_{ee} | \Psi \rangle + \int \rho(\boldsymbol{r}) V_{Ne} d\boldsymbol{r} \right) \tag{2.25}$$

Introducing the universal functional, $F[\rho]$:

$$F[\rho] = \min_{\Psi \to \rho} \langle \Psi | \hat{T} + \hat{V}_{ee} | \Psi \rangle \tag{2.26}$$

$$E_0 = \min_{\rho \to N} \left(F[\rho] + \int \rho(\boldsymbol{r}) V_{Ne} d\boldsymbol{r} \right) \tag{2.27}$$

$F[\rho]$ differs from $F_{\mathrm{HK}}[\rho]$ by the fact that it is defined for all densities that originate from an antisymmetric wave function Ψ. If the input density belongs to the class of V_{ext}-representable densities, $F[\rho] = F_{\mathrm{HK}}[\rho]$.

Summarising, we simply need to examine all the wave functions Ψ associated with the ground state density ρ_0 and select the one for which the energy $E_{\Psi \to \rho_0}$ is lowest, which is then Ψ_0. This one is useless for real applications, we have no access to all these wave functions, and in reality, there is no way whatsoever to identify the correct wave function associated with a particular density. Therefore, even though the ground state wave function is theoretically accessible once the correct ground state density is known (which can be obtained by minimizing the functional $F[\rho]$), we can say that there is no wave function in DFT.

2.3.2.3. Summary

The Hohenberg–Kohn theorems indicate that there is a unique relationship between the ground state density $\rho_0(\boldsymbol{r})$ and the ground state energy E_0, which validates the use of the density as the central variable that has all the information needed for describing a system. However,

they do not offer any practical instructions on how to construct the functional that would yield the ground state energy. The difficulty of the calculations remains unchanged, and the Hohenberg–Kohn theorems do not suggest any specific approximations for the unknown functionals. Moreover, the variational principle only applies to the exact functional, which is unknown. Conventional wave function-based methods such as Hartree–Fock, are variational and the energy is an indicator of the quality of the trial wave function: the lower the energy, the closer is the trial wave function to the ground state wave function. However, in the density functional framework, the energy value obtained by a trial functional has no such meaning, in fact, the energies obtained can be lower than the exact ones: using an approximation for the universal functional makes that we use an approximated Hamiltonian rather than the exact one. Moreover, the constrained–search scheme does not offer a solution for practical considerations, it is impossible to search through all wave functions, therefore setting up the functional in Eq. 2.26 is also impossible. The constrained–search leaves us with a definition of the all-decisive functional $F[\rho]$ that explicitly contains the wave function rather than the density, and what we wanted in the first place was to find a functional that contains an explicit prescription for how uniquely map an electron density onto an energy, avoiding the complicated N-particle wave function.

In the next section we will see that, thankfully, Kohn and Sham proposed a novel approach to approximate this unknown universal functional: they realised that many issues associated with direct density functionals relate to the way the kinetic energy is determined.

2.3.3. The Kohn–Sham Approach

Kohn and Sham devised in 1965[13] a way to approximate the unknown universal functional $F[\rho]$ in which as much information as possible is calculated exactly, leaving a small part of the total energy to be determined by an approximate functional. First: they introduce a fictious reference system of N non-interacting electrons built from a set of orbitals (one-electron functions) that allows for the calculation of the major part of the kinetic energy with a good accuracy. Secondly, the remainder is merged with the non-classical contributions to the electron-electron repulsion, also unknown but usually fairly small. Remember that the ground state energy of an atomic or molecular system can be expressed as Eq. 2.27, where the universal functional $F[\rho]$ contains the individual contributions of the kinetic energy, the classical Coulomb interaction and the non-classical portion due to self-interaction correction, exchange (antisymmetry), and electron correlation effects,

$$F[\rho(\boldsymbol{r})] = T[\rho(\boldsymbol{r})] + J[\rho(\boldsymbol{r})] + E_{ncl}[\rho(\boldsymbol{r})] \tag{2.28}$$

In Eq. 2.28 only $J[\rho(\boldsymbol{r})]$ which is the classical Coulomb interaction functional, is known.

The exact wave functions of non-interacting electrons are Slater determinants, so it is possible to build a non-interacting reference system with a Hamiltonian in which it has been introduced an effective local potential, $V_S(\boldsymbol{r})$:

$$\widehat{H}_S = -\frac{1}{2}\sum_i^N \nabla_i^2 + \sum_i^N V_S(\boldsymbol{r}_i) \tag{2.29}$$

The corresponding ground state wave function, hence, would be:

$$\Theta_S = \frac{1}{\sqrt{N!}}\begin{vmatrix} \varphi_1(\boldsymbol{x}_1) & \varphi_2(\boldsymbol{x}_1) & \cdots & \varphi_N(\boldsymbol{x}_1) \\ \varphi_1(\boldsymbol{x}_2) & \varphi_2(\boldsymbol{x}_2) & \cdots & \varphi_N(\boldsymbol{x}_2) \\ \vdots & \vdots & \ddots & \vdots \\ \varphi_1(\boldsymbol{x}_N) & \varphi_2(\boldsymbol{x}_N) & \cdots & \varphi_N(\boldsymbol{x}_N) \end{vmatrix} \tag{2.30}$$

where the spin orbitals are determined by

$$\hat{f}^{KS}\varphi_i = \varepsilon_i\varphi_i \tag{2.31}$$

with the one-electron Kohn–Sham (KS) operator defined as

$$\hat{f}^{KS} = -\frac{1}{2}\nabla^2 + V_S(\boldsymbol{r}) \tag{2.32}$$

These orbitals are called Kohn–Sham orbitals, or KS orbitals. $V_S(\boldsymbol{r})$ is chosen so that the density resulting from these KS orbitals is the ground state of the target system of interacting electrons

$$\rho_S(\boldsymbol{r}) = \sum_i^N \sum_s |\varphi_i(\boldsymbol{r}, s)|^2 = \rho_0(\boldsymbol{r}) \tag{2.33}$$

The problem, though, is that we need to find a good way to determine the kinetic energy. Since we cannot accurately do it through an explicit functional, Kohn and Sham tried to

compute as much as they could of the true kinetic energy exactly and the remainder in an approximate manner. Therefore, the exact kinetic energy of the non-interacting reference system with the same density as the real (interacting one) system is given by:

$$T_S = -\frac{1}{2}\sum_{i=1}^{N}\langle\varphi_i|\nabla^2|\varphi_i\rangle \tag{2.34}$$

The non-interacting kinetic energy is not equal to the true kinetic energy even if the systems share the same density. The KS approach accounts for the fact that this is not the true kinetic energy, T, of the real system by separating the $F[\rho]$ as:

$$F[\rho(\boldsymbol{r})] = T_S[\rho(\boldsymbol{r})] + J[\rho(\boldsymbol{r})] + E_{XC}[\rho(\boldsymbol{r})] \tag{2.35}$$

where the part of the true kinetic energy not covered by T_S, that is T_C, has been added to the non-classical electrostatic contributions. E_{XC} is the so-called exchange-correlation energy, and is defined as

$$E_{XC}[\rho] \equiv (T[\rho] - T_S[\rho]) + (E_{ee}[\rho] - J[\rho]) = T_C[\rho] + E_{ncl}[\rho] \tag{2.36}$$

That is, E_{XC} is the functional which contains everything that is unknown that is not only the non-classical effects of self-interaction correction, exchange and correlation (which are contributions to the potential energy of the system) but also a portion that belongs to the kinetic energy.

We can express the energy of the interacting real system as an explicit function of orbitals $\{\varphi_i\}$ with $\rho(\boldsymbol{r}) = \sum_{i=1}^{N}|\varphi_i|^2$

$$E[\rho(\boldsymbol{r})] = T_S[\rho] + J[\rho] + E_{Ne}[\rho] + E_{XC}[\rho]$$

$$= T_S[\rho] + \frac{1}{2}\iint\frac{\rho(\boldsymbol{r}_1)\rho(\boldsymbol{r}_2)}{r_{12}}d\boldsymbol{r}_1 d\boldsymbol{r}_2 + \int V_{Ne}\rho(\boldsymbol{r})d\boldsymbol{r} + E_{XC}$$

$$= -\frac{1}{2}\sum_{i}^{N}\langle\varphi_i|\nabla^2|\varphi_i\rangle + \frac{1}{2}\sum_{i}^{N}\sum_{j}^{N}\iint|\varphi_i(\boldsymbol{r}_1)|^2\frac{1}{r_{12}}\left|\varphi_j(\boldsymbol{r}_2)\right|^2 d\boldsymbol{r}_1 d\boldsymbol{r}_2$$

$$-\sum_{i}^{N}\int\sum_{A}^{M}\frac{Z_A}{r_{1A}}|\varphi_i(\boldsymbol{r}_1)|^2 d\boldsymbol{r}_1 + E_{XC}[\rho(\boldsymbol{r})] \tag{2.37}$$

- $T_S[\rho]$: non-interacting kinetic energy functional
- $J[\rho]$: classical Coulomb interaction functional
- $E_{Ne}[\rho]$: nuclei-electron potential functional

} Known, they can be calculated exactly

- $E_{XC}[\rho]$: exchange-correlation functional

} Unknown, it cannot be calculated exactly

Eq. 2.37 may look quite complex, but essentially everything is written in terms of the atomic orbitals $\{\varphi_i\}$, and everything that we do not know is approximated in the exchange-correlation functional, $E_{\mathrm{XC}}[\rho(\boldsymbol{r})]$.

In the second Hohenberg-Kohn theorem, the energy is minimized with respect to the φ_i while keeping them orthonormal $\langle\varphi_i|\varphi_j\rangle = \delta_{ij}$. Derivation of the energy with respect to the orbitals and Lagrange multipliers are used, and the Kohn–Sham equation is obtained:

$$\left(-\frac{1}{2}\nabla^2 + V_{eff}(\boldsymbol{r}_1)\right)\varphi_i = \varepsilon_i\varphi_i \tag{2.38}$$

V_{eff} is identical to V_{S} of Eq. 2.32:

$$V_S(\boldsymbol{r}) \equiv V_{eff}(\boldsymbol{r}) = \int\frac{\rho(\boldsymbol{r}_2)}{r_{12}}d\boldsymbol{r}_2 + V_{XC}(\boldsymbol{r}_1) - \sum_{A}^{M}\frac{Z_A}{r_{1A}} \tag{2.39}$$

Therefore, once we know the contributions in Eq. 2.39, we can have an idea of the potential V_{S} to be inserted into the one-particle equations. These equations, in turn, determine the orbitals and consequently the ground state density and ground state energy by using Eq. 2.37. V_{eff} already depends on the density and thus on the orbitals through the Coulomb term (Eq. 2.37). Thus, the Kohn–Sham one-electron equations need to be solved iteratively.

V_{XC} in Eq. 2.39 is the potential due to the exchange-correlation energy E_{XC}. Since we do not know the form of the exchange correlation energy functional, $E_{\mathrm{XC}}[\rho(\boldsymbol{r})]$, the explicit form of

the associated potential V_{XC} is also unknown, so we define it as the functional derivative of E_{XC} with respect to ρ:

$$V_{XC} \equiv \frac{\delta E_{XC}}{\delta \rho} \tag{2.40}$$

If the exact forms of E_{XC} and V_{XC} were known, the Kohn–Sham approach would lead to the exact energy, that is, the correct eigenvalue of the Hamiltonian operator $\hat{H}$ of the Schrödinger equation. The Hartree–Fock model introduces approximations right in the beginning, where the wave function is assumed to be a single Slater determinant (therefore can never give the true solution). In contrast, the Kohn–Sham approach is in principle exact, approximations are only made when we design an explicit form to the unknown exchange-correlation energy functional and the corresponding potential V_{XC}. The goal of modern DFT is to find better approximations to E_{XC} and V_{XC}.

The Kohn–Sham potential is local, $V_S(\boldsymbol{r})$ is a function only of $\boldsymbol{r}$ and independent on the values at other points in space $\boldsymbol{r'}$. Since $V_S(\boldsymbol{r}) = V_{eff}(\boldsymbol{r})$, $V_{XC}(\boldsymbol{r})$ is also local. In Hartree–Fock the exchange correlation is not local. The Kohn–Sham equations have a structure formally less complicated than Hartree–Fock and in principle are exact. Nevertheless, even though the Kohn–Sham potential is a local potential, it will probably have a very complex non-local dependence on the density: $V_{eff}(\boldsymbol{r})$ will depend on the charge density at all other points, because knowledge of the exact $V_{XC}(\boldsymbol{r})$ is equivalent to exactly solving the Schrödinger equation.

The Kohn–Sham orbitals are a way of getting the exact density $\rho_0(\boldsymbol{r})$, but they do not have a physical meaning. However, they are useful in terms of qualitative molecular orbital considerations since they are not only related with a one-electron potential (which includes all non-classical effects), they are also consistent with the exact ground state density. The true many-electron wave function is not available in DFT, therefore the Slater determinant built from the KS orbitals is not the true many-electron wave function.

2.3.3.1. Summary

As showed, the ground state electron density $\rho(\boldsymbol{r})$ at a location $\boldsymbol{r}$ can be expressed as a set of one-electron orbitals (KS orbitals), as shown in Eq. 2.33. The KS orbitals are determined by solving the KS equation (Eq. 2.38), which can be derived by applying the variational principle

to the electronic energy $E[\rho(\boldsymbol{r})]$ (Eq. 2.37), with the charge density given in Eq. 2.33. Once $E_{XC}[\rho(\boldsymbol{r})]$ is known, $V_{XC}(\boldsymbol{r})$ can be obtained.

The significance of the KS orbitals lies in their role in calculating the electron density as described in Eq. 2.33. The process of solving the KS equation is iterative and self-consistent. It starts with an initial guess for the charge density $\rho(\boldsymbol{r})$, which for a molecular system, can be derived from the superposition of the atomic densities of its constituent atoms. A fixed approximate form of the functional, representing the dependency of the exchange-correlation energy ($E_{XC}[\rho(\boldsymbol{r})]$) on the electron density, is used to calculate the exchange-correlation potential ($V_{XC}(\boldsymbol{r})$). This allows the KS equations to be solved, resulting in an initial set of KS orbitals. These orbitals are then used to compute an improved electron density using Eq. 2.33. The procedure is repeated iteratively until the density and the exchange-correlation energy meet a certain convergence criterion. Once this convergence is achieved, the electronic energy can be calculated using Eq. 2.37.

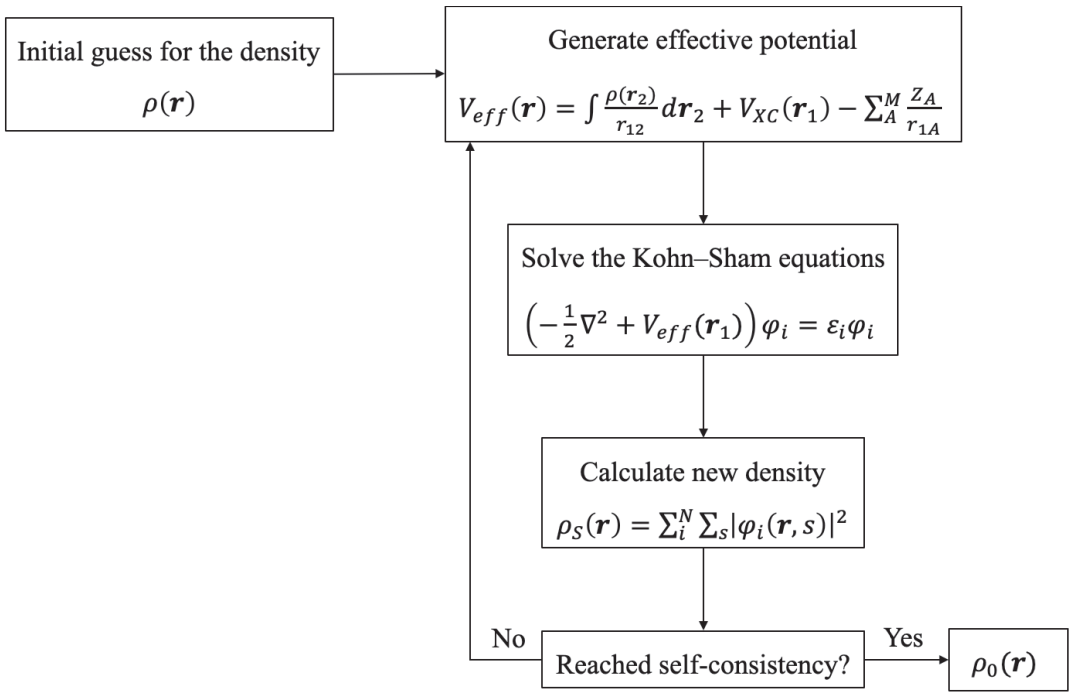

Figure 2.2. Scheme of the steps in the Kohn–Sham approximation.

In each iteration, the KS orbitals are expressed using a set of basis functions. This means that solving the KS equations leads to determine the coefficients for a linear combination of basis functions, similar to the procedure in the HF method. The choice of basis set is therefore

important in DFT. However, the computational time associated scales as the third power of the number of basis functions (in HF it scales as the fourth power).[17]

The exchange-correlation energy E_{XC} is typically divided into two components:

- Exchange term E_X: associated with the interactions between electrons of the same spin.
- Correlation term E_C: associated with the interactions between electrons of opposite spin.

$$E_{XC}[\rho(\boldsymbol{r})] = E_X[\rho(\boldsymbol{r})] + E_C[\rho(\boldsymbol{r})] \tag{2.41}$$

Both $E_X[\rho(\boldsymbol{r})]$ and $E_C[\rho(\boldsymbol{r})]$ are also functionals of the electron density and are known as the exchange functional and the correlation functional, respectively. They can be classified into two types: local functionals, which only depend on the electron density $\rho(\boldsymbol{r})$, and gradient-corrected functionals, which depend on both $\rho(\boldsymbol{r})$ and its gradient $\nabla\rho(\boldsymbol{r})$. This will be reviewed in the next section.

Despite significant progress in the field, it is important to point out that the main source of inaccuracy in DFT often stems from the approximate nature of the exchange-correlation functional.

2.3.4. Thermochemistry

As explained in Section 1, SCO occurs in systems where different electronic states are energetically similar. In these cases, entropy tends to favour the HS state, potentially leading to a transition from the LS to the HS state.[18] This process can be understood thermodynamically as an equilibrium between these different spin states. Assuming an ideal isolated system and neglecting the small pressure-dependent contribution to free enthalpy, the Gibbs free energy change (ΔG) for the spin transition can be expressed as follows:[19,20]

$$\Delta G(T) = G^{HS} - G^{LS} = \Delta H - T\Delta S \tag{2.42}$$

where

$$G^i = H^i - TS^i = E^i_{el} + E^i_{vib} - TS^i \tag{2.43}$$

is the Gibbs free energy corresponding to the spin state *i* at the temperature *T*. E_{el}^{i} is the electronic contribution and E_{vib}^{i} the vibrational one. For molecular systems, the former contribution can be obtained directly from *ab initio* calculations, while the latter contribution can be estimated using the harmonic approximation. The entropy change has two main contributions: the vibrational contribution and the contribution coming from the change in spin multiplicity. The vibrational contribution accounts for a larger portion of ΔS, is system dependent and can be estimated using the harmonic vibration. The contribution from spin multiplicity change, on the other hand, is determined by the total spin of the HS and LS states and can be calculated using Eq. 2.44:

$$\Delta S_{spin} = R \ln \frac{(2S_{HS} + 1)}{(2S_{LS} + 1)} \tag{2.44}$$

For example, in Fe(II) d^6 systems, ΔS_{spin} is 3.20 cal/mol·K.

Experimental measurements of the total entropy change (ΔS) for octahedral Fe(II) complexes range from 8.4 and 19.1 cal/mol·K.[21] Additionally, the Gibbs free energy can be described using the equilibrium constant, K_{eq}, which is defined based on the molar fractions of each spin state as

$$\Delta G(T) = -RT \ln K_{eq} = -RT \ln \frac{\gamma_{HS}}{\gamma_{LS}} = -RT \ln \frac{\gamma_{HS}}{1 - \gamma_{HS}} \tag{2.45}$$

where *R* is the gas constant and *T* the temperature. When the molar fractions of both spin states are equal, $\Delta G(T) = 0$, and hence $\Delta H = T \cdot \Delta S$. This condition defines the transition temperature:

$$T_{1/2} = \frac{\Delta H}{\Delta S} \tag{2.46}$$

Both ΔH and ΔS have some temperature dependence but in principle can be neglected without losing accuracy.[22,23] Finally, the Gibbs free energy can be expressed as

$$\Delta G(T) = \Delta H - T\Delta S = \Delta E_{el} + \Delta H_{vib} - T\Delta S \tag{2.47}$$

where the energy difference between the two electronic states, ΔE_{el}, is explicitly written, as is key to properly model any thermodynamical magnitude. Therefore, the quality of the results

will depend on the accuracy of the calculation of such term, which in turn depends on the choice of the DFT functional.

2.3.5. Exchange-Correlation Functionals

In previous sections we showed that within the Kohn–Sham formalism, $E[\rho(\boldsymbol{r})]$ can be expressed as Eq. 2.37. In that formalism, the classical electron-electron interaction $J[\rho(\boldsymbol{r})]$, the nuclei-electron interaction $E_{Ne}[\rho(\boldsymbol{r})]$, and a large portion of the kinetic energy $T_S[\rho(\boldsymbol{r})]$, are treated exactly. However, the exchange-correlation functional $E_{XC}[\rho(\boldsymbol{r})]$ is the ultimate *deus ex machina* to treat everything we do not know how to deal with, that is, the self-interaction correction, the exchange and correlation and a portion of the kinetic energy. Therefore, the quest for better descriptions for the $E_{XC}[\rho(\boldsymbol{r})]$ functional determines the quality of the Kohn–Sham approach. This search relies on physical or mathematical intuition, and it has a strong trial and error component. Moreover, specific problems require specific $E_{XC}[\rho(\boldsymbol{r})]$, therefore there is a strong need for benchmark, there is no universal functional in algorithm to accurately describe any given electron density. Therefore, we must rely on a collection of functionals, each one with its own strengths and weakness, depending on the systems of study.

There are several strategies to approximate $E_{XC}[\rho(\boldsymbol{r})]$, and functionals are classified based on their construction and mathematical complexity:[17]

- Local uniform functionals, such as local density approximations (LDA), where the energy is a function of electron density.[11,14,15,24]
- Functionals that also depend on the density gradient, known as generalized gradient approximations (GGA).[25–27]
- Functionals that also consider higher-order derivatives like the Laplacian[28] of the density or the kinetic energy density, called meta functionals (meta-GGA).[29]
- Hybrid functionals, which replace part of the exchange functional with non-local exchange derived from a determinant, typically from Hartree–Fock method.[30]
- Double hybrid functionals, which substitute part of the correlation energy by incorporating wave function theory (WFT) correlation, for example from MP2.[31]
- Additional complexity levels are present in range-corrected hybrids.[32,33]

LDA functionals are based on the homogeneous electron gas of density $\rho(\boldsymbol{r})$:

$$E_{XC}^{LDA}[\rho] = \int \rho(\boldsymbol{r})\varepsilon_{XC}^{LDA}\big(\rho(\boldsymbol{r})\big)d\boldsymbol{r} \tag{2.48}$$

where $\varepsilon_{XC}(\rho(\boldsymbol{r}))$ is the exchange-correlation energy per particle. Such energy is weighted with the probability $\rho(\boldsymbol{r})$ that there is in fact an electron at this position in space. If we extend the LDA approximation to the unrestricted case, we arrive at the local spin density approximation, LSDA, which depends on the electron densities of spin-up (ρ_α) and spin-down (ρ_β) electrons:

$$E_{XC}^{LSDA}[\rho_\alpha, \rho_\beta] = \int \rho(\boldsymbol{r}) \varepsilon_{XC}^{LSDA}\left(\rho_\alpha(\boldsymbol{r}), \rho_\beta(\boldsymbol{r})\right) d\boldsymbol{r} \tag{2.49}$$

One example of a LSDA functional is the SVWN.[12,13,34,35]

GGA methods significantly improve over local methods, offering better accuracy in total energies,[36] atomization energies,[27,36,37] energy barriers[38,39] and bond properties. They help to address the overbinding issue seen with LDA[40] by expanding and softening bonds.[37] However, GGA methods still struggle with van der Waals interactions[41,42] and do not always outperform LDA in solid-state calculations[43–49] or when determining ionization potentials and electron affinities.[37,50]

$$E_{XC}^{GGA}[\rho_\alpha, \rho_\beta] = \int \rho(\boldsymbol{r}) \varepsilon_{XC}^{GGA}(\rho_\alpha, \rho_\beta, \nabla\rho_\alpha, \nabla\rho_\beta) d\boldsymbol{r} \tag{2.50}$$

Meta-GGA functionals have been developed by incorporating additional semi-local information beyond the first-order density gradient used in GGA. These functionals depend on higher-order density gradients or the kinetic energy density (τ), improving accuracy for properties like atomization energies. However, they are technically challenging and present difficulties in numerical stability.

$$E_{XC}^{meta}[\rho_\alpha, \rho_\beta] = \int \rho(\boldsymbol{r}) \varepsilon_{XC}^{meta}(\rho_\alpha, \rho_\beta, \nabla\rho_\alpha, \nabla\rho_\beta, \tau_\alpha, \tau_\beta, \ldots) d\boldsymbol{r} \tag{2.51}$$

An example of this kind of functional is the TPSS.[51]

Hybrid functionals (H-GGA) combine the exchange-correlation of conventional GGA methods with a percentage of HF exchange. The exact amount of HF exchange is determined semi-empirically, often by fitting to experimental data like atomization energies, ionization potentials, etc. for a representative set of molecules.[52] These functionals significantly improve many molecular properties, making them very popular. However, their effectiveness is limited

in solid-state physics due to challenges in calculating the exact-exchange component. A notable hybrid functional is B3LYP,[27,29,30,53,54] with 20% of HS exchange.

Hybrid-meta GGA methods are an advanced class of density functionals that build upon meta-GGA functionals. Unlike standard GGAs, they depend on the HF exchange, the electron density, its gradient, and the kinetic energy density. These methods improve the accuracy of calculations, particularly for barrier heights and atomization energies. Another example is the TPSSh[51,55] functional, which contains 10% of exact HF exchange.

Non-hybrid functionals are biased towards the low-spin (LS) state, and hybrid functionals with > 15% HF exchange favour the high-spin (HS) state.[56–59] In SCO complexes, using B3LYP*[60,61] (15% HF exchange), B3LYP**[62] (10% HF exchange), or TPSSh[51,55,63] (10% HF exchange) yields more accurate results than standard B3LYP[35] (20% HF exchange). Since the electronic HS–LS gap varies almost linearly with HF exchange,[27,30,53,54,56] TPSSh with its 10% HF exchange typically performs better than non-hybrid functionals and lies between non-hybrids and B3LYP.[63,64] This functional is the most used in this thesis since previous work has established it as a suitable DFT method for spin-crossover systems[65–68] given its accuracy in determining the spin-state energy gap.[66]

2.4. Multireference Methods and *Ab Initio* Ligand Field Theory

Multi-Configurational Self-Consistent Field (MCSCF) is a method in quantum chemistry used to generate correct reference states of molecules in cases where HF and DFT are not adequate.[69] It uses a linear combination of configuration state functions (CSFs) or determinants to approximate the exact electronic wavefunction of an atom or molecule. The set of coefficients of both the CSFs or determinants and the basis functions in the molecular orbitals are varied to obtain the total electronic wavefunction with the lowest possible energy.

2.4.1. Dynamic and Static Electron Correlation

The primary limitation of the HF method is that it ignores the correlated motion of electrons relative to each other. This is called dynamic correlation and relates to the “instant” correlation between electrons, such as those occupying the same spatial orbital. That is, it refers to the dynamical character of the electron-electron interactions.[1,70,71] Moreover, there is another limitation in the HF method: the static (or non-dynamic) correlation, which arises when we

have systems that cannot be well described by just a single determinant. We could construct a more accurate wave function as a linear combination of multiple determinants,

$$\Psi = c_0\Psi_{HF} + c_1\Psi_1 + c_2\Psi_2 + \cdots \tag{2.52}$$

where c_i is the weight of each determinant in the expansion. Static correlation appears when one or more of these other determinants have weights of similar magnitude to that for the HF wave function, due to near (or exact) degeneracy in frontier orbitals. It is associated with electrons avoiding each other on a more "permanent" way, such as those occupying different spatial orbitals, and it becomes important for systems where different orbitals (configurations) have similar energies.[1,70–73]

Taking this into account, the issue here is not just that the HF approximation ignores the correlated motion of electrons, but that the HF method is inherently limited by its single-determinant nature, which lacks the necessary flexibility to accurately describe certain systems.

KS-DFT[13] somehow tries to include electron correlation through the exchange-correlation functional but the exact form of this functional is unknown and several approximations are used. This method does not involve a wave function but involves a Slater determinant that has the same electron density as the system of study. This determinant is taken as a reference wave function, and in that sense KS-DFT is a single-reference theory. In principle, KS-DFT is exact, but the density functional is unknown and probably unknowable. Therefore, we depend on approximate density functionals, which are less accurate for strongly correlated systems than for single-reference systems.[74,75] Another lack of DFT is that it does not provide good descriptions of empty (virtual) orbitals because they have no electron density. Despite the significant progress, accurately capturing the static correlation remains an unsolved challenge in KS-DFT due to its single reference nature, which requires computationally demanding multi-determinant wavefunction treatments.[76,77]

Significant changes in static correlation often occur upon bond cleavage and in transition metal systems with close-lying d- or f-orbitals.[78] For example, close-lying electronic configurations with variable d-orbital occupations will exhibit greater static correlation energy, particularly in HS complexes with small ligand field splitting, compared to systems where electrons are paired in MOs with big ligand field splittings.[79]

We can overcome this issue by using post-HF methods such as Complete Active Space Self-Consistent Field[80]/N-Electron Valence State Perturbation Theory[81–85] (CASSCF/NEVPT2), for instance. CASSCF/NEVPT2 wave functions do not consist in a single reference, they are fully

optimized within their active space. This makes them essential tools for handling systems with strong static correlation, such as transition metals, and for accurately calculating properties like excitation energies.[86] This post-HF methods help in the recovery of static (CASSCF) and dynamic correlation (NEVPT2). Another way to overcome this is to develop density functional theories that use multiconfigurational reference wave functions, like Multiconfiguration Pair-Density Functional Theory (MC-PDFT).[87]

2.4.2. Complete Active Space Self-Consistent Field (CASSCF)

Including additional possible determinants for excited electron configurations in the ground state improves the quality of the wave function. By selecting only a limited number of determinants from all possible, we can construct a multiconfigurational wave function, which can retrieve the static electron correlation energy. The most popular way to implement this is the Complete Active Space Self-Consistent Field (CASSCF) method.[80] CASSCF method is a widely used approach for addressing multiconfigurational electronic structure problems and its wavefunction serves as a starting point for more sophisticated methods, such as multireference perturbation theory and configuration interaction methods.[88,89]

The starting point is the molecular orbital, and we can form electronic configurations by singly or doubly occupying the orbitals with electrons. In transition metal systems with close-lying d- orbitals different configurations often have similar energies and therefore mix heavily leading to a wave function that is a linear combination of such configurations. Determining which configurations will be significant in a given situation is often challenging. To avoid this, the multiconfigurational CASSCF method divides the orbitals into three sets of spaces: inactive, active, and virtual space (Figure 2.3).

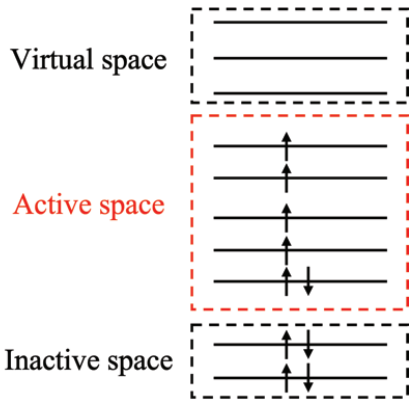

Figure 2.3. Pictorial representation of the three sets of spaces in CASSCF.

Virtual space orbitals remain unoccupied in all the electronic configurations under consideration. The orbitals of the inactive space are doubly occupied across all configurations, representing closed-shell electrons that do not participate in excitation processes or chemical rearrangements on the potential energy surface. The remaining orbitals are in the active space, in which, usually, there are more orbitals than electrons to occupy those orbitals, allowing for multiple possible electronic configurations. The wave function is constructed as a linear combination of all these configurations with the expansion coefficients and all occupied orbitals (inactive and active) simultaneously optimized such that the energy reaches a stationary value.[69,89] Normally, the way to indicate the active space in the literature is the following one: CAS(number of electrons, number of orbitals). For example, if we want to define an active space for a Fe(II) complex consisting in 6 electrons and 8 orbitals, the way to indicate the active space would be CAS(6,8).

The method is called complete active space because it uses all possible configurations to expand the wave function by occupying the active orbitals in every possible way, in consistency with an overall spin and space symmetry. This method is versatile, capable of addressing all kinds of electronic structures: ground and excited states, radicals, ions, etc. It typically provides a good qualitative understanding of electronic structures, but it does not provide good enough accuracy in the quantitative assessment of relative energies, such as excitation energies and energy barriers, because it captures only a portion of the electron correlation energy. In this regard, CASSCF is similar to the Hartree-Fock method but offers better treatment for systems where multiple electronic configurations interact strongly. Hence, this method is convenient and overcomes many problems of HF calculations on open shell systems. However, it is difficult to recover a large portion of the dynamic correlation energy by expanding the active space, its energies miss the effects of dynamic electron correlation. We can solve this problem by using higher-level multireference methods, like the perturbation theory.[69,81,82,86,88–92]

The lowest order of perturbation theory at which electron correlation effects arise is second-order. Given a reference wavefunction of the CASSCF type, second-order Multi-Reference Perturbation Theory (MR-PT2) is already an elaborate undertaking. In this thesis we have used the second-order N-Electron Valence Perturbation Theory (NEVPT2) of Angeli, Malrieu and co-workers,[81–85] but other methods exist such as the Complete Active Space Second-Order Perturbation Theory (CASPT2) developed by Roos and co-workers.[90,93–95]

2.4.3. N-Electron Valence Perturbation Theory (NEVPT2)

The starting point is the CASSCF wave function, which is used as the zeroth-order approximation. NEVPT2, uses an "internal contraction", which means that it applies excitations not to each individual CSF within the CAS, but rather applies the excitation collectively to the entire CASSCF wave function. This method allows for a more efficient calculation by collectively considering excitations across the entire wave function rather than addressing each CSF separately.

The result of a NEVPT2 calculation is a second-order energy correction, ΔE^{PT2}, such that the total energy for each state is[69]

$$E = E^{CAS} + E^{PT2} \tag{2.53}$$

It is important to point out though, that the wave function is not changed by the treatment and remains a CASSCF wave function. Therefore, any calculations of expectation values, magnetic operators, or similar quantities are still based on the CASSCF wavefunction, combined with the second-order corrected total energies.

Although there are still errors and challenges that arise from the electronic structure treatment, NEVPT2 reveals the importance of dynamic correlation and can capture about 70–80% of it.[69] The main limitation of these kind of methods is that they are computationally demanding. The computational costs escalate quickly as a function of the increasing size of the system.

2.4.4. Multiconfiguration Pair-Density Functional Theory (MC-PDFT)

Ten years ago, Manni and co-workers[87,96,97] presented a new theoretical framework called Multiconfiguration Pair-Density Functional Theory (MC-PDFT)[87,96,97] which combines multiconfigurational wave functions with a generalization of DFT. This method is an efficient post-SCF method designed to recover the dynamic correlation missing from multiconfigurational wave functions generated by multireference methods like CASSCF. MC-PDFT calculates the energy of a given reference wave function using an energy expression that includes a term for the on-top energy functional, which depends on both the wave function's density, ρ, and the on-top pair density, Π.[87,98,99] This method adds minimal computational cost to the original multireference approach while achieving, in principle, accuracy comparable to

more traditional, but more expensive, multireference perturbation theories such as CASPT2 or NEVPT2.

As mentioned in previous sections, in KS-DFT[13] the electronic energy is expressed as a functional of the electron spin densities (in the local approximations, LSDA), or their gradients (in the GGA approximations). Moreover, the energy can be expressed as a functional of orbital-dependent quantities such as exchange energy density or kinetic energy density. These types of dependences make this method simpler and more affordable than the WFT methods.[100] However, one of the challenges of DFT is still the treatment of multireference systems and the nearly degenerate states by enforcing their spatial and spin symmetries. While methods like MCSCF, particularly the CASSCF approach, can manage near-degeneracies without ambiguity, they lack the dynamic correlation energy necessary for accurate quantitative predictions of chemical properties like bond and excitation energies. This can be addressed through post-SCF methods like Multireference Perturbation Theory methods such as CASPT2 or NEVPT2, using the CASSCF wave function as a starting point. The problem is that these methods are limited in their applicability due to their high computational cost, which rises steeply as a function of the increasing size of the system. MC-PDFT method combines multiconfigurational WFT with DFT-based methods to efficiently evaluate the electronic energy of strongly correlated systems: it can describe the static correlation (with the multiconfigurational WFT approach) as well as the dynamic correlation (with DFT).[99] This method describes the density functional in terms of the total density, ρ, and the on-top pair density, Π.[87,98,99]

The MC-PDFT method has two steps:

1. Optimization of a multiconfigurational wave function.
2. Calculation of the on-top density functional energy using the obtained one- and two-particle densities.

The first step is to calculate a multiconfiguration wave function, for example, with CASSCF. The total MC-PDFT energy is expressed as[99]

$$E = V_{NN} + \left\langle \Psi^{MC} \middle| \hat{T} \middle| \Psi^{MC} \right\rangle + V_{Ne} + V_C + E_{ot}[\rho, \Pi] \tag{2.54}$$

where V_{NN} is the nuclear-nuclear interaction, $\left\langle \Psi^{MC} \middle| \hat{T} \middle| \Psi^{MC} \right\rangle$ correspond to the kinetic energy, V_{Ne} is the nuclear-electron attraction, V_C is the classical Coulomb interaction of the electronic charge cloud with itself, and the final term is the on-top energy. This energy can be

seen as an extension of the KS-DFT energy with a MCSCF wave function and a functional written in terms of density and on-top pair density $E_{ot}[\rho, \Pi]$.[101] The classical electrostatic energy (V_{NN}, V_{Ne} and V_C) and an approximation to the kinetic energy are directly obtained from the multiconfigurational wave function, Ψ, while the rest of the electronic energy is calculated from an on-top density functional that is, as mentioned, a functional of ρ and Π (probability of finding two electrons on top of each other) of that reference wave function. Eq. 2.54 transforms into[87,99]

$$E = V_{NN} + \sum_{pq} h_{pq} D_{pq} + \frac{1}{2} \sum_{pqrs} g_{pqrs} D_{pq} D_{rs} + E_{ot}[\rho, \Pi, \nabla\rho, \nabla\Pi] \tag{2.55}$$

where $\boldsymbol{D}$ is the one-electron density matrix, $\boldsymbol{h}$ and $\boldsymbol{g}$ contain the one- and two-electron integrals, respectively, and p, q, r, and s are general orbital indices including inactive and active orbitals. Since the second step is based on a density functional, the computational effort is lower than for the first step, and this makes MC-PDFT computationally more affordable than other multireference methods like perturbation theory or configuration interaction.

One issue of multiconfigurational DFT comes from double counting of dynamic correlation since both MCSCF and DFT account, within some extent, for dynamical correlation within the active space. MC-PDFT avoids this problem because only the PDFT is computed, with the MCSCF energy dropped.[101] The KS exchange-correlation functionals depend only on spin-up and spin-down densities and their gradients, and this eliminates double counting of correlation energy.[87]

Using only local densities and their gradients, an exchange-correlation functional for a spin-polarized system can be written as a functional of the total density ρ, the spin magnetization density m (net spin density), and $\rho' \equiv |\nabla\rho|$ and $m' \equiv |\nabla m|$ of their gradients, where[87,99]

$$\rho(\boldsymbol{r}) = \rho_\alpha(\boldsymbol{r}) + \rho_\beta(\boldsymbol{r}) \tag{2.56}$$

$$m(\boldsymbol{r}) = \rho_\alpha(\boldsymbol{r}) - \rho_\beta(\boldsymbol{r}) \tag{2.57}$$

ρ_α is the density of the majority spin-electrons, and ρ_β of the minority spin-electrons at point **r**. This method develops on-top density functionals, what is called "translated" functionals by simply "translate" the previously developed exchange-correlation functionals of spin densities.

In particular, given $E_{XC}(\rho, m, \rho', m')$, the following "translation" protocol from a GGA can be written:[87,99]

$$E_{ot}[\rho(\boldsymbol{r}), \Pi(\boldsymbol{r})] = E_{XC}\begin{pmatrix} \rho(\boldsymbol{r}), \begin{cases} \rho(\boldsymbol{r})(1-R)^{1/2} & \text{if} \quad R \leq 1 \\ 0 & \text{if} \quad R > 1 \end{cases}, \\ \rho'(\boldsymbol{r}), \begin{cases} \rho'(\boldsymbol{r})(1-R)^{1/2} & \text{if} \quad R \leq 1 \\ 0 & \text{if} \quad R > 1 \end{cases} \end{pmatrix} \tag{2.58}$$

where R is the functional $R[\rho(\mathbf{r}), \Pi(\mathbf{r})]$ defined as[87,99]

$$R(\boldsymbol{r}) = \frac{4\Pi(\boldsymbol{r})}{\rho(\boldsymbol{r})^2} \tag{2.59}$$

MC-PDFT has a computational cost that scales similarly as MCSCF methods, but it provides quantitative accuracy comparable to much more expensive multireference perturbation theory methods.[87,102–104] However, the performance of MC-PDFT exhibits a notable dependence on the choice of active space, which is undesirable. This is particularly surprising given that MC-PDFT should perform at least as good as KS-DFT for a minimal active space.[102]

2.4.5. *Ab Initio* Ligand Field Theory (AILFT)

Our goal when working with SCO systems is to obtain meaningful ligand field parameters to properly determine the Δ_o (or $10Dq$) energy gap. This information is obtained through the connection between first-principles CASSCF/NEVPT2 calculations and ligand field theory (LFT).

To make use of this theory, the CASSCF active space needs to be composed of n electrons and 5 orbitals (the 5 orbitals in the active space are of predominantly metal character). After that, a canonicalization of the active orbitals is carried out in order to arrange the orbitals in a convenient manner: the d-orbitals need to be as pure as possible. Of course, these active orbitals are not pure d-orbitals, they contain variable amounts of ligand character, but thanks to the canonicalization, the MOs only have one real d-orbital component each.[105]

In the LFT, one works with fictitious pure d-orbitals of only metal character that are ordered as: $d_{xy}, d_{yz}, d_{z^2}, d_{xz}, d_{x^2-y^2}$. Now the ligand field CSFs can be built by distributing the n-electrons over the 5 ligand field d-orbitals. In the exact same way and order, it is built the actual CAS CSFs, distributing the n active electrons among the d-active orbitals. By this construction

there is a 1:1 correspondence of each and every ligand field CSF with each and every CAS CSFs. Carrying out some mathematical procedures, it is possible to obtain V^{LFT}, which is the effective ligand field potential (the potential created by the ligands at the place of the metal), the *B* and *C* Racah parameters, and the ligand field spin-orbit coupling constant ζ.

After that, there is an additional step which consists in the interpretation of the ligand field matrix in terms of the model used (electrostatic or angular overlap model). This interpretation is not automatic but allows us to dig more deeply into the nature of the ligand field. Using the angular overlap model,[106–109] the theory allows for the quantification of variations in the σ- and π-donor properties of the ligands.

In the end, what can also be extracted is the value of the ligand field splitting energy, Δ_o (or 10*Dq*), which provides valuable information.

2.5. References

1. C. J. Cramer, *Essentials of Computational Chemistry: Theories and Models*, John Wiley & Sons, Ltd, Second Edition., 2004.
2. J. C. Paniagua and P. Alemany, *Química Quàntica*, Llibres de l'Índex, 2017.
3. E. Schrödinger, *Phys. Rev.*, 1926, **28**, 1049–1070.
4. M. Born and R. Oppenheimer, *Ann. Phys.*, 1927, **389**, 457–484.
5. I. N. Levine, *Quantum Chemistry*, Pearson, 2014.
6. A. Szabo and N. S. Ostlund, *Modern Quantum Chemistry*, Dover Publications, Inc., 1996.
7. D. R. Hartree and W. Hartree, *Proc. R. Soc. Lond. A. Math. Phys. Sci.*, 1935, **150**, 9–33.
8. Chr. Møller and M. S. Plesset, *Phys. Rev.*, 1934, **46**, 618–622.
9. R. J. Bartlett and M. Musiał, *Rev. Mod. Phys.*, 2007, **79**, 291–352.
10. B. L. Hammond, W. A. Lester and P. J. Reynolds, *Monte Carlo Methods in Ab Initio Quantum Chemistry*, World Scientific, 1994.
11. E. Fermi, *Rend. Lincei Sci. Fis. Nat.*, 1927, **6**, 602–607.
12. P. Hohenberg and W. Kohn, *Phys. Rev.*, 1964, **136**, B864–B871.
13. W. Kohn and L. J. Sham, *Phys. Rev.*, 1965, **140**, A1133–A1138.
14. L. H. Thomas, *Math. Proc. Camb. Philos. Soc.*, 1927, **23**, 542–548.
15. J. C. Slater, *Phys. Rev.*, 1951, **81**, 385–390.
16. M. Levy, *PNAS*, 1979, **76**, 6062–6065.
17. S. F. Sousa, P. A. Fernandes and M. J. Ramos, *J. Phys. Chem. A*, 2007, **111**, 10439–10452.

18. P. Gütlich and H. A. Goodwin, in *Spin Crossover in Transition Metal Compounds I*, 2004, vol. 233, pp. 1–47.
19. R. Boča and W. Linert, *Monatsh. Chem.*, 2003, **134**, 199–216.
20. P. Gütlich, H. Köppen, R. Link and H. G. Steinhäuser, *J. Chem. Phys.*, 1979, **70**, 3977–3983.
21. J.-P. Tuchagues, A. Bousseksou, G. Molnár, J. J. McGarvey and F. Varret, in *Spin Crossover in Transition Metal Compounds III*, Springer-Verlag, 2004, vol. 235, pp. 85–103.
22. P. Gütlich, A. Hauser and H. Spiering, *Angew. Chem. Int. Ed. Engl.*, 1994, **33**, 2024–2054.
23. H. Paulsen, V. Schünemann and J. A. Wolny, *Eur. J. Inorg. Chem.*, 2013, **2013**, 628–641.
24. P. A. M. Dirac, *Math. Proc. Camb. Philos. Soc.*, 1930, **26**, 376–385.
25. J. P. Perdew, *Phys. Rev. Lett.*, 1985, **55**, 1665–1668.
26. J. P. Perdew, *Phys. Rev. B*, 1986, **33**, 8822–8824.
27. A. D. Becke, *Phys. Rev. A*, 1988, **38**, 3098–3100.
28. P. Jemmer and P. J. Knowles, *Phys. Rev. A*, 1994, **51**, 3571–3575.
29. A. D. Becke, *J. Chem. Phys.*, 1996, **104**, 1040–1046.
30. A. D. Becke, *J. Chem. Phys.*, 1993, **98**, 5648–5652.
31. S. Grimme, *J. Chem. Phys.*, 2006, **124**, 034108.
32. Y. Tawada, T. Tsuneda, S. Yanagisawa, T. Yanai and K. Hirao, *J. Chem. Phys.*, 2004, **120**, 8425–8433.
33. J. Da Chai and M. Head-Gordon, *Phys. Chem. Chem. Phys.*, 2008, **10**, 6615–6620.
34. J. C. Slater, *Phys Today*, 1974, **27**, 49–50.
35. L. Wilk A N and D. M. Nusair, *Can. J. Phys.*, 1980, **58**, 1200–1211.
36. D. C. Langreth and M. J. Mehl, *Phys. Rev. B: Condens. Matter*, 1983, **28**, 1809–1834.
37. J. P. Perdew, J. A. Chevary, S. H. Vosko, K. A. Jackson, M. R. Pederson, D. J. Singh and C. Fiolhais, *Phys. Rev. B.*, 1992, **46**, 6671–6687.
38. A. D. Becke, *J. Chem. Phys.*, 1992, **96**, 2155–2160.
39. E. I. Proynov, E. Ruiz, A. Vela and D. R. Salahub, *Int. J. Quantum Chem.*, 1995, **56**, 61–78.
40. J. P. Perdew, K. Burke and M. Ernzerhof, *Phys. Rev. Lett.*, 1996, **77**, 3865–3868.
41. D. C. Patton and M. R. Pederson, *Phys. Rev. A.*, 1997, **56**, R2495–R2498.
42. J. Tao and J. P. Perdew, *J. Chem. Phys.*, 2005, **122**, 114102.

43. T. C. Leung, C. T. Chan and B. N. Harmon, *Phys. Rev. B*, 1991, **44**, 15–1991.
44. E. Engel and S. H. Vosko, *Phys. Rev. B*, 1994, **50**, 10498–10505.
45. B. Barbiellinit, E. G. Moronit and T. Jarlborgt, *J. Phys.: Condens. Matter*, 1990, **2**, 7597–7611.
46. M. Korling and J. Haglund, *Phys. Rev. B*, 1992, **45**, 13293–13297.
47. D. J. Singh and J. Ashkenazi, *Phys. Rev. B*, 1992, **46**, 11570–11577.
48. P. Dufek, P. Blaha and K. Schwarz, *Phys. Rev. B*, 1994, **50**, 7279–7283.
49. A. Khein and C. J. Umrigar, *Phys. Rev. B*, 1995, **51**, 4105–4109.
50. F. W. Kutzler and G. S. Painter, *Phys. Rev. B*, 1991, **43**, 6865–6872.
51. V. N. Staroverov, G. E. Scuseria, J. Tao and J. P. Perdew, *J. Chem. Phys.*, 2003, **119**, 12129–12137.
52. A. D. Becke, *J. Chem. Phys.*, 1993, **98**, 1372–1377.
53. B. Miehlich, A. Savin, H. Stoll and H. Preuss, *Chem. Phys. Lett.*, 1989, **157**, 200–206.
54. C. Lee, W. Yang and R. G. Parr, *Phys. Rev. B*, 1988, **37**, 785–789.
55. J. Tao, J. P. Perdew, V. N. Staroverov and G. E. Scuseria, *Phys. Rev. Lett.*, 2003, **91**, 146401.
56. M. Reiher, *Inorg. Chem.*, 2002, **41**, 6928–6935.
57. H. Paulsen, L. Duelund, H. Winkler, H. Toftlund and A. X. Trautwein, *Inorg. Chem.*, 2001, **40**, 2201–2203.
58. M. Swart, A. R. Groenhof, A. W. Ehlers and K. Lammertsma, *J. Phys. Chem. A*, 2004, **108**, 5479–5483.
59. R. J. Deeth and N. Fey, *J. Comput. Chem.*, 2004, **25**, 1840–1848.
60. J. Conradie and A. Ghosh, *J. Phys. Chem. B*, 2007, **111**, 12621–12624.
61. O. Salomon, M. Reiher and B. A. Hess, *J. Chem. Phys.*, 2002, **117**, 4729–4737.
62. I. Respondek, L. Bressel, P. Saalfrank, H. Kämpf and A. Grohmann, *Chem. Phys.*, 2008, **347**, 514–522.
63. K. P. Jensen and J. Cirera, *J. Phys. Chem. A*, 2009, **113**, 10033–10039.
64. K. P. Kepp, *J. Inorg. Biochem.*, 2011, **105**, 1286–1292.
65. J. Cirera and F. Paesani, *Inorg. Chem.*, 2012, **51**, 8194–8201.
66. J. Cirera, M. Via-Nadal and E. Ruiz, *Inorg. Chem.*, 2018, **57**, 14097–14105.
67. J. Cirera and E. Ruiz, *Comments Inorg. Chem.*, 2019, **39**, 216–241.
68. F. Furche and J. P. Perdew, *J. Chem. Phys.*, 2006, **124**, 044103.
69. S. K. Singh, J. Eng, M. Atanasov and F. Neese, *Coord. Chem. Rev.*, 2017, **344**, 2–25.

70. F. Jensen, *Introduction to Computational Chemistry*, John Wiley & Sons, Ltd, Third Edition., 2017.
71. D. K. W. Mok, R. Neumann and N. C. Handy, *J. Phys. Chem.*, 1996, **100**, 6003–6361.
72. N. C. Handy and A. J. Cohen, *Mol. Phys.*, 2001, **99**, 403–412.
73. J. W. Hollett and P. M. W. Gill, *J. Chem. Phys.*, 2011, **134**, 114111.
74. H. S. Yu, X. He, S. L. Li and D. G. Truhlar, *Chem. Sci.*, 2016, **7**, 5032–5051.
75. R. Peverati and D. G. Truhlar, *Philos. Trans. A Math. Phys. Eng. Sci.*, 2014, **372**, 1471–2962.
76. D. Gibney, J. N. Boyn and D. A. Mazziotti, *J. Phys. Chem. Lett.*, 2021, **12**, 385–391.
77. Y. Wang, Z. Lin, R. Ouyang, B. Jiang, I. Y. Zhang and X. Xu, *ChemRxiv*, 2024. This content is a preprint and has not been peer-reviewed.
78. G. Frenking and N. Fröhlich, *Chem. Rev.*, 2000, **100**, 717–774.
79. K. P. Kepp, *Coord. Chem. Rev.*, 2013, **257**, 196–209.
80. B. O. Roos, P. R. Taylor and P. E. M. Siegbahn, *Chem. Phys.*, 1980, **48**, 157–173.
81. C. Angeli, R. Cimiraglia, S. Evangelisti, T. Leininger and J. P. Malrieu, *J. Chem. Phys.*, 2001, **114**, 10252–10264.
82. C. Angeli, R. Cimiraglia and J.-P. Malrieu, *Chem. Phys. Lett.*, **350**, 297–305.
83. C. Angeli, R. Cimiraglia and J. P. Malrieu, *J. Chem. Phys.*, 2002, **117**, 9138–9153.
84. C. Angeli, B. Bories, A. Cavallini and R. Cimiraglia, *J. Chem. Phys.*, 2006, **124**, 054108.
85. M. Atanasov, D. Ganyushin, K. Sivalingam and F. Neese, in *Molecular Electronic Structures of Transition Metal Complexes II*, eds. D. M. P. Mingos, P. Day and J. P. Dahl, Springer Berlin, Heidelberg, First Edition., 2012, vol. 143, pp. 149–220.
86. B. O. Roos, K. Andersson, M. P. Fülscher, P.-Å. Malmqvist and L. Serrano-Andrés, in *Advances in Chemical Physics*, eds. I. Prigogine and S. A. Rice, John Wiley & Sons, Inc., 1996, vol. 93, pp. 219–331.
87. G. Li Manni, R. K. Carlson, S. Luo, D. Ma, J. Olsen, D. G. Truhlar and L. Gagliardi, *J. Chem. Theory Comput.*, 2014, **10**, 3669–3680.
88. P. G. Szalay, T. Müller, G. Gidofalvi, H. Lischka and R. Shepard, *Chem. Rev.*, 2012, **112**, 108–181.
89. B. O. Roos, *Acc. Chem. Res.*, 1999, **32**, 137–144.
90. K. Andersson, P. Å. Malmqvist and B. O. Roos, *J. Chem. Phys.*, 1992, **96**, 1218–1226.
91. I. Schapiro, K. Sivalingam and F. Neese, *J. Chem. Theory Comput.*, 2013, **9**, 3567–3580.
92. K. Pierloot, Q. M. Phung and A. Domingo, *J. Chem. Theory Comput.*, 2017, **13**, 537–553.

93. K. Andersson, P.-Å. Malmqvist, B. O. Roos, A. J. Sadlej and K. Wolinski, *J. Phys. Chem.*, 1990, **94**, 5483–5488.
94. B. O. Roos and P.-Å. Malmqvist, *Phys. Chem. Chem. Phys.*, 2004, **6**, 2919–2927.
95. B. O. Roos, M. Fülscher, P.-Å. Malmqvist, M. Merchán and L. Serrano-Andrés, in *Quantum Mechanical Electronic Structure Calculations with Chemical Accuracy*, Springer, Dordrecht, 1995, vol. 13, pp. 357–438.
96. L. Wilbraham, P. Verma, D. G. Truhlar, L. Gagliardi and I. Ciofini, *J. Phys. Chem. Lett.*, 2017, **8**, 2026–2030.
97. J. J. Bao, C. Zhou, Z. Varga, S. Kanchanakungwankul, L. Gagliardi and D. G. Truhlar, *Faraday Discuss.*, 2020, **224**, 348–372.
98. V. N. Staroverov and E. R. Davidson, *Int. J. Quantum Chem.*, 2000, **77**, 651–660.
99. I. Fdez. Galván, M. Vacher, A. Alavi, C. Angeli, F. Aquilante, J. Autschbach, J. J. Bao, S. I. Bokarev, N. A. Bogdanov, R. K. Carlson, L. F. Chibotaru, J. Creutzberg, N. Dattani, M. G. Delcey, S. S. Dong, A. Dreuw, L. Freitag, L. M. Frutos, L. Gagliardi, F. Gendron, A. Giussani, L. González, G. Grell, M. Guo, C. E. Hoyer, M. Johansson, S. Keller, S. Knecht, G. Kovačević, E. Källman, G. Li Manni, M. Lundberg, Y. Ma, S. Mai, J. P. Malhado, P. Å. Malmqvist, P. Marquetand, S. A. Mewes, J. Norell, M. Olivucci, M. Oppel, Q. M. Phung, K. Pierloot, F. Plasser, M. Reiher, A. M. Sand, I. Schapiro, P. Sharma, C. J. Stein, L. K. Sørensen, D. G. Truhlar, M. Ugandi, L. Ungur, A. Valentini, S. Vancoillie, V. Veryazov, O. Weser, T. A. Wesołowski, P. O. Widmark, S. Wouters, A. Zech, J. P. Zobel and R. Lindh, *J. Chem. Theory Comput.*, 2019, **15**, 5925–5964.
100. W. Kohn, *Rev. Mod. Phys.*, 1999, **71**, 1253–1266.
101. G. L. S. Rodrigues, M. Scott and M. G. Delcey, *J. Phys. Chem. A*, 2023, **127**, 9381–9388.
102. S. J. Stoneburner, D. G. Truhlar and L. Gagliardi, *J. Chem. Phys.*, 2018, **148**, 064108.
103. C. E. Hoyer, S. Ghosh, D. G. Truhlar and L. Gagliardi, *J. Phys. Chem. Lett.*, 2016, **7**, 586–591.
104. R. K. Carlson, G. Li Manni, A. L. Sonnenberger, D. G. Truhlar and L. Gagliardi, *J. Chem. Theory Comput.*, 2015, **11**, 82–90.
105. S. K. Singh, J. Eng, M. Atanasov and F. Neese, *Coord. Chem. Rev.*, 2017, **344**, 2–25.
106. C. E. Schäffer and C. K. Jørgensen, *Mol. Phys.*, 1965, **9**, 401–412.
107. C. E. Schäffer, *Pure Appl. Chem.*, 1970, **24**, 361–392.
108. E. Larsen and G. N. La Mar, *J. Chem. Educ.*, 1974, **51**, 633–640.
109. D. E. Richardson, *J. Chem. Educ.*, 1993, **70**, 372–380.

CHAPTER 3

Application of Density Functional Theory Methods to the Study of Unusual Spin-Crossover Systems

3.1. Introduction

In this chapter, we present the computational study of two uncommon spin-crossover (SCO) systems: chromium(II)-based and anionic iron(II)-based complexes. Although this type of compounds has not been widely explored, here we provide models that can help in the design of new systems that can exhibit SCO behaviour and operate at specific temperatures. The presented results provide with guidelines that can be of great help in the synthesis of systems with specific SCO properties, thus directing the synthesis and avoiding unnecessary use of resources.

First, we will introduce the [Cr($^{n\text{-Me}}$indenyl)$_2$] (n = 0–7) family and our study consisting in the functionalization of the indenyl ligands and its effect on the transition temperatures ($T_{1/2}$).[1] Later, we will explain the outcome of our study related to the anionic [Fe(R_1-L_1-pR_2)(L_2)$_3$]$^-$ systems, its several potential functionalizations (L_1 = tris(pyridine-2-yl)R_1methane, where R_1 = CH_2-R or O-R, R = –H, –Me, –Et, –^{n}Pr and –^{n}Bu, R_2 = –NH_2, –OH, –OMe, –Me, –F, –H, –Cl, –Br, –CF_3 and –NO_2, and L_2 = NCO^-, NCS^-, $NCSe^-$ and $NCBH_3^-$), and its implications in tuning the $T_{1/2}$.[2]

3.2. Controlling the Spin-Crossover Behaviour of the [Cr($^{n\text{-Me}}$indenyl)$_2$] Family *via* Ligand Functionalization

In this study, we carried out a computational method to investigate the spin-crossover behaviour within the [Cr($^{n\text{-Me}}$indenyl)$_2$] (n = 0–7) family performing density functional theory (DFT) calculations. Employing the TPSSh[3,4]/Def2-TZVP[5,6] method with the GD3BJ[7] dispersion correction scheme, we determined the thermochemistry and transition temperatures for all family members, which are closely aligned with experimental data. Furthermore, our computational data facilitated the development of a model to elucidate the impact of indenyl ligand functionalization in different positions on the spin-state energy gap ($\Delta E_{HS\text{-}LS}$) and transition temperature. Our results indicate that the C4 and C7 positions of the indenyl ligand significantly influence the SCO properties of these complexes. A model was built that not only quantitatively reproduces the DFT calculations but also serves as a robust tool for analysing and predicting SCO properties within any member of the [Cr($^{n\text{-Me}}$indenyl)$_2$] family.[1]

3.2.1. Spin-Crossover in Cr(II)-Based Complexes

The SCO field is overwhelmingly dominated by d^6-Fe(II) coordination compounds, and multiple examples of such systems exhibiting SCO behaviour have been reported in the literature for mononuclear, polynuclear and extended systems.[8–16] Much less explored is the remaining set of 3d metal ions that can also exhibit SCO behaviour.[17–21] A particularly unexplored set of spin-crossover complexes is the one formed by metallocenes, which are usually low-spin (LS) systems but in some cases can generate a splitting of the d-based molecular orbitals (MO) that allows the occurrence of SCO.

The manganocene systems, delineated by the general formula [Mn($^{n\text{-R}}$Cp)$_2$] (R = Me, ^{i}Pr or ^{t}Bu, n = 0–5, Cp = cyclopentadienyl), manifest SCO behaviour, subject to meticulous investigation *via* both experimental and computational studies.[22–25] Notably, the intricate examination has unveiled the modulatory influence of the interplay between electronic and steric effects on SCO behaviour within these compounds. The indenyl ligand (Ind) is frequently considered to be an analogue of the cyclopentadienyl ring. Moreover, some members of the [Cr($^{n\text{-Me}}$indenyl)$_2$] (n = 0–7) family of metallocene compounds also exhibit SCO behaviour. Bis(indenyl)chromium itself is a dimer but methylation has a structural role that block the dimerization that occurs in the absence of any indenyl substituents.[26–28]

Only few types of d^4-Cr(II) based complexes have shown SCO properties,[26–38] switching from the HS state (S = 2) to the LS state (S = 1) by decreasing the temperature. A plausible explanation for the lack of examples involving this particular ion could lie in the fact that d^4 systems exhibit the smallest entropy gain during spin transition among the d^4–d^7 octahedral complexes. As shown in Chapter 1 and 2:

$$\Delta G = \Delta H - T\Delta S \tag{3.1}$$

$$T_{1/2} = \frac{\Delta H}{\Delta S} \tag{3.2}$$

and the electronic contribution to the entropy change is:

$$\Delta S_{spin} = R\, ln\left(\frac{2S_{HS}+1}{2S_{LS}+1}\right) \tag{3.3}$$

where R is the gas constant and S_i (i = HS, LS) is the total spin. The entropy increase from a change in the spin manifold is minimal with a d^4 electronic configuration, since the spin entropies in octahedral coordination spheres are:

Table 3.1. Spin entropy change when undergoing a spin transition for several electronic configurations.

Electronic configuration	ΔS_{spin}	ΔS_{spin}/J·mol^{-1}·K^{-1}
d^4	R·ln(5/3)	4.24
d^5	R·ln(6/2)	9.13
d^6	R·ln(5/1)	13.38
d^7	R·ln(4/2)	5.76

Although spin entropy may not be the primary factor in initiating the spin-crossover, from the Gibbs energy point of view, a large entropy change favours the spin transition more than a small one.[17,29]

Another possibility for the low number of examples of Cr(II) SCO compounds could lie in their high air sensitivity. Chromium complexes are prone to oxidation, rendering them incapable of showcasing SCO unless strict inert conditions are maintained. In contrast, there are more d^4-Mn(III) SCO active complexes than d^4-Cr(II) by far, probably due to the higher air stability of Mn(III).[17]

3.2.2. Experimentally Reported d^4-Cr(II) Based Spin-Crossover Complexes

The first Cr(II) SCO active complex was reported in 1989 by Halepoto *et al.*,[30,31] and consisted of an octahedral coordination environment with a P_4I_2 coordination sphere: *trans*-[Cr^{II}(depe)$_2I_2$] (depe = 1,2-bis(diethylphosphino)ethane) (Figure 3.1 a).[29–33] This complex undergoes an abrupt transition and shows a thermochromic effect changing from purple-brown at room temperature (HS) to violet at low temperature (LS), with $T_{1/2}$ = 171 K. In 1994, Hughes and co-workers[34] synthesized and characterized the first examples of dinuclear d^4 SCO complexes, specifically the dark green triple-decker organometallic complexes [Cr^{II}_2(μ^2:η^5-P_5)(η^5-C_5Me_5)$_2$]X where X = PF_6^- or SbF_6^- (Figure 3.1 b), in which each chromium is coordinated to a methylated Cp ligand and bridged by a P_5^- heterocycle. Eventually, at a low temperature both complexes undergo abrupt and hysteretic spin transition (PF_6^- $T_{1/2} \approx$ 33 K with $\Delta T_{1/2}$ = 2 K; SbF_6^- $T_{1/2} \approx$ 23 K with $\Delta T_{1/2}$ = 2 K) below which they are essentially

diamagnetic.[34] In 1997 Sitzmann *et al*.[36] studied the $[Cr^{II}(C_5{}^iPr_4)_2]$ chromocene with four isopropyl groups in the cyclopentadienyl ligands, which undergoes a transition at $T_{1/2} \approx 190$ K (Figure 3.1 c), and in 2020 Becker *et al*.[37] found out that the chromium(III) complex $[Cr^{III}(ddpd)_2]^{3+}$ (ddpd = *N,N'*-dimethyl-*N,N'*-dipyridine-2-yl-pyridine-2,6-diamine) can be reduced to form the chromium(II) complex $[Cr^{II}(ddpd)_2]^{2+}$ with a d^4 electron configuration (Figure 3.1 d). The reduced complex can exhibit a reversible SCO that occurs gradually at room temperature.

The d^4-Cr(II) based SCO complexes that we have studied computationally, were reported by O'Hare and co-workers in 1993,[38] and later by Brady and collaborators in 2002,[26–28] corresponding to mononuclear organometallic complexes containing substituted indenyl ligands of the type $[Cr^{II}(\eta^5\text{-R-indenyl})_2]$. In this type of complexes indenyl ligands coordinate the metal centre *via* the Cp unit in a η^5 fashion (Figure 3.1 e, f). These complexes show thermochromic effect being purple in the HS state and green in the LS state.

The rotational orientation of Cp rings on metallocenes normally has no effect on d-orbital energy levels and their splitting, but with related but less symmetrical carbocyclic ligands, the magnetic properties of the associated complexes can be modified by the orientation of the ligands. One example of this is the $[Cr^{II}(\eta^5\text{-R-indenyl})_2]$. Monosubstituted compounds in position 1 with R = ^{t}Bu, $SiMe_3$ are HS species with four unpaired electrons. The unknown monomeric Ind_2Cr, is predicted to have a HS (S = 2) ground state in the staggered configuration (180° rotation angle). However, the 1,3-substituted bis(indenyl) complexes with ^{t}Bu and $SiMe_3$ groups (sterically demanding) are LS complexes with two unpaired electrons (S = 1), and the rings adopt a gauche configuration at a rotation angle near 90º. Steric hindrance from the ^{t}Bu and $SiMe_3$ substituents imposes the indenyl conformations. The change from a staggered to a gauche conformation lowers the symmetry of the Ind_2Cr complex, allowing a greater mixing of the metal and ligand orbitals, resulting in the interaction of nonbonding π orbitals of the indenyl ligand with the chromium d orbitals, which produces bonding and antibonding combinations. The antibonding orbitals remain unoccupied, and the increase in the HOMO–LUMO gap forces the complexes to adopt a LS state configuration. The potential use of sterically imposed ligand rotation for spin-state manipulation makes indenyl compounds a promising source of magnetically adaptable molecules. Moreover, addition of sufficient alkyl groups increases the donor strength of the molecule imposing a LS state. This implies that both steric bulk and electronic effects achieved through selective substitution of the indenyl ligand, can be used to tailor the magnetic properties of the complexes. Consequently, these compounds hold promise as readily adjustable sources of variable-spin molecules.[26]

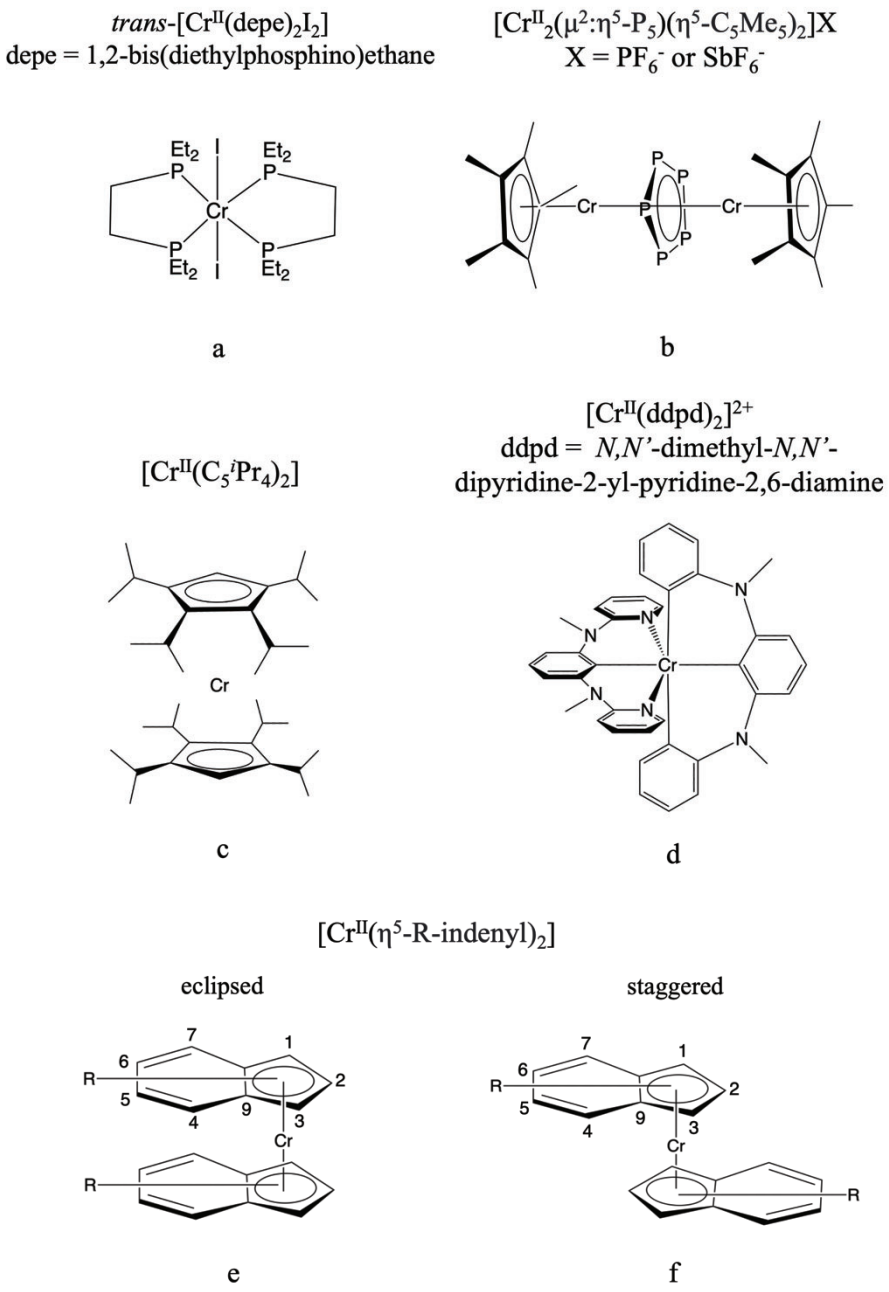

Figure 3.1. Scheme of Cr(II) SCO active complexes. a: *trans*-$[Cr^{II}(depe)_2I_2]$ (depe = 1,2-bis(diethylphosphino)ethane), b: $[Cr^{II}_2(\mu^2{:}\eta^5\text{-}P_5)(\eta^5\text{-}C_5Me_5)_2]X$ (X = PF_6^- or SbF_6^-), c: $[Cr^{II}(C_5{}^iPr_4)_2]$, d: $[Cr^{II}(ddpd)_2]^{2+}$ (ddpd = N,N'-dimethyl-N,N'-dipyridine-2-yl-pyridine-2,6-diamine), e and f: $[Cr^{II}(\eta^5\text{-R-indenyl})_2]$ (eclipsed and staggered, respectively).

In later works by Meredith *et al.*,[27,28] these bis(indenyl)chromium complexes were studied with methyl as substituents, which led to complexes possessing either staggered or eclipsed conformations (Figure 3.1 e, f). They observed that even the presence of a single methyl group on the indenyl ligands disrupts the dimeric form of the unsubstituted ligands compound.

Moreover, the precise location of the methyl group on the ring significantly influences the solid-state geometry of the complex. This change in symmetry results in compounds exhibiting distinct magnetic and structural properties.

Greater interaction between the ligand and the metal orbitals causes the complex to be more responsive to temperature changes, so that the orbital mixing and the HOMO–LUMO gap are increased, which leads to a LS state.

It has been demonstrated that electron-donating groups (EDGs) as substituents can also impact the spin-state of these complexes. For instance, the permethylated complex, [Cr($^{1,2,3,4,5,6,7\text{-Me}}$indenyl)$_2$], despite its staggered configuration, exhibits a LS state. This observation suggests that a combination of symmetry restrictions and site-specific multiple ligand substitutions could yield a diverse range of magnetic behaviours in bis(indenyl)metal complexes, that is, the magnetic properties of these complexes are sensitive to its conformation (staggered, with a 180° rotation angle, eclipsed, with a 0° rotation angle, or gauche with a 90° rotation angle), regardless of whether such conformation is dictated by sterically bulky substituents or arises due to crystal-packing forces. In the solid state and solution, the staggered monomethylated compound [Cr$^{2\text{-Me}}$indenyl)$_2$] has been observed to manifest a HS state, and the [Cr$^{1\text{-Me}}$indenyl)$_2$] adopts an eclipsed conformation in the solid state showing a gradual SCO over a wide temperature range centred at ~130 K, instead of being locked in the HS state as the 2-Me analogue.[28] In polymethylated indenyl ligands, the complexes that have methyl groups located on the benzo portion emerge as crucial in promoting a LS ground state. The preference to exist as a LS complex is approximately:[17,27]

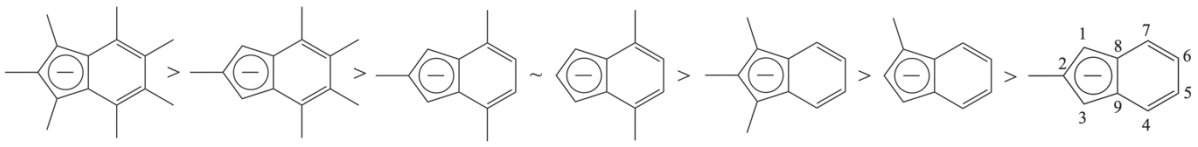

Figure 3.2. Low-spin state stabilization of the indenyl ligands for [Cr$^{n\text{-Me}}$indenyl)$_2$] (n = 1–7) family complexes depending on the number of methyl groups with the approximated corresponding transition temperature values.

The only complex showing a complete and relatively abrupt SCO with $T_{1/2} \approx 150$ K was the 1,2,3-methylated system. The other compounds exhibited gradual and incomplete SCO:

4,7-methylated complex showed a gradual and incomplete transition around 250 K, 2,4,7- and 2,4,5,6,7-methylated systems displayed a gradual SCO starting at 250 K.

3.2.3. Computational Study of d^4-Cr(II) Bis(indenyl)chromium Spin-Crossover Complexes

As previously said, chromocenes can be LS or HS species and can undergo SCO behaviour.[39] It has also been reported that bis(indenyl)chromium complexes can switch between low-spin (S = 1) and high-spin (S = 2) states, depending on the quantity and, significantly, the positioning of methyl groups within the indenyl ligand. These two effects dictate the activation or deactivation of SCO behaviour and large changes in $T_{1/2}$ can be observed.[26–28] Analogously, bis(indenyl)chromium complexes discern variations in SCO between distinct conformations (eclipsed or staggered). Despite empirical observations, still lacks a theoretical framework that comprehensively explains these trends, which is key to the rational design of systems with tailored properties. In this regard, the application of computational tools has demonstrated its potential in dissecting observed trends in $T_{1/2}$ across several families of SCO complexes.[25,40–43]

We analysed the impact of ligand tuning on SCO behaviour within the [Cr($^{n\text{-Me}}$indenyl)$_2$] (n = 0–7) family employing electronic structure calculations. We studied the effects of both ligand methylation and conformation on the splitting of the d-based molecular orbitals for all family members, outlining a model that systematically rationalizes the experimentally observed trends.

3.2.3.1. Computational Details

All DFT calculations have been carried out using the Gaussian 16 (revision B.01) electronic structure suite.[44] All calculations were carried out using a 10^{-8} convergence criterion for the density matrix elements, and the corresponding vibrational analysis ensured that they are minima along the potential energy surface (PES). Although we tested several basis sets and functionals during the benchmarking process, the chosen ones were the triple-ζ basis set with polarization functions (Def2-TZVP)[5,6] for all the elements, and the hybrid *meta*-GGA functional TPSSh.[3] This functional is a hybrid version of the TPSS[4] *meta*-GGA functional with 10% of exact exchange Hartree–Fock. Several post-processing scripts were used to compute the transition temperatures. Grimme's D3 dispersion scheme with Becke–Johnson damping

(GD3BJ)[7] was incorporated to include empirical dispersion. N-Electron Valence Perturbation Theory (NEVPT2)[45] calculations were carried out using Orca 4.0[46] computer code. In these calculations, Def2-TZVPP[5,6] basis set was applied, including the corresponding auxiliary basis set for the correlation and Coulomb fitting. The active space consisted in the 5 d-orbitals of the metal and 4 electrons, and we employed the *ab initio* ligand field theory (AILFT)[47] approach to extract the related orbitals. Isocontours (0.03 $e \cdot a_0^{-3}$) of d-based molecular orbitals were obtained using the IQmol[48] software.

3.2.3.2. Density Functional Theory and Basis Set Benchmarking for the Staggered Configuration of the [Cr($^{1,2,3\text{-Me}}$Indenyl)$_2$] System

Since some of the studied systems have been reported experimentally, the choice of the candidate for the benchmarking is reduced to a few. The candidates for the calibration are the ones with crystallographic and magnetic data reported: [Cr($^{1\text{-Me}}$Indenyl)$_2$], [Cr($^{2\text{-Me}}$Indenyl)$_2$], [Cr($^{4,7\text{-Me}}$Indenyl)$_2$], [Cr($^{1,2,3\text{-Me}}$Indenyl)$_2$], [Cr($^{2,4,7\text{-Me}}$Indenyl)$_2$], [Cr($^{2,4,5,6,7\text{-Me}}$Indenyl)$_2$] and [Cr($^{1,2,3,4,5,6,7\text{-Me}}$Indenyl)$_2$]. Amongst them, [Cr($^{1,2,3\text{-Me}}$Indenyl)$_2$] is the best choice since clearly shows the increasing impact of ligand methylation, exhibiting a complete and relatively abrupt transition with a defined $T_{1/2}$ in the solid state in its staggered configuration.[28]

In order to determine which functional best describes the system of study, full optimization calculations were carried out with several functionals and the Def2-TZVP basis set (Table 3.2). The functional that shows a positive value of the energy difference between HS and LS is the TPSS.[4] Empirical dispersion correction focuses on the performance of minor dispersion forces present in the system to improve the accuracy of DFT calculations, therefore dispersion needs to be added since we have two indenyl rings that can interact in a non-covalent manner. We decided to include the Grimme's D3 dispersion scheme with Becke–Johnson damping (GD3BJ)[7] to the TPSS and TPSSh[3] functionals since previous work has established the TPSSh functional as a suitable DFT method for studying SCO processes in molecular systems given its accuracy in determining the spin-state energy gap.[40,49–51] With this scheme, the combination that presented the most reliable energy differences value was the TPSSh+GD3BJ, which offers a good compromise between computational cost and accuracy.

Table 3.2. Computed energies (in atomic units) of HS and LS as well as the spin-state energy gap (in kcal·mol^{-1}) for different DFT functionals using a Def2-TZVP basis set.

DFT Functional	*E*(HS)/a.u.	*E*(LS)/a.u.	Δ*E*/kcal·mol^{-1}
OLYP	-1974.878667	-1974.867931	-6.74
OPBE	-1974.858439	-1974.849077	-5.87
M06L	-1974.949367	-1974.943597	-3.62
TPSS	-1975.300212	-1975.303802	2.25
B3LYP	-1975.096740	-1975.081618	-9.49
B3LYP*	-1966.046392	-1966.038167	-5.16
TPSSh	-1975.184725	-1975.180622	-2.57
TPSS+GD3BJ	-1975.396260	-1975.405449	5.76
TPSSh+GD3BJ	-1975.275545	-1975.277191	1.03

The accuracy of computational results obtained through DFT methods primarily relies on the chosen exchange correlation functional. Moreover, the selection of the basis set is a critical decision, influencing the level of accuracy in system depiction. A larger basis allows for a more detailed representation of the system but comes with a higher computational cost.

To determine the appropriate basis set for the present study, a full optimization of the staggered [Cr($^{1,2,3\text{-Me}}$Indenyl)$_2$ system was performed for both LS and HS states with different basis sets including Def2-TZV (444 basis functions), Def2-QZV (614 basis functions), Def2-TZVP (945 basis functions), Def2-TZVPP (1172 basis functions), and Def2-QZVP (2232 basis functions). The number of basis functions depends on the chosen basis set (Table 3.4). The functional used for the basis set benchmark was the TPSSh with GD3BJ dispersion correction.

These optimizations aimed to identify when the addition of new basis functions ceases to enhance performance. Increasing the number of basis functions comes with an increase of the computing time, which means an increase of the computational cost. Therefore, we need to find a balance between accuracy and computational cost.

The absence of polarization functions in both Def2-TZV and Def2-QZV basis sets results in slightly larger geometries in both spin states compared to those obtained using basis sets with polarization functions, as can be seen in Table 3.3. This leads to a stabilization of the HS state, obtaining a wrong ordering of the HS/LS energies. These results are consistent with other studies emphasizing the necessity of including polarization functions for an accurate

description of the electrostatic component of the coordination bond.[52,53] Def2-SVP basis set produces slightly smaller Cr–C bonds, consequently increasing the spin-state energy gap.

Table 3.3. Average Cr–C bond lengths using different basis sets for the staggered [Cr($^{1,2,3\text{-Me}}$Indenyl)$_2$] system.

Basis set	d(Cr–C)$_{HS}$/Å	d(Cr–C)$_{LS}$/Å
Def2-SV	2.287	2.159
Def2-SVP	2.280	2.155
Def2-TZV	2.314	2.186
Def2-TZVP	2.286	2.166
Def2-TZVPP	2.285	2.165
Def2-QZV	2.308	2.184
Def2-QZVP	2.285	2.165

As we can see in Figure 3.3, saturation of the properties represented occurs with basis sets larger than Def2-TZVP. We need to point out that Def2-TZVP takes nearly three times longer than Def2-QZV, and Def2-TZVPP takes almost 3.5 times longer. Def2-QZVP takes three times longer than Def2-TZVPP. The observed properties practically do not change when we go from Def2-TZVPP to Def2-QZVP; essentially, Def2-TZVP, Def2-TZVPP and Def2-QZVP provide with very similar results, but the computational cost of the Def2-TZVPP and Def2-QZVP is much bigger than the Def2-TZVP one. Knowing that the change between Def2-TZVP and Def2-TZVPP is relatively small and the change in computational cost is notable, the choice of Def2-TZVP basis set is the most promising to carry out our study.

Table 3.4. Computed energy, enthalpy and entropy change, and transition temperatures using TPSSh functional with the GD3BJ dispersion correction. All energies in kcal·mol^{-1}, entropies in cal·mol^{-1}·K^{-1} and temperatures in K.

Basis set	Number of basis functions	ΔE/kcal·mol^{-1}	ΔH/kcal·mol^{-1}	ΔS/cal·mol^{-1}·K^{-1}	$T_{1/2}$/K
Def2-TZV	444	-2.82	-2.83	9.138	-310
Def2-QZV	614	-1.88	-2.08	10.482	-199
Def2-TZVP	945	1.03	0.60	11.686	52
Def2-TZVPP	1172	1.42	1.00	11.336	88
Def2-QZVP	2232	1.56	1.14	11.833	96

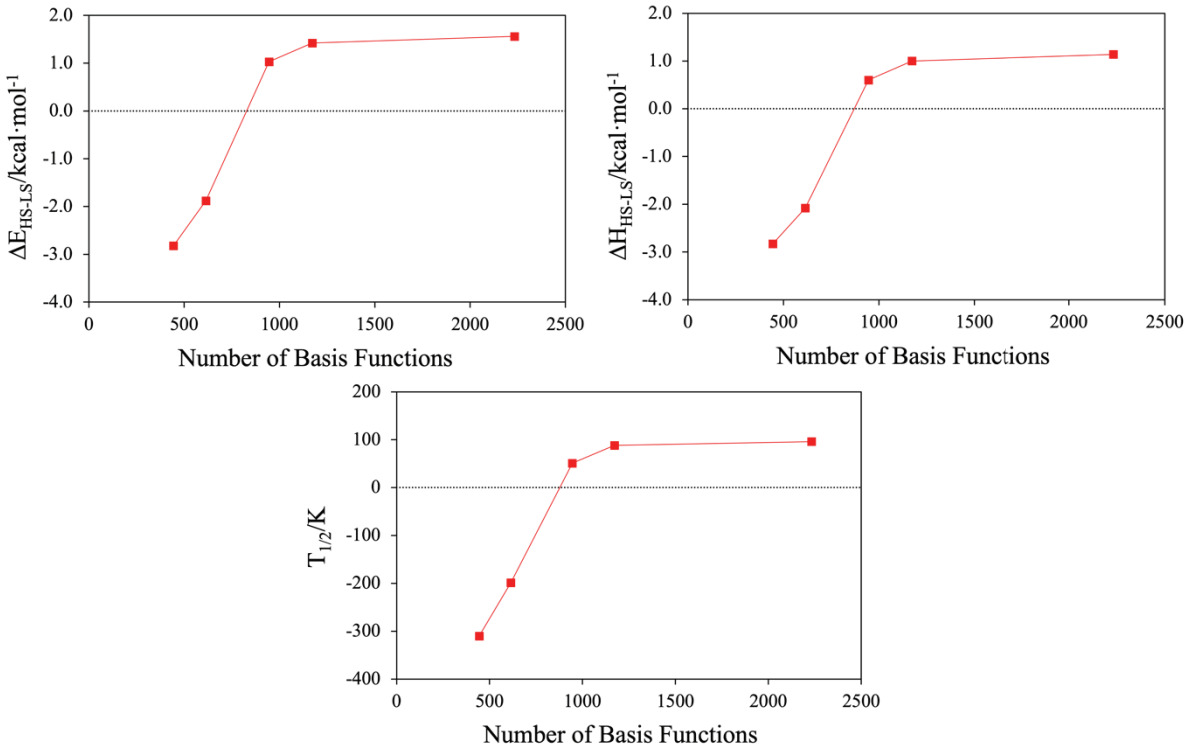

Figure 3.3. Convergence of ΔE, ΔH and $T_{1/2}$ with the basis set size for the [Cr($^{1,2,3\text{-Me}}$Indenyl)$_2$] complex. The basis sets are ordered as Def2-TZV, Def2-QZV, Def2-TZVP Def2-TZVPP and Def2-QZVP. Top: energy and enthalpy change dependence on the number of basis functions, respectively. Bottom: transition temperature dependence on the number of basis functions.

In order to compute thermochemical quantities (*i.e*, ΔS, ΔH, ΔG and, from such quantities, $T_{1/2}$), we need a minimum along the potential energy surface, which returns all positive

harmonic frequencies when the vibrational analysis is done. This step is key in modelling the transition temperatures and requires our structures to be fully optimized. In summary, the method of choice to perform our study is the Def2-TZVP/TPSSh+GD3BJ, providing a computed $T_{1/2}$ = 52 K. This value is slightly below the experimental one (150 K) and it corresponds only to 1.15 kcal·mol^{-1} error in the calculation of the spin-state energy gap (Eq. 3.4), although it could seem quite a large error in temperature. It is important to note that accurately determining the spin-state energy gap is a significant challenge for any electronic structure method[54–57] and that this error is similar to the previously reported values obtained using DFT methods for such quantity.[40,49,51]

$$\Delta H = \left| T_{1/2} - T_{1/2_{exp}} \right| \cdot \Delta S \tag{3.4}$$

To calculate the energy error, we assume that $\Delta E \sim \Delta H$ (Figure 3.4). Because infrared spectrum, *i.e* molecular vibrations, account for the largest portion of the entropy change (ΔS), and they are essentially independent of the chosen functional, it is possible to assume that ΔS should be constant regardless of the method of choice.

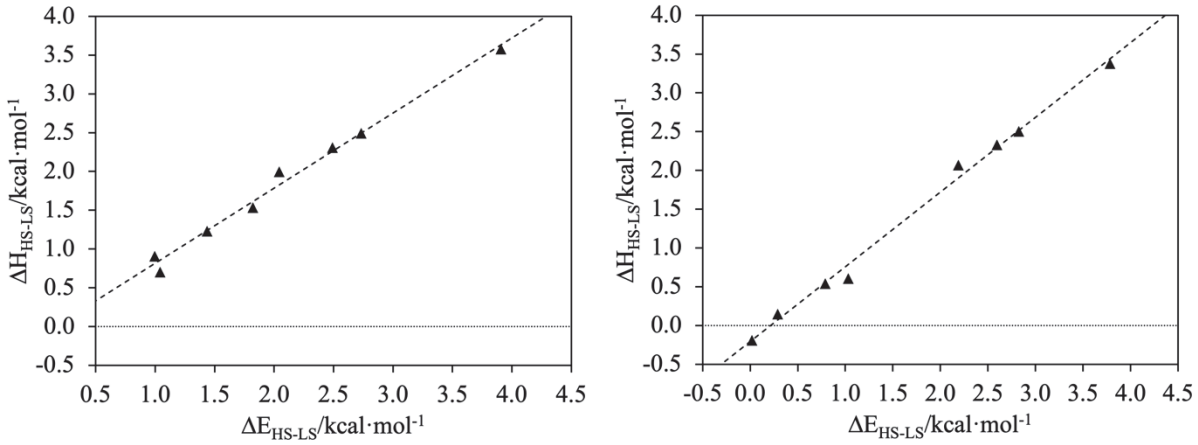

Figure 3.4. Computed spin-state energy gap and enthalpy change correlation for systems with experimental information: [Cr($^{1\text{-Me}}$Indenyl)$_2$], [Cr($^{2\text{-Me}}$Indenyl)$_2$], [Cr($^{1,3\text{-Me}}$Indenyl)$_2$], [Cr($^{4,7\text{-Me}}$Indenyl)$_2$], [Cr($^{1,2,3\text{-Me}}$Indenyl)$_2$], [Cr($^{2,4,7\text{-Me}}$Indenyl)$_2$], [Cr($^{2,4,5,6,7\text{-Me}}$Indenyl)$_2$] and [Cr($^{1,2,3,4,5,6,7\text{-Me}}$Indenyl)$_2$]. Left: eclipsed configuration (R^2 = 0.99) and right: staggered configuration (R^2 = 0.99).

Table 3.5. Computed average Cr–C bond lengths in both spin states and ligand configurations. The experimental data (when available) is presented in parenthesis. All bond lengths are in Angstrom. [a]Experimental data of [Cr($^{1,3\text{-}i\text{Pr}}$Indenyl)$_2$]. [b]The experimental data is in between high-spin and low-spin states; its experimental $T_{1/2}$ is 150 K and the crystal was obtained at 173 K. [c]First crystal was obtained at 173 K and second crystal at 293 K. Both are low-spin since the experimental $T_{1/2}$ > 350 K.

System	Eclipsed		Staggered		Refcode[58]	Reference
	HS	LS	HS	LS		
[Cr(Indenyl)$_2$]	2.320	2.162	2.313	2.168	–	–
[Cr($^{1\text{-Me}}$Indenyl)$_2$]	2.313 (2.262)	2.165 (2.179)	2.304	2.165	TERGAZ02, TERGAZ	[27]
[Cr($^{2\text{-Me}}$Indenyl)$_2$]	2.329	2.164	2.305 (2.308)	2.169	TERFUS	[27]
[Cr($^{6\text{-Me}}$Indenyl)$_2$]	2.318	2.162	2.314	2.167	–	–
[Cr($^{7\text{-Me}}$Indenyl)$_2$]	2.318	2.160	2.311	2.165	–	–
[Cr($^{1,3\text{-Me}}$Indenyl)$_2$]	2.304	2.164	2.296 (2.317)[a]	2.164	–	–
[Cr($^{4,7\text{-Me}}$Indenyl)$_2$]	2.318	2.161 (2.174)	2.309	2.163	EGUNIE	[28]
[Cr($^{5,6\text{-Me}}$Indenyl)$_2$]	2.321	2.161	2.298	2.167	–	–
[Cr($^{1,2,3\text{-Me}}$Indenyl)$_2$]	2.296	2.164	2.286 (2.239)[b]	2.166 (2.239)[b]	EGUNOK	[28]
[Cr($^{2,4,7\text{-Me}}$Indenyl)$_2$]	2.311	2.161 (2.168, 2.187)[c]	2.299 (2.227)	2.163 (2.172)	EGUNUQ01, EGUNUQ	[28]
[Cr($^{2,4,5,6,7\text{-Me}}$Indenyl)$_2$]	2.312	2.159	2.298	2.161 (2.168)	EGUPAY	[28]
[Cr($^{1,2,3,4,5,6,7\text{-Me}}$Indenyl)$_2$]	2.300	2.160	2.286	2.161 (2.182)	YALPEG	[38]

This methodology also reproduces the average C–Cr bond length in both spin states and configurations. The average Cr–C bond lengths are 2.30 Å (HS) and 2.17 Å (LS), and the mean average error concerning experimental data, when available, is only 0.004 Å.

Additionally, we overlapped the computed and crystallographic structures for the only system that has crystallographic data for both spin states for the same system: eclipsed [Cr($^{1\text{-Me}}$indenyl)$_2$] (refcode in the Cambridge Structural Database (CSD):[58] TERGAZ[27] (S = 1) and TERGAZ02[27] (S = 2)). In Figure 3.5 one can see that there are very little differences in the low-spin state with a root mean square deviation of (RMSD) of 0.125 Å, while in the high-spin state, the molecule is more flexible and larger differences in the ring

orientation can be seen with a RMSD of 0.639 Å, but nevertheless, a very good agreement with the Cr–C bond lengths is achieved.

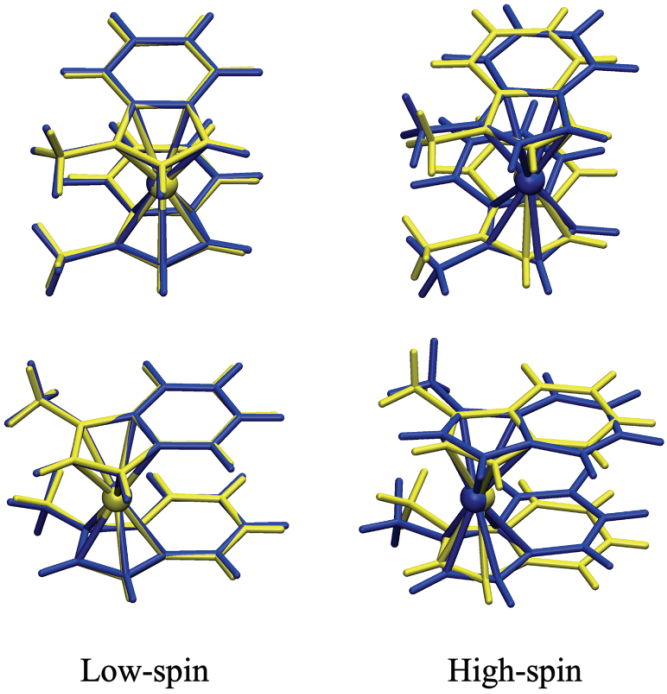

Figure 3.5. Overlap between the optimized (blue) and the crystallographic (yellow) structures for the LS (left) and HS (right) states of the eclipsed [Cr($^{1\text{-Me}}$indenyl)$_2$] system.

3.2.3.3. Methylation of the Indenyl Ligands

With our calibrated method, we decided to systematically study the impact of adding methyl groups in the indenyl ligand on $T_{1/2}$.

SCO has been experimentally observed in both eclipsed and staggered configurations, and the methylation of the indenyl ligand has been proven to have a tuning effect on the transition temperatures of these systems (Figure 3.2). As observed in the experimental studies, we see that the number of methyl groups in the indenyl ligand is relevant in the stabilisation of the LS state. In general, an increasing number of methyl groups induces strong electron donation from the alkylated ring, which, despite symmetry restrictions, effectively increases the HOMO–LUMO gap, favouring the LS state. This is observed specially in the permethylated complex.[28] This is obviously translated to larger ΔE_{HS-LS} and therefore higher transition temperature values. This trend has also been observed in the [Mn($^{n\text{-Me}}$Cp)$_2$] family[25] and is consistent for both eclipsed and staggered configurations, although sensitive differences in $T_{1/2}$ for similar

ΔE_{HS-LS} are observed in some cases (see Table 3.6 [Cr($^{1,2,3,4,5,6,7\text{-Me}}$Indenyl)$_2$]). It is also noteworthy that the addition of just a few methyl groups leads to significant variations in ΔE_{HS-LS} depending on the configuration of the ligand.

Table 3.6. Computed spin-state energy gaps (ΔE_{HS-LS}) and transition temperatures ($T_{1/2}$) for the different members of the [Cr($^{n\text{-Me}}$Indenyl)$_2$] (n = 0–7) family. Experimental values in parenthesis (when available).[26–28] All energies in kcal·mol^{-1} and all temperatures in Kelvin.

System	Eclipsed		Staggered	
	ΔE_{HS-LS}/kcal·mol^{-1}	$T_{1/2}$/K	ΔE_{HS-LS}/kcal·mol^{-1}	$T_{1/2}$/K
[Cr(Indenyl)$_2$]	0.728	143	-0.148	–
[Cr($^{1\text{-Me}}$Indenyl)$_2$]	0.998	169 (130)	0.288	20
[Cr($^{2\text{-Me}}$Indenyl)$_2$]	1.041	119	0.020	–
[Cr($^{6\text{-Me}}$Indenyl)$_2$]	0.821	259	0.556	44
[Cr($^{7\text{-Me}}$Indenyl)$_2$]	1.387	349	1.051	69
[Cr($^{1,3\text{-Me}}$Indenyl)$_2$]	1.437	198	0.790	61
[Cr($^{4,7\text{-Me}}$Indenyl)$_2$]	2.044	388 (> 250)	2.188	168
[Cr($^{5,6\text{-Me}}$Indenyl)$_2$]	1.334	266	0.903	82
[Cr($^{1,2,3\text{-Me}}$Indenyl)$_2$]	1.821	192	1.032	52 (150)
[Cr($^{2,4,7\text{-Me}}$Indenyl)$_2$]	2.492	300	2.595	218 (> 350)
[Cr($^{2,4,5,6,7\text{-Me}}$Indenyl)$_2$]	2.732	256	2.825	218 (> 350)
[Cr($^{1,2,3,4,5,6,7\text{-Me}}$Indenyl)$_2$]	3.908	399	3.784	248

Although in some cases the spin-state energy gap is close for both ligand configurations, significantly differences are observed in the computed $T_{1/2}$. To understand such differences, we performed a vibrational analysis and computed the thermochemical quantities for all the members of the family in both configurations. After adding methyl groups on positions C4 and C7, the energy (Table 3.6) and the enthalpy change (Table 3.7) is essentially equal for both configurations. However, the entropy change is significantly influenced by the configuration, being on average, 50% larger for the staggered one.

Table 3.7. Computed enthalpy and entropy change for [Cr($^{n\text{-Me}}$Indenyl)$_2$] (n = 0–7) family. All enthalpies in kcal·mol^{-1} and entropies in cal·mol^{-1}·K^{-1}.

System	Eclipsed		Staggered	
	ΔH/kcal·mol^{-1}	ΔS/cal·mol^{-1}·K^{-1}	ΔH/kcal·mol^{-1}	ΔS/cal·mol^{-1}·K^{-1}
[Cr(Indenyl)$_2$]	0.72	5.03	-0.25	8.22
[Cr($^{1\text{-Me}}$Indenyl)$_2$]	0.90	5.34	0.15	7.32
[Cr($^{2\text{-Me}}$Indenyl)$_2$]	0.70	5.88	-0.19	7.92
[Cr($^{6\text{-Me}}$Indenyl)$_2$]	0.82	3.18	0.45	10.31
[Cr($^{7\text{-Me}}$Indenyl)$_2$]	1.35	3.86	0.96	13.99
[Cr($^{1,3\text{-Me}}$Indenyl)$_2$]	1.23	6.21	0.54	8.80
[Cr($^{4,7\text{-Me}}$Indenyl)$_2$]	2.00	5.14	2.07	12.29
[Cr($^{5,6\text{-Me}}$Indenyl)$_2$]	1.27	4.77	0.77	9.50
[Cr($^{1,2,3\text{-Me}}$Indenyl)$_2$]	1.53	7.98	0.60	11.69
[Cr($^{2,4,7\text{-Me}}$Indenyl)$_2$]	2.31	7.69	2.33	10.68
[Cr($^{2,4,5,6,7\text{-Me}}$Indenyl)$_2$]	2.49	9.75	2.50	11.46
[Cr($^{1,2,3,4,5,6,7\text{-Me}}$Indenyl)$_2$]	3.58	8.96	3.38	13.60

We also observed that the electronic term is twice as important as the vibrational one in tuning $T_{1/2}$ for the eclipsed configuration, but five times more important for the staggered one. The statistical analysis of the quantitative effect that the thermodynamic quantities have on the transition temperature was performed, which consisted in a standardized analysis of the ΔH and ΔS effect over $T_{1/2}$. To assess the respective contributions that ΔH and ΔS have over the tuning of $T_{1/2}$, it is essential to compute the standardized multilinear regression coefficients. This statistical criterion is only applicable to models developed with linear methods and is used to assess whether a descriptor is significant within a model, that is to say, whether or not this descriptor is providing predictive power to the model. In this case, the descriptors must be autoscaled. Autoscaling is simply a procedure in which, for each descriptor, its average value is subtracted and then is divided by its standard deviation. In this way, new descriptors are obtained that are more compact with each other since the average value for all of them is zero and their dispersion is 1.

Once the descriptors are autoscaled, the model is built, and the standardized regression coefficients are obtained by dividing the individual regression coefficient by its error. With this

working method, it is possible to state the exact order of importance of the descriptors within the model.

With this scheme, we performed a standardized multilinear regression analysis of the dependence of $T_{1/2}$ on the ΔH and ΔS values for both configurations. For this, we assume that ΔH is essentially the electronic spin-state energy gap, and that the entropy change is predominantly driven by the vibrations (excluding its electronic contribution does not affect this analysis). Although this may not be entirely precise, it proves to be a very good estimation as can be seen in the Tables 3.6 and 3.7. Building upon this assumption, we can get the relative weight of both thermodynamic quantities in the transition temperature. As previously said, this analysis shows that for the eclipsed configuration, the electronic term is twice as much important as the vibrational, and for the staggered one, the electronic term has five times more effect on $T_{1/2}$ (Table 3.8). For this reason, changes in ΔS in the eclipsed configuration have a larger impact on $T_{1/2}$, which is responsible for the larger range of values observed for such property in such configuration (Table 3.6). This statistical analysis is included below:

The relationship $T_{1/2} = \Delta H/\Delta S$ was linearized using logarithms:

$$ln(T_{1/2}) = a_1\, ln(\Delta H) - a_2\, ln(\Delta S) + b \tag{3.5}$$

We subtracted the electronic contribution to the entropy change because it is constant in both configurations and quite small since all systems switch between $S = 1$ (LS) and $S = 2$ (HS) (see Eq. 3.3) but, as mentioned, this subtraction does not affect the analysis.

Table 3.8. Results of the standardized analysis of the ΔH and ΔS effect over $T_{1/2}$.

	Eclipsed Configuration	**Staggered Configuration**
a_1 (electronic term)	0.5169	0.9743
a_2 (vibrational term)	0.3318	0.2005
b	5.4676	4.4729
R^2	0.9988	0.9999

The ratio between a_1 and a_2 gives information about the weight of such quantities in tuning the transition temperature.

A clear trend is observed when plotting the spin-state energy gap against the number of methyl groups (Figure 3.6). Moreover, it is observed that the same number of methyl groups

added in different positions cause different effects on the spin-state energy gap (Table 3.6). For instance, the systems [Cr($^{1,3\text{-Me}}$Indenyl)$_2$] and [Cr($^{4,7\text{-Me}}$Indenyl)$_2$] have the same number of methyl substituents, yet the energy gap is larger for the latter as well as the enthalpy change. This suggests an additional influence of the substituent's position on the SCO properties.

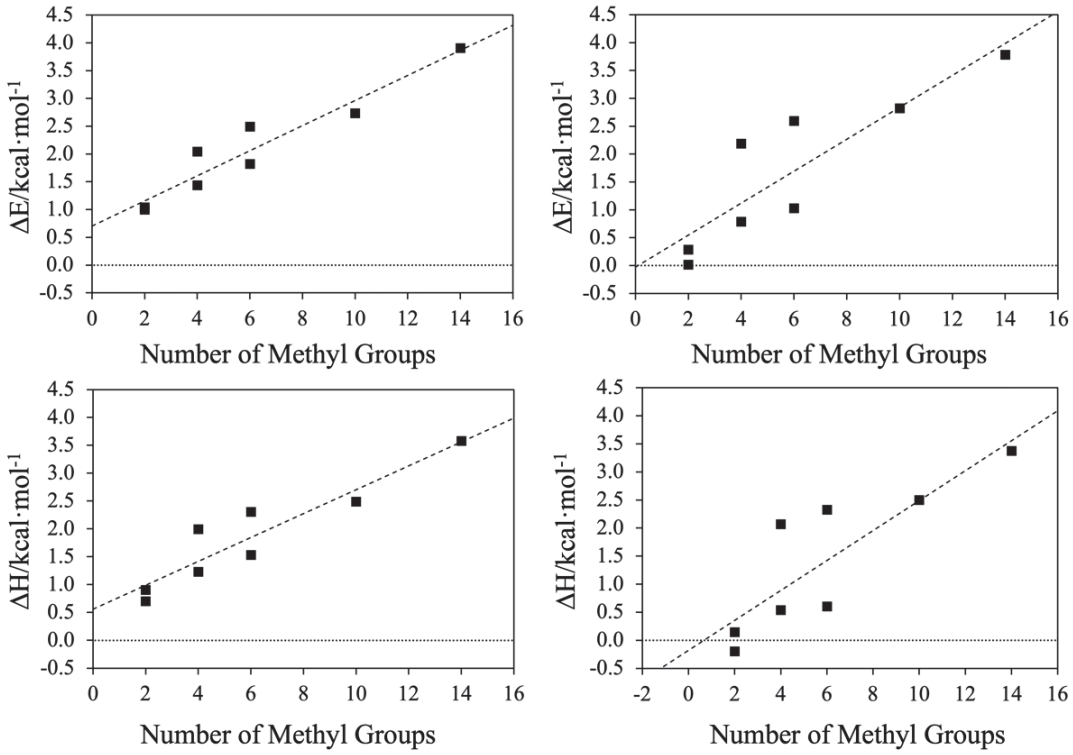

Figure 3.6. Computed spin-state energy gap and enthalpy change against the number of methyl groups for systems with experimental information: [Cr($^{1\text{-Me}}$Indenyl)$_2$], [Cr($^{2\text{-Me}}$Indenyl)$_2$], [Cr($^{1,3\text{-Me}}$Indenyl)$_2$], [Cr($^{4,7\text{-Me}}$Indenyl)$_2$], [Cr($^{1,2,3\text{-Me}}$Indenyl)$_2$], [Cr($^{2,4,7\text{-Me}}$Indenyl)$_2$], [Cr($^{2,4,5,6,7\text{-Me}}$Indenyl)$_2$] and [Cr($^{1,2,3,4,5,6,7\text{-Me}}$Indenyl)$_2$]. The upper row belongs to the spin-state energy gap: eclipsed configuration (left, $R^2 = 0.92$) and staggered configuration (right, $R^2 = 0.77$). The lower row represents the enthalpy change: eclipsed configuration (left, $R^2 = 0.87$) and staggered configuration (right, $R^2 = 0.72$).

In Table 3.7 it is observed that for the staggered configuration, the enthalpy change is almost four times larger for the [Cr($^{4,7\text{-Me}}$Indenyl)$_2$] than for the [Cr($^{1,3\text{-Me}}$Indenyl)$_2$] system, both having two methyl groups. This suggests a different effect on the electronic energies that not only depends on the number of methyl groups but depends also on the position in which the methyl groups are inserted in the indenyl ligands.

Analysing the results, we could categorize the indenyl ligand carbons into three types (Figure 3.7): C_A (C2), C_B (C1, C3, C5 and C6) and C_C (C4 and C7).

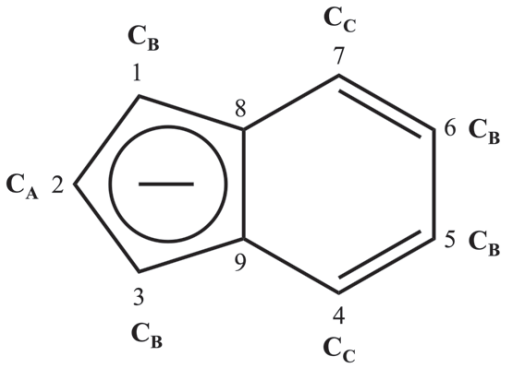

Figure 3.7. Indenyl ligand's type of carbons.

Starting from data from systems with reported experimental information, we constructed a multilinear regression model that expresses $\Delta E_{HS\text{-}LS}$ as a function of three variables: C_A, C_B, and C_C, with each variable weighted by its corresponding coefficient (ω_A, ω_B, and ω_C). These ω_i coefficients represent the relative influence of each carbon type on the spin-state energy gap.

$$\Delta E_{HS-LS} = \omega_A \cdot C_A + \omega_B \cdot C_B + \omega_C \cdot C_C + b \tag{3.6}$$

This model, which is based on the $\Delta E_{HS\text{-}LS}$, can also be used to predict the $\Delta H_{HS\text{-}LS}$ without further modification.

The model reproduces the DFT results for experimentally known systems in both configurations but also predicts $\Delta E_{HS\text{-}LS}$ for systems that have not been obtained experimentally yet. Specifically, we used the model to predict $\Delta E_{HS\text{-}LS}$ for [Cr(Indenyl)$_2$], [Cr($^{6\text{-Me}}$Indenyl)$_2$], [Cr($^{7\text{-Me}}$Indenyl)$_2$], [Cr($^{5,6\text{-Me}}$Indenyl)$_2$] systems achieving excellent agreement with DFT calculations with a mean average error of 0.11 kcal·mol^{-1} (ΔE) and 0.15 kcal·mol^{-1} (ΔH) for the whole data set.

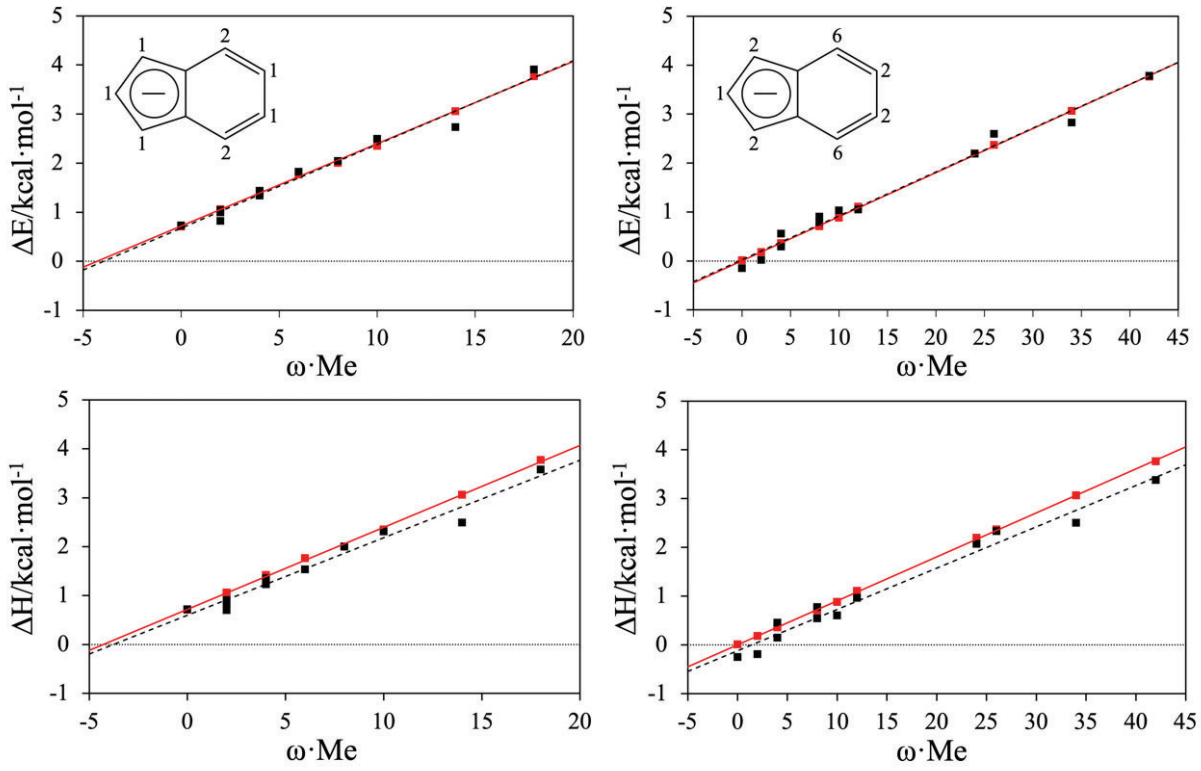

Figure 3.8. Spin-state energy gap and enthalpy change against the weight coefficient of methyl groups (ω·Me) for the [Cr($^{n\text{-Me}}$Indenyl)$_2$] family (n = 0–7). Black squares correspond to the DFT results and the dashed black line is the linear fit of the DFT results. The upper row belongs to the spin-state energy gap: eclipsed configuration (left, R^2 = 0.98) and staggered configuration (right, R^2 = 0.98). The lower row represents the enthalpy change: eclipsed configuration (left, R^2 = 0.97) and staggered configuration (right, R^2 = 0.98). Red squares correspond to the predictions made by our multilinear model and the solid red line is the linear fit of the data using our model. Inset shows the weight that the carbon atoms have in the ligand.

Figure 3.8 reveals the ability of the model to quantify the relative influence of different carbon atoms on $\Delta E_{\text{HS-LS}}$. In the eclipsed configuration, positions C4 and C7 have twice the impact compared to other carbons. This effect is even greater in the staggered configuration, having six times the impact compared to the C2 position, and three times the impact of C1, C3, C5 and C6 (Table 3.9).

Table 3.9. Weights obtained with the multilinear model.

	Eclipsed	**Staggered**
ω_A	0.3481	0.1699
ω_B	0.3547	0.3488
ω_C	0.6471	1.0927
b	0.7066	0.0116
R^2	0.9765	0.9865

This insight allows us to develop the weight coefficient for methyl groups, ω·Me, which is calculated by multiplying the number of methyl groups on each carbon atom by its corresponding weight. For example, consider the eclipsed [Cr($^{2,4,7\text{-Me}}$Indenyl)$_2$]. It has one methyl group at C2, one methyl group at C4 and another one at C7. This is ω·Me = 1·1 + 1·0 + 2·2 = 5, multiplied by two indenyl ligands it is ω·Me = 10. For the staggered configuration, the same complex will be ω·Me = 1·1 + 2·0 + 6·2 = 13, multiplied by two indenyl ligands it is ω·Me = 26.

Table 3.10. Data for the construction of the model. All energies in kcal·mol^{-1}.

Position	C_A	C_B	C_C	**Eclipsed**			**Staggered**		
				ω·Me	**ΔE(DFT)**	**ΔE(Model)**	**ω·Me**	**ΔE(DFT)**	**ΔE(Model)**
–	0	0	0	0	0.728	0.707	0	-0.148	0.012
1	0	1	0	2	0.998	1.061	4	0.288	0.360
2	1	0	0	2	1.041	1.055	2	0.020	0.182
6	0	1	0	2	0.821	1.061	4	0.556	0.360
7	0	0	1	4	1.387	1.354	12	1.051	1.104
1,3	0	2	0	4	1.437	1.416	8	0.790	0.709
4,7	0	0	2	8	2.044	2.001	24	2.188	2.197
5,6	0	2	0	4	1.334	1.416	8	0.903	0.709
1,2,3	1	2	0	6	1.821	1.764	10	1.032	0.897
2,4,7	1	0	2	10	2.492	2.349	26	2.595	2.367
2,4,5,6,7	1	2	2	14	2.732	3.059	34	2.825	3.064
1,2,3,4,5,6,7	1	4	2	18	3.908	3.768	42	3.784	3.763

These coefficients significantly improve the correlation between the model's predictions and the computed and experimental data. Using these coefficients, a clear correlation is obtained for both configurations. Furthermore, the model suggests a correlation with the computed $T_{1/2}$, particularly evident in the staggered configuration (Figure 3.9).

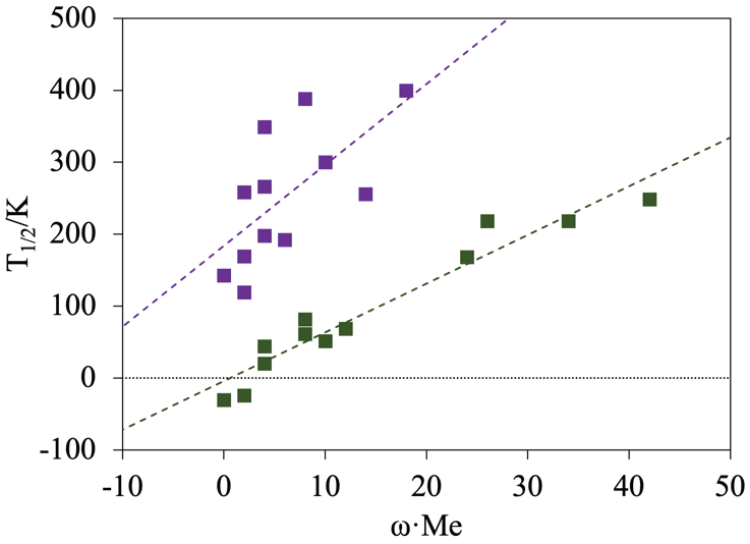

Figure 3.9. Computed transition temperature, $T_{1/2}$, against the weight coefficient of the methyl groups, ω·Me for the [Cr($^{n\text{-Me}}$Indenyl)$_2$] family (n = 0–7). Violet: eclipsed configuration (R^2 = 0.43), green: staggered configuration (R^2 = 0.93).

3.2.3.4. N-Electron Valence Perturbation Theory Calculations and Ab Initio Ligand Field Theory Formalism

Tables 3.6 and 3.7 reveal significant differences between the eclipsed and the staggered configurations of the non-methylated system, [Cr(Indenyl)$_2$], both in terms of spin-state energy gap and ΔH. Indeed, the eclipsed configuration exhibits SCO (computed $T_{1/2}$ = 143 K), while the staggered one does not. Some structural differences might seem an explanation at first glance, however, a closer examination shows nearly identical average Cr–C bond lengths for the LS state (~2.16 Å) in both configurations (Table 3.5). This suggests the origin of such differences lies within the electronic structure of the molecules. To study this effect, N-Electron Valence Perturbation Theory (NEVPT2) calculations were performed on the optimized LS geometries, and the results were analysed using the *ab initio*-based ligand field theory (AILFT) formalism (Table 3.11 and Figure 3.10).

Table 3.11. Ligand-field splitting energies (Δ_o) results for both configurations in cm^{-1}.

System	Δ_o/cm^{-1}	
	Eclipsed	**Staggered**
[Cr(Indenyl)$_2$]	17040	14952
[Cr($^{1\text{-Me}}$Indenyl)$_2$]	17265	15318
[Cr($^{2\text{-Me}}$Indenyl)$_2$]	17025	14935
[Cr($^{6\text{-Me}}$Indenyl)$_2$]	17154	15288
[Cr($^{7\text{-Me}}$Indenyl)$_2$]	17317	15419
[Cr($^{1,3\text{-Me}}$Indenyl)$_2$]	17507	15714
[Cr($^{4,7\text{-Me}}$Indenyl)$_2$]	17449	15851
[Cr($^{5,6\text{-Me}}$Indenyl)$_2$]	17160	15381
[Cr($^{1,2,3\text{-Me}}$Indenyl)$_2$]	17568	15785
[Cr($^{2,4,7\text{-Me}}$Indenyl)$_2$]	17519	15961
[Cr($^{2,4,5,6,7\text{-Me}}$Indenyl)$_2$]	17597	16230
[Cr($^{1,2,3,4,5,6,7\text{-Me}}$Indenyl)$_2$]	18313	17162

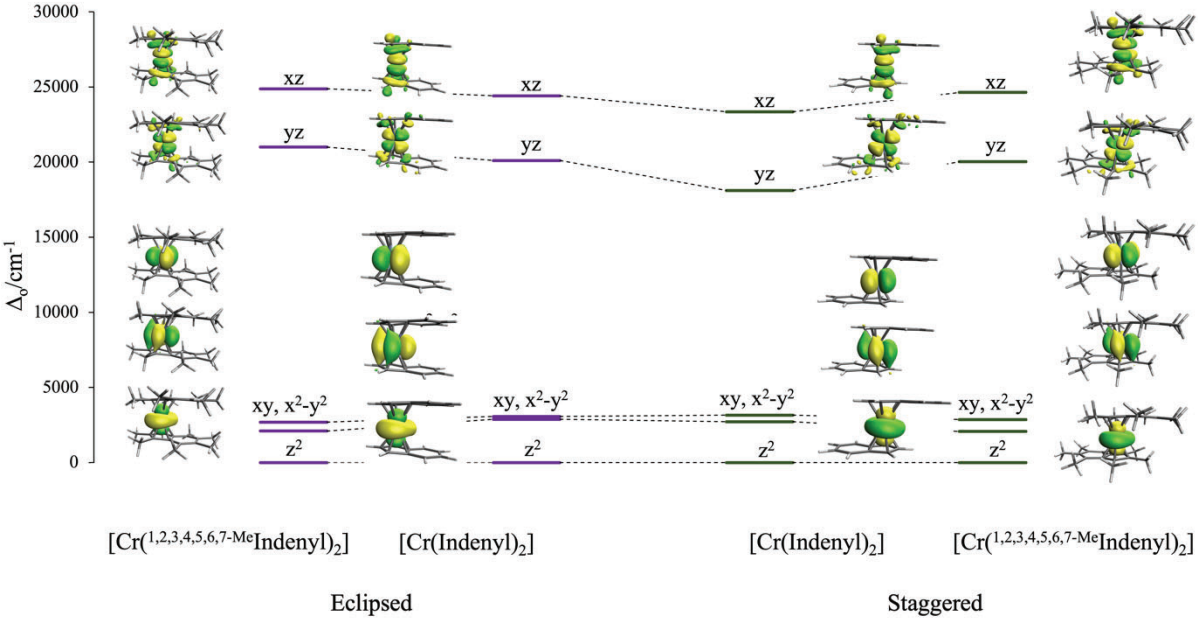

Figure 3.10. d-based molecular orbital diagram (0.03 $e \cdot a_0^{-3}$ isovalue contour) for the non-methylated and permethylated systems in both eclipsed (left) and staggered (right) configurations.

The ligand-field splitting is the energy difference between antibonding and non-bonding orbitals. We can observe that the ligand-field splitting is 2088 cm^{-1} larger in the eclipsed configuration than in the staggered one for the non-methylated system. In fact, the staggered configuration's splitting for such system is too small for SCO to occur. This translates to a stronger antibonding character of the d_{xz} and d_{yz} orbitals in the eclipsed form. Similar to the [Mn($^{n\text{-Me}}$Cp)$_2$] (n = 0–5) family,[23,25] adding methyl groups to the indenyl ligand further enhances the antibonding character of these orbitals. This effect is quantified by analysing the ligand-field splitting of the [Cr($^{1,2,3,4,5,6,7\text{-Me}}$Indenyl)$_2$] family, which shows larger splitting in both configurations compared to the unsubstituted [Cr(Indenyl)$_2$] system. Interestingly, methylation has a more pronounced effect on the staggered conformation than on the eclipsed one. Figure 3.10 summarises these findings.

3.2.3.5. Role of the Ligand Configuration in the Total Entropy Change

Ligand configuration significantly impacts the total entropy change, ΔS, and consequently the transition temperature. As shown in Table 3.7, the staggered configuration generally exhibits higher ΔS values. This translates to lower $T_{1/2}$ for systems with the same degree of methyl substitution, as evident in both Figure 3.9 and Table 3.6. The electronic contribution to ΔS is minimal and constant (1.015 $cal \cdot K^{-1} \cdot mol^{-1}$) in both configurations because all systems switch from S = 1 to S = 2 (Eq. 3.3). The key difference lies in the intrinsic flexibility of the molecule. The staggered configuration experiences less π–π stacking interactions, allowing for greater conformational freedom and ultimately a larger entropy change (Appendix section, Figure A3.1). The impact of ligand configuration on ΔS and $T_{1/2}$ is evident in systems that have the positions C4 and C7 substituted with methyl groups, as shown in Table 3.7. For instance, ΔH for the eclipsed and staggered configurations of [Cr($^{4,7\text{-Me}}$Indenyl)$_2$] are nearly identical (2.00 $kcal \cdot mol^{-1}$ and 2.07 $kcal \cdot mol^{-1}$, respectively). However, the ΔS value for the staggered configuration is significantly larger, roughly double that of the eclipsed form. Consequently, the calculated $T_{1/2}$ values differ considerably: 388 K for the eclipsed configuration and 168 K for the staggered one.

Finally, our model for calculating $\Delta E_{HS\text{-}LS}$ (and $\Delta H_{HS\text{-}LS}$) as a function of methyl group position in the indenyl ligand proves valuable in two ways. First, it accurately predicts this parameter quickly and second, it identifies the positions that most significantly affect $\Delta E_{HS\text{-}LS}$. In both eclipsed and staggered configurations, positions C4 and C7 have the greatest impact on increasing the energy changes. This effect is particularly pronounced in the staggered

configuration, where $\Delta H_{HS\text{-}LS}$ for the [Cr($^{4,7\text{-Me}}$Indenyl)$_2$] complex is four times higher compared to the [Cr($^{1,3\text{-Me}}$Indenyl)$_2$].

3.2.4. Summary

This work introduces a quantitative method for accurately calculating spin-state energy gaps in [Cr($^{n\text{-Me}}$Indenyl)$_2$] complexes (n = 0–7). Using the TPSSh/Def2-TZVP model with GD3BJ dispersion correction, we can precisely compute $T_{1/2}$ not only for experimentally characterized systems of the family but also for some new ones proposed in this work. As observed in other SCO metallocenes, adding methyl groups to the indenyl ligand generally increases both the spin-state energy gap and $T_{1/2}$. However, our analysis reveals additional factors that can modulate the transition temperature. The first key factor is the ligand configuration. The indenyl ligand in these complexes exhibits two possible configurations. Our calculations demonstrate that the eclipsed configuration leads to a larger $\Delta E_{HS\text{-}LS}$, resulting in a higher transition temperature. This effect is further amplified because the entropy change upon spin transition in the eclipsed configuration tends to be smaller compared to the staggered configuration. Therefore, the combination of both factors leads to a higher $T_{1/2}$ in the eclipsed configuration.

The second factor influencing $T_{1/2}$ is the position of the methyl group on the indenyl ligand. Positions C4 and C7 have a significantly greater impact on $\Delta E_{HS\text{-}LS}$, translating to higher $T_{1/2}$ values. While generally, a higher degree of methylation increases $T_{1/2}$ across the board, this work highlights the potential for fine-tuning this property. By strategically selecting the number and position of methyl groups, and the configuration of the indenyl ligand coordinated to the chromium centre, we can achieve precise control over the transition temperature.

With the generated DFT data, we constructed a model that quantitatively predicts $\Delta E_{HS\text{-}LS}$ based on the influence of methyl group substitution on different indenyl ligand carbon atoms. The model identifies C4 and C7 as the positions with the strongest impact on $\Delta E_{HS\text{-}LS}$, with this effect being even more pronounced in the staggered configuration. This model effectively predicts the spin-state energy gap of systems that have not been reported yet (as shown in Figure 3.8) and can, in principle, be applied to any indenyl methylation pattern. This tool serves as a valuable asset for the rational design of novel [Cr($^{n\text{-Me}}$Indenyl)$_2$] complexes with desired $T_{1/2}$ values.

3.3. Exploring the Computational Design of Anionic Fe(II)-Based Spin-Crossover Systems

This study delves into the systematic ligand design within the parent anionic spin-crossover system $[Fe(OEt\text{-}L_1\text{-}pH)(NCS)_3]^-$ (with OEt-L_1-pH = tris(pyridine-2-yl)ethoxymethane) to obtain a high degree of tunning of its transition temperature, $T_{1/2}$. Employing the TPSSh[3]/Def2-TZVP[5,6] method, our calculations accurately reproduce experimental reported data and provide valuable insights into adjusting the $T_{1/2}$ value up or down. The substitution of the thiocyanate ligand with similar groups such as NCO^-, $NCSe^-$, and $NCBH_3^-$, induces significant changes in $T_{1/2}$, while finer adjustments are achievable through functionalizing the *para* position of the pyridyl groups. Overall, $[Fe(OEt\text{-}L_1\text{-}pH)(NCS)_3]^-$ serves as a unique platform for investigating how ligand design can yield tailored properties in new anionic SCO materials.[2]

3.3.1. Spin-Crossover in Anionic Fe(II)-Based Complexes

Due to extensive synthetic efforts, systems based on Co(II),[59–63] Mn(III)[64–66] and Fe(III)[67–78] have been investigated to an increasing extent over the last years. However, those based on the d^6-Fe(II) ion remain the most extensively reported systems.[10,79–100] Nonetheless, despite the growing interest, the majority of SCO complexes tend to be either cationic or neutral, and the few reported anionic SCO systems are restricted to Fe(III)[70–78] and Fe(II)[86,87,95–102] metal ions. The lack of more anionic SCO systems is somehow an issue since such complexes play a crucial role in designing multifunctional materials, like fluorescent or conducting switchable materials.[103,104]

3.3.2. Experimentally Reported Anionic Fe(II)-Based Spin-Crossover Systems

In 2003 Yamada *et al.*[86] reported a system based on the neutral H_3L^{Me} and on the deprotonated $(L^{Me})^{3-}$ hexadentate N_6 tripod-like ligands, which consists of a supramolecular 2D array comprising SCO cationic $[Fe^{II}H_3L^{Me}]^{2+}$ and anionic $[Fe^{II}L^{Me}]^-$ complexes: $[Fe^{II}H_3L^{Me}][Fe^{II}L^{Me}]X$, with X = ClO_4^-, BF_4^-, PF_6^-, AsF_6^-, SbF_6^-, and H_3L^{Me} = tris[2-(((2-methylimidazol-4-yl)methylidene)amino)ethyl]amine.

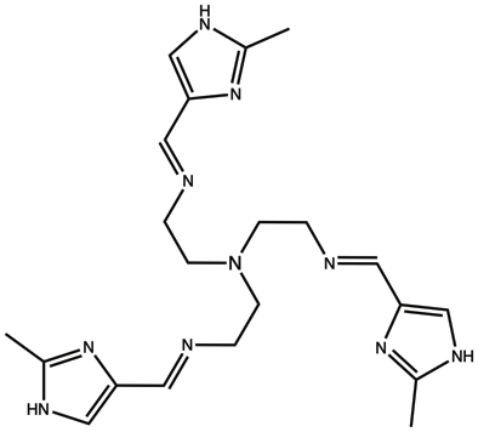

Figure 3.11. H_3L^{Me} tripod-like hexadentate ligand.

In the 295-200 K range, the SCO does not occur at the iron of $[Fe^{II}H_3L^{Me}]^{2+}$ but it does at the iron of $[Fe^{II}L^{Me}]^{-}$. The SCO occurred at $[Fe^{II}H_3L^{Me}]^{2+}$ in the 200-100 K range. The magnetic susceptibility data thus demonstrated a two-step (HS-$[Fe^{II}H_3L^{Me}]^{2+}$ + HS-$[Fe^{II}L^{Me}]^{-}$) ⇄ (HS-$[Fe^{II}H_3L^{Me}]^{2+}$ + LS-$[Fe^{II}L^{Me}]^{-}$) ⇄ (LS-$[Fe^{II}H_3L^{Me}]^{2+}$ + LS-$[Fe^{II}L^{Me}]^{-}$) SCO, being the second step involving $[Fe^{II}H_3L^{Me}]^{2+}$, steeper than the high temperature one.

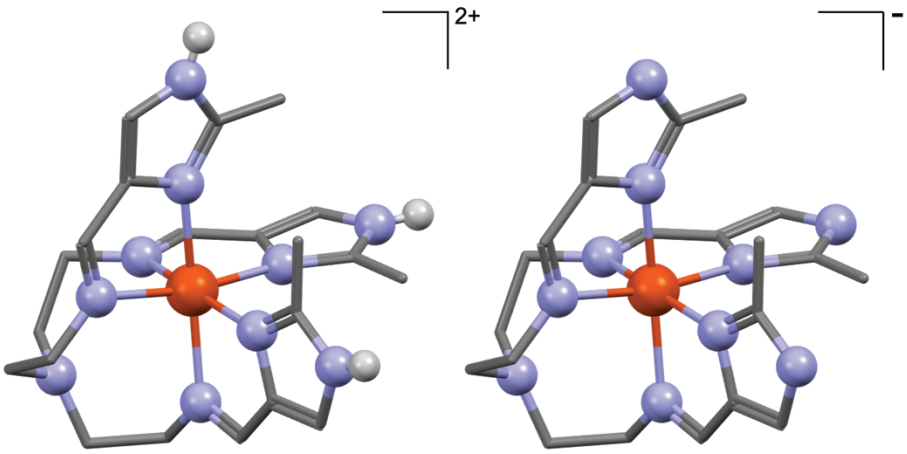

Figure 3.12. $[Fe^{II}H_3L^{Me}]^{2+}$ and $[Fe^{II}L^{Me}]^{-}$ complexes. Orange: Fe, violet: N, gray: C, yellow: S, white: H.

In 2015 Gómez *et al.*[87] reported a system which consists of discrete trinuclear anionic $[Fe^{II}_3(\mu\text{-L})_6(H_2O)_6]^{6-}$ units, based on a substituted triazole L^{2-} anionic ligand, L^{2-} = 4-(1,2,4-triazol-4-yl)ethanedisulfonate. Above room temperature, this system exhibits a transition from HS-HS-HS to HS-LS-HS states, accompanied by a large hysteresis loop (> 85 K).

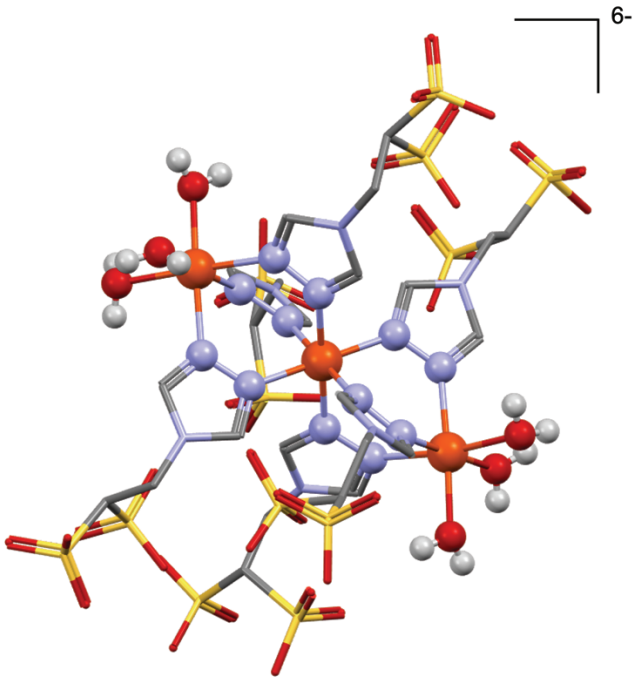

Figure 3.13. $[Fe^{II}_3(\mu\text{-}L)_6(H_2O)_6]^{6-}$ anionic SCO system. Orange: Fe, violet: N, gray: C, yellow: S, red: O, white: H.

Finally, we centred our interest in complexes similar to the parent mononuclear $[Fe(py_4C)(NCS)_3]^-$ SCO anionic complex, reported in 2012 by Hirosawa *et al*,[95] based on the tripodal ligand py_4C = tetrakis(2-pyridyl)methane. The complex with chemical formula $[Fe(py_4C)_2][Fe(py_4C)(NCS)_3]_2$ comprises one low-spin (LS) complex cation, $[Fe(py_4C)_2]^{2+}$, and two SCO complexes $[Fe(py_4C)(NCS)_3)]^-$.

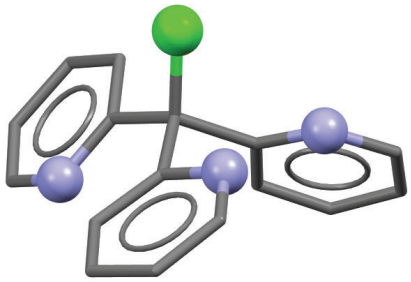

Figure 3.14. Rigid tripodal ligand py_3C-R. Violet: N, gray: C, green: R group. Tetrakis(2-pyridyl)methane when R = py.

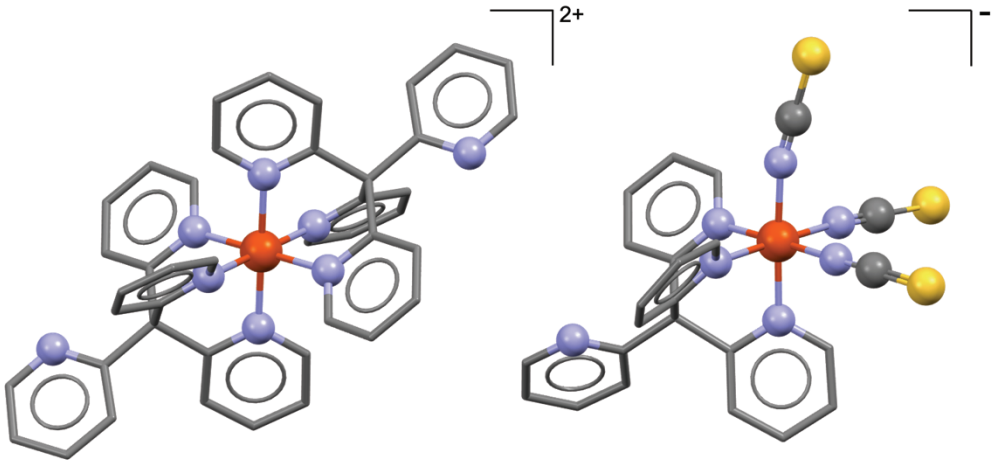

Figure 3.15. $[Fe(py_4C)_2]^{2+}$ cation and $[Fe(py_4C)(NCS)_3]^-$ anion. Orange: Fe, violet: N, gray: C, yellow: S.

Since its inception, this series has been expanded to include other parent examples of the general formula $[Me_4N][Fe(py_3C\text{-}R)(NCS)_3]$,[96–99] where R = OH, CH_3, *n*-$C_{18}H_{37}$). Among these, the $[Me_4N][Fe(py_3C\text{-}OH)(NCS)_3]\cdot H_2O$ complex demonstrates abrupt hysteretic behaviour ($T_{1/2}\downarrow$ = 224 K and $T_{1/2}\uparrow$ = 246 K) with a relatively significant heating-rate dependence.[96,97]

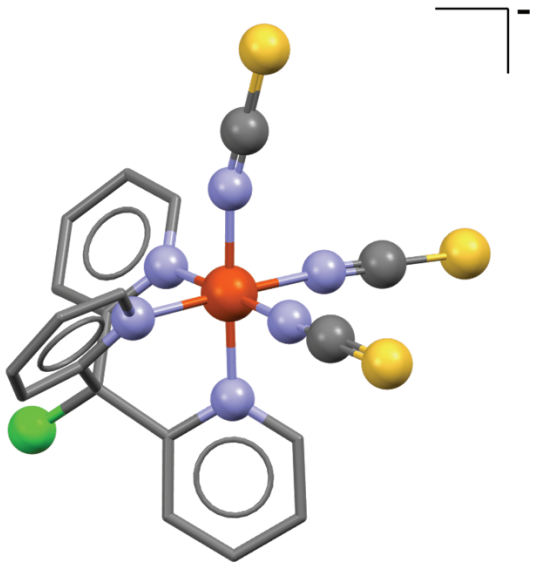

Figure 3.16. $[Fe(py_3C\text{-}R)(NCS)_3]^-$ anion. Orange: Fe, violet: N, gray: C, yellow: S, green: R group (OH, CH_3, *n*-$C_{18}H_{37}$).

More recently, in 2020 Cuza and co-workers[100] focused effort to elucidate the influence of linear ancillary coligands, specifically NCE^- (E = S, BH_3), on the $T_{1/2}$. In this pursuit, a study detailed two isomorphic complexes with a general formula of $[Fe(py_3C\text{-}OEt)_2][Fe(py_3C\text{-}OEt)(NCE)_3]_2 \cdot 2CH_3CN$, where NCE^- can either be NCS^- or $NCBH_3^-$. These complexes share a similar tripodal ligand structure (in Figure 3.16, R would be an ethoxy group) and interestingly, the counterion corresponds to the LS $[Fe(py_3C\text{-}OEt)_2]^{2+}$ complex, similar of observed in $[Fe(py_4C)_2][Fe(py_4C)(NCS)_3]_2$.[95] This study showed two different behaviours without hysteretic effects. For E = S, the transition was gradual and incomplete at 205 K with residual HS fraction of ~10%, whereas for E = BH_3 was a complete and gradual two-step-like transition centred around 245 K and 380 K.

Kashiro and co-workers[101] continued studying the $[Fe(py_3C\text{-}R)(NCS)_3]^-$ complexes, varying the side chain R of the py_3C-R group with linear alkyl (R = C_nH_{2n+1}, n = 1–7) and acyloxyl derivatives (R = $C_nH_{2n+1}CO_2$, n = 1–6). Essentially, they observed that all the compounds exhibited SCO, varying from 289 to 338 K for the alkylated ones, and from 216 to 226 K for the acyloxylated ones. They concluded that it exists an n odd-even effect on $T_{1/2}$ related with the ΔS across the SCO rather than crystal field modification or intermolecular interaction.

Finally, Cuza *et al.*[102] in 2021 reported two mononuclear Fe(II) polymorphs: $[(C_2H_5)_4N]_2[Fe(py_3C\text{-}OEt)(NCS)_3]_2$ which exhibits an abrupt and complete transition at ~132 K, and $[(C_2H_5)_4N][Fe(py_3C\text{-}OEt)(NCS)_3]$ which does not undergo SCO and remains HS over the entire studied temperature range.

We based our computational study in this kind of anionic SCO systems, as it will be shown in the next section.

3.3.3. Computational Study of Anionic d^6-Fe(II) Spin-Crossover Complexes

The transition temperature is key not only for the physical characterization of SCO systems,[105] but also for operational purposes, as one may want to preselect the transition temperature at which the transition takes place. However, achieving this goal experimentally is highly challenging. Despite significant progress in this domain, understanding how to modulate the transition temperature through ligand design remains a challenging task in tailoring the properties of new SCO systems. Given this inherent challenge, computational tools have emerged as valuable help, offering insights into temperature modulation within SCO systems. These tools encompass diverse electronic structural methods across various theoretical levels and even employ machine learning protocols.[1,40,41,51,106–109]

The synthesis of new anionic SCO systems with tailored properties is an important target towards the rational design of multifunctional materials that can operate at specific temperatures since they are important for designing fluorescent multifunctional materials and conducting switchable materials. For this reason, we decided to study in detail the anionic SCO system $[Fe(OEt\text{-}L_1\text{-}pH)(NCS)_3]^-$ with OEt-L_1-pH = tris(pyridine-2-yl)ethoxymethane, since it offers a high degree of functionalization within the molecular skeleton.

The objective is to study the impact of such modifications on the spin-state energy gap, the corresponding transition temperatures, and the overall SCO behaviour of such systems. To do so, we delve into the impact that chemical functionalization at three different potential sites can have over the $T_{1/2}$ of the family of $[Fe(R_1\text{-}L_1\text{-}pR_2)(L_2)_3]^-$ with R_1 = CH_2-R or O-R (R = –H, –Me, –Et, –^{n}Pr and –^{n}Bu), R_2 = $–NH_2$, –OH, –OMe, –Me, –F, –H, –Cl, –Br, $–CF_3$ and $–NO_2$, and L_2 = NCO^-, NCS^-, $NCSe^-$ and $NCBH_3^-$.

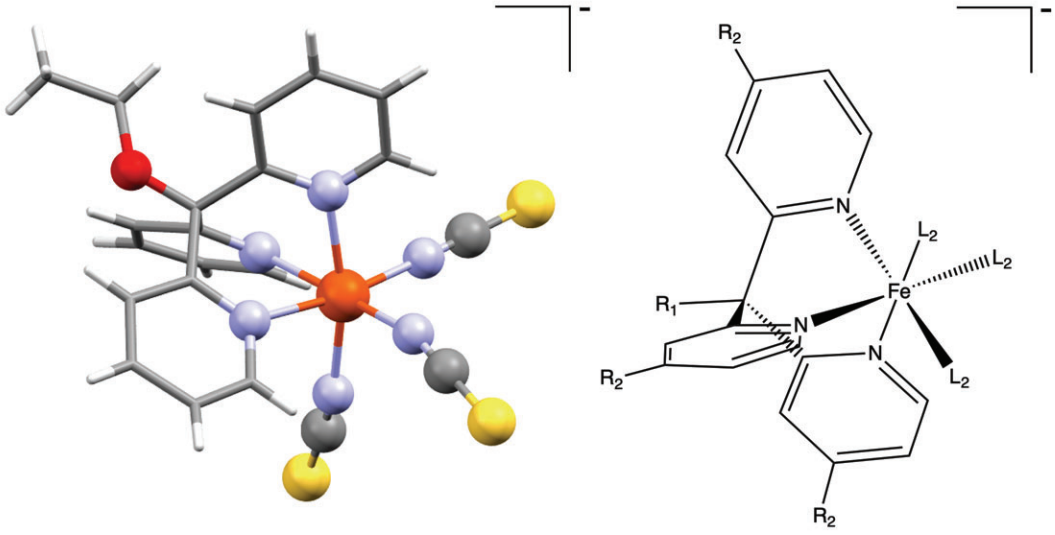

Figure 3.17. Anionic Fe(II)-based SCO complex for the computational study. Left: $[Fe(OEt\text{-}L_1\text{-}pH)(NCS)_3]^-$ (orange: Fe, violet: N, gray: C, yellow: S, red: O, white: H), right: schematic representation of the system of study $[Fe(R_1\text{-}L_1\text{-}pR_2)(L_2)_3]^-$ indicating the potential functionalization sites R_1, R_2 and L_2.

3.3.3.1. Computational Details

All DFT calculations have been carried out with the Gaussian 16 (revision B0.1)[44] electronic structure package with a 10^{-8} convergence criterion for the density matrix elements, using the triple-ζ basis set with polarization functions for all elements (Def2-TZVP).[5,6] For all systems, the exchange correlation functional TPSSh[3,4] has been used, which has been recently reported as the most accurate one towards transition metal ions d^4–d^7 in terms of the spin-state energy gaps.[40,49–51] However, employing DFT methods for calculating these energy gaps is still a challenge.[110–113] Therefore, a benchmark study on the $[Fe(OEt\text{-}L_1\text{-}pH)(NCS)_3]^-$ system was performed (see next section). The corresponding vibrational analysis was performed for all optimized structures to ensure that they were global minima along the PES, and $T_{1/2}$ were estimated using the thermochemistry quantities obtained from this analysis. To study the d-MOs energy gap in LS systems ($S = 0$), NEVPT2[45] calculations were performed using the Orca 4.0 computer code.[46] In these calculations, we employed the Def2-TZVPP[5,6] basis set, including the corresponding auxiliary basis set for the correlation and Coulomb fitting. The active space used contains the 5 d orbitals of the metal and 6 electrons, and the AILFT approach was employed to extract the related orbitals.[47]

3.3.3.2. Density Functional Theory Benchmarking for the $[Fe(OEt\text{-}L_1\text{-}pH)(NCS)_3]^-$ System

The benchmark shows that only TPSSh and OPBE[114–117] among several exchange/correlation functionals provide the correct spin-state energy gap (Table 3.12). TPSSh functional, a hybrid version of the TPSS[4] meta-GGA functional with 10% of exact exchange Hartree–Fock, was chosen due to its overall performance towards SCO systems.[49] The basis set chosen is the Def2-TZVP since has proven efficiency in this kind of studies.[49]

Table 3.12. Computed energy, enthalpy and entropy changes, and transition temperatures using several functionals. All energies in kcal·mol^{-1}, entropies in cal·mol^{-1}·K^{-1}, and temperatures in Kelvin.

Method	ΔE/kcal·mol^{-1}	ΔH/kcal·mol^{-1}	ΔS/cal·mol^{-1}·K^{-1}	$T_{1/2}$/K
B3LYP	-7.83	-9.14	23.78	-384
B3LYP*	-5.54	-6.86	21.65	-317
M06L	-4.84	-6.30	19.77	-319
OLYP	-9.39	-10.89	21.44	-508
OPBE	2.39	0.79	22.29	35
TPSSh	6.94	5.59	24.67	226

Table 3.13. Experimental data reported for different $[Fe(R_1\text{-}L_1\text{-}pR_2)(L_2)_3]^-$. Transition temperatures in Kelvin. [a]Two-step transition, py_3C-OEt = tris(2-pyridyl)ethoxymethane, py_4C = tetrakis(2-pyridyl)methane, [n]R = nonadecane.

System	Counterion	$T_{1/2}$/K	Refcode[58]	Reference
$[Fe(OEt\text{-}L_1\text{-}pH)(NCS)_3]^-$	$[NEt_4]^+$	132.3	IROMOU	102
$[Fe(OEt\text{-}L_1\text{-}pH)(NCS)_3]^-$	$[Fe(py_3C\text{-}OEt)_2]^+$	205	ZANLEJ	100
$[Fe(OEt\text{-}L_1\text{-}pH)(NCBH_3)_3]^-$	$[Fe(py_3C\text{-}OEt)_2]^+$	245(1), 380(2)	ZANLOT[a]	100
$[Fe(OH\text{-}L_1\text{-}pH)(NCS)_3]^-$	$[NEt_4]^+$	224($T_{1/2}\downarrow$) 246($T_{1/2}\uparrow$)	XOPDAJ	96,97
$[Fe(CH_3\text{-}L_1\text{-}pH)(NCS)_3]^-$	$[NBu_4]^+$	330	IHEKEN	97
$[Fe(CH_3\text{-}L_1\text{-}pH)(NCS)_3]^-$	$[PPh_4]^+$	290	UXOHEW	98
$[Fe(CH_3\text{-}L_1\text{-}pH)(NCS)_3]^-$	$[NMe_4]^+$	313.4	–	101
$[Fe(Et\text{-}L_1\text{-}pH)(NCS)_3]^-$	$[NMe_4]^+$	338.2	–	101
$[Fe(^n Pr\text{-}L_1\text{-}pH)(NCS)_3]^-$	$[NMe_4]^+$	298.4	VULHES	101
$[Fe(^n Bu\text{-}L_1\text{-}pH)(NCS)_3]^-$	$[NMe_4]^+$	315.4	KUYFES	101
$[Fe(py\text{-}L_1\text{-}pH)(NCS)_3]^-$	$[Fe(py_4C)_2]^+$	161	GECHED	95
$[Fe(^n R\text{-}L_1\text{-}pH)(NCS)_3]^-$	$[NMe_4]^+$	185.6	RIDGUJ	99

As previously mentioned, there are limited anionic SCO systems reported in the literature.[70–78,86,87,95–102] Among these, the Fe(II) compound $[Fe(OEt\text{-}L_1\text{-}pH)(NCS)_3]^-$ provides an opportunity to explore how various chemical modifications on the ligand can influence the physical properties of the compound, potentially enabling precise tuning of $T_{1/2}$. In Figure 3.17 the molecular structure of the parent compound is presented, along with a schematic representation showing three sites where chemical modifications can be applied to modify the ligand field around the metal centre in $[Fe(R_1\text{-}L_1\text{-}pR_2)(L_2)_3]^-$ and consequently its SCO properties:

- R_1 group: ethoxy in the parent system.
- R_2 group: *para* position of the pyridyl groups, H in the parent system.
- L_2 group: NCS^- in the parent system.

Therefore, once the DFT functional and the basis set are chosen, a systematic study can be carried out to observe how modifications at such sites affect the spin-state energy gap in the system. Overall, we denote the system of study by the generic formula $[Fe(R_1\text{-}L_1\text{-}pR_2)(L_2)_3]^-$,

representing the three positions in which we will apply chemical modifications to the molecule. The study of the several chemical modifications will be shown in the next sections.

3.3.3.3. Addition of Counterions and Modification of R_1 side chain in $[Fe(R_1\text{-}L_1\text{-}pH)(NCS)_3]^-$ System

We carried out some control calculations to evaluate if the inclusion of counterions was needed. There is experimental data (Table 3.13) of a family of systems ($[Fe(Me\text{-}L_1\text{-}pH)(NCS)_3]^-$) that has been characterized with three different counterions: $[NBu_4]^+$, $[PPh_4]^+$ and $[NMe_4]^+$. The experimental transition temperature values for such systems are 330 K, 290 K and 313 K, respectively. These results suggest a minor impact of the counterion on $T_{1/2}$, however, we computed the corresponding $[C][Fe(Me\text{-}L_1\text{-}pH)(NCS)_3]$ systems, with C = $[NBu_4]^+$, $[PPh_4]^+$ and $[NMe_4]^+$, to assess the impact of including the counterion in the calculations.

The combination of basis functions results in delocalized MOs that can encompass multiple atoms. This delocalization across a molecule is acceptable, but complications arise when considering interactions between two molecules. Calculating the interaction energy between molecular fragments introduces an artificial stabilization because electrons from one molecule can occupy atomic orbitals (AOs) (or their basis functions) centred on atoms from the other molecule, and that is known as the basis set superposition error (BSSE). After correcting the spin-state energy gap for the BSSE, the computed values across the series turned out to be quite similar and slightly higher than the computed value for the anionic species:

Table 3.14. Computed ΔE, ΔH, ΔS and $T_{1/2}$ for the $[C][Fe(Me\text{-}L_1\text{-}pH)(NCS)_3]$ molecule without and with counterions C = $[NBu_4]^+$, $[PPh_4]^+$ and $[NMe_4]^+$. All energies in kcal·mol^{-1}, entropies in cal·mol^{-1}·K^{-1} and temperatures in Kelvin. Experimental values in parenthesis.

C	ΔE/kcal·mol^{-1}	ΔE(BSSE)/kcal·mol^{-1}	ΔH/kcal·mol^{-1}	ΔS/cal·mol^{-1}·K^{-1}	$T_{1/2}$/K	Refcode[58]	Reference
–	10.48	10.48	9.15	23.500	389	–	–
$[NBu_4]^+$	12.55	11.71	11.29	21.075	536 (330)	IHEKEN	97
$[PPh_4]^+$	12.37	11.46	11.04	24.136	458 (290)	UXOHEW	98
$[NMe_4]^+$	12.83	12.63	11.49	21.361	538 (313)	–	101

The counterion does modify the SCO behaviour within a minimal range but does not suppress or induce it. The spin-state energy gap changes very little, and remarkably, the calculations can model the decrease in $T_{1/2}$ when the counterion $[PPh_4]^+$ is added.

There are however, two issues in adding the counterions. One is that we do not have experimental counterions for most of the systems studied in this work, and the potential candidates as counterions are quite large to account for all of them. Besides, we are addressing the impact of tuning the electronic structure of the SCO molecule, which, as indicated above, does not change significantly upon addition of the counterion. Second, the inclusion of the counterions forces us to correct our spin-state energy gaps for the BSSE, which we did, but we cannot BSSE correct the thermal contributions to enthalpy and entropy, thus making the estimation of $T_{1/2}$ less reliable. This can be corrected using a periodic approach, but as we will see later on, this does not provide with any further insight in the presented case here.

To further evaluate whether the counterions influenced the predicted trends, we computed the entire series for $[NMe_4][Fe(Me\text{-}L_1\text{-}pH)(L_2)_3]$ (where L_2 = NCO^-, NCS^-, $NCSe^-$, and $NCBH_3^-$) with and without counterion, and compared it with the trends computed for the anionic families of $[Fe(Me\text{-}L_1\text{-}pH)(L_2)_3]^-$ and $[Fe(OEt\text{-}L_1\text{-}pH)(L_2)_3]^-$ systems. These findings indicate that adding the counterions does not change the reported trends in this work in a significant way. By plotting the computed $T_{1/2}$ against the *f* factor[118] (*f* factor gives information about the strength of the ligand, the spectrochemical series of ligands is given by the variation of such factor. The stronger the ligand, the larger the *f* factor), the reported trend is the same with and without the counterion (Figure 3.18), and the most significant difference arises from changing the R_1 = OEt group by an R_1 = Me group in the tridentate ligand (Table 3.15), which has a much greater impact than considering calculations with counterions.

It is generally possible to write Δ_o in octahedral complexes as the product of two functions, each of only one variable:[118]

$$\Delta_o = f(ligands) \cdot g(central\ ion) \tag{3.7}$$

The spectrochemical series of ligands is given by the variation of *f*, which it is chosen to be written as a pure number relative to the hexa-aqua ion. The experimental Δ_o value of $[Cr(H_2O)_6]^{3+}$ is reported and the *f* factor of water is considered to be $f(H_2O) = 1.00$. From there, one can obtain $g(Cr^{3+})$. To obtain the *f* values for the rest of ligands, different complexes are

explored. For example, knowing the experimental Δ_o reported value of $[CrCl_6]^{3-}$ and $g(Cr^{3+})$, $f(Cl^-)$ can be obtained. The *f* factors used are NEVPT2 level computed.

Table 3.15. *f* factor and computed transition temperatures in Kelvin for the systems $[NMe_4][Fe(Me\text{-}L_1\text{-}pH)(L_2)_3]$, $[Fe(Me\text{-}L_1\text{-}pH)(L_2)_3]^-$ and $[Fe(OEt\text{-}L_1\text{-}pH)(L_2)_3]^-$, with L_2 = NCS^-, $NCSe^-$, $NCBH_3^-$ and NCO^-.

L_2	*f*	$T_{1/2}$/K		
		$[NMe_4][Fe(Me\text{-}L_1\text{-}pH)(L_2)_3]$	$[Fe(Me\text{-}L_1\text{-}pH)(L_2)_3]^-$	$[Fe(OEt\text{-}L_1\text{-}pH)(L_2)_3]^-$
NCS^-	1.2	538	389	226
$NCSe^-$	1.23	588	445	281
$NCBH_3^-$	1.29	723	612	441
NCO^-	1.09	293	240	24

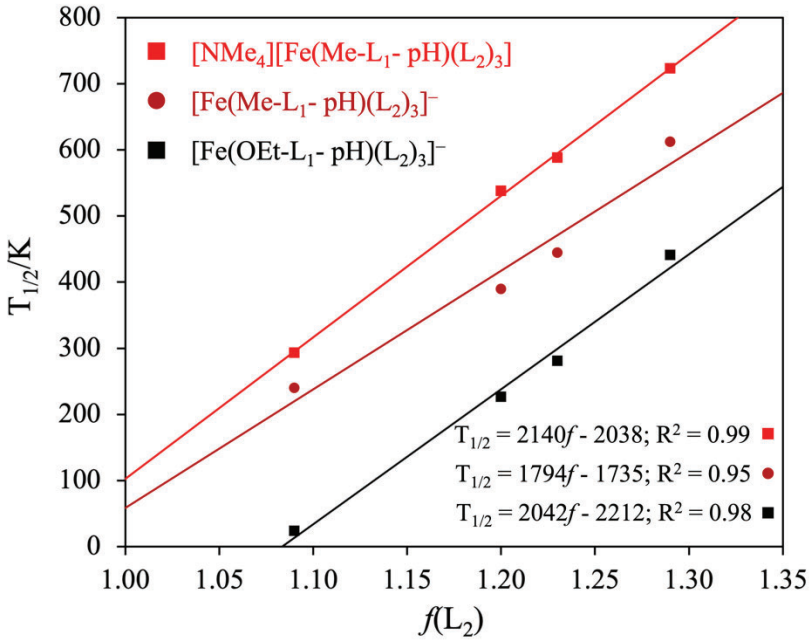

Figure 3.18. Transition temperature against the *f* factor for $[NMe_4][Fe(Me\text{-}L_1\text{-}pH)(L_2)_3]$ (red squares, $R^2 = 0.99$), $[Fe(Me\text{-}L_1\text{-}pH)(L_2)_3]^-$ (maroon circles, $R^2 = 0.95$) and $[Fe(OEt\text{-}L_1\text{-}pH)(L_2)_3]^-$ (black squares, $R^2 = 0.98$) systems, with L_2 = NCS^-, $NCSe^-$, $NCBH_3^-$ and NCO^-.

Adding the counterions introduces a shift due to different issues discussed above, but the trends are fully consistent. In fact, the experimental shift in $T_{1/2}$ between $[NEt_4][Fe(OEt\text{-}L_1\text{-}pH)(NCS)_3]$ (132 K) and $[NMe_4][Fe(Me\text{-}L_1\text{-}pH)(NCS)_3]$ (313 K) is 181 K, quite close to the

shift computed without counterions, 163 K. This reinforce the idea that the calculations clearly grasp the effects of the electronic structure tuning over the transition temperature and accurately capture the changes in the ligand field strength around the Fe(II) metal centre.

Notice that small changes in the spin-state energy gap have a larger impact in the computed $T_{1/2}$, thus making more important the trends than the absolute value.

The aim of this work is to evaluate by means of computational tools how to tune the ligand field in anionic SCO systems to achieve a fine degree of control over such property. A different issue would be pursuing to reproduce the shape of the experimental spin-transition curve which is not available for most of the computed systems, and it is out of the scope of this work. In such case, a different computational approach is needed. Within our research group, studies of SCO systems with a calibrated DFT+U method were carried out,[107] but such methods often need a specific parameterization of the U term to reproduce experimental data, which penalizes the predicting capabilities of the presented results. Periodic calculations using a pure *meta*-GGA functional were also carried out in the group,[119] but such methods overestimate the spin-state energy gap and show a lower performance towards spin-state energy gaps than TPSSh. Additionally, the calculation of the thermochemical quantities involves a huge computational cost, because analytical gradients are not implemented. However, from the previous works one can extract that the entropy per molecule barely changes between the isolated or periodic calculation (12.8 vs 11.3 $cal \cdot K^{-1} \cdot mol^{-1}$, respectively for the $[Fe(bpp)_2][BF_4]_2$ system),[119] thus making the largest source of error the accurate calculation of the spin-state energy gap. Therefore, as long as the method captures properly such quantity, the expansion to a periodic system does not provide with any significant additional information when discussing the thermochemistry of the system (and the $T_{1/2}$), which again, is the main point of this work. This accuracy can only be achieved by the TPSSh functional, that unfortunately is not implemented in most periodic boundary codes.

We also modified the length of the R_1 group in $[Fe(R_1\text{-}L_1\text{-}pR_2)(L_2)_3]^-$ maintaining the other substituents as the parent system (R_2 = H and L_2 = NCS^-). Two sets of substituents were studied: alkyl groups ranging from the methyl up to the *n*-butyl group (R_1 = CH_2-R, R = –H, –Me, –Et, –^{n}Pr and –^{n}Bu), and alkoxy groups starting from hydroxy up to the *n*-butoxy group (R_1 = O-R, R = –H, –Me, –Et, –^{n}Pr and –^{n}Bu). The results can be found in Table 3.16.

Table 3.16. Computed ΔE, ΔH, ΔS and $T_{1/2}$ for the $[Fe(R_1\text{-}L_1\text{-}pH)(NCS)_3]^-$ systems. All energies in kcal·mol^{-1}, entropies in cal·mol^{-1}·K^{-1} and temperatures in Kelvin. Experimental values in parenthesis when available. [a]Average experimental $T_{1/2}$ value.

$[Fe(R_1\text{-}L_1\text{-}pH)(NCS)_3]^-$	ΔE/kcal·mol^{-1}	ΔH/kcal·mol^{-1}	ΔS/cal·mol^{-1}·K^{-1}	$T_{1/2}$/K	Reference
R_1 = H	8.32	7.02	23.82	295	–
R_1 = Me	10.48	9.15	23.50	389 (311)[a]	97,98
R_1 = Et	6.97	5.63	24.66	228 (338)	101
R_1 = ^{n}Pr	9.22	7.83	22.01	356 (298)	101
R_1 = ^{n}Bu	9.34	7.97	23.84	334 (315)	101
R_1 = OH	9.03	7.70	23.32	330 (235)[a]	96,97
R_1 = OMe	7.92	6.59	26.47	249	–
R_1 = OEt	6.94	5.59	24.67	226 (169)[a]	100,102
R_1 = O^{n}Pr	9.42	8.00	23.15	346	–
R_1 = O^{n}Bu	7.12	5.75	24.39	236	–

While O-donor and C-donor substituents exhibit different effects on $T_{1/2}$, with C-donors resulting in higher $T_{1/2}$ values, the transition temperature appears to be independent of the length of the R_1 side chain from an electronic point of view. This observation is illustrated in Figure 3.19, where the correlation between $T_{1/2}$ and the number of C atoms in the side chain appears to be independent for both types of donors. O-donor groups tend to stabilize at a $T_{1/2}$ value of 235 K, while C-donor groups lead to a higher $T_{1/2}$ value of 356 K. Therefore, although distinct behaviours are observed between C-donor and O-donor groups, no clear dependence on the length of the –R group for the R_1 substituent can be discerned. These findings align with experimental studies on how alkyl/acyloxyl side chains impact $T_{1/2}$.[101] It is important to note that while no significant electronic effects are observed, the length of this side chain and the odd-even effect[101] (particularly for long chains) may influence crystal packing, thereby modulating the overall shape of the spin transition. However, from an electronic perspective, the length of the side chain appears to have minimal impact on the SCO properties of the $[Fe(R_1\text{-}L_1\text{-}pR_2)(L_2)_3]^-$ systems.

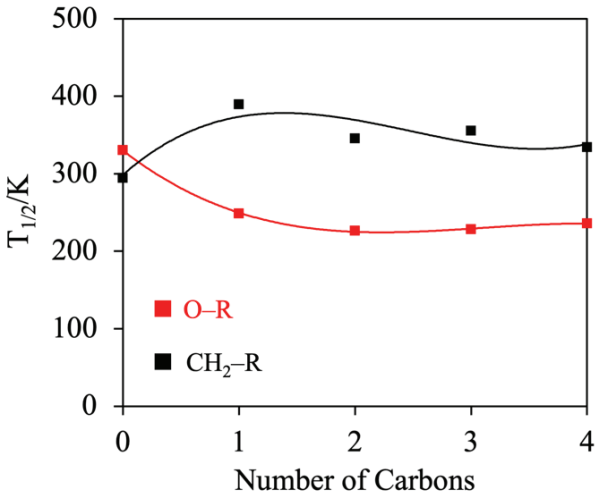

Figure 3.19. Computed transition temperatures against the number of carbons of the R_1 group side chain. Red: R_1 = O-R, black: R_1 = CH_2-R, with R = –H, –Me, –Et, –^{n}Pr and –^{n}Bu.

3.3.3.4. Modification of L_2 in $[Fe(OEt\text{-}L_1\text{-}pH)(L_2)_3]^-$ System

We studied the impact of substituting the thiocyanate (NCS^-) ligand by other similar ligands, such as selenocyanate ($NCSe^-$) and cyanoborohydride ($NCBH_3^-$), which are stronger ligands than NCS^-. Moreover, in order to get a broader picture of the effect that L_2 has on the SCO properties of the $[Fe(OEt\text{-}L_1\text{-}pH)(L_2)_3]^-$ system, we tested the influence of the cyanate ligand (NCO^-), which is a weaker one. The results are shown in Table 3.17.

Table 3.17. Computed energy, enthalpy and entropy variations, and transition temperatures. All energies in kcal·mol^{-1}, entropies in cal·mol^{-1}·K^{-1} and $T_{1/2}$ in K. [a]Average experimental value of $T_{1/2}$.

$[Fe(OEt\text{-}L_1\text{-}pH)(L_2)_3]^-$	ΔE/kcal·mol^{-1}	ΔH/kcal·mol^{-1}	ΔS/cal·mol^{-1}·K^{-1}	$T_{1/2}$/K	Reference
$L_2 = NCS^-$	6.94	5.59	24.67	226 (169)[a]	100,102
$L_2 = NCSe^-$	8.32	6.92	24.63	281	–
$L_2 = NCBH_3^-$	12.28	10.78	24.45	441 (313)[a]	100
$L_2 = NCO^-$	1.73	0.49	20.70	24	–

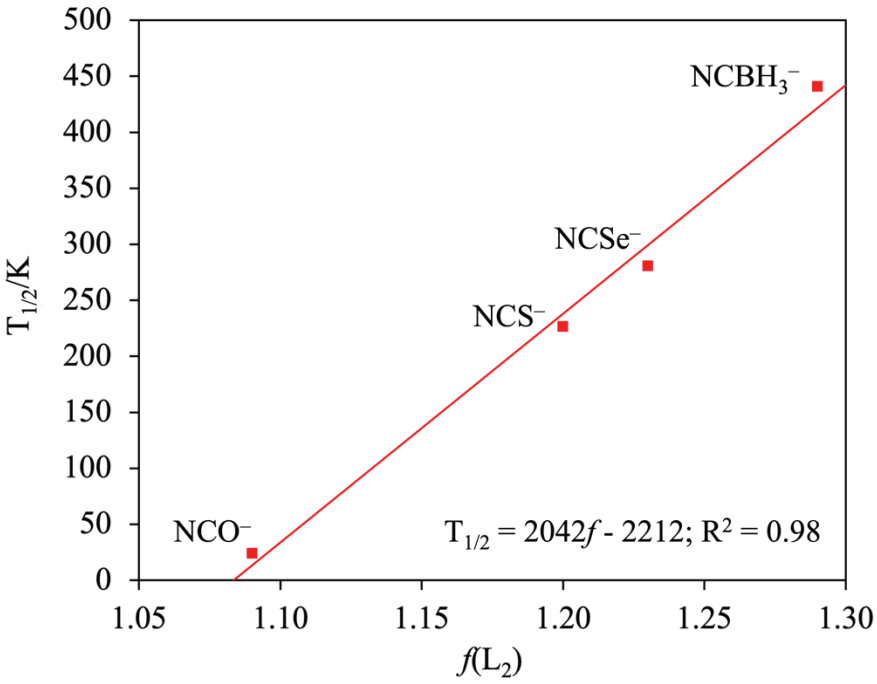

Figure 3.20. Correlation between the ligands' *f* factor and the computed transition temperatures ($R^2 = 0.98$).

It is clear that modifying L_2 in the $[Fe(OEt\text{-}L_1\text{-}pH)(L_2)_3]^-$ systems significantly influences the ligand field splitting of the Fe(II) metal centre. The increasing ligand strength, ranging from $NCO^- < NCS^- < NCSe^- < NCBH_3^-$, is clearly reflected in the progressive shift in the computed $T_{1/2}$ value, consistent with experimental observations for some systems.[100] A strong correlation emerges between the ligand *f* factor, which measures the ligand strength, and the computed $T_{1/2}$, as depicted in Figure 3.20.

By making use of the *ab initio* ligand field theory, we could quantify accurately the d-MO splitting to analyse the results of NEVPT2 calculations carried out starting from the optimized DFT geometries for all $[Fe(OEt\text{-}L_1\text{-}pH)(L_2)_3]^-$ LS systems. Computed Δ_o values against the ligands' *f* factor further highlight the increasing gap among the d-based MOs, from 17200 cm^{-1} to 18200 cm^{-1} between the weakest (NCO^-) and the strongest ($NCBH_3^-$) ligand. This can be seen in Table 3.18 and Figure 3.21.

Table 3.18. Computed NVEPT2 level ligand-field splitting, Δ_o, in cm^{-1}.

$[Fe(OEt\text{-}L_1\text{-}pH)(L_2)_3]^-$	Δ_o/cm^{-1}
$L_2 = NCO^-$	17261
$L_2 = NCS^-$	17751
$L_2 = NCSe^-$	17862
$L_2 = NCBH_3^-$	18295

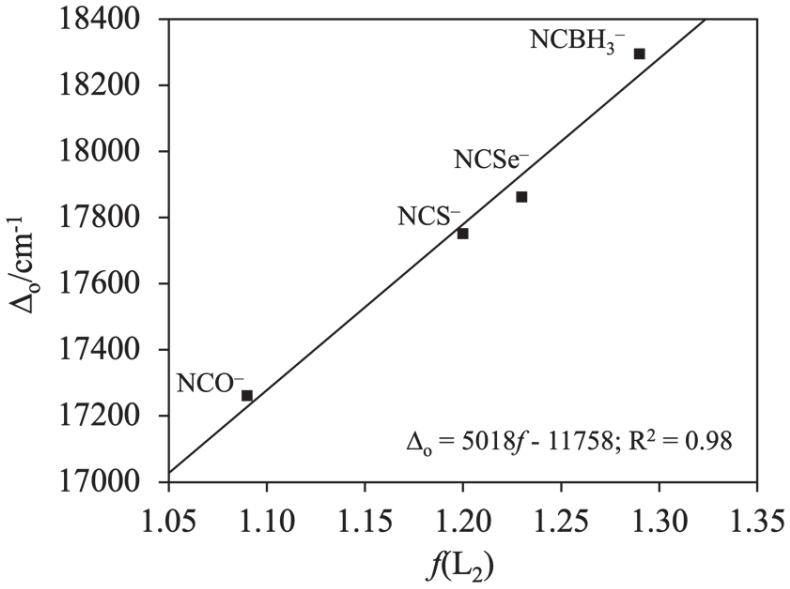

Figure 3.21. Correlation between the ligands' *f* factor and the computed ligand-field splitting energies ($R^2 = 0.98$).

The increasing gap is attributed to the loss of the partial antibonding character of the t_{2g} orbitals. Initially this set of orbitals are non-bonding for the perfect octahedron with 6 σ-donor ligands, but gains antibonding character due to the presence of π-type orbitals from the L_2 (NCE^-) ligands that can interact in a π-antibonding manner with the d_{xz}, d_{yz} and d_{xy} orbitals. However, as the L_2 ligand becomes stronger, these π-type orbitals decrease in energy, effectively decreasing the interaction of the d-MO, which recover the non-bonding character, and giving rise to higher Δ_o values. Figure 3.22 illustrates such effects by plotting the HOMO for the $[Fe(OEt\text{-}L_1\text{-}pH)(L_2)_3]^-$ systems ($L_2 = NCO^-$, NCS^-, $NCSe^-$ and $NCBH_3^-$).

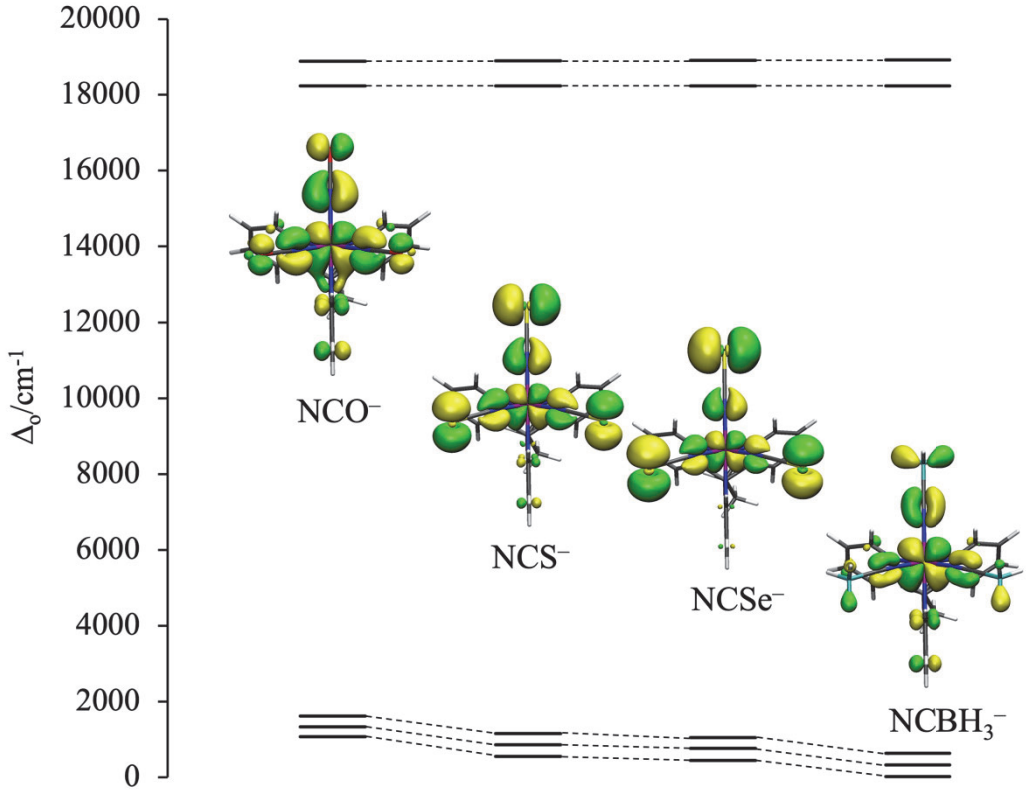

Figure 3.22. d-based molecular orbital diagram for the $[Fe(OEt\text{-}L_1\text{-}pH)(L_2)_3]^-$ systems with $L_2 = NCO^-$, NCS^-, $NCSe^-$ and $NCBH_3^-$, and isosurfaces of the HOMO d-based MOs (0.03 $e \cdot a_0^{-3}$ isovalue contour).

3.3.3.5. Modification of R_2 and L_2 in $[Fe(OEt\text{-}L_1\text{-}pR_2)(L_2)_3]^-$ System

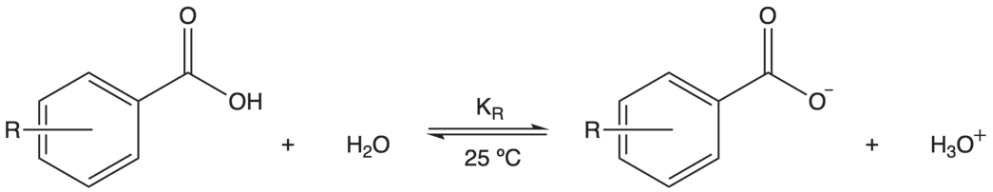

Figure 3.23. Ionization of benzoic acids.

In organic chemistry, it is important to understand how the structure of an organic compound influences its chemical reactivity. Numerous experiments designed to illustrate this structure-reactivity relationship focused on the linear Gibbs energy relationship of the Hammett equation (Eq. 3.8). Introduced by L. P. Hammett,[120,121] this equation is commonly used to demonstrate

these relationships in organic reactions, and is based on the ionization of benzoic acids in water at 25 ºC (Figure 3.23):

$$log\left(\frac{K_R}{K_H}\right) = \sigma\rho \tag{3.8}$$

K_R and K_H are the acid constants of *meta*- or *para*-substituted and unsubstituted aromatic compounds, respectively, ρ is the reaction constant and σ is the substituent constant which represents the electronic effect of the substituent R on the ionization of benzoic acid.

Substituents can stabilise or destabilise the benzoate anion through resonance or inductive effects. An electron-withdrawing substituent (EWG) at a specific position will stabilise the benzoate anion, resulting in a positive σ value. On the contrary, an electron-donating substituent (EDG) at that position will destabilise it, leading to a negative σ value.

The Swain–Lupton equation[122] is based on the same reaction and is a refinement of the Hammett equation to include both field and resonance effects. The concept is based on the idea that no more than two variables (resonance effects and field effects) are needed to describe the impact of any given substituent. Field effects, denoted as *F*, encompass all inductive and pure field effects and similarly, resonance effects, *R*, represent the average of electron-donating and electron-accepting abilities.

Having said that, another more subtle way of tuning $T_{1/2}$ in the system of study involves using EDGs or EWGs as substituents at the *para* position of the pyridyl rings. This approach, previously reported in other SCO systems with similar ligands, shows that the $T_{1/2}$ shifts towards higher values as the EWG character of the *para*-substituent increases.[123–136]

There are two major electronic effects from substituents in the *para* position of the pyridyl groups: inductive effect along the σ electron network and mesomeric effect along the π electron network. The mesomeric effect refers to the polarity generated between atoms in a conjugated system through electron transfer or π-bond electron transfer. It occurs when electrons in a conjugated orbital system move away from or towards a substituent group, and it is used qualitatively to explain the electron-withdrawing or electron-donating properties of substituents based on relevant resonance structures.[125,130] The relationship between the ligand field and the spin-state of the central metal ion is determined by a fine balance of opposing M–L σ- and π-bonding effects. There is some sort of competition between these two effects since they cause opposite results.

There is strong evidence for the presence of a substituent dependent M–L π-bonding interaction, the substituent in the *para* position of the pyridyl directly influences the electronic properties of the iron(II) centre.[127,128] According to the ligand-field theory, the magnitude of the splitting, Δ_o, is higher when increasing the π-acceptor character of the ligands. EWGs, such as NO_2, at the *para* position of the pyridyl ring would inductively attract electronic density, weakening the L→M σ-bonding but increasing the M→L π-backdonation. EWG reduce the electron-richness of the pyridyl rings, which are then more available for π-backdonation from the iron t_{2g} d-subshell.[123] This causes an increasing bonding character of the t_{2g} orbitals, which get energetically stabilized, and Δ_o becomes larger, favouring the LS state of the metal centre. Although OMe substituent (as well as OH and NH_2) can inductively attract electronic density due to the electronegative oxygen atom (or nitrogen atom), the conjugative effect contributes larger than the inductive effect, and it is considered an EDG. This donation of electrons into the ring, although can reinforce the L→M σ-bond, increases the electron density in the pyridyl ring in a more important way, preventing the M→L π-backbonding interaction and thus, favouring the HS state of the central metal.[124] That is, the rich electron density lifts the t_{2g} energy level through the dπ–pπ interaction, resulting in a narrow t_{2g}–e_g* energy gap, Δ_o, and favoring the HS state and low $T_{1/2}$.[125,130]

Overall, EWGs decrease the energy of the pyridyl π orbitals and increase Δ_o favouring the LS state, whereas EDGs increase the energy of the pyridyl π orbitals and decrease Δ_o favouring the HS state. Therefore, EWGs make the pyridyl a better π-acceptor while the opposite happens with EDGs.

We investigated how these substitutions affect the SCO properties by functionalizing the pyridyl groups of the OEt-L_1-pR_2 ligand (R_2 = –NH_2, –OH, –OMe, –Me, –F, –H, –Cl, –Br, –CF_3, and –NO_2) in the $[Fe(OEt\text{-}L_1\text{-}pR_2)(NCS)_3]^-$ system. As expected, EDGs result in lower $T_{1/2}$ values, and this parameter can be increased by replacing the R_2 group with a stronger EWG substituent. This behaviour correlates with the Hammett σ_p and σ_p^+ parameters[120,121,137] as observed in other SCO systems[123–128,138] (Figures 3.24, 3.25, 3.26 and 3.27). σ_p^+ is a modified Hammett parameter accounting for conjugation of the ligand substituents with a positively charged reaction centre.

It also exists even better correlation with the *R* Swain–Lupton parameter[122,137] (Figures 3.28 and 3.29). We also tested the correlation with the natural population analysis (performed with the natural bond orbital (NBO)[139–144] charges) of the nitrogen atom of the ligand's pyridyl rings, N_{py}, based on previous studies in this type of ligands[130] (Figures 3.30 and 3.31).

This trends allow for precise tuning of $T_{1/2}$ in the $[Fe(OEt\text{-}L_1\text{-}pR_2)(NCS)_3]^-$ system, prompting us to explore if similar behaviour occurs in other $[Fe(OEt\text{-}L_1\text{-}pR_2)(L_2)_3]^-$ systems. Our findings show a comparable degree of fine-tuning regardless of the L_2 ligand (L_2 = NCS^-, $NCSe^-$, and $NCBH_3^-$), indicating that one can select a broad temperature range with L_2 and achieve finer $T_{1/2}$ tuning *via* the R_2 substituent of the pyridyl ligands. A similar trend is observed for NCO^-, though its weaker nature generally results in a HS system, with only the strongest EWGs increasing $T_{1/2}$ (Figure A3.2).

Table 3.19. Hammett, Swain–Lupton parameters, and NBO charges on the N atom of the pyridyl rings of the ligand, and computed transition temperatures in Kelvin for the $[Fe(OEt\text{-}L_1\text{-}pR_2)(L_2)_3]^-$ system with L_2 = NCO^-, NCS^-, $NCSe^-$, $NCBH_3^-$.

R_2	σ_p Hammett	σ_p^+ Hammett	*R* Swain–Lupton	qN_{py}(NBO)	$T_{1/2}$/K			
					NCO^-	NCS^-	$NCSe^-$	$NCBH_3^-$
NH_2	-0.66	-1.30	-0.68	-0.219	–	21	180	343
OH	-0.37	-0.92	-0.64	-0.213	-38	143	211	367
OMe	-0.27	-0.78	-0.50	-0.213	-307	167	221	381
Me	-0.17	-0.31	-0.14	-0.204	-2	200	251	515
H	0.00	0.00	0.00	-0.201	24	226	281	441
F	0.06	-0.07	-0.34	-0.207	–	157	213	378
Cl	0.23	0.11	-0.16	-0.202	3	197	247	405
Br	0.23	0.15	-0.18	-0.201	9	201	250	411
CF_3	0.54	0.61	0.19	-0.194	62	251	294	458
NO_2	0.78	0.79	0.16	-0.191	–	229	309	504

Using a linear regression model in which the slope can be any of the parameters described above (σ_p, σ_p^+, *R*, qN_{py}(NBO)), we can write the following equation:

$$T_{1/2} = a \cdot parameter + b \tag{3.9}$$

Table 3.20. Correlations between the Hammett parameters, Swain–Lupton parameter and the NBO charge on the N atom of the pyridyl rings of the ligand, and the computed $T_{1/2}$.

L_2	σ_p Hammett			σ_p^+ Hammett			*R* Swain–Lupton			qN_{py}(NBO)		
	a	***b***	R^2	***a***	***b***	R^2	***a***	***b***	R^2	***a***	***b***	R^2
NCS^-	122	175	0.65	83	194	0.73	184	222	0.75	6599	1530	0.77
$NCSe^-$	82	243	0.76	55	255	0.80	127	275	0.92	4490	1165	0.91
$NCBH_3^-$	85	417	0.40	60	430	0.48	155	456	0.67	5285	1502	0.62

We computed also the correlations with the spin-state energy gap and, as expected, we observe that the $\Delta E_{HS\text{-}LS}$ is larger when EWGs are in the *para* positions of the pyridyl groups of the ligand, and smaller when EDGs are placed there, as observed in Table 3.21.

Table 3.21. Computed energy differences in kcal·mol^{-1} for the $[Fe(OEt\text{-}L_1\text{-}pR_2)(L_2)_3]^-$ system with $L_2 = NCO^-$, NCS^-, $NCSe^-$, $NCBH_3^-$.

R_2	ΔE/kcal·mol^{-1}			
	NCO^-	NCS^-	$NCSe^-$	$NCBH_3^-$
NH_2	–	2.26	5.02	9.95
OH	0.25	5.19	6.72	10.37
OMe	-5.07	5.30	6.85	10.67
Me	1.20	6.51	7.92	11.87
H	1.73	6.94	8.32	12.28
F	–	5.37	6.79	10.97
Cl	1.33	6.41	7.76	11.96
Br	1.48	6.51	7.86	12.09
CF_3	2.64	7.61	8.89	13.26
NO_2	–	6.37	8.50	14.53

Table 3.22. Computed enthalpy (in kcal·mol^{-1}) and entropy differences (in cal·mol^{-1}·K^{-1}) for the [Fe(OEt-L$_1$-pR$_2$)(L$_2$)$_3$]$^-$ system with L$_2$ = NCO$^-$, NCS$^-$, NCSe$^-$, NCBH$_3^-$.

R$_2$	Δ*H*/kcal·mol^{-1}				Δ*S*/cal·mol^{-1}·K^{-1}			
	NCO$^-$	**NCS$^-$**	**NCSe$^-$**	**NCBH$_3^-$**	**NCO$^-$**	**NCS$^-$**	**NCSe$^-$**	**NCBH$_3^-$**
NH$_2$	–	0.25	3.58	8.52	–	11.79	19.92	24.80
OH	-0.85	3.92	5.37	8.93	22.52	27.36	25.41	24.32
OMe	-6.07	4.01	5.49	9.24	19.78	23.96	24.85	24.27
Me	-0.04	5.15	6.49	9.76	20.70	25.74	25.87	18.96
H	0.49	5.59	6.92	10.78	20.70	24.67	24.63	24.45
F	–	4.09	5.45	9.51	12.40	26.03	25.60	25.13
Cl	0.07	5.04	6.35	10.44	20.32	25.54	25.67	25.81
Br	0.19	5.14	6.44	10.56	20.47	25.59	25.76	25.71
CF$_3$	1.22	6.17	7.44	11.71	19.77	24.53	25.33	25.56
NO$_2$	–	4.50	6.62	12.75	–	19.63	21.45	25.31

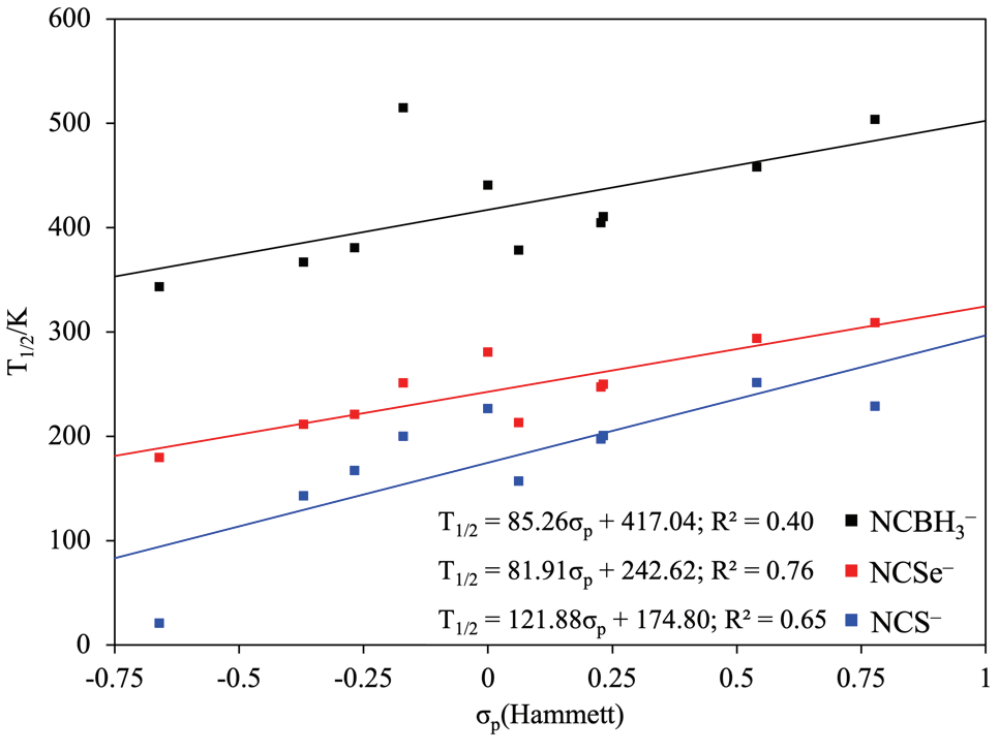

Figure 3.24. Computed transition temperatures against the σ_p Hammett parameter[122,137] for [Fe(OEt-L$_1$-pR$_2$)(L$_2$)$_3$]$^-$ system, with L$_2$ = NCS$^-$ (blue), NCSe$^-$ (red) and NCBH$_3^-$ (black), and R$_2$ = –NH$_2$, –OH, –OMe, –Me, –F, –H, –Cl, –Br, –CF$_3$ and –NO$_2$.

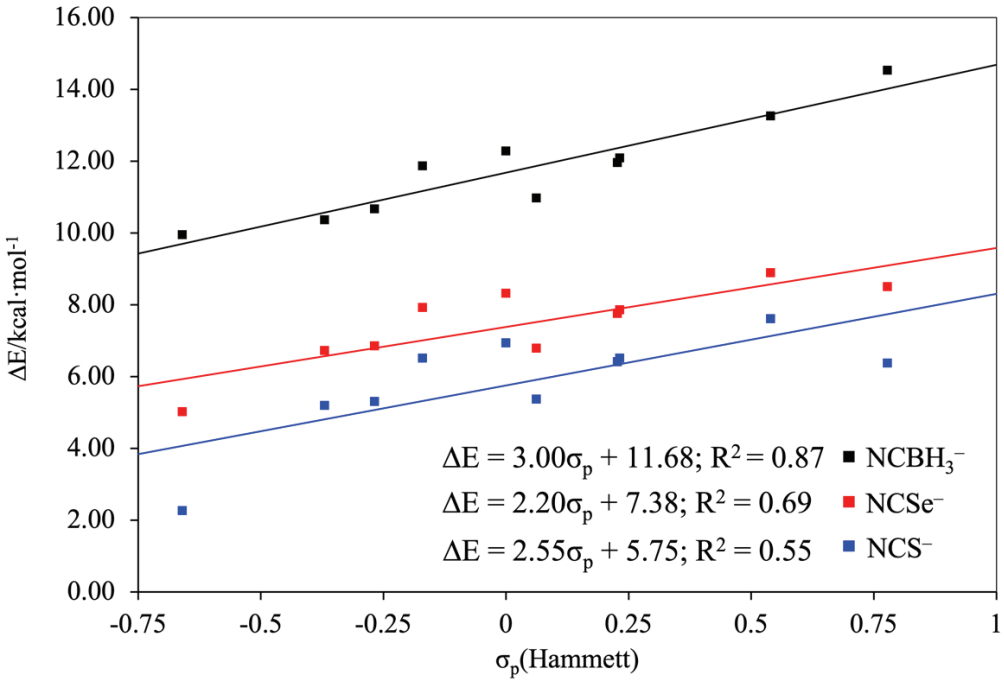

Figure 3.25. Computed energy differences against the σ_p Hammett parameter for $[Fe(OEt\text{-}L_1\text{-}pR_2)(L_2)_3]^-$ system, with $L_2 = NCS^-$ (blue), $NCSe^-$ (red) and $NCBH_3^-$ (black), and $R_2 = –NH_2$, –OH, –OMe, –Me, –F, –H, –Cl, –Br, $–CF_3$ and $–NO_2$.

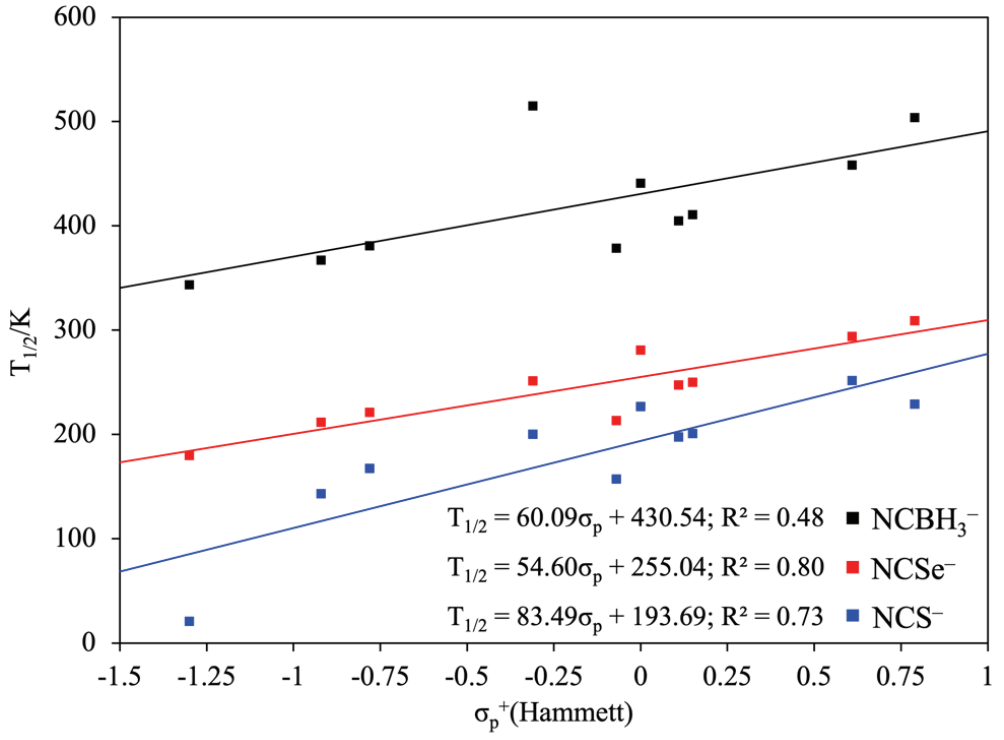

Figure 3.26. Computed transition temperatures against the σ_p^+ Hammett parameter[137] for $[Fe(OEt\text{-}L_1\text{-}pR_2)(L_2)_3]^-$ system, with $L_2 = NCS^-$ (blue), $NCSe^-$ (red) and $NCBH_3^-$ (black), and $R_2 = –NH_2$, –OH, –OMe, –Me, –F, –H, –Cl, –Br, $–CF_3$ and $–NO_2$.

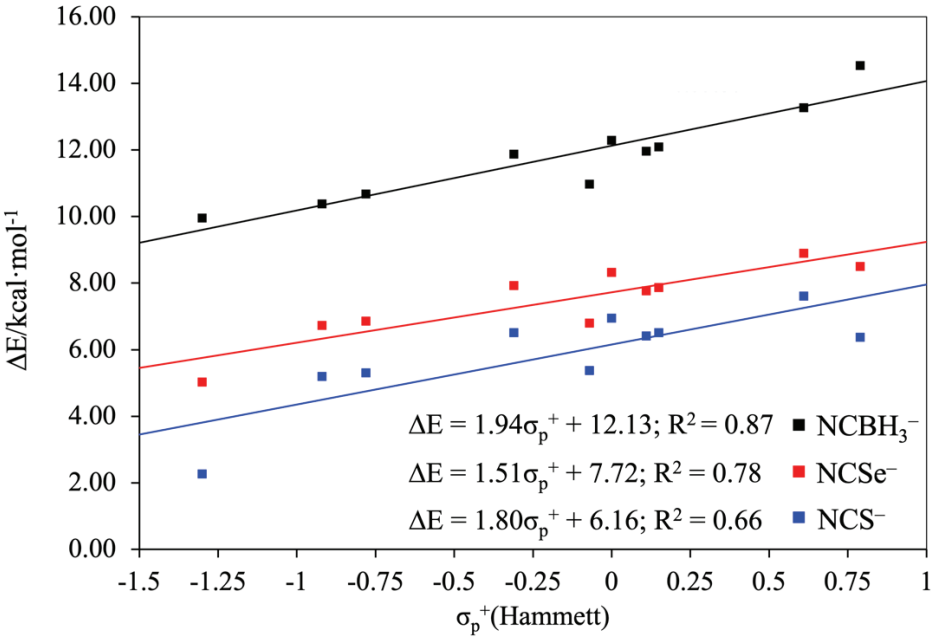

Figure 3.27. Computed energy differences against the σ_p^+ Hammett parameter for $[Fe(OEt\text{-}L_1\text{-}pR_2)(L_2)_3]^-$ system, with $L_2 = NCS^-$ (blue), $NCSe^-$ (red) and $NCBH_3^-$ (black), and R_2 = –NH2, –OH, –OMe, –Me, –F, –H, –Cl, –Br, $–CF_3$ and $–NO_2$.

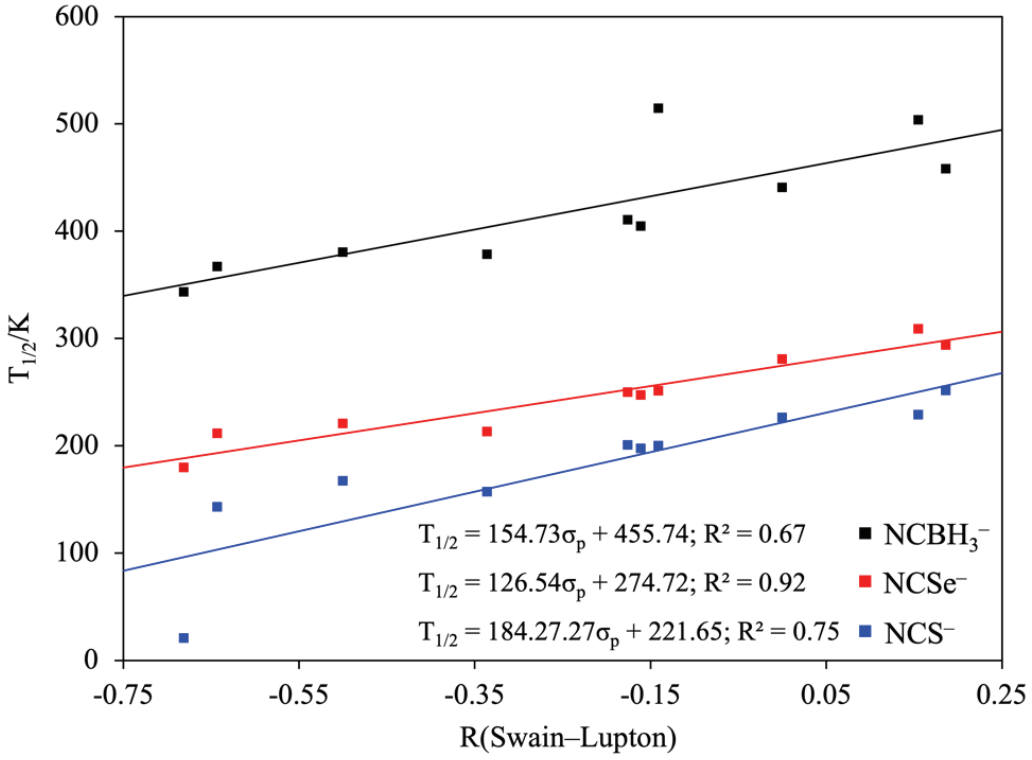

Figure 3.28. Computed transition temperatures against the *R* Swain–Lupton parameter[122] for $[Fe(OEt\text{-}L_1\text{-}pR_2)(L_2)_3]^-$ system, with $L_2 = NCS^-$ (blue), $NCSe^-$ (red) and $NCBH_3^-$ (black), and $R_2 = –NH_2$, –OH, –OMe, –Me, –F, –H, –Cl, –Br, $–CF_3$ and $–NO_2$.

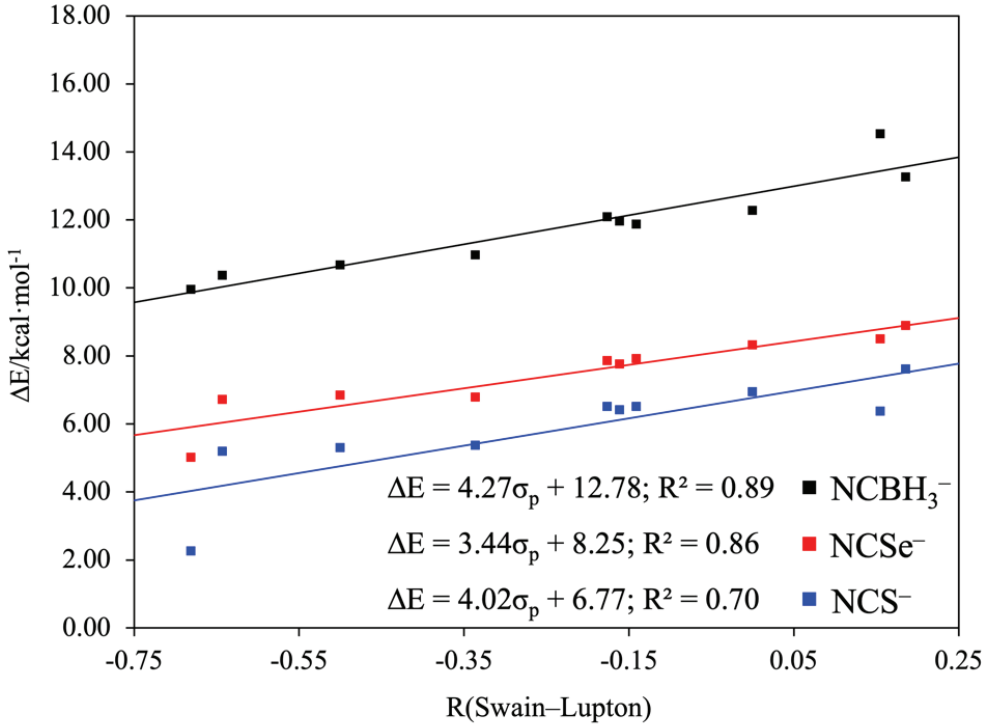

Figure 3.29. Computed energy differences against the *R* Swain–Lupton parameter for [Fe(OEt-L_1-pR_2)(L_2)$_3$]$^-$ system, with L_2 = NCS^- (blue), $NCSe^-$ (red) and $NCBH_3^-$ (black), and R_2 = –NH_2, –OH, –OMe, –Me, –F, –H, –Cl, –Br, –CF_3 and –NO_2.

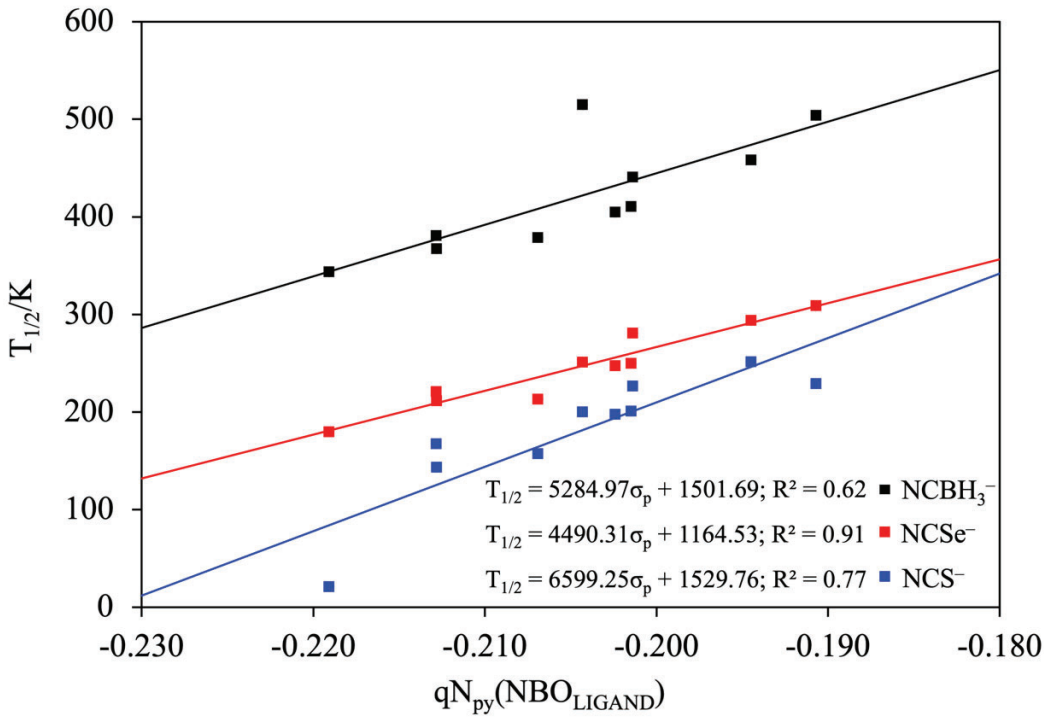

Figure 3.30. Computed transition temperatures against the NBO charges on the N atom of the pyridyl rings of the ligand for [Fe(OEt-L_1-pR_2)(L_2)$_3$]$^-$ system, with L_2 = NCS^- (blue), $NCSe^-$ (red) and $NCBH_3^-$ (black), and R_2 = –NH_2, –OH, –OMe, –Me, –F, –H, –Cl, –Br, –CF_3 and –NO_2.

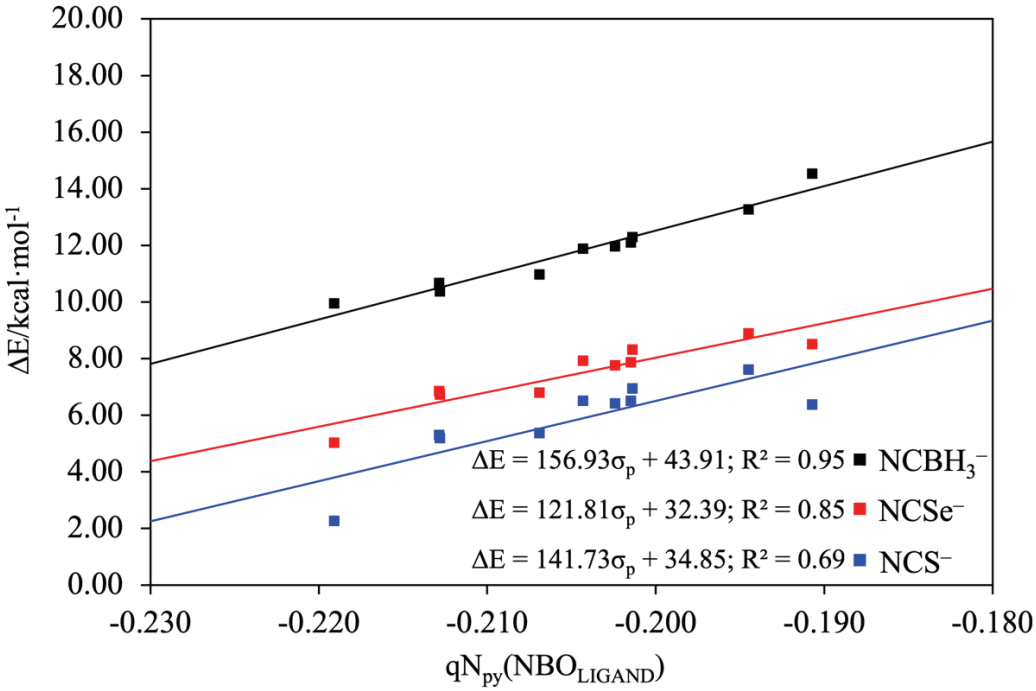

Figure 3.31. Computed energy differences against the NBO charges on the N atom of the pyridyl rings of the ligand for $[Fe(OEt\text{-}L_1\text{-}pR_2)(L_2)_3]^-$ system, with $L_2 = NCS^-$ (blue), $NCSe^-$ (red) and $NCBH_3^-$ (black), and $R_2 = –NH_2$, –OH, –OMe, –Me, –F, –H, –Cl, –Br, $–CF_3$ and $–NO_2$.

In the appendix one can see other tested correlations such as with the Mulliken[145] charges of the ligand, and the NBO charges of the HS and LS systems.

3.3.4. Summary

In this work, we used the TPSSh functional to analyse the SCO properties of the $[Fe(OEt\text{-}L_1\text{-}pH)(NCS)_3]^-$ system, one of the few anionic SCO molecules reported in the literature.[95–104] To expand this family of compounds and design systems with specific physical properties, we applied our computational methodology to examine how different functionalizations affect the spin-state energy gap in different members of the $[Fe(R_1\text{-}L_1\text{-}pR_2)(L_2)_3]^-$ family, exploring multiple chemical modifications to the basic molecular structure. While functionalization of R_1 causes some variations, the length of the aliphatic chain appears to have a minor impact on the modulation of $T_{1/2}$. Nonetheless, the side chain's role in altering SCO properties through crystal packing effects should not be ignored. Alternatively, modifying the L_2 ligands allows access to a wide range of transition temperatures, which can be fine-tuned using the R_2 groups of the pyridyl ligand. Our findings suggest a two-knob model, where different L_2 ligands can set higher or lower $T_{1/2}$ values depending on their strength (the more ligand-field strength, the

higher $T_{1/2}$), and precise adjustments can be achieved through pyridyl functionalization at the *para* position, the latter one leading to higher $T_{1/2}$ values when adding EWGs, and lower $T_{1/2}$ when adding EDGs. All observed trends are explained by the electronic structure of the studied systems, with several correlations identified to predict changes in $T_{1/2}$ upon ligand modification. We believe our results will significantly help in the future design of new anionic SCO systems that can operate at specific transition temperatures.

3.4. Conclusions

In this chapter, unusual SCO systems, such as Cr(II)-based and anionic Fe(II)-based SCO systems, have been studied computationally with the method TPSSh/Def2-TZVP (adding GD3BJ dispersion correction for the Cr(II) systems) that can accurately predict the properties of such systems, based on experimental results. Moreover, some correlations could be outlined, which allows for a fine degree of tunning the transition temperatures which in turns, leads us to the design of new compounds with tailored properties not obtained experimentally. The results of both projects can help in the future design of new SCO systems that can operate at specific transition temperatures.

3.5. Appendix

We performed an analysis of the Non-Covalent Interaction (NCI) using NCIPLOT software[146,147] and Multiwfn 3.7 program.[148,149] The NCI isosurfaces were generated for a reduced density gradient s = 0.3 a.u., coloured according to a BGR scheme and visualized by Visual Molecular Dynamics (VMD) 1.9.3 program.[150] These isosurfaces have been used to identify regions of different interactions by examining their colours. Green colour indicates van der Waals interactions, red belongs to the ring tension, and blue is related to strong attractive interactions such as hydrogen bonds or covalent bonds.

As can be seen from Figure A3.1, in the eclipsed configuration exists van der Waals interactions between the two rings of the indenyl ligands. We attribute this NCI to π-π stacking interactions (we have represented the HS system but the same can be seen for the LS one).

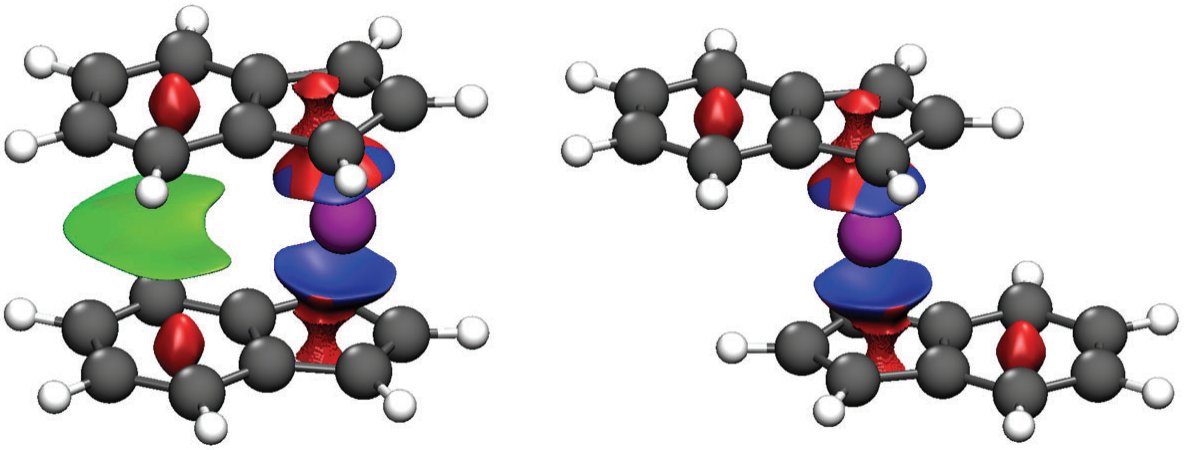

Figure A3.1. NCI isosurfaces for the HS system in eclipsed (left) and staggered (right) configurations. Violet: Cr, gray: C, white: H. Reduced density gradient of 0.3 a.u.

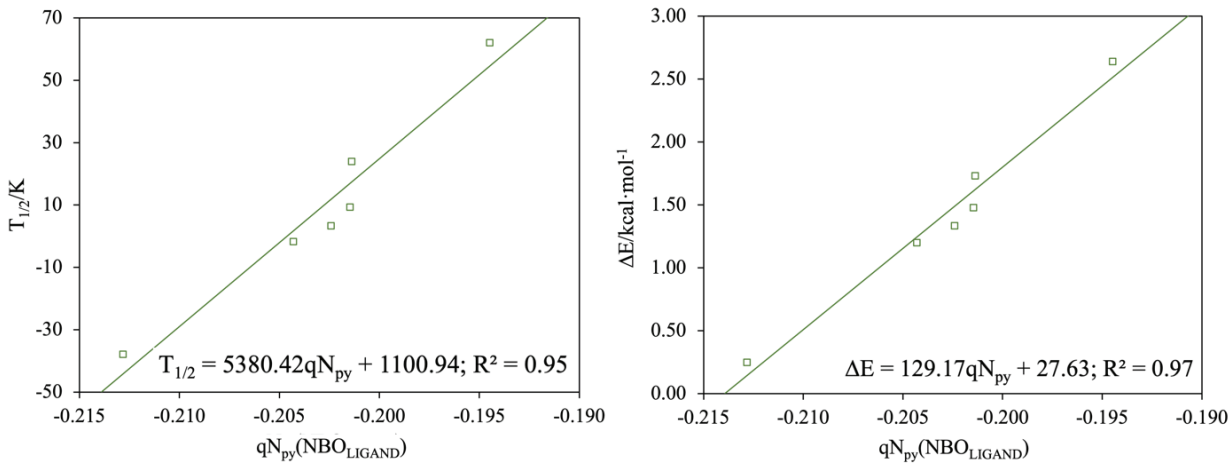

Figure A3.2. Computed transition temperatures and energy differences against the NBO charges on the N atom of the pyridyl rings of the ligand for $[Fe(OEt\text{-}L_1\text{-}pR_2)(NCO)_3]^-$ system.

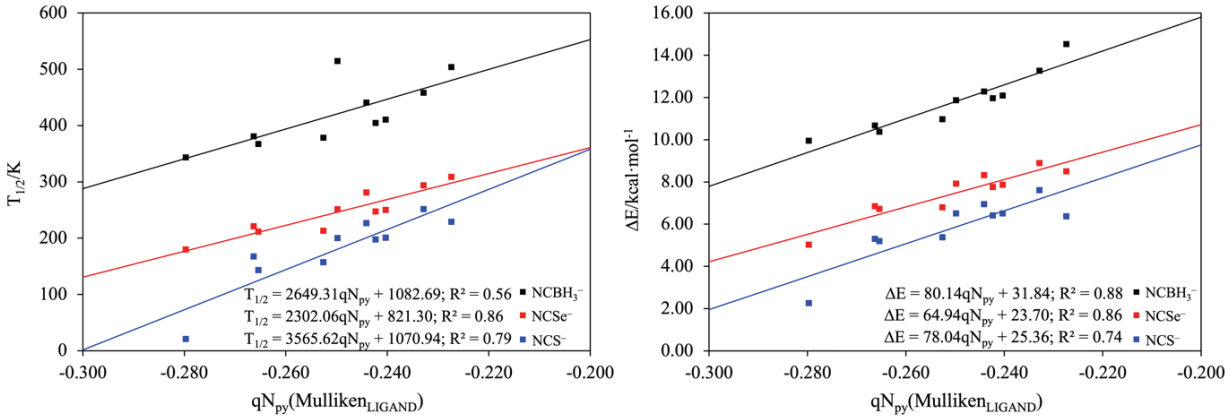

Figure A3.3. Computed transition temperatures and energy differences against the Mulliken charges on the N atom of the pyridyl rings of the ligand for $[Fe(OEt\text{-}L_1\text{-}pR_2)(L_2)_3]^-$ system, with $L_2 = NCS^-$ (blue), $NCSe^-$ (red) and $NCBH_3^-$ (black), and $R_2 = –NH_2$, –OH, –OMe, –Me, –F, –H, –Cl, –Br, $–CF_3$ and $–NO_2$.

We tested the correlations with the NBO charges of the HS and LS systems with $L_2 = NCS^-$ and $R_2 = –NH_2$, –OH, –OMe, –Me, –F, –H, –Cl, –Br, $–CF_3$ and $–NO_2$. We observe that exists better correlation with the HS data. If the correlations were better, and the slopes were more similar between the HS and LS, ultimately it would not be needed to perform the calculations for both spin-sates to predict the transition temperatures and energy differences as observed in other studies.[151] These values would be accurately predicted without having to perform two DFT calculations. Only one DFT calculation would be required, thus reducing the amount of computing time needed. Unfortunately, that is not the case.

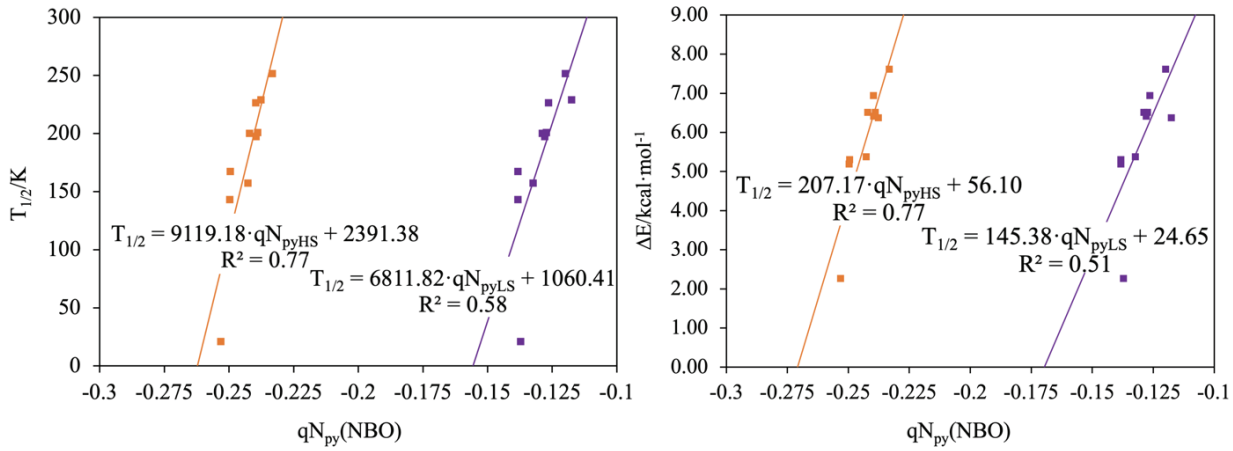

Figure A3.4. Computed energy differences against the NBO charges on the N atom of the pyridyl rings of the $[Fe(OEt\text{-}L_1\text{-}pR_2)(NCS)_3]^-$ system in the HS (orange) and LS (purple) states, with $R_2 = –NH_2$, –OH, –OMe, –Me, –F, –H, –Cl, –Br, $–CF_3$ and $–NO_2$.

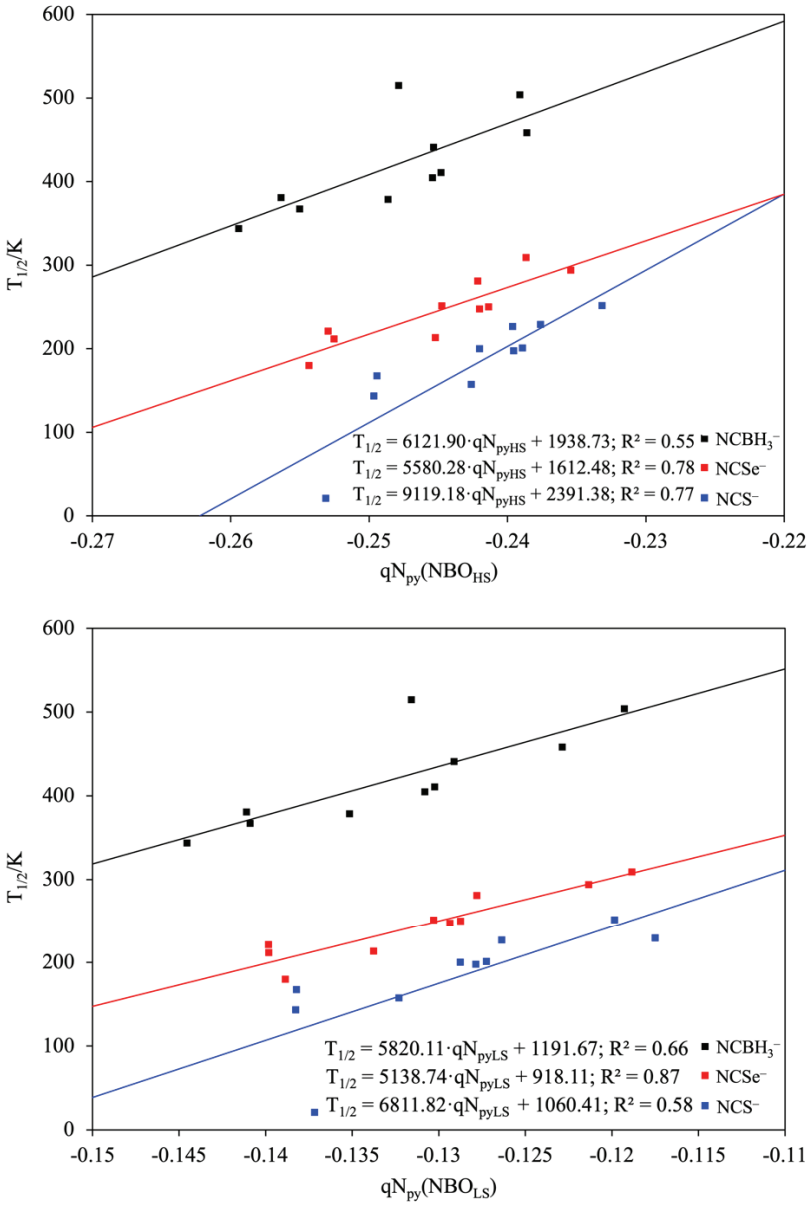

Figure A3.5. Computed transition temperatures against the NBO charges on the N atom of the pyridyl rings of the $[Fe(OEt\text{-}L_1\text{-}pR_2)(L_2)_3]^-$ system in the HS (top) and LS (bottom) states, with $L_2 = NCS^-$ (blue), $NCSe^-$ (red) and $NCBH_3^-$ (black), and $R_2 = –NH_2$, –OH, –OMe, –Me, –F, –H, –Cl, –Br, $–CF_3$ and $–NO_2$.

3.6. References

1. L. Navarro, F. Rodriguez and J. Cirera, *Dalton Trans.*, 2021, **50**, 8704–8710.
2. L. Navarro and J. Cirera, *Inorg. Chem. Front.*, 2022, **10**, 250–258.
3. V. N. Staroverov, G. E. Scuseria, J. Tao and J. P. Perdew, *J. Chem. Phys.*, 2003, **119**, 12129–12137.
4. J. Tao, J. P. Perdew, V. N. Staroverov and G. E. Scuseria, *Phys. Rev. Lett.*, 2003, **91**, 146401.
5. F. Weigend and R. Ahlrichs, *Phys. Chem. Chem. Phys.*, 2005, **7**, 3297–3305.
6. F. Weigend, *Phys. Chem. Chem. Phys.*, 2006, **8**, 1057–1065.
7. S. Grimme, S. Ehrlich and L. Goerigk, *J. Comput. Chem.*, 2011, **32**, 1456–1465.
8. R. W. Hogue, S. Singh and S. Brooker, *Chem. Soc. Rev.*, 2018, **47**, 7303–7338.
9. H. S. Scott, R. W. Staniland and P. E. Kruger, *Coord. Chem. Rev.*, 2018, **362**, 24–43.
10. K. Senthil Kumar and M. Ruben, *Coord. Chem. Rev.*, 2017, **346**, 176–205.
11. G. A. Craig, O. Roubeau and G. Aromí, *Coord. Chem. Rev.*, 2014, **269**, 13–31.
12. P. Gütlich, Y. Garcia and H. A. Goodwin, *Chem. Soc. Rev.*, 2000, **29**, 419–427.
13. H. A. Goodwin, *Coord. Chem. Rev.*, 1976, **18**, 293–325.
14. V. Niel, M. C. Muñoz, A. B. Gaspar, A. Galet, G. Levchenko and J. A. Real, *Chem. Eur. J.*, 2002, **8**, 2446–2453.
15. M. Ohba, K. Yoneda, G. Agusti, M. C. Muñoz, A. B. Gaspar, J. A. Real, M. Yamasaki, H. Ando, Y. Nakao, S. Sakaki and S. Kitagawa, *Angew. Chem. Int. Ed.*, 2009, **48**, 4767–4771.
16. S. M. Neville, G. J. Halder, K. W. Chapman, M. B. Duriska, B. Moubaraki, K. S. Murray and C. J. Kepert, *J. Am. Chem. Soc.*, 2009, **131**, 12106–12108.
17. J. Olguín, *Coord. Chem. Rev.*, 2020, **407**, 213148.
18. D. J. Harding, P. Harding and W. Phonsri, *Coord. Chem. Rev.*, 2016, **313**, 38–61.
19. Y. Garcia and P. Gütlich, in *Spin Crossover in Transition Metal Compounds II*, 2004, vol. 234, pp. 49–62.
20. K. S. Murray, *Eur. J. Inorg. Chem.*, 2008, 3101–3121.
21. D. A. Pantazis, C. A. Murillo and J. E. McGrady, *Dalton Trans.*, 2007, 608–614.
22. M. L. Hays, *Organometallics*, 1998, **17**, 5521–5527.
23. M. D. Walter, C. D. Sofield, C. H. Booth and R. A. Andersen, *Organometallics*, 2009, **28**, 2005–2019.

24. M. E. Switzer, R. Wang, M. F. Rettig and A. H. Maki, *J. Am. Chem. Soc.*, 1974, **96**, 7669–7674.
25. J. Cirera and E. Ruiz, *Inorg. Chem.*, 2018, **57**, 702–709.
26. E. D. Brady, J. S. Overby, M. B. Meredith, A. B. Mussman, M. A. Cohn, T. P. Hanusa, G. T. Yee and M. Pink, *J. Am. Chem. Soc.*, 2002, **124**, 9556–9566.
27. M. B. Meredith, J. A. Crisp, E. D. Brady, T. P. Hanusa, G. T. Yee, N. R. Brooks, B. E. Kucera and V. G. Young, *Organometallics*, 2006, **25**, 4945–4952.
28. M. B. Meredith, J. A. Crisp, E. D. Brady, T. P. Hanusa, G. T. Yee, M. Pink, W. W. Brennessel and V. G. Young, *Organometallics*, 2008, **27**, 5464–5473.
29. M. Sorai, Y. Yumoto, D. M. Halepoto and L. F. Larkworthy, *J. Phys. Chem. Solids*, 1993, **54**, 421–430.
30. D. M. Halepoto, D. G. L. Holt, L. F. Larkworthy, D. C. Povey, G. W. Smith and G. J. Leigh, *Polyhedron*, 1989, **8**, 1821–1822.
31. D. M. Halepoto, D. G. L. Holt, L. F. Larkworthy, G. J. Leigh, D. C. Povey and G. W. Smitha, *J. Chem. Soc., Chem. Commun.*, 1989, 1322–1323.
32. V. Ksenofontov, A. B. Gaspar, G. Levchenko, B. Fitzsimmons and P. Gütlich, *J. Phys. Chem. B*, 2004, **108**, 7723–7727.
33. P. Gütlich, A. B. Gaspar, Y. Garcia and V. Ksenofontov, *C. R. Chim.*, 2007, **10**, 21–36.
34. A. K. Hughes, V. J. Murphy and D. O'Hare, *J. Chem. Soc., Chem. Commun.*, 1994, 163–164.
35. A. E. Goeta, J. A. K. Howard, A. K. Hughes, D. O'Hare and R. C. B. Copley, *J. Mater. Chem.*, 2007, **17**, 485–492.
36. H. Sitzmann, M. Schar, E. Dormann and M. Kelemen, *Z. Anorg. Allg. Chem.*, 1997, **623**, 1850–1852.
37. P. M. Becker, C. Förster, L. M. Carrella, P. Boden, D. Hunger, J. van Slageren, M. Gerhards, E. Rentschler and K. Heinze, *Chem. Eur. J.*, 2020, **26**, 7199–7204.
38. D. O'Hare, V. J. Murphy and N. Kaltsoyannis, *J. Chem. Soc., Dalton Trans.*, 1993, 383–392.
39. H. Bauer, J. Weismann, D. Saurenz, C. Färber, M. Schär, W. Gidt, I. Schädlich, G. Wolmershäuser, Y. Sun, S. Harder and H. Sitzmann, *J. Organomet. Chem.*, 2016, **809**, 63–73.
40. J. Cirera and F. Paesani, *Inorg. Chem.*, 2012, **51**, 8194–8201.
41. J. Cirera and E. Ruiz, *Inorg. Chem.*, 2016, **55**, 1657–1663.
42. G. Drabik, J. Szklarzewicz and M. Radoń, *Phys. Chem. Chem. Phys.*, 2021, **23**, 151–172.

43. S. Ketkov, *Dalton Trans.*, 2020, **49**, 569–577.
44. M. J. Frisch, G. W. Trucks, H. B. Schlegel, G. E. Scuseria, M. a. Robb, J. R. Cheeseman, G. Scalmani, V. Barone, G. a. Petersson, H. Nakatsuji, X. Li, M. Caricato, a. V. Marenich, J. Bloino, B. G. Janesko, R. Gomperts, B. Mennucci, H. P. Hratchian, J. V. Ortiz, a. F. Izmaylov, J. L. Sonnenberg, Williams, F. Ding, F. Lipparini, F. Egidi, J. Goings, B. Peng, A. Petrone, T. Henderson, D. Ranasinghe, V. G. Zakrzewski, J. Gao, N. Rega, G. Zheng, W. Liang, M. Hada, M. Ehara, K. Toyota, R. Fukuda, J. Hasegawa, M. Ishida, T. Nakajima, Y. Honda, O. Kitao, H. Nakai, T. Vreven, K. Throssell, J. a. Montgomery Jr., J. E. Peralta, F. Ogliaro, M. J. Bearpark, J. J. Heyd, E. N. Brothers, K. N. Kudin, V. N. Staroverov, T. a. Keith, R. Kobayashi, J. Normand, K. Raghavachari, a. P. Rendell, J. C. Burant, S. S. Iyengar, J. Tomasi, M. Cossi, J. M. Millam, M. Klene, C. Adamo, R. Cammi, J. W. Ochterski, R. L. Martin, K. Morokuma, O. Farkas, J. B. Foresman and D. J. Fox, *Gaussian Inc., Wallingford CT*, 2016, Revision B.01.
45. C. Angeli, R. Cimiraglia and J. P. Malrieu, *J. Chem. Phys.*, 2002, **117**, 9138–9153.
46. F. Neese, *Wiley Interdiscip. Rev. Comput. Mol. Sci.*, 2018, **8**, e1327.
47. S. K. Singh, J. Eng, M. Atanasov and F. Neese, *Coord. Chem. Rev.*, 2017, **344**, 2–25.
48. A. Gilbert, *IQmol: The Smart Choice in Molecular Visualization Software User Guide,* 2020, 2.15.0, http://iqmol.org/.
49. J. Cirera, M. Via-Nadal and E. Ruiz, *Inorg. Chem.*, 2018, **57**, 14097–14105.
50. F. Furche and J. P. Perdew, *J. Chem. Phys.*, 2006, **124**, 044103.
51. J. Cirera and E. Ruiz, *Comments Inorg. Chem.*, 2019, **39**, 216–241.
52. C. J. Cramer, *Essentials of Computational Chemistry: Theories and Models*, John Wiley & Sons, Ltd, Second Edition., 2004.
53. F. Jensen, *Introduction to Computational Chemistry*, John Wiley & Sons, Ltd, Third Edition., 2017.
54. N. Suaud, M. L. Bonnet, C. Boilleau, P. Labèguerie and N. Guihéry, *J. Am. Chem. Soc.*, 2009, **131**, 715–722.
55. S. Vancoillie, H. Zhao, M. Radoń and K. Pierloot, *J. Chem. Theory Comput.*, 2010, **6**, 576–582.
56. K. Pierloot, Q. M. Phung and A. Domingo, *J. Chem. Theory Comput.*, 2017, **13**, 537–553.
57. L. M. Lawson Daku, F. Aquilante, T. W. Robinson and A. Hauser, *J. Chem. Theory Comput.*, 2012, **8**, 4216–4231.

58. C. R. Groom, I. J. Bruno, M. P. Lightfoot and S. C. Ward, *Acta Crystallogr. B Struct. Sci. Cryst. Eng. Mater.*, 2016, **72**, 171–179.
59. P. Guionneau, M. Marchivie, G. Bravic, J. F. Létard and D. Chasseau, *J. Mater. Chem.*, 2002, **12**, 2546–2551.
60. A. B. Gaspar, M. C. Muñoz, V. Niel and J. A. Real, *Inorg. Chem.*, 2001, **40**, 9–10.
61. J. Zarembowitch and O. Kahn, *Inorg. Chem*, 1984, **23**, 589–593.
62. F. Fürmeyer, D. Münzberg, L. M. Carrella and E. Rentschler, *Molecules*, 2020, **25**, 855.
63. N. M. J. Nik Ibrahim, S. M. Said, A. Mainal, M. F. Mohd Sabri, N. Abdullah, M. M. I. Megat Hasnan, H. Che Hassan, M. F. Mohd Salleh and W. A. Wan Mohd Mahiyiddin, *Mater. Res. Bull.*, 2020, **126**, 110828.
64. D. Villaman, C. J. McMonagle, M. R. Probert, O. Peña, Y. Moreno and M. Fuentealba, *CrystEngComm*, 2020, **22**, 3221–3233.
65. G. G. Morgan, K. D. Murnaghan, H. Müller-Bunz, V. McKee and C. J. Harding, *Angew. Chem. Int. Ed.*, 2006, **45**, 7192–7195.
66. A. J. Fitzpatrick, E. Trzop, H. Müller-Bunz, M. M. Dîrtu, Y. Garcia, E. Collet and G. G. Morgan, *Chem. Commun.*, 2015, **51**, 17540–17543.
67. K. D. Murnaghan, C. Carbonera, L. Toupet, M. Griffin, M. M. Dîrtu, C. Desplanches, Y. Garcia, E. Collet, J. F. Létard and G. G. Morgan, *Chem. Eur. J.*, 2014, **20**, 5613–5618.
68. M. Griffin, S. Shakespeare, H. J. Shepherd, C. J. Harding, J. F. Létard, C. Desplanches, A. E. Goeta, J. A. K. Howard, A. K. Powell, V. Mereacre, Y. Garcia, A. D. Naik, H. Müller-Bunz and G. G. Morgan, *Angew. Chem. Int. Ed.*, 2011, **50**, 896–900.
69. A. J. Fitzpatrick, H. M. O'Connor and G. G. Morgan, *Dalton Trans.*, 2015, **44**, 20839–20842.
70. W. Phonsri, B. A. I. Lewis, G. N. L. Jameson and K. S. Murray, *Chem. Commun.*, 2019, **55**, 14031–14034.
71. W. Phonsri, D. S. Macedo, B. A. I. Lewis, D. F. Wain and K. S. Murray, *Magnetochemistry*, 2019, **5**, 37.
72. S. Murata, K. Takahashi, T. Sakurai, H. Ohta, T. Yamamoto, Y. Einaga, Y. Shiota and K. Yoshizawa, *Crystals*, 2016, **6**, 49.
73. K. Takahashi, K. Kawamukai, M. Okai, T. Mochida, T. Sakurai, H. Ohta, T. Yamamoto, Y. Einaga, Y. Shiota and K. Yoshizawa, *Chem. Eur. J.*, 2016, **22**, 1253–1257.
74. C. Cook, F. Habib, T. Aharen, R. Clérac, A. Hu and M. Murugesu, *Inorg. Chem.*, 2013, **52**, 1825–1831.

75. Z. Y. Li, J. W. Dai, Y. Shiota, K. Yoshizawa, S. Kanegawa and O. Sato, *Chem. Eur. J.*, 2013, **19**, 12948–12952.
76. S. Floquet, M. L. Boillot, E. Rivière, F. Varret, K. Boukheddaden, D. Morineau and P. Négrier, *New J. Chem.*, 2003, **27**, 341–348.
77. S. Floquet, N. Guillou, P. Négrier, E. Rivière and M. L. Boillot, *New J. Chem.*, 2006, **30**, 1621–1627.
78. S. K. Karuppannan, A. Martín-Rodríguez, E. Ruiz, P. Harding, D. J. Harding, X. Yu, A. Tadich, B. Cowie, D. Qi and C. A. Nijhuis, *Chem. Sci.*, 2021, **12**, 2381–2388.
79. M. A. Halcrow, *Spin-Crossover Materials: Properties and Applications*, John Wiley & Sons, Ltd., 2013.
80. N. Pittala, F. Thétiot, S. Triki, K. Boukheddaden, G. Chastanet and M. Marchivie, *Chem. Mat.*, 2017, **29**, 490–494.
81. H. Phan, J. J. Hrudka, D. Igimbayeva, L. M. Lawson Daku and M. Shatruk, *J. Am. Chem. Soc.*, 2017, **139**, 6437–6447.
82. N. Pittala, F. Thétiot, C. Charles, S. Triki, K. Boukheddaden, G. Chastanet and M. Marchivie, *Chem. Commun.*, 2017, **53**, 8356–8359.
83. E. Milin, V. Patinec, S. Triki, E. E. Bendeif, S. Pillet, M. Marchivie, G. Chastanet and K. Boukheddaden, *Inorg. Chem.*, 2016, **55**, 11652–11661.
84. M. Shatruk, H. Phan, B. A. Chrisostomo and A. Suleimenova, *Coord. Chem. Rev.*, 2015, **289–290**, 62–73.
85. C. Atmani, F. El Hajj, S. Benmansour, M. Marchivie, S. Triki, F. Conan, V. Patinec, H. Handel, G. Dupouy and C. J. Gómez-García, *Coord. Chem. Rev.*, 2010, **254**, 1559–1569.
86. M. Yamada, M. Ooidemizu, Y. Ikuta, S. Osa, N. Matsumoto, S. Iijima, M. Kojima, F. Dahan and J. P. Tuchagues, *Inorg. Chem.*, 2003, **42**, 8406–8416.
87. V. Gómez, C. Sáenz De Pipaón, P. Maldonado-Illescas, J. C. Waerenborgh, E. Martin, J. Benet-Buchholz and J. R. Galán-Mascarós, *J. Am. Chem. Soc.*, 2015, **137**, 11924–11927.
88. Y. Maximilian Klein, N. F. Sciortino, C. E. Housecroft, C. J. Kepert and S. M. Neville, *Magnetochemistry*, 2016, **2**, 2–7.
89. D. Savard, C. Cook, G. D. Enright, I. Korobkov, T. J. Burchell and M. Murugesu, *CrystEngComm*, 2011, **13**, 5190–5197.
90. O. G. Shakirova, L. G. Lavrenova, Y. G. Shvedenkov, G. A. Berezovskii, D. Y. Naumov, L. A. Sheludyakova, G. V Dolgushin and S. V Larionov, *Russ. J. Coord. Chem.*, 2004, **30**, 507–513.

91. Y. Garcia, P. Guionneau, G. Bravic, D. Chasseau, J. A. K. Howard, O. Kahn, V. Ksenofontov, S. Reiman and P. Gütlich, *Eur. J. Inorg. Chem.*, 2000, 1531–1538.
92. J. J. A. Kolnaar, G. Van Dijk, H. Kooijman, A. L. Spek, V. G. Ksenofontov, P. Gu, J. G. Haasnoot and J. Reedijk, *Inorg. Chem.*, 1997, **36**, 2433–2440.
93. M. Thomannj, O. Kahn, J. Guilhem and F. Varreta, *Inorg. Chem*, 1994, **33**, 6029–6037.
94. Ger. Vos, R. A. Le Fêbre, R. A. G. de Graaf, J. G. Haasnoot and J. Reedijk, *J. Am. Chem. Soc.*, 1983, **105**, 1682–1683.
95. N. Hirosawa, Y. Oso and T. Ishida, *Chem. Lett.*, 2012, **41**, 716–718.
96. M. Yamasaki and T. Ishida, *Polyhedron*, 2015, **85**, 795–799.
97. M. Yamasaki and T. Ishida, *J. Mater. Chem. C*, 2015, **3**, 7784–7787.
98. T. Ishida, T. Kanetomo and M. Yamasaki, *Acta Cryst.*, 2016, **C72**, 797–801.
99. A. Kashiro, K. Some, Y. Kobayashi and T. Ishida, *Inorg. Chem.*, 2019, **58**, 7672–7676.
100. E. Cuza, S. Benmansour, N. Cosquer, F. Conan, S. Pillet, C. J. Gómez-García and S. Triki, *Magnetochemistry*, 2020, **6**, 26.
101. A. Kashiro, W. Kohno and T. Ishida, *Inorg. Chem.*, 2020, **59**, 10163–10171.
102. E. Cuza, C. D. Mekuimemba, N. Cosquer, F. Conan, S. Pillet, G. Chastanet and S. Triki, *Inorg. Chem.*, 2021, **60**, 6536–6549.
103. B. Benaicha, K. Van Do, A. Yangui, N. Pittala, A. Lusson, M. Sy, G. Bouchez, H. Fourati, C. J. Gómez-Garciá, S. Triki and K. Boukheddaden, *Chem. Sci.*, 2019, **10**, 6791–6798.
104. E. Coronado, J. R. Galán-Mascarós, C. J. Gómez-García and V. Laukhin, *Nature*, 2000, **408**, 447–449.
105. O. Kahn, *Molecular Magnetism*, VCH Publishers, Inc., New York, 1993.
106. A. Rudavskyi, C. Sousa, C. De Graaf, R. W. A. Havenith and R. Broer, *J. Chem. Phys.*, 2014, **140**, 184318.
107. S. Vela, S. Vela, M. Fumanal, J. Cirera and J. Ribas-Arino, *Phys. Chem. Chem. Phys.*, 2020, **22**, 4938–4945.
108. J. P. Janet, L. Chan and H. J. Kulik, *J. Phys. Chem. Lett.*, 2018, **9**, 1064–1071.
109. D. Vidal, J. Cirera and J. Ribas-Arino, *Dalton Trans.*, 2021, **50**, 17635–17642.
110. M. Swart, *J. Chem. Theory Comput.*, 2008, **4**, 2057–2066.
111. M. Swart, *Int. J. Quantum Chem.*, 2013, **113**, 2–7.
112. K. P. Kepp, *Inorg. Chem.*, 2016, **55**, 2717–2727.
113. K. P. Jensen and J. Cirera, *J. Phys. Chem. A*, 2009, **113**, 10033–10039.
114. N. C. Handy and A. J. Cohen, *Mol. Phys.*, 2001, **99**, 403–412.
115. W.-M. Hoe, A. J. Cohen and N. C. Handy, *Chem. Phys. Lett.*, 2001, **341**, 319–328.

116. J. P. Perdew, K. Burke and M. Ernzerhof, *Phys. Rev. Lett.*, 1996, **77**, 3865–3868.
117. J. P. Perdew, K. Burke and M. Ernzerhof, *Phys. Rev. Lett.*, 1997, **78**, 1396.
118. C. K. Jørgensen, *Modern Aspects of Ligand Field Theory*, North-Holland Publishing Co., Amsterdam, 1971.
119. J. Cirera and E. Ruiz, *J. Phys. Chem. A*, 2020, **124**, 5053–5058.
120. L. P. Hammett, *Chem. Rev.*, 1935, **17**, 125–136.
121. L. P. Hammett, *J. Am. Chem. Soc.*, 1937, **59**, 96–103.
122. C. G. Swain and E. C. Lupton Jr., *J. Am. Chem. Soc.*, 1968, **90**, 4328–4337.
123. R. Kulmaczewski, M. J. Howard and M. A. Halcrow, *Dalton Trans.*, 2021, **50**, 3464–3467.
124. H. C. Liang, Y. Pan, H. L. Zhu, Y. S. Meng, C. H. Liu, T. Liu and Y. Y. Zhu, *Inorg. Chem. Front*, 2022, **9**, 2343–2352.
125. A. Kimura and T. Ishida, *Inorganics*, 2017, **5**, 52.
126. L. J. Kershaw Cook, R. Kulmaczewski, R. Mohammed, S. Dudley, S. A. Barrett, M. A. Little, R. J. Deeth and M. A. Halcrow, *Angew. Chem. Int. Ed.*, 2016, **55**, 4327–4331.
127. I. Prat, A. Company, T. Corona, T. Parella, X. Ribas and M. Costas, *Inorg. Chem.*, 2013, **52**, 9229–9244.
128. M. F. Tweedle and L. J. Wilson, *J. Am. Chem. Soc.*, 1976, **98**, 4824–4834.
129. D. C. Ashley and E. Jakubikova, *Inorg. Chem.*, 2018, **57**, 9907–9917.
130. A. Kimura and T. Ishida, *ACS Omega*, 2018, **3**, 6737–6747.
131. K. Nakano, N. Suemura, K. Yoneda, S. Kawata and S. Kaizaki, *Dalton Trans.*, 2005, 740–743.
132. K. Senthil Kumar, S. Vela, B. Heinrich, N. Suryadevara, L. Karmazin, C. Bailly and M. Ruben, *Dalton Trans.*, 2020, **49**, 1022–1031.
133. H. J. Lin, D. Siretanu, D. A. Dickie, D. Subedi, J. J. Scepaniak, D. Mitcov, R. Clérac and J. M. Smith, *J. Am. Chem. Soc.*, 2014, **136**, 13326–13332.
134. B. Dey, S. Mehta, A. Mondal, J. Cirera, E. Colacio and V. Chandrasekhar, *ACS Omega*, 2022, **7**, 39268–39279.
135. J. G. Park, I. R. Jeon and T. D. Harris, *Inorg. Chem.*, 2015, **54**, 359–369.
136. F. Milocco, F. De Vries, I. M. A. Bartels, R. W. A. Havenith, J. Cirera, S. Demeshko, F. Meyer and E. Otten, *J. Am. Chem. Soc.*, 2020, **142**, 20170–20181.
137. C. Hansch, A. Leo and R. W. Taft, *Chem. Rev.*, 1991, **91**, 165–195.
138. J.-F. Létard, C. Carbonera, J. A. Real, S. Kawata and S. Kaizaki, *Chem. Eur. J.*, 2009, **15**, 4146–4155.

139. A. E. Reed and F. Weinhold, *J. Chem. Phys.*, 1983, **78**, 4066–4073.
140. J. E. Carpenter and F. Weinhold, *J. Mol. Struct. THEOCHEM*, 1988, **169**, 41–62.
141. A. E. Reed, R. B. Weinstock and F. Weinhold, *J. Chem. Phys.*, 1985, **83**, 735–746.
142. A. E. Reed and F. Weinhold, *J. Chem. Phys.*, 1985, **83**, 1736–1740.
143. J. P. Foster and F. Weinhold, *J. Am. Chem. Soc.*, 1980, **102**, 7211–7218.
144. A. E. Reed, L. A. Curtiss and F. Weinhold, *Chem. Rev.*, 1988, **88**, 899–926.
145. R. S. Mulliken, *J. Chem. Phys.*, 1955, **23**, 1833–1840.
146. J. Contreras-García, E. R. Johnson, S. Keinan, R. Chaudret, J. P. Piquemal, D. N. Beratan and W. Yang, *J. Chem. Theory Comput.*, 2011, **7**, 625–632.
147. E. R. Johnson, S. Keinan, P. Mori-Sánchez, J. Contreras-García, A. J. Cohen and W. Yang, *J. Am. Chem. Soc.*, 2010, **132**, 6498–6506.
148. T. Lu and F. Chen, *J. Comput. Chem.*, 2012, **33**, 580–592.
149. T. Lu, *J. Chem. Phys.*, 2024, **161**, 082503.
150. W. Humphrey, A. Dalke and K. Schulten, *VMD – Visual Molecular Dynamics, J. Molec. Graphics*, 1996, **14**, 33–38.
151. D. Vidal, J. Cirera and J. Ribas-Arino, *Phys. Chem. Chem. Phys.*, 2023, **25**, 12490–12499.

CHAPTER 4

Multiconfiguration Pair-Density Functional Theory Applied to Spin-Crossover

4.1. Introduction

As explained in Chapter 2, DFT tries to include electron correlation through the exchange-correlation functional, but the exact form of this functional is unknown and several approximations are used. Moreover, DFT does not provide good description of virtual orbitals, and accurately capturing the static correlation remains an unsolved challenge due to its single reference nature.[1,2]

CASSCF can capture the static correlation by constructing a multiconfigurational wave function.[3] However, it does not provide good enough accuracy because it only captures a portion of the correlation energy. It is difficult to recover a large portion of the dynamic correlation energy by expanding the active space, but this can be solved by using higher-level multireference methods like the perturbation theory,[4–18] using the CASSCF wave function as a starting point. The problem is that using higher level methods, increase considerably the computational cost and therefore their applicability is limited.

Multiconfiguration Pair-Density Functional Theory (MC-PDFT)[19] method combines multiconfigurational WFT with DFT-based methods in a way that it can describe the static correlation (with the multiconfigurational WFT approach) as well as the dynamic correlation (with DFT).[20]

In this chapter we present the work developed during the thesis' internship at University of Oxford under the supervision of Prof. John E. McGrady. The aim of this study is to test the accuracy and the improvement of the MC-PDFT method by studying a known and well-described system: the bis(isothiocyanato)bis(1,10-phenanthroline)iron, $[Fe(phen)_2(NCS)_2]$[21] (phen = phenantroline).

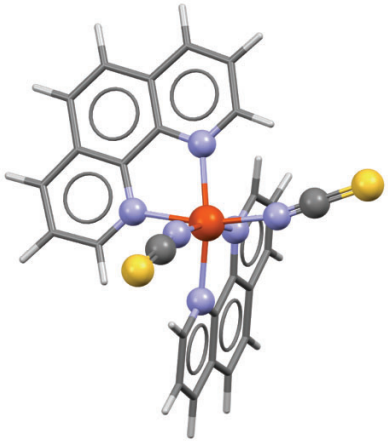

Figure 4.1. $[Fe(phen)_2(NCS)_2]$.

The results will be compared, among others, with the ones obtained in the benchmarking study performed in the group in 2018 by Jordi Cirera *et al*.[22]

Table 4.1. Experimental[21,22] and computed[22] transition temperature values of $[Fe(phen)_2(NCS)_2]$. BS1: the fully optimized contracted triple-ζ (TZV)[23] all-electron Gaussian basis set for all the elements, and a quadruple-ζ basis set with polarization functions (QZVP) on the metal centre.[24,25] BS2: triple-ζ basis set including polarization functions (TZVP)[23] for all atoms.

	Experimental $T_{1/2}$/K	**TPSSh/BS1**		**TPSSh/BS2**	
		ΔE/kcal·mol^{-1}	**$T_{1/2}$/K**	**ΔE/kcal·mol^{-1}**	**$T_{1/2}$/K**
$[Fe(phen)_2(NCS)_2]$	176.5	9.57	454	6.05	237

4.2. Computational Details

All DFT, CASSCF and MC-PDFT calculations were performed using the OpenMolcas (Version 23.02) program.[26] The calculations were converged to 10^{-8} for the density matrix elements. For the KS-DFT calculations, the OPBE[27–30] functional was used. Several basis sets are used: Ahlrichs VDZ,[31] ANO-L-VTZP[32–34] and ANO-S-VDZ,[35] several active spaces are tested: (10,10) and (6,8), and several MC-PDFT translated functionals are also used: tOPBE,[19,27–30] tBLYP[19,36–39] and tLSDA.[19,40–43]

An initial guess for the CASSCF calculations is required, thus, single-point KS-DFT calculations were carried out to be the starting point of the CASSCF calculations, and this is in turn the starting point for the MC-PDFT calculations. These steps are performed for both spin-states: high-spin (HS) and low-spin (LS).

1. SCF calculation to obtain the initial guess. In our case, we performed KS-DFT calculations.
2. Choice of the active space to perform the CASSCF calculation.
3. MC-PDFT calculation.
4. Energy correction with the harmonic approximation.

We used the optimized geometries obtained in Ref.[22] with TPSSh[44,45] and BS1 (the fully optimized contracted triple-ζ (TZV)[23] all-electron Gaussian basis set developed by Ahlrichs and co-workers was employed for all the elements, and a quadruple-ζ basis set with polarization functions (QZVP) was used on the metal centre).[24,25] We performed also some calculations using the optimized geometry in Reff.[22] with TPSSh/BS2 (a triple-ζ basis set including

polarization functions (TZVP)[23] for all atoms) to check if the results were notably different than the ones obtained with BS1, and they were not.

We run DFT optimizations and frequencies calculations with Gaussian 16 (revision B.01) electronic structure suite[46] to compare the entropic contribution for several functionals (TPSSh,[44,45] OPBE,[24–27] BLYP[33–36] and SVWN[37–40]) and different basis sets (Ahlrichs VDZ[31] and Def2-TZVP[23,25,31]).

For the HS state, there are three possible arrangements of the electrons, that is, three possible states that are so similar in energy. Openmolcas makes it possible to perform orbital optimization for the average energy of a number of states. To obtain the MCSCF and MC-PDFT energies, we averaged the energy of the three possible states.

4.3. Active Space (10,10) for High-Spin and (10,10) for Low-Spin

The first strategy we chose was to use the same size for the active space for both spin-states: (10,10). Therefore, there are 10 electrons and 10 orbitals in the active space, with 131 inactive orbitals for the system of study. There are two doubly occupied metal–ligand σ-bonding orbitals to take into account static correlation effects associated with the covalent metal–ligand interactions,[47] there are six electrons in the five Fe(3d) orbitals, a second Fe(3d') shell to account for the double-shell effect.[48]

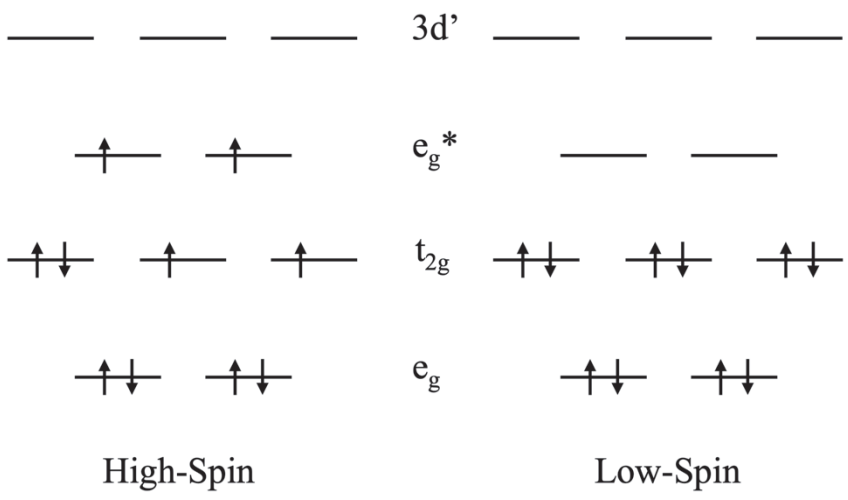

Figure 4.2. Active spaces for HS (10,10) and LS (10,10).

The geometry used is the optimized geometry of BS1 with TPSSh of the benchmarking paper,[22] and the calculations were performed for different basis sets and different MC-PDFT functionals. As it can be seen from Table 4.2, generally good results are obtained if the tBLYP functional is used. Actually, the combination of tBLYP/Ahlrichs VDZ (7.955 kcal·mol^{-1}) provides with very similar results to the one that TPSSh provides (BS1: 9.57 kcal·mol^{-1}, BS2: 6.05 kcal·mol^{-1}).[22]

Table 4.2. Differences of energy HS-LS of CASSCF and MC-PDFT calculations for BS1 optimized geometry[22] with (10,10) active space for both HS and LS states.

	ΔE_{HS-LS}/kcal·mol^{-1}			
	MCSCF Reference Energy	**Total MC-PDFT Energy**		
		tOPBE	**tBLYP**	**tLSDA**
Ahlrichs VDZ	-34.230	-2.977	7.955	33.732
ANO-L-VTZP	-26.073	-11.087	-0.531	22.256
ANO-S-VDZ	-25.881	-6.779	1.527	25.599

Since tBLYP/Ahlrichs VDZ provides with good results, we performed tBLYP/Ahlrichs VDZ calculations using the optimized geometries with TPSSh/BS2 of the reference paper,[22] and the total ΔE_{HS-LS} MC-PDFT Energy is 7.132 kcal·mol^{-1}, also close to the results obtained in the benchmarking paper. tOPBE results do not provide with good results since they do not correctly predict the spin-state energies' ordering, and tLSDA provide with too large energy differences, not predicting properly an SCO system.

4.4. Active Space (6,8) for High-Spin and (10,10) for Low-Spin

Another strategy we have followed is trying to reduce the active space for the HS state to (6,8). Therefore, there are 6 electrons and 8 orbitals in the active space, with 133 inactive orbitals for the system of study. We did not reduce the active space for the LS state because we have double excitation correlations, and the upper unoccupied orbitals are necessary.

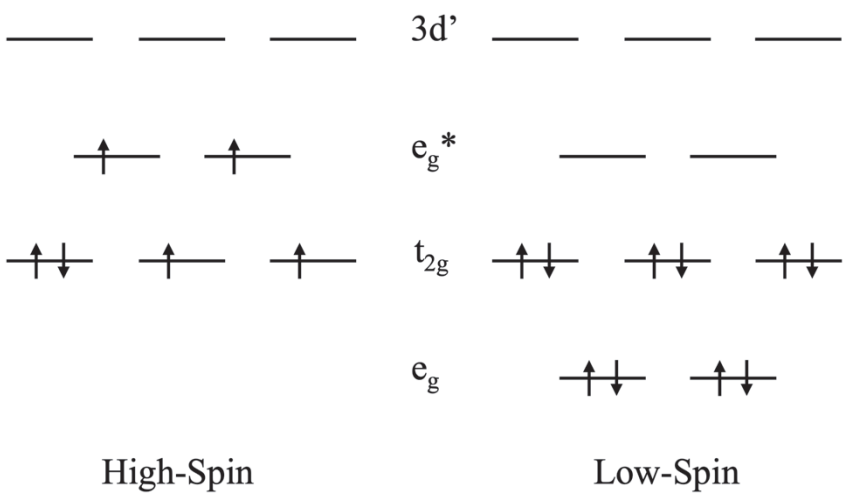

Figure 4.3. Active spaces for HS (6,8) and LS (10,10).

The geometry used is the optimized geometry of BS1 with TPSSh of the benchmarking paper. As it can be seen from Table 4.3, generally good results are obtained again when the tBLYP functional is used. Actually, the combination of tBLYP/Ahlrichs VDZ (9.545 kcal·mol^{-1}) provides with very similar results to the one that TPSSh provides (BS1: 9.57 kcal·mol^{-1}, BS2: 6.05 kcal·mol^{-1}).

Table 4.3. Differences of energy HS-LS in kcal·mol^{-1} of CASSCF and MC-PDFT calculations for BS1 optimized geometry with (6,8) active space for the HS sate and (10,10) active space for the LS state.

	ΔE_{HS-LS}/kcal·mol^{-1}			
	MCSCF Reference Energy	**Total MC-PDFT Energy**		
		tOPBE	**tBLYP**	**tLSDA**
Ahlrichs VDZ	-31.965	-1.518	9.545	35.605
ANO-L-VTZP	-23.970	-9.289	1.365	24.470
ANO-S-VDZ	-23.627	-5.307	3.090	27.425

We performed the tBLYP/Ahlrichs VDZ calculations using the optimized geometries with TPSSh/BS2 of the reference paper, and the total ΔE_{HS-LS} MC-PDFT Energy is 8.599 kcal·mol^{-1}, close to the results obtained in the benchmarking paper. Again, tOPBE results do not correctly predict the spin-state energies' ordering and tLSDA provide with too large energy differences.

That is, in principle, the numbers are, at least, equally good to the TPSSh ones obtained in the benchmarking paper, and it is possible that the results applying the energy correction with the harmonic frequencies surpass the ones obtained with DFT TPSSh when computing the $T_{1/2}$.

4.5. Energy Correction with the Harmonic Frequencies

The next step was to correct the energies obtained from the MC-PDFT calculations (results from using the optimized geometry of BS1 from the benchmarking reference paper) with the DFT harmonic frequencies obtained from the computation of the thermochemistry. Optimizations and frequency calculations with several DFT methods (TPSSh,[44,45] OPBE,[24–27] BLYP[33–36] and SVWN[37–40]) and different basis sets (Ahlrichs VDZ[31] and Def2-TZVP[23,25,31]) were performed with Gaussian.[46]

Table 4.4. Average Fe–N bond lengths (in Angstrom) using different basis sets and functionals for the $[Fe(phen)_2(NCS)_2]$ system.

		d(Fe–N)$_{HS}$/Å	**d(Fe–N)$_{LS}$/Å**
TPSSh	Ahlrichs VDZ	2.129	1.939
	Def2-TZVP	2.170	1.956
OPBE	Ahlrichs VDZ	2.140	1.916
	Def2-TZVP	2.167	1.925
BLYP	Ahlrichs VDZ	2.148	1.959
	Def2-TZVP	2.192	1.979
SVWN	Ahlrichs VDZ	2.048	1.870
	Def2-TZVP	2.078	1.882

As can be seen from Table 4.4, the bond lengths are similar across the different functionals and basis sets. For the local SVWN functional, bond lengths are slighter shorter, but still within the range of HS/LS bond lengths.

Table 4.5. Computed DFT ΔE, ΔH and ΔS for different functionals and basis sets. Electronic energies and enthalpies in kcal·mol^{-1} and entropies in cal·mol^{-1}·K^{-1}.

		ΔE/kcal·mol^{-1}	ΔH/kcal·mol^{-1}	ΔS/cal·mol^{-1}·K^{-1}	$T_{1/2}$/K
BLYP	Ahlrichs VDZ	18.749	17.505	13.872	1262
	Def2-TZVP	12.413	11.288	16.965	665
OPBE	Ahlrichs VDZ	4.721	3.315	16.120	206
	Def2-TZVP	2.284	0.990	19.452	51
TPSSh	Ahlrichs VDZ	11.850	10.503	15.044	698
	Def2-TZVP	7.037	5.813	18.814	309
SVWN	Ahlrichs VDZ	52.457	50.518	17.301	2920
	Def2-TZVP	44.108	42.477	12.881	3298

The differences of $\Delta E_{\text{HS-LS}}$ and $\Delta H_{\text{HS-LS}}$ are quite huge when changing the functional, but when we compare the entropic contribution, we see that ΔS remains almost constant regardless of the functional. Of course, these small differences can have an impact when computing $T_{1/2} = \Delta H/\Delta S$, but it seems that the changes in ΔH are way larger than the ones in ΔS. That means that, in principle, this contribution is more or less constant, and harmonic vibrations can be (in principle) used to estimate the $T_{1/2}$ using the harmonic approximation. For instance, when plotting the harmonic frequencies for different functionals, they are practically identic regardless of the functional, particularly the first ten (Figure 4.4, Figure A4.1). In general, BLYP and SVWN cannot describe properly the energies and therefore the transition temperatures.

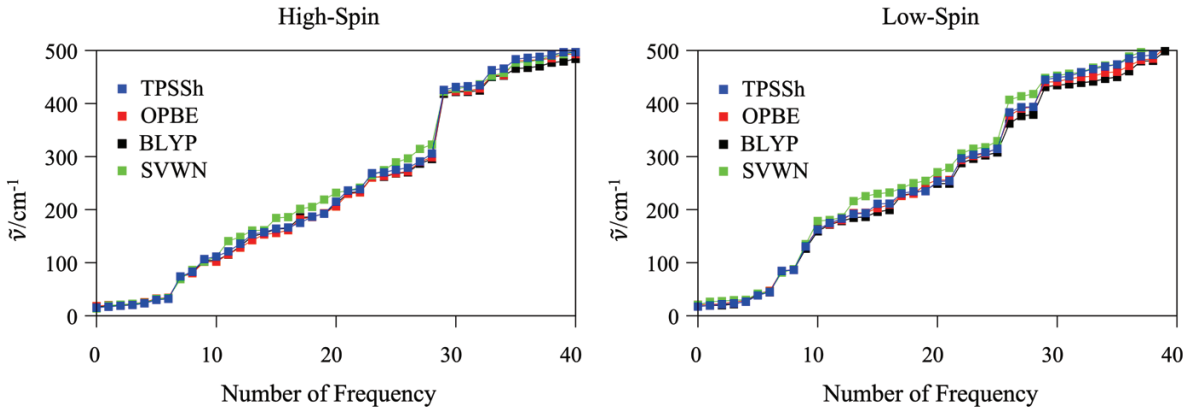

Figure 4.4. Frequencies for several functionals using the Ahlrichs VDZ basis set. Blue: TPSSh, red: OPBE, black: BLYP and green: SVWN. Left: high-spin, right: low-spin.

We correct the energies of each spin state with the harmonic frequencies for temperatures ranging from 10 K to 1000 K, and therefore we obtain the Gibbs free energy dependence on temperature:[49]

$$G^i = H^i - TS^i = E^i_{el} + E^i_{vib} - TS^i = E^i_{MC-PDFT} + k_B T \sum_{\lambda} \ln\left(1 - e^{-\frac{h\nu_\lambda}{k_B T}}\right) \qquad (4.1)$$

where i = HS or LS, and the sum runs over all the vibration modes λ.

$$\Delta G(T) = G^{HS}\left(T, \nu^{HS}_\lambda\right) - G^{LS}\left(T, \nu^{LS}_\lambda\right) = -RT \ln \frac{\gamma_{HS}(T)}{\gamma_{LS}(T)} = -RT \ln \frac{\gamma_{HS}(T)}{1 - \gamma_{HS}(T)} \qquad (4.2)$$

From there, we can calculate ΔG at each temperature and determine $T_{1/2}$ since it is the temperature at which $\gamma_{HS} = \gamma_{LS}$ and therefore, $\Delta G = 0$.

This procedure has been carried out for the positive and reasonable $\Delta E_{MC\text{-}PDFT}$ values obtained.

4.5.1. Correction of the HS(10,10) and LS(10,10) Results

The frequencies used are obtained with several DFT functionals (BLYP, OPBE, TPSSh, SVWN) and basis sets (Ahlrichs VDZ, Def2-TZVP). The correction is applied, in this case, to the MC-PDFT results obtained with the tBLYP translated MC-PDFT functional and both Ahlrichs VDZ and ANO-S-VDZ basis sets, which are the ones that presented positive and small values of $\Delta E_{MC\text{-}PDFT}$ (Table 4.2).

Table 4.6. Transition temperatures in Kelvin obtained from the thermochemistry calculation through the harmonic approximation correction of the MC-PDFT energies. The MC-PDFT energies are those obtained from tBLYP translated MC-PDFT functional with two different basis sets: Ahlrichs VDZ and ANO-S-VDZ. The frequencies used are obtained for several DFT functionals: BLYP, OPBE, TPSSh and SVWN, and the basis sets: Ahlrichs VDZ and Def2-TZVP.

$T_{1/2}$/K		DFT Functional/Ahlrichs VDZ				DFT Functional/Def2-TZVP			
		BLYP	OPBE	TPSSh	SVWN	BLYP	OPBE	TPSSh	SVWN
MC-PDFT tBLYP	Ahlrichs VDZ	667	555	599	487	534	453	470	678
	ANO-S-VDZ	128	106	115	94	103	87	90	130

The key in the energy correction is that in principle the frequencies seem to be independent regardless of the DFT functional used for the optimization and frequency calculations. Thus, Table 4.6 shows, similar transition temperatures with all the functionals used for the same basis set. That is, even though we see that the transition temperatures in Table 4.5 are not well predicted for functionals like BLYP or SVWN at the DFT level, the correction of the MC-PDFT energies with the harmonic frequencies obtained with such functionals can provide with consistent and good results of $T_{1/2}$ (Table 4.6 ANO-S-VDZ).

This methodology reduces the $T_{1/2}$ values compared to the DFT methodology for the case of the ANO-S-VDZ basis set in MC-PDFT calculations, making them closer to the experimental value (176 K). For instance, the $T_{1/2}$ value obtained from DFT TPSSh/Ahlrichs VDZ in Table 4.5 (698 K) at the DFT level is way bigger than the one obtained from the MC-PDFT tBLYP/ANO-S-VDZ energy correction with TPSSh/Ahlrichs VDZ in Table 4.6 (115 K). There are differences in $T_{1/2}$ depending on the chosen MC-PDFT basis set.

There are small changes in $T_{1/2}$ depending on the basis set used to obtain the DFT frequencies (Ahlrichs VDZ and Def2-TZVP) but they are not significant, the effect of the basis set on the harmonic frequencies is practically negligible. For instance, when plotting the harmonic frequencies for TPSSh and different basis sets, they are practically identic regardless of the basis set used (Figure 4.5, Figure A4.2, A4.3, A4.4).

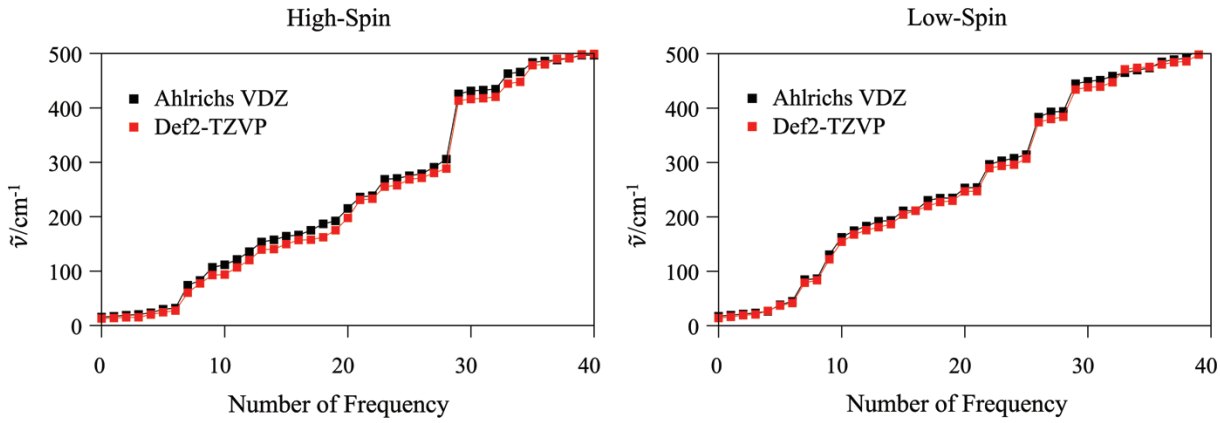

Figure 4.5. Frequencies for TPSSh functional using the Ahlrichs VDZ (black) and the Def2-TZVP (red) basis sets. Left: high-spin, right: low-spin.

4.5.2. Correction of the HS(6,8) and LS(10,10) Results

In the case of the MC-PDFT calculations using active spaces of HS(6,8) and LS(10,10), the correction is applied to the MC-PDFT results obtained with the tBLYP translated MC-PDFT functional and Ahlrichs VDZ, ANO-L-VTZP and ANO-S-VDZ basis sets, which are the ones that presented positive and small values of $\Delta E_{\text{MC-PDFT}}$ (Table 4.3).

Table 4.7. Transition temperatures in Kelvin obtained from the thermochemistry calculation through the harmonic approximation correction of the MC-PDFT energies. The MC-PDFT energies are those obtained from tBLYP translated MC-PDFT functional with three different basis sets: Ahlrichs VDZ, ANO-L-VTZP and ANO-S-VDZ. The frequencies used are obtained for several DFT functionals: BLYP, OPBE, TPSSh and SVWN, and the basis sets: Ahlrichs VDZ and Def2-TZVP.

$T_{1/2}$/K		DFT Functional/Ahlrichs VDZ				DFT Functional/Def2-TZVP			
		BLYP	OPBE	TPSSh	SVWN	BLYP	OPBE	TPSSh	SVWN
MC-PDFT tBLYP	Ahlrichs VDZ	800	665	719	584	641	544	564	814
	ANO-L-VTZP	114	95	103	84	92	78	81	116
	ANO-S-VDZ	259	215	233	189	208	176	183	163

With these active spaces, we see that in general this methodology reduces the $T_{1/2}$ values compared to the DFT methodology for the case of the ANO-L-VTZP and ANO-S-VDZ basis

sets in MC-PDFT calculations, making them closer to the experimental value (176 K). Again, there are small changes in $T_{1/2}$ depending on the basis set used to obtain the DFT frequencies (Ahlrichs VDZ and Def2-TZVP), but they are not significant. There are also differences in $T_{1/2}$ depending on the chosen MC-PDFT basis set.

Based on our study, the method that provides with better results when comparing it to the experimental value of $T_{1/2}$ is the one obtained from HS(6,8)/LS(10,10) with the tBLYP and ANO-S-VDZ basis set, using the harmonic frequencies from DFT calculations with Def2-TZVP and any of the functionals, but especially, using the OPBE functional for the calculation of frequencies.

4.6. Conclusions

The choice of HS(6,8) and LS(10,10) active spaces give better results in terms of $\Delta E_{\text{HS-LS}}$ than the HS(10,10) and LS(10,10) active spaces. This translates to better results of $T_{1/2}$ for the HS(6,8) and LS(10,10) active spaces when applying the harmonic approximation to the MC-PDFT energies.

The Ahlrichs VDZ basis set in MC-PDFT is not sufficient to describe the transition temperatures, the $T_{1/2}$ values obtained are too big. For the ANO-L-VTZP and ANO-S-VDZ basis sets, the results obtained are close to the $T_{1/2}$ experimental value, but do not significantly improve our DFT results obtained for functionals such as TPSSh or OPBE with a Def2-TZVP basis set, nor those obtained in the reference paper. Of course, there is an improvement of the transition temperature values, but the effort and computational cost involved in this study has not been worth it compared to DFT.

Although the main goal of the MC-PDFT method is to correct the methodological deficiencies of DFT (*i.e* the lack of explicit static correlation contribution in the calculation) and CASSCF (its difficulty in recovering a large portion of the dynamic correlation) calculations, from our results is hard to tell to which extend this is happening, because the results still highly dependent on the choice of tMC-PDFT method, as well as the basis set used in the calculations.

Overall, from this study is difficult to assess if the MC-PDFT method is a better or worse choice than DFT methods. Only one system has been studied, and it is possible to compute exactly the experimental $T_{1/2}$ value, but the cost in terms of setting up the calculations, and the computational time associated to them, makes the MC-PDFT option a choice that needs to be carefully thought before using it.

4.7. Appendix

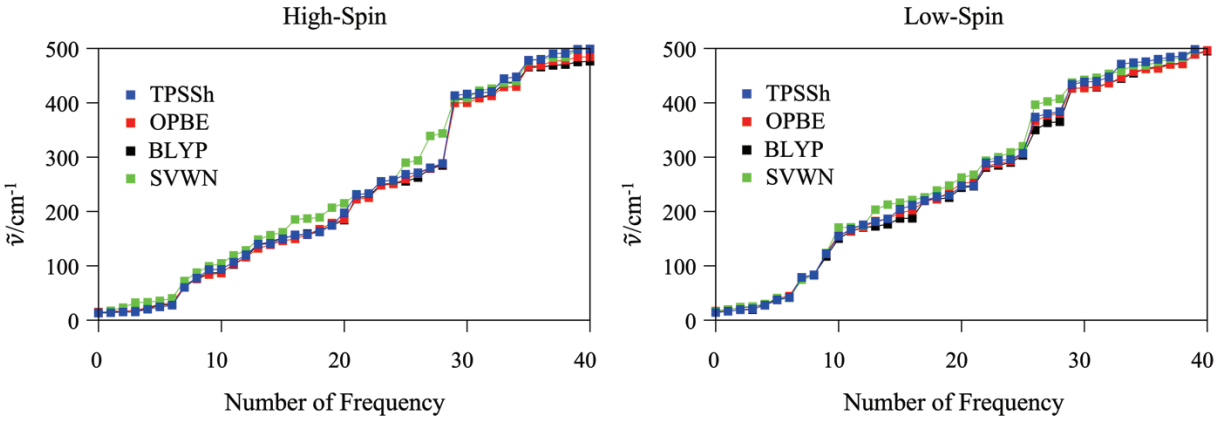

Figure A4.1. Frequencies for several functionals using the Def2-TZVP basis set. Blue: TPSSh, red: OPBE, black: BLYP and green: SVWN. Left: high-spin, right: low-spin.

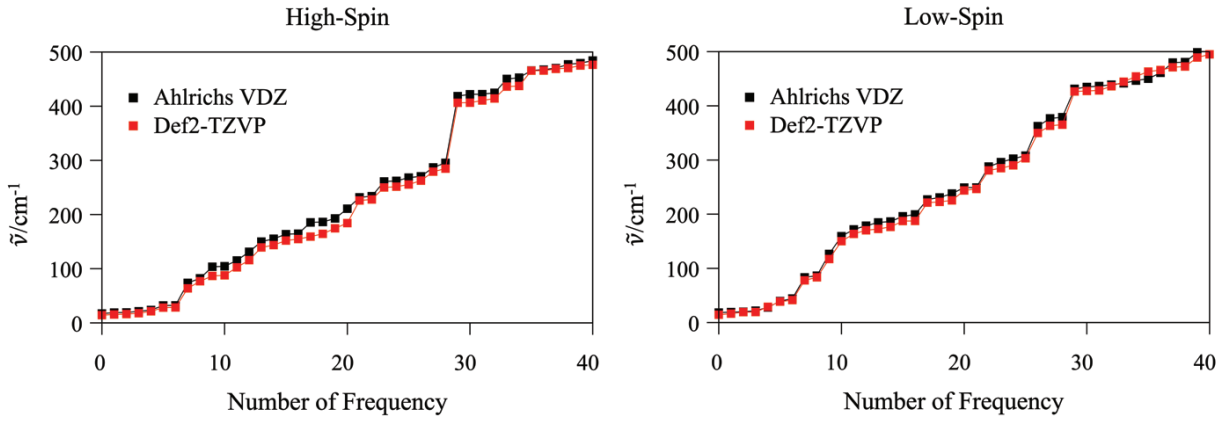

Figure A4.2. Frequencies for BLYP functional using the Ahlrichs VDZ (black) and the Def2-TZVP (red) basis set. Left: high-spin, right: low-spin.

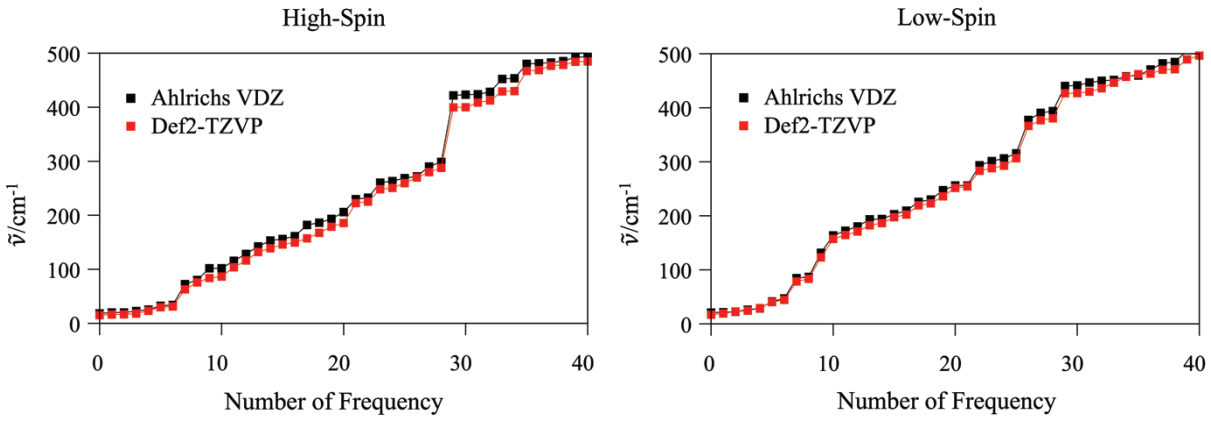

Figure A4.3. Frequencies for OPBE functional using the Ahlrichs VDZ (black) and the Def2-TZVP (red) basis set. Left: high-spin, right: low-spin.

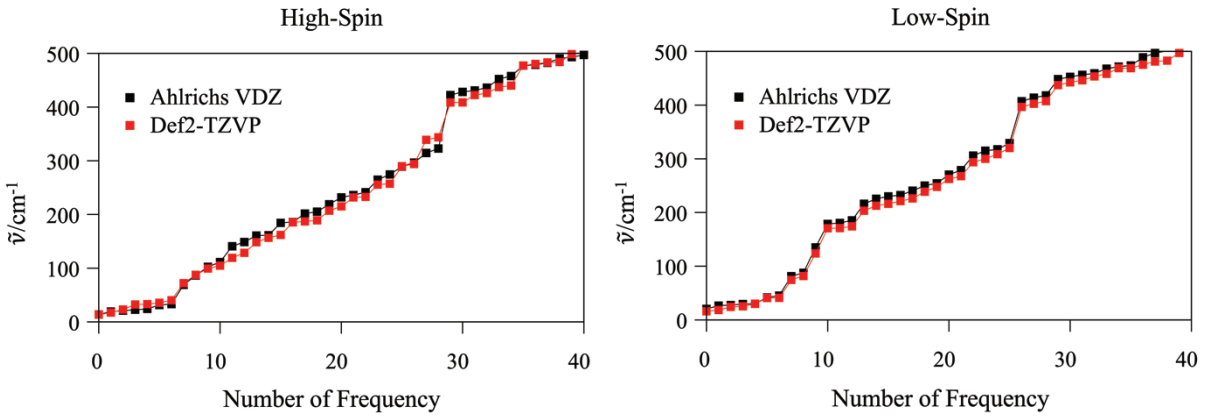

Figure A4.4. Frequencies for SVWN functional using the Ahlrichs VDZ (black) and the Def2-TZVP (red) basis set. Left: high-spin, right: low-spin.

4.8. References

1. D. Gibney, J. N. Boyn and D. A. Mazziotti, *J. Phys. Chem. Lett.*, 2021, **12**, 385–391.
2. Y. Wang, Z. Lin, R. Ouyang, B. Jiang, I. Y. Zhang and X. Xu, *ChemRxiv*, 2024. This content is a preprint and has not been peer-reviewed.
3. B. O. Roos, P. R. Taylor and P. E. M. Siegbahn, *Chem. Phys.*, 1980, **48**, 157–173.
4. B. O. Roos, *Acc. Chem. Res.*, 1999, **32**, 137–144.
5. K. Andersson, P. Å. Malmqvist and B. O. Roos, *J. Chem. Phys.*, 1992, **96**, 1218–1226.
6. B. O. Roos, K. Andersson, M. P. Fülscher, P.-Å. Malmqvist and L. Serrano-Andrés, in *Advances in Chemical Physics*, eds. I. Prigogine and S. A. Rice, John Wiley & Sons, Inc., 1996, vol. 93, pp. 219–331.

7. P. G. Szalay, T. Müller, G. Gidofalvi, H. Lischka and R. Shepard, *Chem. Rev.*, 2012, **112**, 108–181.
8. I. Schapiro, K. Sivalingam and F. Neese, *J. Chem. Theory Comput.*, 2013, **9**, 3567–3580.
9. C. Angeli, R. Cimiraglia, S. Evangelisti, T. Leininger and J. P. Malrieu, *J. Chem. Phys.*, 2001, **114**, 10252–10264.
10. K. Pierloot, Q. M. Phung and A. Domingo, *J. Chem. Theory Comput.*, 2017, **13**, 537–553.
11. S. K. Singh, J. Eng, M. Atanasov and F. Neese, *Coord. Chem. Rev.*, 2017, **344**, 2–25.
12. C. Angeli, R. Cimiraglia and J.-P. Malrieu, *Chem. Phys. Lett.*, **350**, 297–305.
13. C. Angeli, B. Bories, A. Cavallini and R. Cimiraglia, *J. Chem. Phys.*, 2006, **124**, 054108.
14. C. Angeli, R. Cimiraglia and J. P. Malrieu, *J. Chem. Phys.*, 2002, **117**, 9138–9153.
15. M. Atanasov, D. Ganyushin, K. Sivalingam and F. Neese, in *Molecular Electronic Structures of Transition Metal Complexes II*, eds. D. M. P. Mingos, P. Day and J. P. Dahl, Springer Berlin, Heidelberg, First Edition., 2012, vol. 143, pp. 149–220.
16. B. O. Roos, M. Fülscher, P.-Å. Malmqvist, M. Merchán and L. Serrano-Andrés, in *Quantum Mechanical Electronic Structure Calculations with Chemical Accuracy*, Springer, Dordrecht, 1995, vol. 13, pp. 357–438.
17. B. O. Roos and P.-Å. Malmqvist, *Phys. Chem. Chem. Phys.*, 2004, **6**, 2919–2927.
18. K. Andersson, P.-Å. Malmqvist, B. O. Roos, A. J. Sadlej and K. Wolinski, *J. Phys. Chem.*, 1990, **94**, 5483–5488.
19. G. Li Manni, R. K. Carlson, S. Luo, D. Ma, J. Olsen, D. G. Truhlar and L. Gagliardi, *J. Chem. Theory Comput.*, 2014, **10**, 3669–3680.
20. I. Fdez. Galván, M. Vacher, A. Alavi, C. Angeli, F. Aquilante, J. Autschbach, J. J. Bao, S. I. Bokarev, N. A. Bogdanov, R. K. Carlson, L. F. Chibotaru, J. Creutzberg, N. Dattani, M. G. Delcey, S. S. Dong, A. Dreuw, L. Freitag, L. M. Frutos, L. Gagliardi, F. Gendron, A. Giussani, L. González, G. Grell, M. Guo, C. E. Hoyer, M. Johansson, S. Keller, S. Knecht, G. Kovačević, E. Källman, G. Li Manni, M. Lundberg, Y. Ma, S. Mai, J. P. Malhado, P. Å. Malmqvist, P. Marquetand, S. A. Mewes, J. Norell, M. Olivucci, M. Oppel, Q. M. Phung, K. Pierloot, F. Plasser, M. Reiher, A. M. Sand, I. Schapiro, P. Sharma, C. J. Stein, L. K. Sørensen, D. G. Truhlar, M. Ugandi, L. Ungur, A. Valentini, S. Vancoillie, V. Veryazov, O. Weser, T. A. Wesołowski, P. O. Widmark, S. Wouters, A. Zech, J. P. Zobel and R. Lindh, *J. Chem. Theory Comput.*, 2019, **15**, 5925–5964.
21. B. Gallois, J. A. Real, C. Haw and J. Zarembowitch, *Inorg. Chem.*, 1990, **29**, 1152–1158.
22. J. Cirera, M. Via-Nadal and E. Ruiz, *Inorg. Chem.*, 2018, **57**, 14097–14105.

23. A. Schäfer, C. Huber and R. Ahlrichs, *J. Chem. Phys.*, 1994, **100**, 5829–5835.
24. F. Weigend, *Phys. Chem. Chem. Phys.*, 2006, **8**, 1057–1065.
25. F. Weigend and R. Ahlrichs, *Phys. Chem. Chem. Phys.*, 2005, **7**, 3297–3305.
26. G. Li Manni, I. Fdez. Galván, A. Alavi, F. Aleotti, F. Aquilante, J. Autschbach, D. Avagliano, A. Baiardi, J. J. Bao, S. Battaglia, L. Birnoschi, A. Blanco-González, S. I. Bokarev, R. Broer, R. Cacciari, P. B. Calio, R. K. Carlson, R. Carvalho Couto, L. Cerdán, L. F. Chibotaru, N. F. Chilton, J. R. Church, I. Conti, S. Coriani, J. Cuéllar-Zuquin, R. E. Daoud, N. Dattani, P. Decleva, C. de Graaf, M. G. Delcey, L. De Vico, W. Dobrautz, S. S. Dong, R. Feng, N. Ferré, M. Filatov, L. Gagliardi, M. Garavelli, L. González, Y. Guan, M. Guo, M. R. Hennefarth, M. R. Hermes, C. E. Hoyer, M. Huix-Rotllant, V. K. Jaiswal, A. Kaiser, D. S. Kaliakin, M. Khamesian, D. S. King, V. Kochetov, M. Krośnicki, A. A. Kumaar, E. D. Larsson, S. Lehtola, M. B. Lepetit, H. Lischka, P. López Ríos, M. Lundberg, D. Ma, S. Mai, P. Marquetand, I. C. D. Merritt, F. Montorsi, M. Mörchen, A. Nenov, V. H. A. Nguyen, Y. Nishimoto, M. S. Oakley, M. Olivucci, M. Oppel, D. Padula, R. Pandharkar, Q. M. Phung, F. Plasser, G. Raggi, E. Rebolini, M. Reiher, I. Rivalta, D. Roca-Sanjuán, T. Romig, A. A. Safari, A. Sánchez-Mansilla, A. M. Sand, I. Schapiro, T. R. Scott, J. Segarra-Martí, F. Segatta, D. C. Sergentu, P. Sharma, R. Shepard, Y. Shu, J. K. Staab, T. P. Straatsma, L. K. Sørensen, B. N. C. Tenorio, D. G. Truhlar, L. Ungur, M. Vacher, V. Veryazov, T. A. Voß, O. Weser, D. Wu, X. Yang, D. Yarkony, C. Zhou, J. P. Zobel and R. Lindh, *J. Chem. Theory Comput.*, 2023, **19**, 6933–6991.
27. N. C. Handy and A. J. Cohen, *Mol. Phys.*, 2001, **99**, 403–412.
28. W.-M. Hoe, A. J. Cohen and N. C. Handy, *Chem. Phys. Lett.,* 2001, **341**, 319–328.
29. J. P. Perdew, K. Burke and M. Ernzerhof, *Phys. Rev. Lett.*, 1996, **77**, 3865–3868.
30. J. P. Perdew, K. Burke and M. Ernzerhof, *Phys. Rev. Lett.*, 1997, **78**, 1396.
31. A. Schäfer, H. Horn and R. Ahlrichs, *J. Chem. Phys.*, 1992, **97**, 2571–2577.
32. R. Pou-Amérigo, M. Merchán, I. Nebot-Gil, P.-O. Widmark and B. O. Roos, *Theor. Chim. Acta*, 1995, **92**, 149–181.
33. P.-O. Widmark, B. J. Persson and B. O. Ross, *Theor. Chim. Acta*, 1991, **79**, 419–432.
34. P.-O. Widmark, P.-Å. Malmqvist and B. O. Roos, *Theor. Chim. Acta*, 1990, **77**, 291–306.
35. K. Pierloot, B. Dumez, P.-O. Widmark and B. O. Roos, *Theor. Chim. Acta*, 1995, **90**, 87–114.
36. A. D. Becke, *Phys. Rev. A*, 1988, **38**, 3098–3100.
37. C. Lee, W. Yang and R. G. Parr, *Phys. Rev. B*, 1988, **37**, 785–789.
38. B. Miehlich, A. Savin, H. Stoll and H. Preuss, *Chem. Phys. Lett.,* 1989, **157**, 200–206.

39. G. Li Manni, R. K. Carlson, S. Luo, D. Ma, J. Olsen, D. G. Truhlar and L. Gagliardi, *J. Chem. Theory Comput.*, 2014, **10**, 3669–3680.
40. P. Hohenberg and W. Kohn, *Phys. Rev.*, 1964, **136**, B864–B871.
41. J. C. Slater, *Phys. Today*, 1974, **27**, 49–50.
42. W. Kohn and L. J. Sham, *Phys. Rev.*, 1965, **140**, A1133–A1138.
43. L. Wilk A N and D. M. Nusair, *Can. J. Phys.*, 1980, **58**, 1200–1211.
44. V. N. Staroverov, G. E. Scuseria, J. Tao and J. P. Perdew, *J. Chem. Phys.*, 2003, **119**, 12129–12137.
45. J. Tao, J. P. Perdew, V. N. Staroverov and G. E. Scuseria, *Phys. Rev. Lett.*, 2003, **91**, 146401.
46. M. J. Frisch, G. W. Trucks, H. B. Schlegel, G. E. Scuseria, M. a. Robb, J. R. Cheeseman, G. Scalmani, V. Barone, G. a. Petersson, H. Nakatsuji, X. Li, M. Caricato, a. V. Marenich, J. Bloino, B. G. Janesko, R. Gomperts, B. Mennucci, H. P. Hratchian, J. V. Ortiz, a. F. Izmaylov, J. L. Sonnenberg, Williams, F. Ding, F. Lipparini, F. Egidi, J. Goings, B. Peng, A. Petrone, T. Henderson, D. Ranasinghe, V. G. Zakrzewski, J. Gao, N. Rega, G. Zheng, W. Liang, M. Hada, M. Ehara, K. Toyota, R. Fukuda, J. Hasegawa, M. Ishida, T. Nakajima, Y. Honda, O. Kitao, H. Nakai, T. Vreven, K. Throssell, J. a. Montgomery Jr., J. E. Peralta, F. Ogliaro, M. J. Bearpark, J. J. Heyd, E. N. Brothers, K. N. Kudin, V. N. Staroverov, T. a. Keith, R. Kobayashi, J. Normand, K. Raghavachari, a. P. Rendell, J. C. Burant, S. S. Iyengar, J. Tomasi, M. Cossi, J. M. Millam, M. Klene, C. Adamo, R. Cammi, J. W. Ochterski, R. L. Martin, K. Morokuma, O. Farkas, J. B. Foresman and D. J. Fox, *Gaussian Inc., Wallingford CT*, 2016, Revision B.01.
47. K. Pierloot, in *Computational Organometallic Chemistry*, ed. T. R. Cundari, Marcel Dekker, Inc., New York, 2001, pp. 123–158.
48. K. Andersson and B. O. Roos, *Chem. Phys. Lett.,* 1992, **191**, 507–514.
49. D. A. McQuarrie and J. D. Simon, *Physical Chemistry: A Molecular Approach*, University Science Books, Sausalito, 1997.

CHAPTER 5

Study of Dinuclear Fe(II)-Based Spin-Crossover Metal-Organic Cages

5.1. Introduction

Metal-organic cages (MOCs)[1–7] have demonstrated significant potential in molecular recognition,[8–11] guest stabilization,[12,13] and catalysis.[14–21] These applications depend on the ability of the cage cavities to host guests.[22–33] The guest-binding capability is influenced by several factors, including the size and shape compatibility between the host cavity and the guest,[34,35] charge complementarity,[36–38] hydrophobic effects,[39] and the cavity enclosure.[40] In MOCs, these properties are primarily determined by the organic ligands that form the host structure. Additionally, the metal vertices play a crucial role since metal ions with different radii can fine-tune the cavity volume, affecting the affinity for different guests. For a given metal, oxidation states can alter the overall charge of the host, thereby influencing its guest-binding properties.[41,42]

As mentioned in previous sections, certain transition metal ions, especially Fe(II) in an octahedral coordination environment, can exist in either a diamagnetic low-spin (LS) state or a paramagnetic high-spin (HS) state. Spin-crossover (SCO) between these two states can be induced by external stimuli like temperature,[43] pressure[44–46] or electromagnetic radiation.[47–52] However, extensive research in the field has expanded the range to include other metals and oxidation states such as Cr(II),[53–66] Mn(III),[67–70] Mn(II),[71–73] Fe(III),[74–86] Co(II),[87–92] and Ni(II)[93–97] along with various coordination numbers, donor atoms, and geometries.[98,99] Additionally, more complex SCO molecules featuring multiple metal centres, extending to 2D and 3D systems, have also been reported over the last years.[100–106]

There has been a growing surge of interest in discrete polynuclear SCO systems due to their potential application in multifunctional devices.[107,108] The number of systems exhibiting SCO with multiple metal centres has notably increased in recent years.[109–112] This opens exciting possibilities, since each metal centre can undergo its own spin transition, leading to multistep transitions. Additionally, some can even act as hosts for guest molecules adjusting the SCO properties shifting the value of $T_{1/2}$ depending on the guest nature, making these molecules ideal candidates for sensing applications.[113] These unique properties make them promising candidates for the development of nanoscale-based sensor devices.[114] The presence of SCO in cages enhances their potential applications, this dual behaviour makes these systems ideal candidates for molecular-level switches and hence there has been significant interest in studying and designing new SCO-based materials for applications in data storage, display devices, molecular sensors, and other nanotechnological uses.[107,115–118]

In this chapter, we will introduce a computational study in which we examine how ligand functionalization and guest effects influence the transition temperature ($T_{1/2}$) and the SCO behaviour (one- or two-step transitions) in the $[Fe_2(L_1^R)_3]^{4+}@X^-$ family of MOCs, where L_1 = 1,3-bis-(3-(pyridin-2-yl)-1*H*-pyrazol-5-yl)benzene, X^- = H^-, F^-, Cl^-, Br^-, I^-, or $[BF_4]^-$, and R = H, F, or CH_3, using the TPSSh[119,120]/TZVP[121,122] method. This new family of MOCs featuring two Fe(II) metal centres that can undergo SCO behaviour was reported first by Darawsheh *et al.*[123] in 2016, and use the bis-chelating ligand to form a Fe(II) dinuclear species ([Fe_2]) capable of encapsulating different halides (Cl^-, Br^-).

Our findings show that ligand functionalization with electron-donor or electron-withdrawing groups can significantly impact $T_{1/2}$, and the guest effect on lowering $T_{1/2}$ shows a linear correlation with increasing guest size. Additionally, smaller guests tend to move away from the cavity centre, enhancing the two-step nature of the transition. These observations can be explained by analysing the electronic structure of the systems in terms of relevant d-based molecular orbitals. These insights can aid in the rational design of new MOCs that can act as sensors at specific temperatures, therefore accelerating the development of new spin-crossover devices with tailored properties.[124]

5.2. Experimentally Reported d^6-Fe(II) Based Spin-Crossover [Fe_2] Metal-Organic Cages

The first two-step spin transition presented by a polynuclear system was reported by Real and co-workers[125] in 1992, and it consisted in an iron(II) dinuclear compound: $[Fe(bt)(NCS)_2]_2$bpym (bt: 2,2'-bi-2-thiazoline, bpym: 2,2'-bipyrimidine).

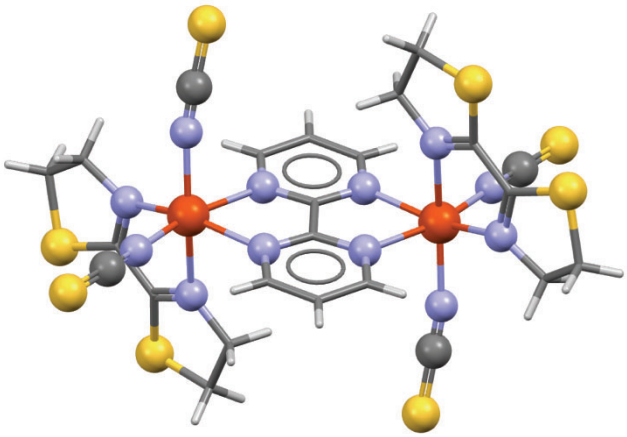

Figure 5.1. $Fe(bt)(NCS)_2]_2$bpym with bt: 2,2'-bi-2-thiazoline and bpym: 2,2'-bipyrimidine. Orange: Fe, violet: N, gray: C, white: H, yellow: S.

Their studies showed an overall $S = 2$ (high-spin, HS) ⇄ $S = 0$ (low-spin, LS) SCO behaviour, with the transition taking place in two steps. That is, they could observe two transition temperatures related to each step:

- Step 1: [LS-LS] ⇄ [HS-LS] with $T_{1/2}$ ~ 163 K.
- Step 2: [HS-LS] ⇄ [HS-HS] with $T_{1/2}$ ~ 197 K.

As can be seen from Figure 5.1, despite this dinuclear system does not belong to the MOC family, the $[Fe(bt)(NCS)_2]_2$bpym molecule and the study of its multistep transition was used as a starting point to construct our software to calculate the transition temperatures in dinuclear MOCs, building upon a variation of the Slicher and Drickamer[126] model applied to these systems.

The reported system we based our study on features the 1,3-bis(3-(pyridine-2-yl)-1*H*-pyrazol-5-yl)benzene ligand (L), to form functional $[Fe_2L_3]^{4+}$ metallohelicates.[123]

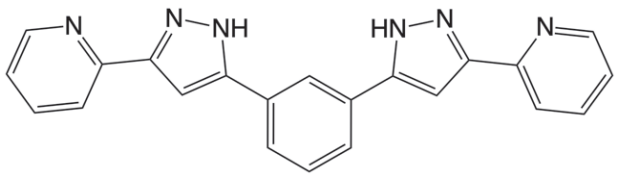

Figure 5.2. 1,3-bis(3-(pyridine-2-yl)-1*H*-pyrazol-5-yl)benzene ligand (L).

Darawsheh *et al.*[123] obtained six derivatives encapsulating chloride or bromide anions. They tried to encapsulate iodide, but the large volume of such anion exceeded the space available inside the cage.

The study revealed that the three possible magnetic states [LS-LS], [HS-LS], and [HS-HS], can be accessed over a wide temperature range due to the structural non-equivalence of the Fe(II) centres. The type of guest (Cl^- vs. Br^-) shifts the $T_{1/2}$ by approximately 40 K. Additionally, metastable [LS-HS] or [HS-HS] states can be induced through irradiation. All helicates $([Fe_2L_3]@X)^{3+}$ remain stable in solution.

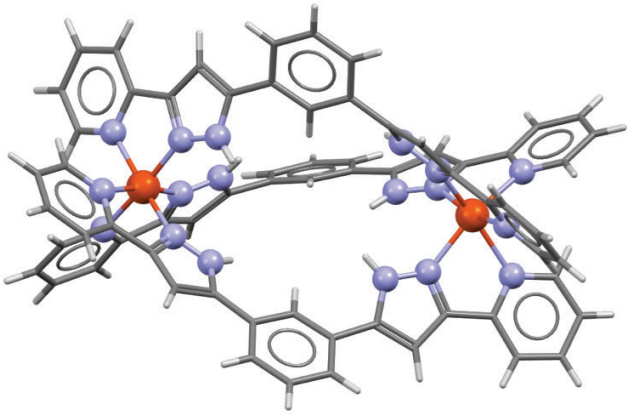

Figure 5.3. $[Fe_2L_3]^{2+}$ metal-organic cage with L = 1,3-bis(3-(pyridine-2-yl)-1*H*-pyrazol-5-yl)benzene. Orange: Fe, violet: N, gray: C, white: H.

Since we based our study in the cage showed in Figure 5.3, we will briefly introduce some other similar dinuclear Fe(II)-based SCO [Fe_2] cages, based on the parent molecule.

In 2017, the same research group developed a structure based on the same ligand as the previous system (Figure 5.2) which forms mononuclear spin-crossover complexes $[FeL_3]^{2+}$ with pendant arms, leading to dimerization through various intermolecular interactions, resulting in supramolecular $([FeL_3]_2@X)^{3+}$ cations (Figure 5.4 and 5.5).[113] These complexes are not exactly dinuclear MOCs *per se*. They consist in two mononuclear subunits attached through intermolecular interactions with a cavity in between, but they are not really a [Fe_2] as defined in the previous reported cage. However, they can encapsulate Cl^-, Br^-, or I^-, allowing for the tuning of magnetic properties both in the solid state and in solution.

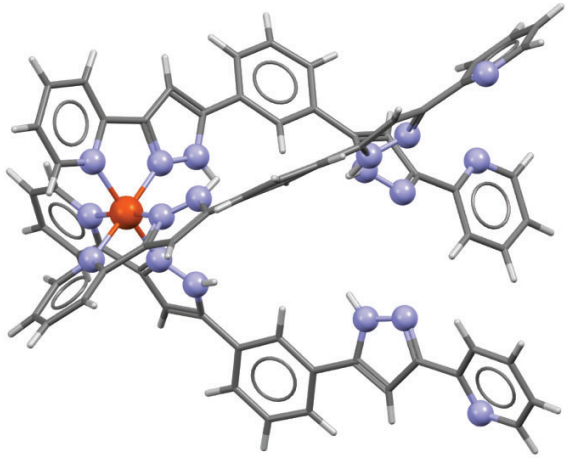

Figure 5.4. Mononuclear subunit $[FeL_3]^{2+}$ with L = 1,3-bis(3-(pyridine-2-yl)-1*H*-pyrazol-5-yl)benzene. Orange: Fe, violet: N, gray: C, white: H.

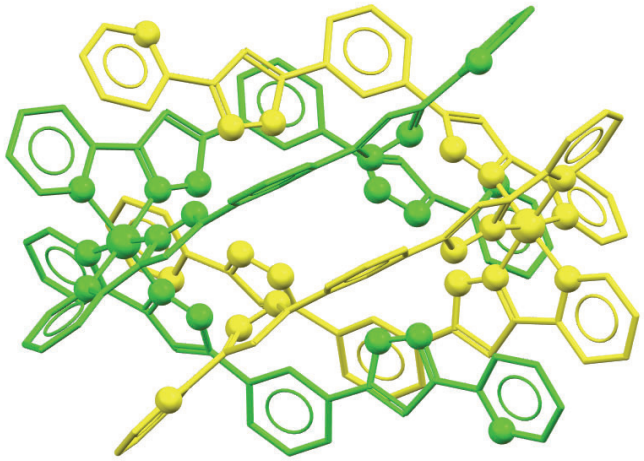

Figure 5.5. Supramolecular $([FeL_3]_2)^{4+}$ cations formed by two mononuclear subunits, one in green and the other one in yellow (hydrogens hidden to better understand the structure).

In 2018, the same research group synthesised a novel coordination $[Fe_2]$ helicate[127] enlarging the ligand used on the previous studies: $[Fe_2L_3]^{4+}$ with L = 3,3'-bis(3-(pyridin-2-yl)-1*H*-pyrazol-5-yl)-1,1'-biphenyl (Figure 5.6).

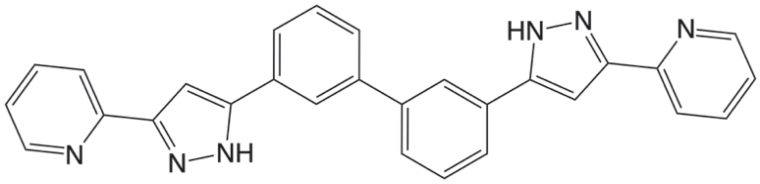

Figure 5.6. 3,3'-bis(3-(pyridin-2-yl)-1*H*-pyrazol-5-yl)-1,1'-biphenyl ligand.

This MOC exhibits SCO and can effectively encapsulate a $[Cr(ox)_3]^{3-}$ (ox = oxalate) complex anion as shown in Figure 5.7, revealing for the first time single-ion slow relaxation of the magnetization for this metal. The dynamics of this relaxation, as well as the performance of the Cr(III) centre as a qubit, can be tuned by generating metastable HS Fe(II) centres in the host through irradiation with green light at low temperatures.

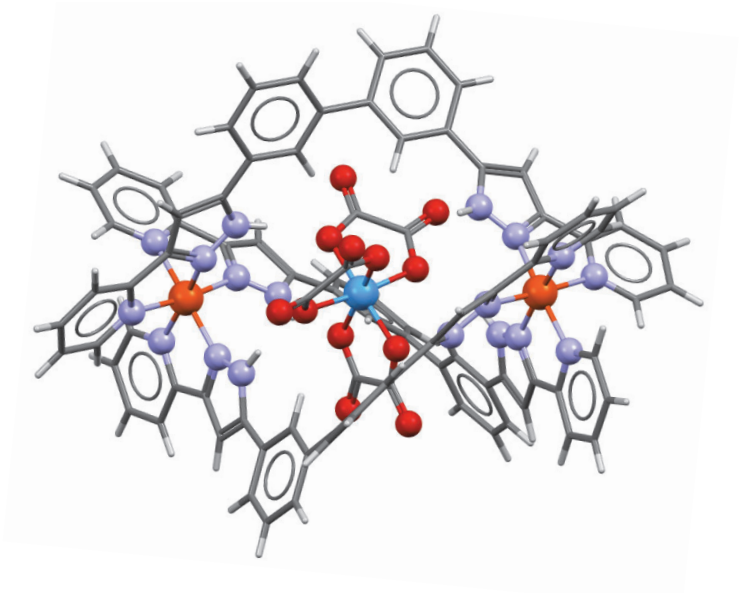

Figure 5.7. $([Fe_2L_3]@[Cr(ox)_3])^+$ with L = 3,3'-bis(3-(pyridin-2-yl)-1*H*-pyrazol-5-yl)-1,1'-biphenyl. Orange: Fe, violet: N, gray: C, white: H, blue: Cr, red: O.

5.3. Computational Study of d^6-Fe(II) Based Spin-Crossover [Fe_2] Metal-Organic Cages

As mentioned, polynuclear SCO metal-organic cages offer a wide range of potential applications, since they can lead to multistep transitions. Moreover, some of these systems can encapsulate guests inside their cavity, which can alter the SCO properties of the MOCs. However, the mechanism behind the host-guest interaction in adjusting $T_{1/2}$ is not well understood, which somewhat restricts the potential use of these systems as molecular-level sensors. To address this, we developed a computational study of the $([Fe_2(L_1^R)_3]@X)^{3+}$ family (L_1 = 1,3-bis-(3-(pyridin-2-yl)-1*H*-pyrazol-5-yl)benzene, X = H^-, F^-, Cl^-, Br^-, I^-, and $[BF_4]^-$, R = H, F, and CH_3) to analyse the origin of this tuning behaviour. We aimed to understand the impact of guest molecules and ligand functionalization on the system's overall electronic structure and its implications for the single-step or two-step transitions observed in these dinuclear systems.

5.3.1. Computational Details

All DFT calculations were performed using the Gaussian 16 (Revision B.01) electronic structure suite.[128] The calculations were converged to 10^{-8} for the density matrix elements and vibrational analysis was performed to ensure that the structures were minima on the potential energy surface (PES). A triple-ζ basis set with polarization functions (TZVP)[129,130] was used

for all elements, providing a good balance between computational cost and accuracy. The TPSSh[119,120] exchange-correlation functional was used for all systems because it has recently been reported to be the most accurate for spin-state energy gaps in d^4 to d^7 transition metal ions.[131–134] However, the calculation of these energies with DFT methods remains challenging.[131,135,136]

To address this, a benchmark study (see next section) was carried out on the mononuclear $[Fe(L_2^R)_3]^{2+}$ system (L_2 = 3-(2-pyridyl)pyrazole), which closely mimics the coordination environment of the dinuclear cage, and the TPSSh was the functional selected to carry out the calculations for the dinuclear $[Fe_2]$ cage.

Different spin topologies were generated using the fragments option in the Gaussian 16 code to study the dinuclear cages. To compute the transition temperatures, we used an in-house Python code (version 3.8.3)[137] that build on the Slichter and Driackamer model[125,126] applied to dinuclear species. This will be explained later in the chapter (section 5.3.4).

To study the d-MO energy gap, N-Electron Valence Perturbation Theory (NEVPT2)[138] calculations were performed using Orca 4.0.[139] The Def2-TZVPP[129,130] basis set, along with the corresponding auxiliary basis set for correlation and Coulomb fitting were used in these calculations. The active space included the 5 d-orbitals of the metal and 6 electrons. The *ab initio* ligand field theory (AILFT)[140] approach was employed to compute the splitting between the antibonding and non-bonding sets of d-based MOs.

Continuous Shape Measures (CShM)[141,142] were performed using SHAPE (version 2.1)[143] to quantify distortions in octahedral geometries.

5.3.2. Density Functional Theory Benchmarking for the $[Fe(L_2)_3]^{2+}$ Mononuclear System

The calculations for the dinuclear system are computationally expensive, hence, we reduced the system size to only one metal centre with three L_2 ligands, L_2 = 3-(2-pyridyl)pyrazole, abbreviated usually as 3ppH in the literature, which properly mimics the coordination environment of the parent system (Figure 5.8).

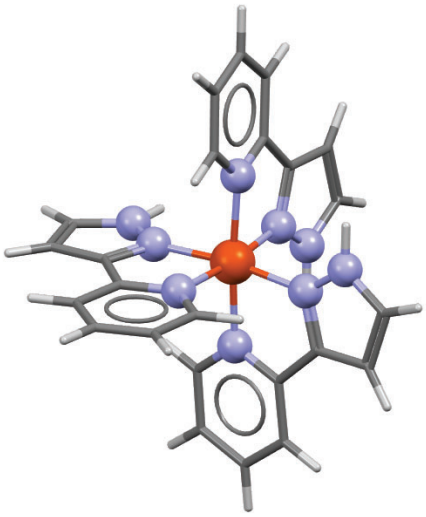

Figure 5.8. $[Fe(L_2)_3]^{2+}$ mononuclear system with L_2 = 3-(2-pyridyl)pyrazole. Orange: Fe, violet: N, gray: C, white: H.

Table 5.1. Computed ΔE, ΔH, ΔS and $T_{1/2}$ for the $[Fe(L_2^R)_3]^{2+}$ with L_2 = 3-(2-pyridyl)pyrazole. Electronic energies and enthalpies in kcal·mol^{-1}. Entropies in cal·mol^{-1}·K^{-1} and all temperatures in K.

Method	ΔE/kcal·mol^{-1}	ΔH/kcal·mol^{-1}	ΔS/cal·mol^{-1}·K^{-1}	$T_{1/2}$/K
TPSSh	10.28	9.45	18.577	509
OPBE	5.67	4.84	20.208	239
OLYP	1.70	0.88	20.913	42
B3LYP	-2.87	-3.64	18.415	-198
B3LYP*	4.05	3.31	18.987	174
M06L	4.18	3.46	18.367	188

The transition of this mononuclear system was reported in 1999 by Harimanow *et al.*[144] It was observed that the transition for the $[Fe(3ppH)_3][CF_3SO_3]_2{\cdot}2H_2O$ is continuous and centered above room temperature while that in the anhydrous triflate salt is discontinuous and centered below room temperature with a thermal hysteresis loop of width 12 K, $T_{1/2}\downarrow$ = 229 K and $T_{1/2}\uparrow$ = 241 K.

Table 5.2. Experimental values for different $[Fe_2(L_1)_3]^{4+}$ systems with L_1 = 1,3-bis(3-(pyridine-2-yl)-1*H*-pyrazol-5-yl)benzene reported systems. All structures recovered from Ref.[123]

System	$T_{1/2}$/K		Refcode[145]
	Magnetic susceptibility	Calorimetry studies	
$Cl@[Fe_2(L_1)_3]Cl(PF_6)_2 \cdot 5.7CH_3OH$	305	302.1(3)	INUGIJ
$Br@[Fe_2(L_1)_3]Br(PF_6)_2 \cdot 4CH_3OH$	265	258.2(3)	INUJOS
$Cl@[Fe_2(L_1)_3]Cl(PF_6)_2 \cdot 3CH_3OH \cdot H_2O$	160, 265	185.0(3), 258.9(3)	INUPEO
$Br@[Fe_2(L_1)_3]Br(PF_6)_2 \cdot CH_3OH \cdot H_2O$	≈ 200 gradual	≈ 200 gradual	INUFII
$Cl@[Fe_2(L_1)_3](I_3)_3 \cdot 3Et_2O$	–	–	INUGAB
$Br@[Fe_2(L_1)_3](I_3)_3 \cdot 3Et_2O$	–	–	INUGEF

In the experimental reported systems (Table 5.2), the transitions of INUGIJ and INUJOS are from [HS-HS] to [HS-LS] states when cooling, and INUPEO shows a two-step transition upon cooling ([HS-HS] to [HS-LS] and [HS-LS] to [LS-LS]).

The asymmetric structure of INUGIJ causes its Fe(II) centres to be in two different spin-states at 100 K, and the asymmetric structure of INUPEO shows non-equivalent Fe(II) centres, and that causes a two-step transition arising from the slightly different magnetic behaviour of each metal site in the helicate. In contrast, INUFII shows a gradual, nearly complete SCO (about 85% completion) with $T_{1/2}$ around 200 K.

The results showed that only TPSSh and OPBE,[146,147] another functional known to accurately calculate spin-state energy gaps,[136,147] provided the correct spin-state energy gap. Ultimately, the TPSSh functional, a hybrid version of the TPSS[119] meta-GGA functional with 10% accurate Hartree–Fock exchange, was selected for its overall performance on SCO systems.[131–134] In addition, TPSSh has demonstrated the ability to correlate $T_{1/2}$ trends with the underlying electronic structure, which is crucial for the rational design of new SCO systems with tailored properties.[133,148,149]

5.3.3. Functionalization of the $[Fe(L_2^R)_3]^{2+}$ Mononuclear System

To decide which functionalizations add to the $[Fe_2]$ cages, we functionalized the mononuclear system since allows us to more quickly study the effect of ligand functionalization

over the Fe(II) metal centre. We added EDGs and EWGs, as shown in Figure 5.9, in different positions (R_1, R_2 and R_1R_2 simultaneously) to see how this affects the $T_{1/2}$, with R = –OCH_3, –CH_3, –H, –F, and –Cl. For this particular case, in which there is only one metal centre, the only possible transition is from the LS ($S = 0$) to the HS ($S = 2$).

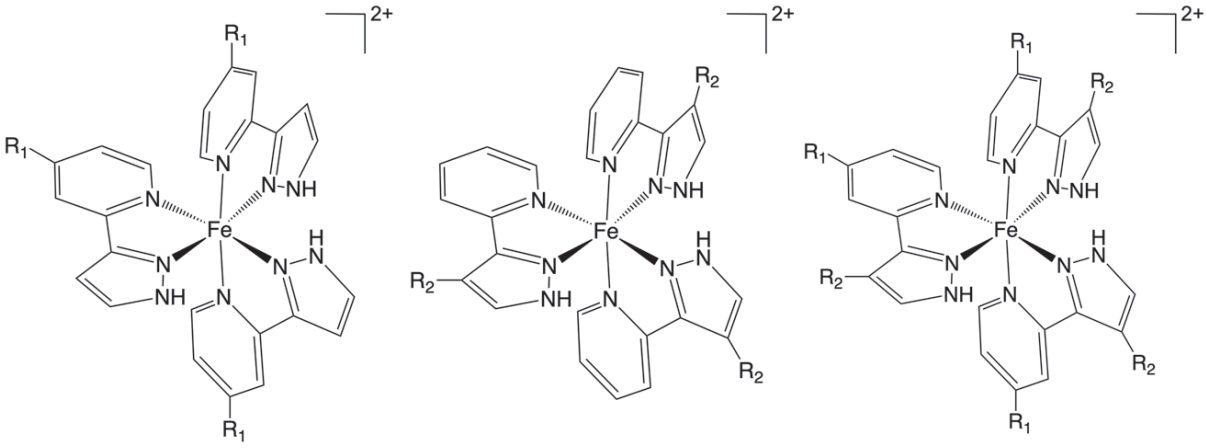

Figure 5.9. Scheme of the functionalized positions of the mononuclear system, with R = –OCH_3, –CH_3, –H, –F, and –Cl.

Table 5.3. Computed results for the functionalization of the mononuclear $[Fe(L_2^R)_3]^{2+}$ system. All energies and enthalpies in kcal·mol^{-1}, entropies in cal·mol^{-1}·K^{-1} and temperatures in K.

$[Fe(L_2^R)_3]^{2+}$		ΔE/kcal·mol^{-1}	ΔH/kcal·mol^{-1}	ΔS/cal·mol^{-1}·K^{-1}	$T_{1/2}$/K
	R_1	9.16	8.45	18.073	467
–OCH_3	R_2	10.80	10.00	17.676	566
	R_1R_2	9.50	8.84	16.917	523
	R_1	10.27	9.45	18.915	500
–CH_3	R_2	11.75	10.99	18.060	609
	R_1R_2	11.91	11.13	17.933	621
–H	R_1R_2	10.28	9.45	18.577	509
	R_1	9.09	8.31	18.486	450
–F	R_2	9.19	8.48	17.757	477
	R_1R_2	7.79	7.13	17.496	408
	R_1	9.64	8.85	18.518	478
–Cl	R_2	10.93	10.19	20.060	508
	R_1R_2	10.04	9.39	17.643	532

Results for the thermochemistry data and computed transition temperatures are listed in Table 5.3. Functionalization with R groups significantly impacts the ligand field and, consequently, the $T_{1/2}$. This indicates that the thermochemistry of the dinuclear $[Fe_2(L_1)_3]^{4+}$ can be tuned by modifying the L_1 ligand.

The computed data for this mononuclear system is in good agreement with the available results for R = H.[144] The influence of substituents at the *para* position of the pyridyl or pyrazole ring has been explored by various researchers across different systems.[150–154] This includes studies on Fe(III) SCO complexes.[155,156] Thus, we studied the effect of functionalizing only the pyridyl or pyrazole ring in the mononuclear system.

We conducted an in-depth analysis of the different role that ligand functionalization has on the $T_{1/2}$, and compared it with the current available data.[150–156] We compiled published literature on similar systems and analysed the data, making clear that functionalization of the pyridyl ring (R_1), although can be correlated with the σ_p^+ Hammett parameter[157–159] for the bpp ligand (bpp = 2,6-di(pyrazol-1-yl)pyridine),[154] correlates, at least for the tested substituents (–H, –F, –Cl, –Br, –I, $–CH_3$ and –OMe), much better with the electronegativity of the atom attached to the *para* position. This can be seen in the following plots, which have been generated from the corresponding published data. This data seems to point out that the *para*-functionalization of the ring essentially increases or reduces the Lewis base character of this donor group.

Table 5.4. Experimental transition temperatures ($T_{1/2}$) in Kelvin, electronegativities (χ) and *para* Hammett parameter (σ_p^+) for different systems with similar ligands (bpp,[154] thio-pybox,[153] 1,4-benzoquinone derivatives[150]) as the computed one $L_2^{R_1}$. L_2 = 3-(2-pyridyl)pyrazole, bpp = 2,6-di(pyrazol-1-yl)pyridine and thio-pybox = 2,6-bis(4,4-dimethyl-4,5-dihydrothiazol-2-yl)pyridine.

			$T_{1/2}$/K			
R_1	**χ**	**σ_p^+**	**bpp**	**thio-pybox**	**1,4-benzoquinone**	**Computed L_2^{R1}**
–H	2.20	0.00	248	239	160	509
–Me	2.55	-0.31	216	–	–	500
–OMe	3.44	-0.78	158	–	–	467
–F	3.98	-0.07	215	–	110	450
–Cl	3.16	0.11	226	223	121	478
–Br	2.96	0.15	–	229	124	–
–I	2.66	0.14	–	234	–	–

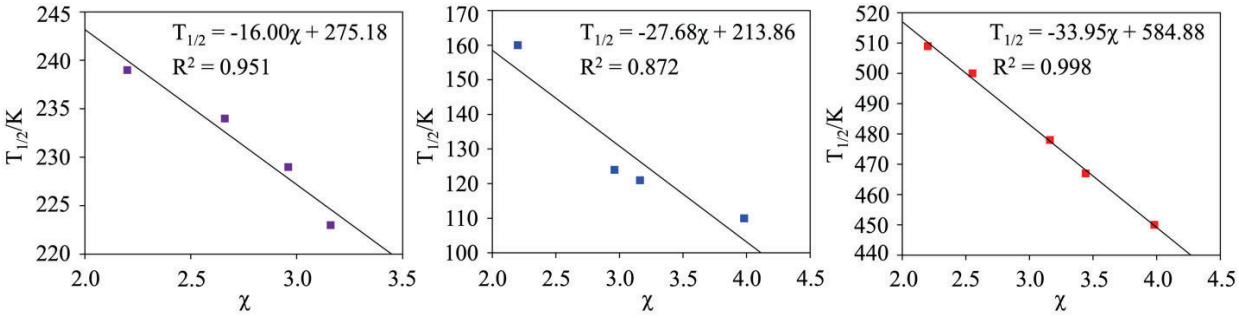

Figure 5.10. Correlation between the electronegativity of the atom in *para* and the experimental $T_{1/2}$ for thio-pybox[153] (left) and 1,4-benzoquinone[150] (centre), and computed $T_{1/2}$ for the $[Fe(L_2^{R_1})_3]^{2+}$ with L_2 = 3-(2-pyridyl)pyrazole, with the pyridyl ring functionalized (right, this work), respectively.

As the electronegativity of the atom in the *para* position increases, it decreases the electron density on the N atom of the ring, thereby weakening its σ-donor abilities (inductive effect). In turn, this reduces the metal-ligand antibonding interaction, since we are weakening the ligand field around the metal centre, an effect that has been observed in other systems as well.[150,153] That is why more electronegative substituents lead to lower $T_{1/2}$. However, functionalization with methyl groups has very little effect compared to hydrogen. Since this substituent is in the *para* position, low resonance effects are expected.

A different situation is the functionalization of the pyrazole ring (R_2). In that case, and similarly as it happens with the bpp ligand,[154] the ring functionalization correlates much better with the σ_m Hammett parameter[157–159] than with the electronegativity (Figure 5.11). Thus, the pyrazole ring modulates $T_{1/2}$ *via* resonance effects rather than electronegativity ones.

Table 5.5. Experimental transition temperatures ($T_{1/2}$) in Kelvin, and *meta* Hammett parameter (σ_m) for a system with similar ligand (bpp[154]) as the computed one (L_2^{R2}, L_2 = 3-(2-pyridyl)pyrazole).

R_2	σ_m	bpp	Computed L_2^{R2}
–H	0.00	248	509
–Me	-0.069	273	609
–OMe	0.115	–	566
–F	0.337	–	477
–Cl	0.373	231	508

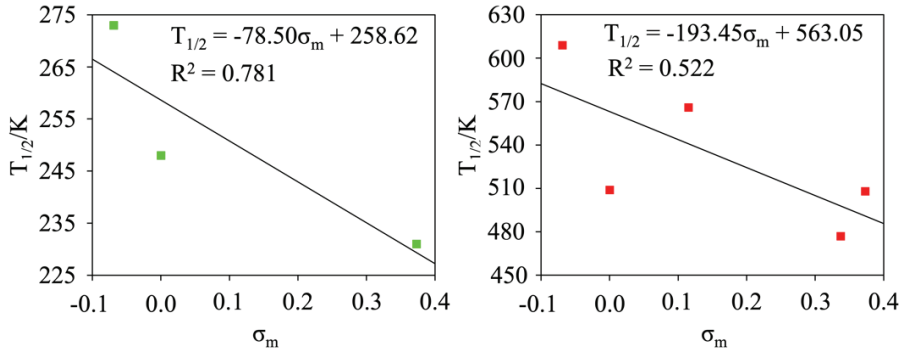

Figure 5.11. Correlation between the Hammett *meta*-parameter (σ_m) and the experimental $T_{1/2}$ for the bpp ligand[154] (left) and the computed $T_{1/2}$ and Hammett constant (σ_m) for the $[Fe(L_2^{R_2})_3]^{2+}$ with L_2 = 3-(2-pyridyl)pyrazole, with the pyrazole ring functionalized (right, this work).

Functionalization of the pyrazole ring has larger resonance effects, which show a better correlation with the σ_m Hammett parameters than with the substituent's electronegativity. This results in EDGs, such as methyl, increasing the ligand field around the metal centre, leading to an increase in $T_{1/2}$, while EWG, such as fluorine, have the opposite effect. This effect is much more pronounced compared to that observed in the pyridyl group, and methyl functionalization of the pyrazole ring significantly increases $T_{1/2}$ compared with the subtle effect that has the methyl functionalization of the pyridyl on such quantity.

From the above, one would expect therefore than pyrazole functionalization with methyl groups should rise the $T_{1/2}$, while pyridyl functionalization with the same substituent should have a less pronounced effect, as the electronegativities of H and C become similar. To evaluate this, we computed the spin-state energy differences ($\Delta E_{[HS\text{-}HS]-[LS\text{-}LS]}$) for the dinuclear systems with only pyridyl or pyrazole functionalization (with $-CH_3$ and –F because they generate the lowest and highest spin-state energy gap for the mononuclear system). The computed energies do indeed support this hypothesis, this is, methyl functionalization leads to higher $T_{1/2}$, but if this functionalization occurs in the pyridyl ring, the increase in $T_{1/2}$ is less pronounced than if this functionalization occurs in the pyrazole ring. We also computed the dinuclear systems with I^- as guest, to validate that, indeed, the decrease in the $T_{1/2}$ as the guest size increases is kept even if we only functionalize the pyridyl or the pyrazole ring (Table 5.6).

Table 5.6. Computed energy differences for the dinuclear system (empty and with I^-) with different substitutions: R_1 (pyridyl ring), R_2 (pyrazole ring) and R_1R_2 (both rings) with $–CH_3$ and –F.

	ΔE/kcal·mol^{-1}					
	$[Fe_2(L_1)_3]^{4+}$			$([Fe_2(L_1)_3]@I)^{3+}$		
R	**Pyridyl (R_1)**	**Pyrazole (R_2)**	**Both (R_1R_2)**	**Pyridyl (R_1)**	**Pyrazole (R_2)**	**Both (R_1R_2)**
$–CH_3$	17.73	22.60	22.75	8.67	14.72	14.72
–H	17.61	17.61	17.61	8.70	8.70	8.70
–F	15.18	14.77	12.29	6.43	6.18	3.84

5.3.4. Computation of the Transition Temperatures of the Dinuclear [Fe_2] Cages

Before showing the results for the dinuclear cages, we need to introduce how the transition temperatures were computed.

Among the several theoretical models developed to study multi-step spin-crossover transitions in mononuclear systems, including those based on elastic interactions[160,161] and microscopic Ising-like models,[162] the Slichter and Drickamer[126] approach stands out due to its ease of implementation in software. Furthermore, this model has been shown to work effectively for dinuclear systems in previous studies.[125,148]

We developed an in-house Python code to model the transition curve for a dinuclear SCO system. The purpose of the code is to model the transition curve for a dinuclear SCO system. To achieve this, we used a variant of the Slichter and Drickamer[125,126] model tailored for a dinuclear system. In this approach, the Gibbs free energy can be calculated as follows:

$$G = xG_{SS} + yG_{SQ} + zG_{QQ} + \Gamma(x, y, z) - TS_{mix} \tag{5.1}$$

where x, y and z are the molar fractions of the [LS-LS] (singlet-singlet, SS), [LS-HS] (singlet-quintet, SQ) and [HS-HS] (quintet-quintet, QQ) states, respectively. G_{SS}, G_{SQ}, and G_{QQ} are their Gibbs free energy on the pure phases. Γ is a function related to the intermolecular interactions between cells and is defined as

$$\Gamma(x, y, z) = \gamma(xy + \alpha yz + \beta zx) \tag{5.2}$$

In the Slichter and Drickamer model, it is assumed that the interaction occurs between a metal in the HS state and another metal in the LS state. γ is the interaction parameter between SS–SQ molecules, $\alpha\gamma$ between SQ–QQ, and $\beta\gamma$ between SS–QQ. We assume that only the interactions between S and Q iron(II) that belong to two different dinuclear species occur in $\Gamma(x,y,z)$.[125] Consequently, the interaction between SS–SQ is equal to SQ–QQ and twice that of SS–QQ. Based on this assumption, $\alpha = 1$ and $\beta = 2$.

S_{mix}, defined as the mixing entropy, accounts for the system being in a mixed phase rather than a pure phase. This mixing entropy can be expressed as:

$$\begin{aligned} S_{mix} &= k_B(N\ \ln N - Nx\ln Nx - Ny\ln Ny - Nz\ln Nz) \\ &= -R(x\ln x + y\ln y + z\ln z) \end{aligned} \tag{5.3}$$

Therefore, the expression of the Gibbs free energy becomes:

$$G = xG_{SS} + yG_{SQ} + zG_{QQ} + \gamma(xy + \alpha yz + \beta zx) + RT(x\ln x + y\ln y + z\ln z) \tag{5.4}$$

Assuming that the state SS is taken as both the enthalpy and entropy origin, and that $\alpha = 1$ and $\beta = 2$, the expression becomes:

$$\begin{aligned} \Delta G = y(\Delta H_1 - T\Delta S_1) + z(\Delta H - T\Delta S) + \gamma(xy + yz + 2zx) + \\ RT(x\ln x + y\ln y + z\ln z) \end{aligned} \tag{5.5}$$

Where ΔH_1 and ΔS_1 are the enthalpy and entropy difference from SS to SQ and ΔH and ΔS are the enthalpy and entropy difference from SS to QQ. The equilibrium conditions of this system are:

$$\begin{cases} x + y + z = 1 \\ \left(\dfrac{\partial \Delta G(x,y)}{\partial x}\right)_T = 0 \\ \left(\dfrac{\partial \Delta G(x,y)}{\partial y}\right)_T = 0 \end{cases} \tag{5.6}$$

The problem has no analytical solution, hence, the equilibrium conditions have been solved at various temperatures, obtaining the x, y and z values that satisfy the conditions for each temperature. In that way, $x = f(T)$, $y = f(T)$ and $z = f(T)$ are obtained. To use the code, one just

needs to specify the ΔS, ΔS_1, ΔH, γ, and W. W is another way to introduce ΔH_1 as it is defined as follows:

$$W = \Delta H_1 - \frac{\Delta H}{2} \tag{5.7}$$

The temperature at which $x(T) = y(T)$ corresponds to that of the first step, that is, the transition SS–SQ, and when $y(T) = z(T)$ the temperature corresponds to that of the second step, that is, SQ–QQ. Logically, when $x(T) = z(T)$, we obtain the transition temperature for the SS–QQ transition.

To determine the effective magnetic moment at each temperature, we multiply 4.9 μ_B (the spin-only value for a Fe^{2+} ion with 4 unpaired electrons) by the y value and add it two times 4.9 μ_B multiplied by the z molar fraction (since QQ contains two iron ions in the high-spin state, while SQ contains only one). Thus, μ_{eff} can be estimated using the following expression:

$$\mu_{eff}(T) = 4.9\big(y(T) + 2z(T)\big) \tag{5.8}$$

If $\partial\mu_{eff}/\partial T$ has two maxima, we assume a two-step transition, if it only has one maximum, we say we have a one-step transition.

We defined another parameter, ρ, as

$$\rho = \frac{2W}{\Delta H} \tag{5.9}$$

which quantifies the stabilisation of the intermediate spin-state SQ (Figure 5.12): if ΔH_1 does not lay right at $\Delta H/2$, the intermediate spin-state can be stabilised or not. The SQ will be stabilised if ΔH_1 lays below $\Delta H/2$, and hence, W take negative values (Eq. 5.7). If ΔH_1 lays above $\Delta H/2$, W is positive and SQ is destabilised. Therefore, based on Eq. 5.9, for systems with $\rho < 0$, a two-step transition in principle, is expected, and two transition temperatures have been computed.[125]

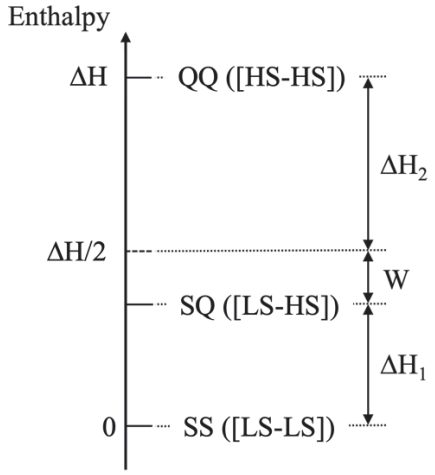

Figure 5.12. Schematic representation of the enthalpies involved in the process.

While this model is effective, it is important to point out that it does not fully consider the behaviour at extremely low and high temperatures. At these extremes, the system tends to stay primarily in either the low-spin or high-spin state. Despite this limitation, the model still provides an accurate picture of the magnetic properties for the studied systems.

5.3.5. Functionalization of the $[Fe_2(L_1^R)_3]^{4+}$ Dinuclear System

The research began by checking whether electronic structure methods could accurately model the empty MOC $[Fe_2(L_1^R)_3]^{4+}$ with L_1 = 1,3-bis-(3-(pyridin-2-yl)-1*H*-pyrazol-5-yl)benzene. The system has three possible spin-state configurations for its iron(II) centres:

- [HS-HS] configuration: both iron(II) in the high-spin state.
- [HS-LS] configuration: one iron(II) in the high-spin state and the other in the low-spin state.
- [LS-LS] configuration: both iron(II) in the low-spin state.

Our calculations successfully confirmed that the chosen computational method correctly reproduces the relative ordering of the different spin states: as shown in Table 5.7, the molecule with both metal centres in the low-spin state ([LS-LS]) has the lowest energy, followed by the configuration with one metal in each spin state ([HS-LS]), and finally, the most energetic one in which both metals are in the high-spin state ([HS-HS]).

Table 5.7. Enthalpy changes for the [LS-LS] to [HS-HS] transition (ΔH), [LS-LS] to [HS-LS] transition (ΔH_1) and [HS-LS] to [HS-HS] transition (ΔH_2), W and ρ parameters, and computed transition temperatures ($T_{1/2}$) for the dinuclear $[Fe_2(L_1^R)_3]^{4+}$ empty cages (R = $-CH_3$, –H and –F). All enthalpies in kcal·mol^{-1}, and all temperatures in Kelvin.

$[Fe_2(L_1^R)_3]^{4+}$	ΔH/kcal·mol^{-1}	ΔH_1/kcal·mol^{-1}	ΔH_2/kcal·mol^{-1}	W/kcal·mol^{-1}	ρ	$T_{1/2}$/K
$-CH_3$	22.63	11.33	11.30	0.01	0.00	688
–H	17.79	8.94	8.85	0.04	0.00	502
–F	12.98	6.53	6.45	0.04	0.01	368

After that, we added the substituents that generated the lowest (–F) and highest ($-CH_3$) spin-state for the mononuclear system. As observed for the mononuclear system, the effect of the substituents (both rings are functionalized) produces an increasing trend of the $T_{1/2}$: $[Fe_2(L_1^F)_3]^{4+} < [Fe_2(L_1^H)_3]^{4+} < [Fe_2(L_1^{CH_3})_3]^{4+}$.

To further investigate the origins of these effects, we computed the magnitudes of the d-based molecular orbitals using the AILFT method to process outputs from NEVPT2 calculations on the low-spin optimized geometries of the $[Fe_2(L_1^R)_3]^{4+}$ systems (Table 5.8). To compute the ligand-field splitting, Δ_o, at the NEVPT2 level, we reduce the dinuclear structure into two mononuclear ones, using the DFT optimized geometries of the systems and adding H atoms where the ligand is cut (Figure 5.13).

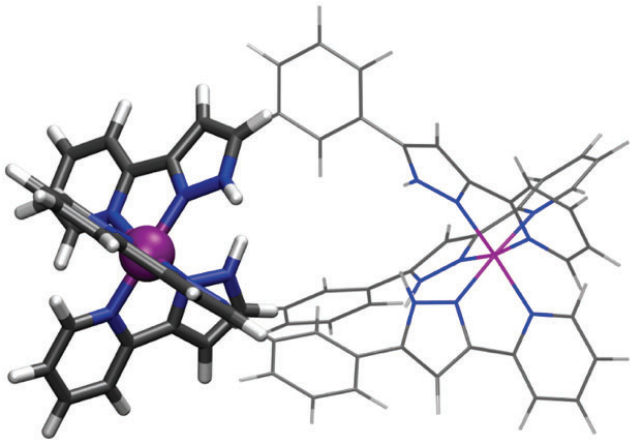

Figure 5.13. Treatment of the molecule to calculate the ligand-field splitting Δ_o at the NEVPT2 level for each Fe(II) centre.

These calculations reveal the ligand field splitting between the antibonding and non-bonding d-based molecular orbitals (average of Fe_1 and Fe_2): 15835 cm^{-1} for $[Fe_2(L_1^F)_3]^{4+}$, 16167 cm^{-1} for $[Fe_2(L_1^H)_3]^{4+}$ and 16651 cm^{-1} for $[Fe_2(L_1^{CH_3})_3]^{4+}$. A detailed examination of the optimized geometries shows that the average Fe–N bond length remains essentially unchanged by L_1 functionalization. This indicates that the tuning effect of the R group on $T_{1/2}$ is purely electronic.

Table 5.8. d-MO splitting for the functionalized system without guest $[Fe_2(L_1^R)_3]^{4+}$ with R = –F, –H and $–CH_3$.

$[Fe_2(L_1^R)_3]^{4+}$	Δ_o/cm^{-1}	
	Fe_1	**Fe_2**
–F	15838	15832
–H	16175	16158
$–CH_3$	16655	16648

5.3.6. Introducing Anionic Guests into the $[Fe_2(L_1^R)_3]^{4+}$ Dinuclear System

After computing the empty cage, we wanted to know how several guests affect the transitions, since it has been experimentally reported that different guest molecules are able to tune the transition temperatures in this type of MOCs. Hence, we performed different calculations with guests of different size to understand what the origin of the observed behaviours is. We did this for the non-functionalized system (Table 5.9), and for the systems with –F (Table 5.10) and $–CH_3$ (Table 5.11) functionalizations.

The transition temperatures obtained are larger than those reported experimentally, a common issue that has systematically been observed when using the TPSSh method for computing such quantity for SCO systems.[131,148,149,163] However, the calculated $T_{1/2}$ values are still within an acceptable range (Table 5.9). It is important to note that the stability of the intermediate spin state (where one iron is high-spin and the other is low-spin, [HS-LS]) plays a role in determining whether a dinuclear Fe(II) SCO system undergoes a single- or two-step transition. The strength of this effect can be measured using the W and ρ parameters.

Table 5.9. Enthalpy changes for the [LS-LS] to [HS-HS] transition (ΔH), [LS-LS] to [HS-LS] transition (ΔH_1) and [HS-LS] to [HS-HS] transition (ΔH_2), W and ρ parameters, and computed transition temperatures ($T_{1/2}$) for the dinuclear $([Fe_2(L_1^H)_3]@X)^{3+}$ cages (X = H^-, F^-, Cl^-, Br^-, I^- and $[BF_4]^-$). For two-step transitions, both temperature values are provided. All enthalpies in kcal·mol^{-1}, and all temperatures in Kelvin.

$([Fe_2(L_1^H)_3]@X)^{3+}$	ΔH/kcal·mol^{-1}	ΔH_1/kcal·mol^{-1}	ΔH_2/kcal·mol^{-1}	W/kcal·mol^{-1}	ρ	$T_{1/2}$/K
–	17.79	8.94	8.85	0.04	0.00	502
H^-	15.84	5.84	10.00	-2.08	-0.26	301, 608
F^-	15.21	5.27	9.94	-2.33	-0.31	288, 563
Cl^-	14.20	6.68	7.52	-0.42	-0.06	372
Br^-	12.62	6.06	6.55	-0.24	-0.04	337
I^-	9.95	4.68	5.27	-0.30	-0.06	263
$[BF_4]^-$	10.52	5.12	5.40	-0.14	-0.03	285

Table 5.10. Enthalpy changes for the [LS-LS] to [HS-HS] transition (ΔH), [LS-LS] to [HS-LS] transition (ΔH_1) and [HS-LS] to [HS-HS] transition (ΔH_2), W and ρ parameters, and computed transition temperatures ($T_{1/2}$) for the dinuclear $([Fe_2(L_1^F)_3]@X)^{3+}$ cages (X = H^-, F^-, Cl^-, Br^-, I^- and $[BF_4]^-$). For two-step transitions, both temperature values are provided. All enthalpies in kcal·mol^{-1}, and all temperatures in Kelvin.

$([Fe_2(L_1^F)_3]@X)^{3+}$	ΔH/kcal·mol^{-1}	ΔH_1/kcal·mol^{-1}	ΔH_2/kcal·mol^{-1}	W/kcal·mol^{-1}	ρ	$T_{1/2}$/K
–	12.98	6.53	6.45	0.04	0.01	368
H^-	11.13	3.45	7.68	-2.11	-0.38	178, 436
F^-	10.50	2.87	7.63	-2.38	-0.45	149, 451
Cl^-	9.46	4.24	5.22	-0.49	-0.10	250
Br^-	8.00	3.76	4.24	-0.24	-0.06	219
I^-	5.53	2.49	3.04	-0.28	-0.10	154
$[BF_4]^-$	6.26	3.00	3.25	-0.12	-0.04	177

Table 5.11. Enthalpy changes for the [LS-LS] to [HS-HS] transition (ΔH), [LS-LS] to [HS-LS] transition (ΔH_1) and [HS-LS] to [HS-HS] transition (ΔH_2), W and ρ parameters, and computed transition temperatures ($T_{1/2}$) for the dinuclear $([Fe_2(L_1^{CH_3})_3]@X)^{3+}$ cages (X = H^-, F^-, Cl^-, Br^-, I^- and $[BF_4]^-$). All enthalpies in kcal·mol^{-1}, and all temperatures in Kelvin.

$([Fe_2(L_1^{CH_3})_3]@X)^{3+}$	ΔH/kcal·mol^{-1}	ΔH_1/kcal·mol^{-1}	ΔH_2/kcal·mol^{-1}	W/kcal·mol^{-1}	ρ	$T_{1/2}$/K
–	22.63	11.33	11.33	0.01	0.00	688
H^-	22.70	10.06	12.64	-1.29	-0.11	662
F^-	22.16	9.51	12.65	-1.57	-0.14	665
Cl^-	20.98	9.97	11.00	-0.51	-0.05	593
Br^-	18.98	9.07	9.92	-0.42	-0.04	587
I^-	15.96	7.50	8.46	-0.48	-0.06	511
$[BF_4]^-$	15.52	7.26	8.26	-0.50	-0.06	486

The results presented above reveal some trends in the interplay between ligand functionalization and guest effects on the transition temperature in the $[Fe_2(L_1^R)_3]^{4+}$ systems.

First, it is evident that the functionalization of the L_1^R ligand can effectively shift the $T_{1/2}$ value either higher or lower depending on the nature of the R group. EWGs lower the $T_{1/2}$, while EDGs raise it, similar to observations in other systems with this type of functionalization.[154]

Tables 5.9, 5.10, and 5.11 clearly demonstrate the trend in ΔH, with $[Fe_2(L_1^F)_3]^{4+}$ < $[Fe_2(L_1^H)_3]^{4+}$ < $[Fe_2(L_1^{CH_3})_3]^{4+}$ (ΔH values of, 12.98, 17.79, and 22.63 kcal·mol^{-1}, respectively). This trend reflects the impact of L_1 functionalization on the metal centre's ligand field. Although we only explored extreme cases, the potential for fine-tuning through ligand functionalization is significant. By adjusting the EWG or EDG character of the substituents, one can clearly modulate the $T_{1/2}$ value.

The second consistent effect extracted from the computed data is that larger guests result in lower $T_{1/2}$ values. This trend, which has been observed experimentally,[113,123,164] holds true regardless of L_1 functionalization, and the calculations reproduce the experimental available data (Table 5.2).[123] Furthermore, a linear relationship between $T_{1/2}$ and the DFT ionic radii[165,166] of the guest molecule is evident (Table 5.12 and Figure 5.15), clearly indicating that larger guests lead to smaller $T_{1/2}$ values. To ensure the robustness of this correlation, different sets of anionic radii were analysed, and the trend was consistently reproduced across all sets (Figures A5.2, A5.3 and A5.4 in the Appendix section).

$[BF_4]^-$ is not a spherical guest, rather than a tetrahedral one. One can estimate the radii of $[BF_4]^-$ by studying the average B–F bond length in the Cambridge structural database, which is 137 ± 3 pm (averaged from 10272 $[BF_4]^-$ fragments, 99% confidence interval), and adding to this value the covalent radii of F (57 pm). This returns a value of 193.8 pm. Notice that this value could change if another set of covalent radii is used. In any case, this value can be added in the correlations, and no significant difference is obtained compared with the correlations obtained without $[BF_4]^-$ (Figure A5.1). However, the shape of $[BF_4]^-$ is unique, and so it is its spatial arrangement within the cavity (Figure 5.14). That is the reason that makes the analogy with spherical guest quite difficult.

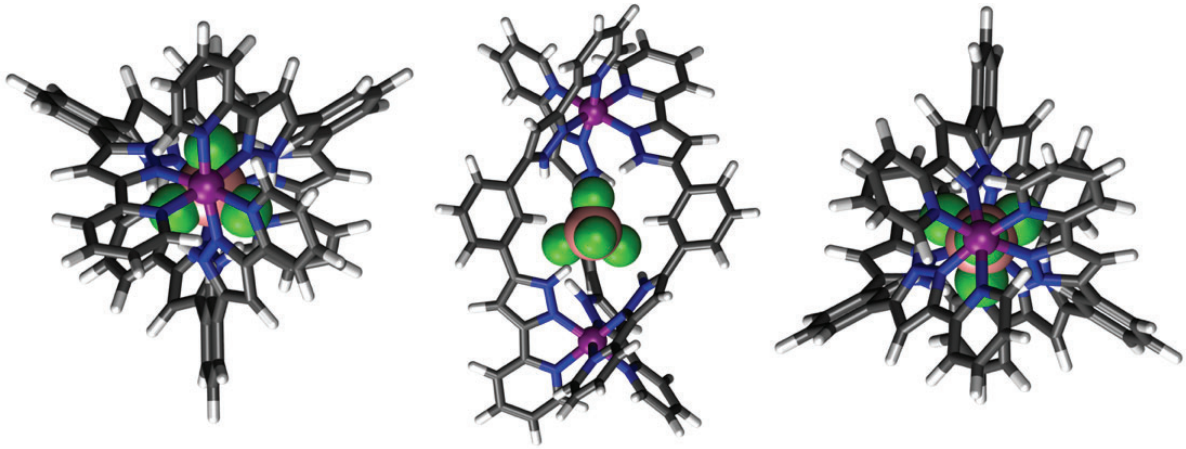

Figure 5.14. Spatial arrangement of the $[BF_4]^-$ inside the cavity.
Purple: Fe, blue: N, green: F, pink: B, gray: C, white: H.

Also, the B atom is not in the central part of the molecule, which means that one vertex of the tetrahedron is pointing towards one of the Fe(II) metal centres. The estimated radii for the $[BF_4]^-$ anion, which is the largest across the tested guests, should lead to the smallest $T_{1/2}$ in all cases. However, this is only observed for the $([Fe_2(L_1{}^{CH_3})_3]@X)^{3+}$ family, probably due to the spatial arrangement that the $[BF_4]^-$ adopts inside the cavity.

Table 5.12. Summary of the computed $T_{1/2}$ for different functionalizations and guests. Guest radii in picometre, $T_{1/2}$ in Kelvin. [a]Average $T_{1/2}$ value when a two-step transition.

$([Fe_2(L_1^R)_3]@X)^{3+}$		$T_{1/2}$/K		
Guest X	**radius/pm**	**R = –F**	**R = –H**	**R = –CH$_3$**
–	0.0	368	502	688
H^-	92.2	307[a]	455[a]	662
F^-	102.8	300[a]	426[a]	665
Cl^-	140.0	250	372	593
Br^-	152.0	219	337	587
I^-	169.8	154	263	511
$[BF_4]^-$	193.8	177	285	486

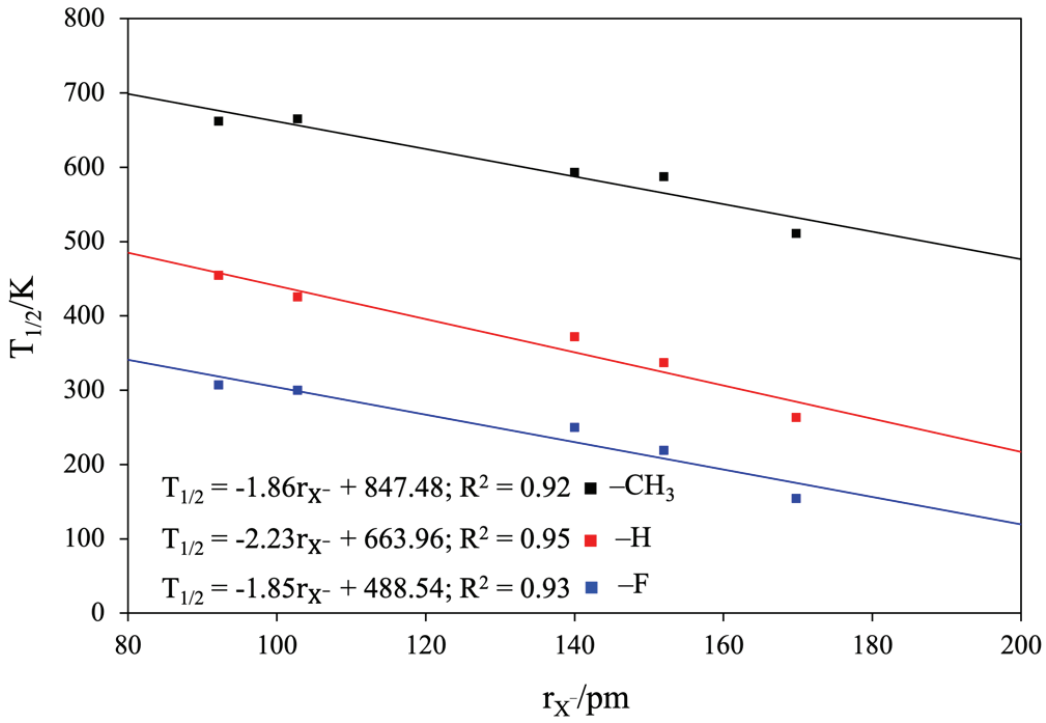

Figure 5.15. Computed transition temperatures as a function of the guest radius (DFT computed ionic radii)[165,166] without $[BF_4]^-$. Black: R = –CH$_3$, red: R = –H and blue: R = –F. All temperatures in Kelvin and radii in pm.

When the guest molecules are inserted inside the cavity, it is possible to obtain a correlation between the Fe–N bond lengths and the guest size (Figure 5.16).

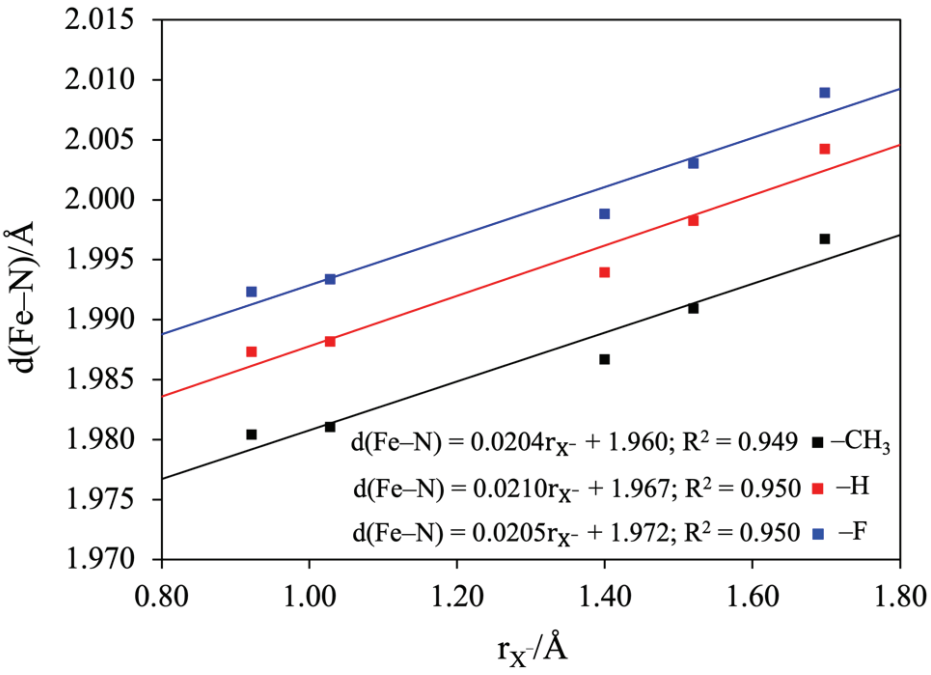

Figure 5.16. Correlation between the Fe–N average bond length and the guest size (DFT computed ionic radii)[165,166] for the $([Fe_2(L_1^R)_3]@X)^{3+}$ (without $[BF_4]^-$). Black: R = –CH_3, red: R = –H and blue: R = –F. Bond lengths and radii in Angstrom.

The guests force the system to expand from the inside (like pumping a balloon), enlarging the Fe–N bond lengths (increase of 0.015 Å from empty to @I^- system), which causes a weakening of the ligand field around the metal centre. This reduction in the energy gap between the d-based MOs, which can be quantified and shows a notable decrease between the $[Fe_2(L_1)_3]^{4+}$ and $([Fe_2(L_1)_3]@I)^{3+}$ systems (16167 cm^{-1} and 15401 cm^{-1}, respectively), is responsible for the corresponding decrease in $T_{1/2}$ (Table 5.13, Figure 5.17). This trend is observed also in the substituted cages with –F and –CH_3. The decrease in Δ_o and therefore in $T_{1/2}$ with the guest size is illustrated as well in Figure 5.18.

Table 5.13. d-MO splitting for the functionalized dinuclear system with several guests $[Fe_2(L_1^R)_3]^{4+}@X^-$, R = –F, –H and $–CH_3$ and X = H^-, F^-, Cl^-, Br^-, I^- and $[BF_4]^-$.

	Δ_o/cm^{-1}					
$([Fe_2(L_1^R)_3]@X)^{3+}$	R = F		R = H		R = CH_3	
Guest X^-	Fe_1	Fe_2	Fe_1	Fe_2	Fe_1	Fe_2
–	15838	15832	16175	16158	16655	16648
H^-	15698	16010	16026	16417	16564	16852
F^-	15581	16004	16243	16410	16463	16859
Cl^-	15555	15555	15929	15923	16388	16381
Br^-	15336	15332	15712	15706	16154	16139
I^-	15049	15044	15407	15395	15841	15822
$[BF_4]^-$	15038	15045	15389	15393	15785	15805

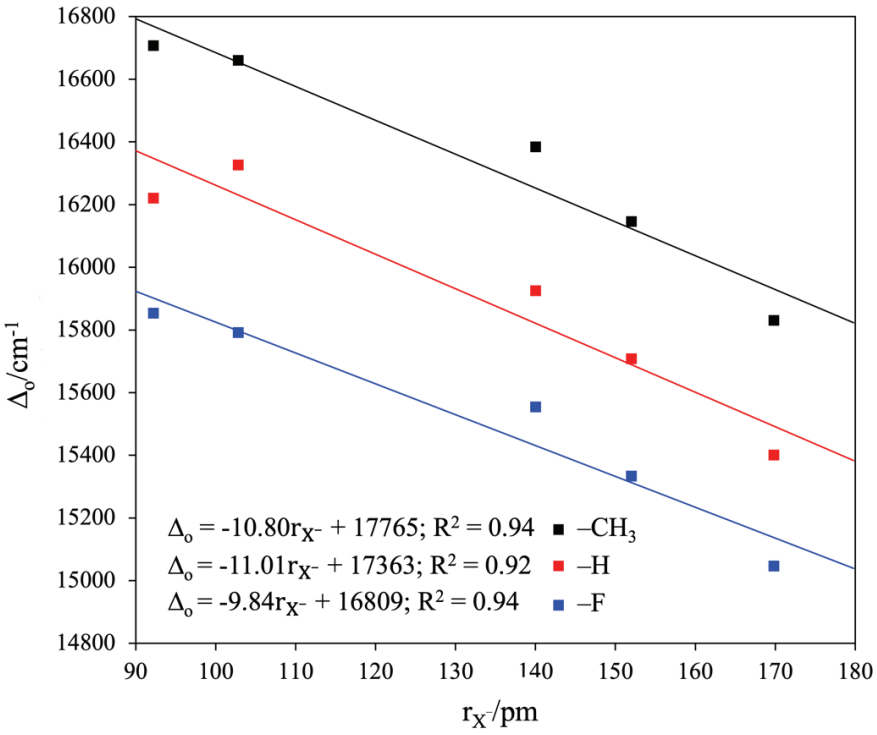

Figure 5.17. Correlation between the guest radii and the computed ligand-field splitting energies (without $[BF_4]^-$). Black: R = $–CH_3$, red: R = –H and blue: R = –F.

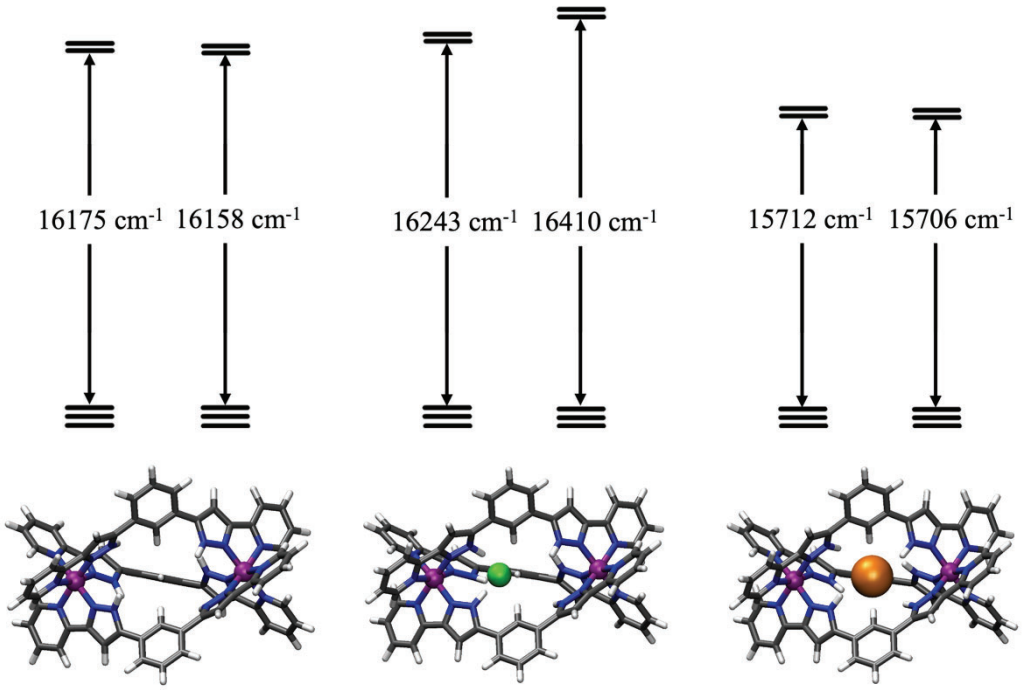

Figure 5.18. Diagram of the d-based MOs of the non-substituted dinuclear cages $[Fe_2(L_1^H)_3]^{4+}@X^-$, empty and with X^- = F^- and Br^-, respectively. Violet: Fe, blue: N, gray: C, white: H, green: F^-, orange: Br^-.

A more intriguing effect is seen in the guest-induced two-step behaviour. As indicated in Tables 5.9, 5.10 and 5.11, the smallest guests (H^- and F^-) yield the largest negative values for the ρ term, which measures the tendency of a dinuclear system to exhibit a two-step transition. To trace the origin of this effect, we examined the electronic structures and geometries of the $([Fe_2(L_1^R)_3]@F)^{3+}$ (R = –H, –F and $–CH_3$). Notably, small guest molecules do not remain at the centre of the cavity but instead shift closer to one of the Fe(II) metal centres. This asymmetry is not present for larger guests, which maintain an equivalent distance to both Fe(II) metals. The proximity of the guest molecule to one metal centre influences the electronic structure, making it more likely to undergo the SCO transition (Figures 5.18, A5.5 and A5.6).

The computed splitting of the d-based MOs is, on average, 330 cm^{-1} smaller for the metal centre positioned closer to the guest molecule (Fe_1 in Tables 5.13 and 5.14). Additionally, although the Fe–N bond lengths are similar for both metal centres, the coordination environment of the metal closer to the guest is more distorted. This distortion can be quantified using the Continuous Shape Measures (CShM) for an octahedral geometry:[141,142]

Table 5.14. CShM(OC-6)–F for the Fe_1/Fe_2 and F^- distance to each metal centre. OC-6 stands for octahedral. Distances in Å.

	R = F		**R = H**		**R = CH_3**	
	Fe_1	**Fe_2**	**Fe_1**	**Fe_2**	**Fe_1**	**Fe_2**
CShM(OC-6)–F	1.15	0.90	1.12	0.87	1.10	0.93
d(Fe–F)	3.906	5.957	3.882	6.002	3.862	5.946
CShM(OC-6)–Br	0.890	0.891	0.866	0.867	0.916	0.916
d(Fe–Br)	4.759	4.760	4.766	4.767	4.766	4.767

The subtle distortion caused by the guest in the coordination sphere of the metal centre appears to be sufficient to stress the two-step nature of the transition. Once the guest is in the centre of the cavity, this effect vanishes, leading the transition to be single-step. This trend is also evident when analysing the $([Fe_2(L_1^R)_3]@Br)^{3+}$ systems, for instance, where the bromide is positioned equidistantly between the two iron centres. In this case, both metals are geometrically equivalent, reducing the differences that enhance the two-step transition. As a result, although two transition temperatures can still be calculated, the gap between them becomes small, and the transition curve exhibits more of a single-step character. This effect is illustrated in Figure 5.19 for the $([Fe_2(L_1^H)_3]@X)^{3+}$ systems ($X = F^-$ or Br^-). As shown, the $([Fe_2(L_1^H)_3]@F)^{3+}$ system clearly exhibits a two-step transition, as the [HS-LS] spin-state remains stable over a certain temperature range. In contrast, we can determine two transition temperatures for the $([Fe_2(L_1^H)_3]@Br)^{3+}$ system, but they are so close that the magnetic moment curve essentially resolves into a single-step transition, making impossible to distinguish the two $T_{1/2}$ values. This is further illustrated by the significant difference in the ρ values between the systems (Table 5.9, with ρ = -0.31 and -0.04 for F^- and Br^-, respectively).

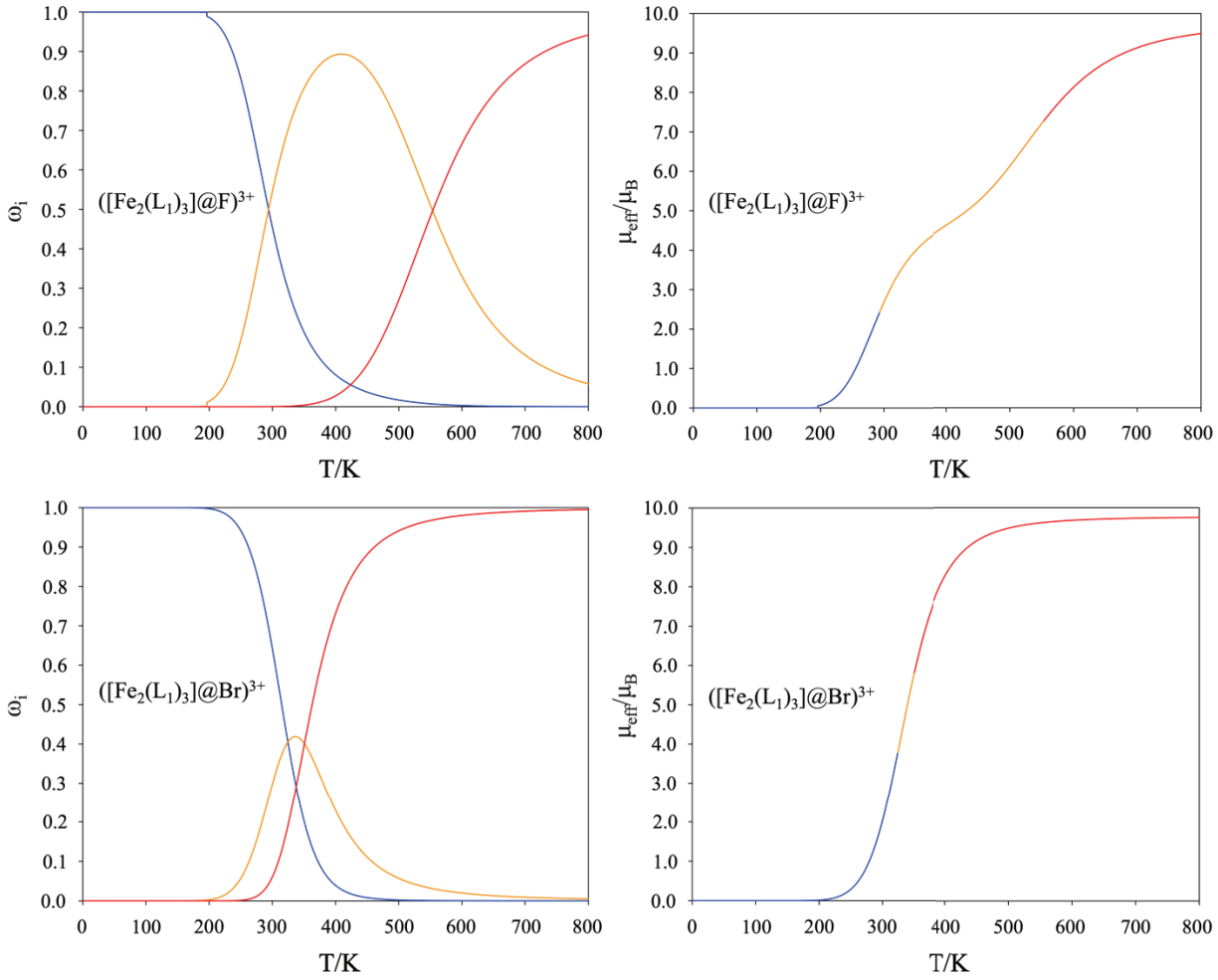

Figure 5.19. Left: spin state populations (ω_i) for the $([Fe_2(L_1^H)_3]@X)^{3+}$ systems, right: magnetic moment computed form the corresponding spin-state populations. Top: X = F^- with ρ = -0.31, bottom: X = Br^- with ρ = -0.06. *i* = [LS-LS] (blue), [HS-LS] (orange) and [HS-HS] (red).

It is important to note that even with relatively large negative values of ρ, in absence of cooperativity (γ = 0) the magnetic moment curve exhibits a single-step, as can be seen, for instance, for the $([Fe_2(L_1^{CH_3})_3]@F)^{3+}$ system, which despite having a ρ = -0.14, exhibits a single step transition (Figure 5.20).

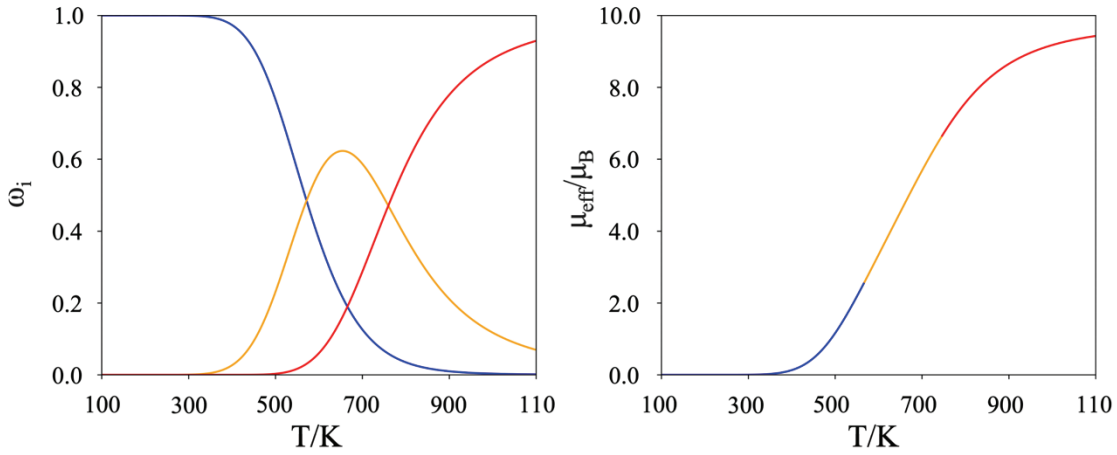

Figure 5.20. Left: spin state populations (ω_i) for the $([Fe_2(L_1^{CH_3})_3]@F)^{3+}$ system, with ρ = -0.14 and γ = 0 J·mol^{-1}. Right: magnetic moment computed form the corresponding spin-state populations. *i* = [LS-LS] (blue), [HS-LS] (orange) and [HS-HS] (red).

It is important to point out that when ρ < -0.20, a two-step transition is observed when modelling the magnetic moment as a function of temperature. However, in all our cases, γ is set to zero, as our calculations do not account for intermolecular interactions. Using the computational approach outlined in section 5.3.4, we tested the impact of increasing intermolecular interactions by adjusting γ values between zero and γ_c (where γ_c is defined as $2 \cdot R \cdot \Delta H/\Delta S$)[126] on systems with ρ values ranging from -0.20 to -0.05. The results show that as γ increases, the transition curve becomes sharper, making the two-step character more pronounced. Figure 5.21 and 5.22 illustrate this effect for the $([Fe_2(L_1^F)_3]@Cl)^{3+}$ system, where ρ is -0.10 (as shown in Table 5.10).

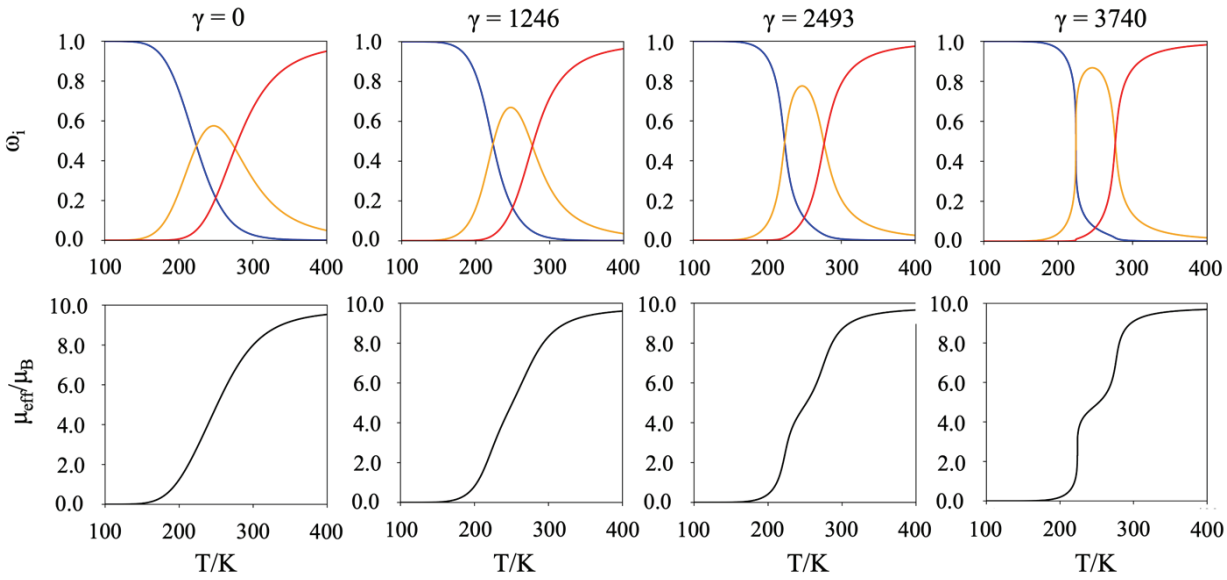

Figure 5.21. Impact of γ value on rate of change of the spin-state populations and the shape of the spin-transition for the $([Fe_2(L_1^F)_3]@Cl)^{3+}$ system. For that system, ρ = -0.10, which leads to a single step transition if γ = 0 and a two-step transition if γ = 3740 J·mol^{-1}. i = [LS-LS] (blue), [HS-LS] (orange) and [HS-HS] (red). Notice that increasing γ does not change the crossing point temperature between spin-state populations.

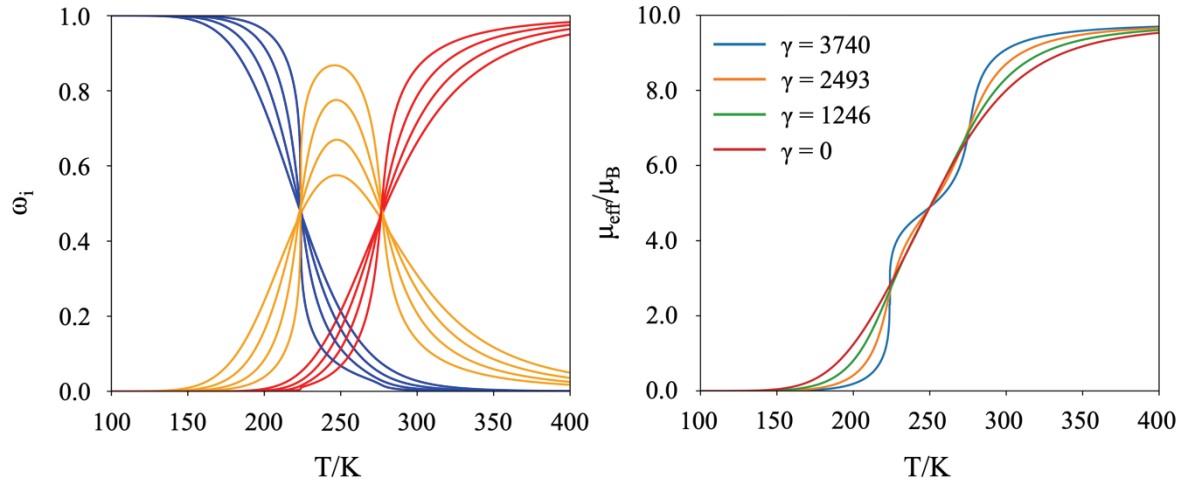

Figure 5.22. Same information as in Figure 5.21 but all condensed to a single figure.

When γ = 0, the transition occurs in a single step. However, with γ_c (the largest tested value), a two-step transition is observed. The role of γ is to increase the slope, that is, the rate at which each spin-state appears/disappears. This effect is demonstrated by the thermal behaviour of the spin-state populations, which vary according to the value of γ. Intermediate γ values have also been tested, showing a gradual tendency towards a two-step transition in the magnetic moment

curve as γ increases. It is important to note that increasing γ does not affect the crossing points between different spin-state populations, meaning the transition temperatures remain constant and only depend on the system's thermodynamic properties (ΔH, ΔS, and W).

This feature of our software can be helpful for fitting experimental data, as it allows to entangle the cooperative effects from the electronic contributions to the two-step nature of the transition.

5.4. Conclusions

This work introduces a computational methodology for determining the $T_{1/2}$ in dinuclear $[Fe_2(L_1^R)]^{4+}$ (R = –H, –F, or $–CH_3$) systems. Using the TPSSh exchange-correlation functional, this approach allows for the calculation of the corresponding thermochemical quantities within an acceptable error. These calculations provide insights into trends related to $T_{1/2}$, based on the electronic structure of the studied systems. Functionalization with EWGs reduces the energy gap between the non-bonding and antibonding orbitals of each Fe(II) centre, leading to a decrease in $T_{1/2}$. In contrast, EDGs increase this gap, thus raising $T_{1/2}$, consistent with findings from other spin-crossover systems.[154]

A much more interesting effect is observed when guests molecules are inserted into the MOCs, leading to $([Fe_2(L_1)_3]@X)^{3+}$ systems (X = H^-, F^-, Cl^-, Br^-, I^- and $[BF_4]^-$). Our calculations showed a linear dependency of the $T_{1/2}$ with the size of the guest molecule: the larger the guest, the lower the $T_{1/2}$ across all studied ligands. This suggests a dual influence: ligand functionalization, which allows for significant variation in $T_{1/2}$, and guest molecule size, which causes a more gradual reduction in $T_{1/2}$. Moreover, small guests (H^- and F^- in particular) can shift from the centre of the cavity, inducing small differences between the two Fe(II) metal sites. This effect stresses the two-step character of the transition for such systems, an effect that is not observed for the empty systems, which always display single-step transitions.

The calculated thermochemical values allow to obtain the populations of each spin-state as a function of temperature. From this data, we can analyse the electronic influence on having a single-step or two-step transition, based on the values of W and ρ, and we can calculate the different $T_{1/2}$ values. Our findings show that a clear two-step transition is only observed when $\rho < -0.20$, despite being able to compute two separate transition temperatures when $\rho > -0.20$. For $\rho > -0.20$, the [HS-LS] species cannot generate the characteristic two-step shape in the magnetic moment curve, resulting in a single-step transition. However, two-step transitions can be enhanced if large cooperativity is present.

Our study reveals how the balance between ligand functionalization and host-guest interactions can effectively tune $T_{1/2}$. This interplay offers valuable insights for the rational design of new dinuclear systems that can undergo spin transition at specific temperatures.

5.5. Appendix

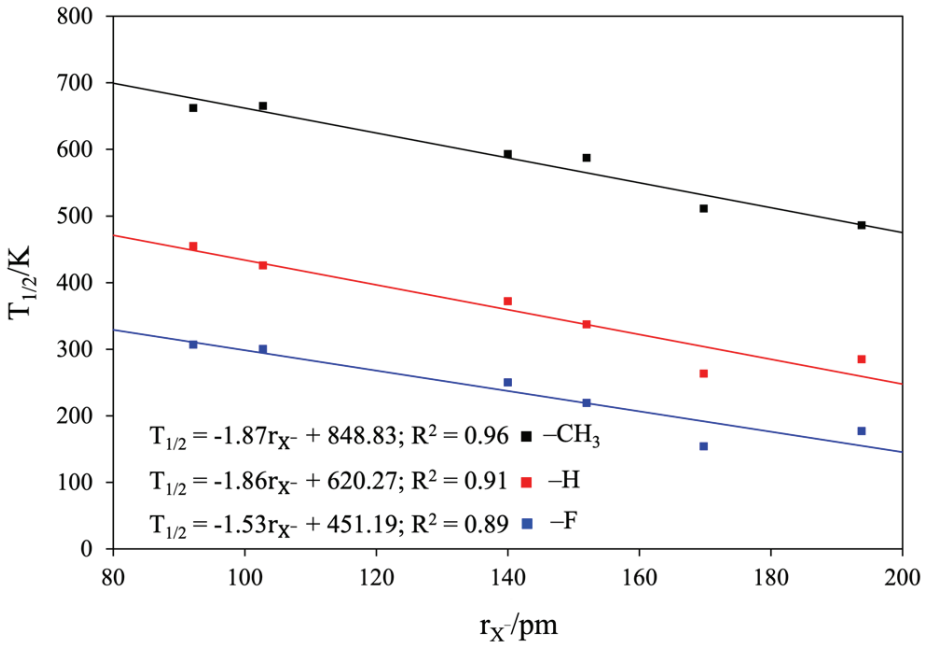

Figure A5.1. Computed transition temperatures as a function of the guest radius (DFT computed ionic radii)[165,166] with $[BF_4]^-$. Black: R = $–CH_3$, red: R = –H and blue: R = –F.

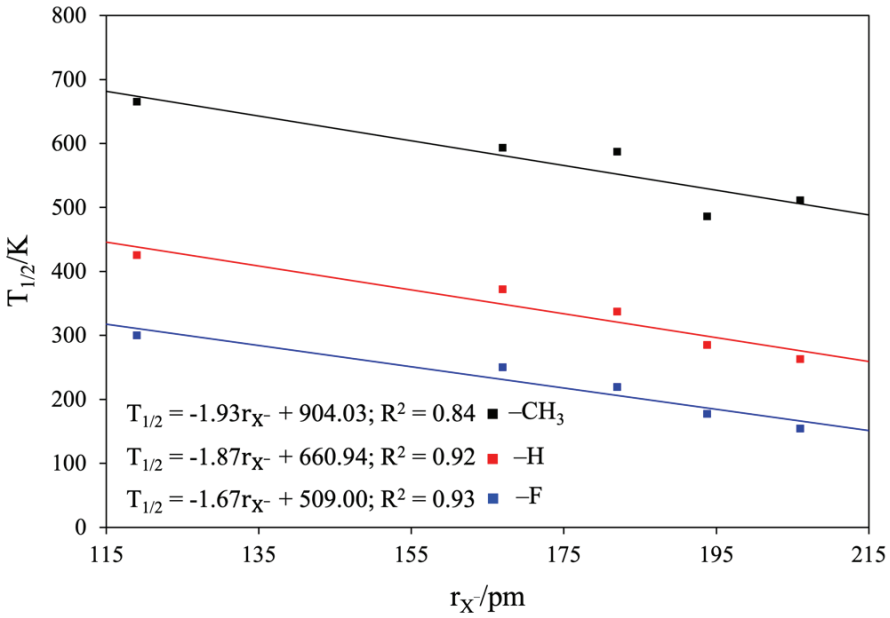

Figure A5.2. Transition temperature dependence on the guest ionic radius[167,168] with $[BF_4]^-$. Black: R = $–CH_3$, red: R = –H and blue: R = –F.

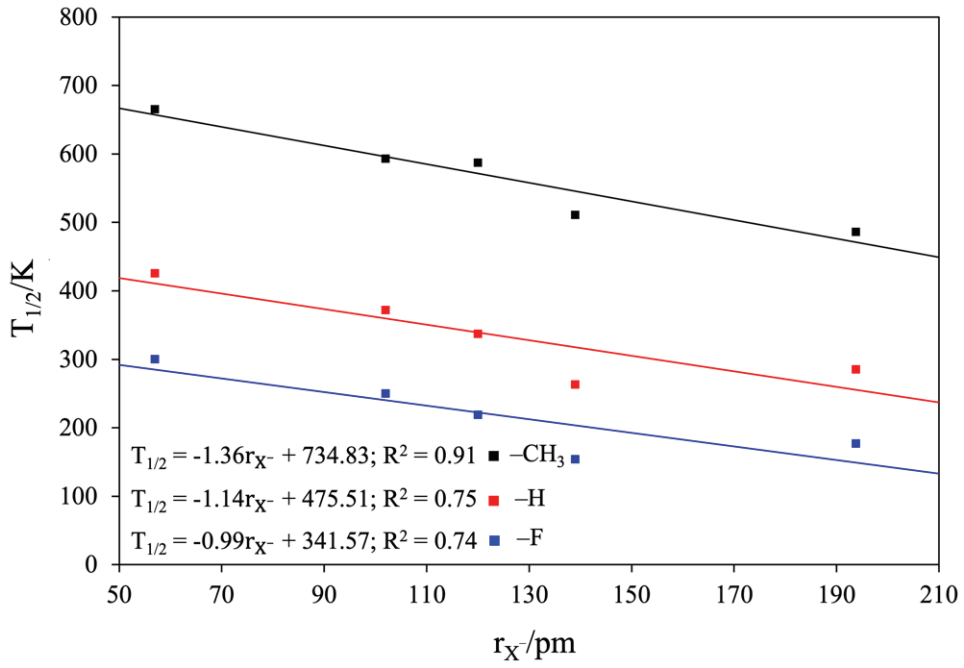

Figure A5.3. Transition temperature dependence on the guest covalent radius[169] with $[BF_4]^-$. Black: R = $–CH_3$, red: R = –H and blue: R = –F.

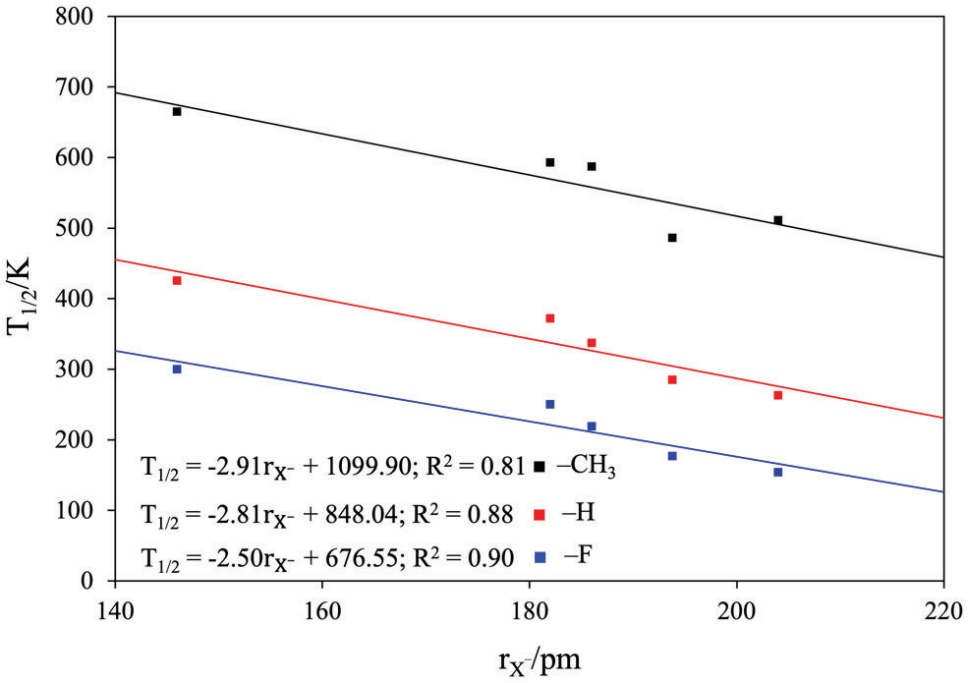

Figure A5.4. Transition temperature dependence on the guest van der Waals radius[170] with $[BF_4]^-$. Black: R = $–CH_3$, red: R = –H and blue: R = –F.

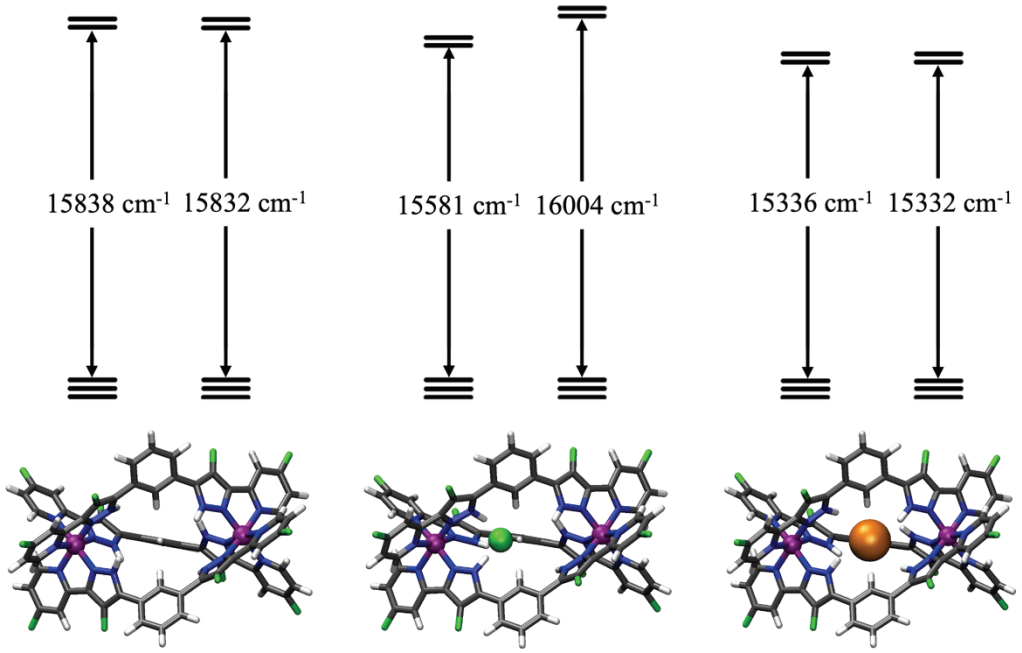

Figure A5.5. Diagram of the d-based MOs of the F-substituted dinuclear cages $[Fe_2(L_1^F)_3]^{4+}@X^-$, empty and with $X^- = F^-$ and Br^-, respectively. Violet: Fe, blue: N, gray: C, white: H, green: F^-, orange: Br^-.

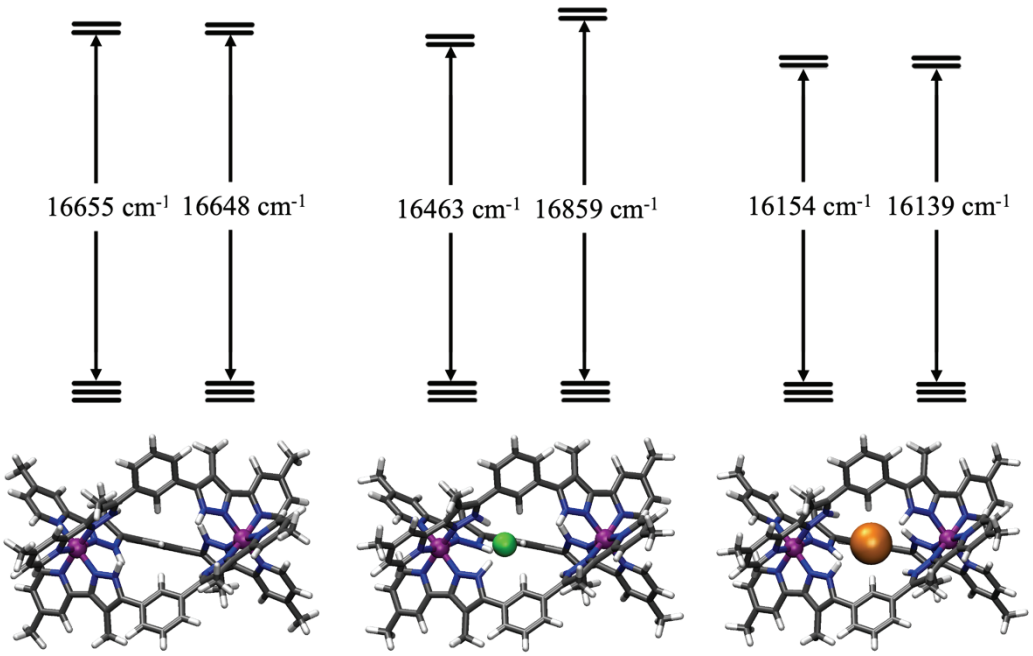

Figure A5.6. Diagram of the d-based MOs of the CH_3-substituted dinuclear cages $[Fe_2(L_1^{CH_3})_3]^{4+}@X^-$, empty and with $X^- = F^-$ and Br^-, respectively. Violet: Fe, blue: N, gray: C, white: H, green: F^-, orange: Br^-.

5.6. References

1. R. Chakrabarty, P. S. Mukherjee and P. J. Stang, *Chem. Rev.*, 2011, **111**, 6810–6918.
2. T. R. Cook and P. J. Stang, *Chem. Rev.*, 2015, **115**, 7001–7045.
3. L. L. Yan, L. Y. Yao, M. Ng and V. W. W. Yam, *J. Am. Chem. Soc.*, 2021, **143**, 19008–19017.
4. A. J. Gosselin, C. A. Rowland and E. D. Bloch, *Chem. Rev.*, 2020, **120**, 8987–9014.
5. E. O. Bobylev, D. A. Poole, B. de Bruin and J. N. H. Reek, *Chem. Sci.*, 2021, **12**, 7696–7705.
6. B. Huang, L. Mao, X. Shi and H. B. Yang, *Chem. Sci.*, 2021, **12**, 13648–13663.
7. A. Tarzia, J. E. M. Lewis and K. E. Jelfs, *Angew. Chem. Int. Ed.*, 2021, **60**, 20879–20887.
8. R. Custelcean, *Chem. Soc. Rev.*, 2014, **43**, 1813–1824.
9. P. Ballester, *Chem. Soc. Rev.*, 2010, **39**, 3810–3830.
10. M. D. Ward, C. A. Hunter and N. H. Williams, *Acc. Chem. Res.*, 2018, **51**, 2073–2082.
11. Y. Tamura, H. Takezawa and M. Fujita, *J. Am. Chem. Soc.*, 2020, **142**, 5504–5508.
12. M. Yamashina, Y. Sei, M. Akita and M. Yoshizawa, *Nat. Commun.*, 2014, **5**, 4662.
13. A. Galan and P. Ballester, *Chem. Soc. Rev.*, 2016, **45**, 1720–1737.
14. M. D. Pluth, R. G. Bergman and K. N. Raymond, *Science*, 2007, **316**, 85–88.
15. H. Takezawa, K. Shitozawa and M. Fujita, *Nat. Chem.*, 2020, **12**, 574–578.
16. Y. Fang, J. A. Powell, E. Li, Q. Wang, Z. Perry, A. Kirchon, X. Yang, Z. Xiao, C. Zhu, L. Zhang, F. Huang and H. C. Zhou, *Chem. Soc. Rev.*, 2019, **48**, 4707–4730.
17. K. Wang, J. H. Jordan, X. Y. Hu and L. Wang, *Angew. Chem. Int. Ed.*, 2020, **59**, 13712–13721.
18. X. W. Zhu, F. L. Zhuang, Z. Y. Chen, S. Zhou, Y. B. Wei, X. P. Zhou and D. Li, *Inorg. Chem.*, 2021, **60**, 14721–14730.
19. W. Cullen, A. J. Metherell, A. B. Wragg, C. G. P. Taylor, N. H. Williams and M. D. Ward, *J. Am. Chem. Soc.*, 2018, **140**, 2821–2828.
20. R. Zaffaroni, N. Orth, I. Ivanović-Burmazović and J. N. H. Reek, *Angew. Chem. Int. Ed.*, 2020, **59**, 18485–18489.
21. C. Ngai, C. M. Sanchez-Marsetti, W. H. Harman and R. J. Hooley, *Angew. Chem. Int. Ed.*, 2020, **59**, 23505–23509.
22. X. Q. Guo, L. P. Zhou, S. J. Hu, L. X. Cai, P. M. Cheng and Q. F. Sun, *J. Am. Chem. Soc.*, 2021, **143**, 6202–6210.

23. J. Jiao, C. Tan, Z. Li, Y. Liu, X. Han and Y. Cui, *J. Am. Chem. Soc.*, 2018, **140**, 2251–2259.
24. Y. J. Hou, K. Wu, Z. W. Wei, K. Li, Y. L. Lu, C. Y. Zhu, J. S. Wang, M. Pan, J. J. Jiang, G. Q. Li and C. Y. Su, *J. Am. Chem. Soc.*, 2018, **140**, 18183–18191.
25. E. Ubasart, O. Borodin, C. Fuertes-Espinosa, Y. Xu, C. García-Simón, L. Gómez, J. Juanhuix, F. Gándara, I. Imaz, D. Maspoch, M. von Delius and X. Ribas, *Nat. Chem.*, 2021, **13**, 420–427.
26. Y. R. Zheng, K. Suntharalingam, T. C. Johnstone and S. J. Lippard, *Chem. Sci.*, 2015, **6**, 1189–1193.
27. S. Pullen, J. Tessarolo and G. H. Clever, *Chem. Sci.*, 2021, **12**, 7269–7293.
28. X. Zhang, X. Dong, W. Lu, D. Luo, X. W. Zhu, X. Li, X. P. Zhou and D. Li, *J. Am. Chem. Soc.*, 2019, **141**, 11621–11627.
29. C. Garciá-Simón, C. Colomban, Y. A. Çetin, A. Gimeno, M. Pujals, E. Ubasart, C. Fuertes-Espinosa, K. Asad, N. Chronakis, M. Costas, J. Jiménez-Barbero, F. Feixas and X. Ribas, *J. Am. Chem. Soc.*, 2020, **142**, 16051–16063.
30. C. Fuertes-Espinosa, C. García-Simón, M. Pujals, M. Garcia-Borràs, L. Gómez, T. Parella, J. Juanhuix, I. Imaz, D. Maspoch, M. Costas and X. Ribas, *Chem*, 2020, **6**, 169–186.
31. R. Saha, B. Mondal and P. S. Mukherjee, *Chem. Rev.*, 2022, **122**, 12244–12307.
32. P. F. Cui, X. R. Liu, Y. J. Lin, Z. H. Li and G. X. Jin, *J. Am. Chem. Soc.*, 2022, **144**, 6558–6565.
33. A. Dhamija, C. K. Das, Y. H. Ko, Y. Kim, R. D. Mukhopadhyay, A. Gunnam, X. Yu, I. C. Hwang, L. V. Schäfer and K. Kim, *Chem*, 2022, **8**, 543–556.
34. S. Mecozzi and J. Rebek, *Chem. Eur. J.*, 1998, **4**, 1016–1022.
35. S. Turega, W. Cullen, M. Whitehead, C. A. Hunter and M. D. Ward, *J. Am. Chem. Soc.*, 2014, **136**, 8475–8483.
36. M. D. Wise, J. J. Holstein, P. Pattison, C. Besnard, E. Solari, R. Scopelliti, G. Bricogne and K. Severin, *Chem. Sci.*, 2015, **6**, 1004–1010.
37. W. Cullen, K. A. Thomas, C. A. Hunter and M. D. Ward, *Chem. Sci.*, 2015, **6**, 4025–4028.
38. S. Sudan, F. Fadaei-Tirani, R. Scopelliti, K. E. Ebbert, G. H. Clever and K. Severin, *Angew. Chem. Int. Ed.*, 2022, **61**, e202201823.
39. E. Grunwald and C. Steel, *J. Am. Chem. Soc.*, 1995, **117**, 5687–5692.
40. T. K. Ronson, W. Meng and J. R. Nitschke, *J. Am. Chem. Soc.*, 2017, **139**, 9698–9707.

41. G. Szalóki, V. Croué, M. Allain, S. Goeb and M. Sallé, *Chem. Commun.*, 2016, **52**, 10012–10015.
42. P. R. Symmers, M. J. Burke, D. P. August, P. I. T. Thomson, G. S. Nichol, M. R. Warren, C. J. Campbell and P. J. Lusby, *Chem. Sci.*, 2015, **6**, 756–760.
43. P. Gütlich, A. B. Gaspar and Y. Garcia, *Beilstein J. Org. Chem.*, 2013, **9**, 342–391.
44. V. Ksenofontov, G. Levchenko, H. Spiering, P. Gütlich, J.-F. Letard, Y. Bouhedja and O. Kahn, *Chem. Phys. Lett.*, 1998, **294**, 545–553.
45. G. G. Levchenko, A. V. Khristov and V. N. Varyukhin, *Low Temp. Phys.*, 2014, **40**, 571–585.
46. H. A. Ewald, R. L. Martin, I. G. Ross and A. H. White, *The Royal Society*, 1964, **280**, 235–257.
47. Y. Qi, E. W. Müller, H. Spiering and P. Gütlich, *Chem. Phys. Lett.*, 1983, **101**, 503–505.
48. S. Bonhommeau, G. Molnár, M. Goiran, K. Boukheddaden and A. Bousseksou, *Phys. Rev. B*, 2006, **74**, 064424.
49. P. Gütlich and H. A. Goodwin, in *Spin Crossover in Transition Metal Compounds I*, eds. P. Gütlich and H. A. Goodwin, Springer-Verlag Berlin Heidelberg, 2004, vol. 233, pp. 1–47.
50. G. Chastanet, C. Desplanches, C. Baldé, P. Rosa, M. Marchivie and P. Guionneau, *Chem. Sq.*, 2018, **2**, 1–18.
51. J.-F. Létard, *J. Mater. Chem.*, 2006, **16**, 2550–2559.
52. J. J. Mcgarvey and I. Lawthers, *J. Chem. Soc., Chem. Commun.*, 1982, **16**, 906–907.
53. E. D. Brady, J. S. Overby, M. B. Meredith, A. B. Mussman, M. A. Cohn, T. P. Hanusa, G. T. Yee and M. Pink, *J. Am. Chem. Soc.*, 2002, **124**, 9556–9566.
54. M. B. Meredith, J. A. Crisp, E. D. Brady, T. P. Hanusa, G. T. Yee, N. R. Brooks, B. E. Kucera and V. G. Young, *Organometallics*, 2006, **25**, 4945–4952.
55. M. B. Meredith, J. A. Crisp, E. D. Brady, T. P. Hanusa, G. T. Yee, M. Pink, W. W. Brennessel and V. G. Young, *Organometallics*, 2008, **27**, 5464–5473.
56. M. Sorai, Y. Yumoto, H. Dost M. and L. F. Larkworthy, *J. Phys. Chem. Solids*, 1993, **54**, 421–430.
57. D. M. Halepoto, D. G. L. Holt, L. F. Larkworthy, G. J. Leigh, D. C. Povey and G. W. Smith, *J. Chem. Soc. Chem. Commun.*, 1989, 1322–1323.
58. D. M. Halepoto, D. G. L. Holt, L. F. Larkworthy, D. C. Povey, G. W. Smith and G. J. Leigh, *Polyhedron*, 1989, **8**, 1821–1822.

59. V. Ksenofontov, A. B. Gaspar, G. Levchenko, B. Fitzsimmons and P. Gütlich, *J. Phys. Chem. B*, 2004, **108**, 7723–7727.
60. P. Gütlich, A. B. Gaspar, Y. Garcia and V. Ksenofontov, *C. R. Chim.*, 2007, **10**, 21–36.
61. A. K. Hughes, V. J. Murphy and D. O'Hare, *J. Chem. Soc., Chem. Commun.*, 1994, 163–164.
62. A. E. Goeta, J. A. K. Howard, A. K. Hughes, D. O'Hare and R. C. B. Copley, *J. Mater. Chem.*, 2007, **17**, 485–492.
63. H. Sitzmann, M. Schar, E. Dormann and M. Kelemen, *Z. Anorg. Allg. Chem.*, 1997, **623**, 1850–1852.
64. P. M. Becker, C. Förster, L. M. Carrella, P. Boden, D. Hunger, J. van Slageren, M. Gerhards, E. Rentschler and K. Heinze, *Chem. Eur. J.*, 2020, **26**, 7199–7204.
65. D. O'Hare, V. J. Murphy and N. Kaltsoyannis, *J. Chem. Soc., Dalton Trans.*, 1993, 383–392.
66. H. Bauer, J. Weismann, D. Saurenz, C. Färber, M. Schär, W. Gidt, I. Schädlich, G. Wolmershäuser, Y. Sun, S. Harder and H. Sitzmann, *J. Organomet. Chem.*, 2016, **809**, 63–73.
67. D. Villaman, C. J. McMonagle, M. R. Probert, O. Peña, Y. Moreno and M. Fuentealba, *CrystEngComm*, 2020, **22**, 3221–3233.
68. G. G. Morgan, K. D. Murnaghan, H. Müller-Bunz, V. McKee and C. J. Harding, *Angew. Chem. Int. Ed.*, 2006, **45**, 7192–7195.
69. A. J. Fitzpatrick, E. Trzop, H. Müller-Bunz, M. M. Dîrtu, Y. Garcia, E. Collet and G. G. Morgan, *Chem. Commun.*, 2015, **51**, 17540–17543.
70. Z. Liu, S. Liang, X. Di and J. Zhang, *Inorg. Chem. Commun*, 2008, **11**, 783–786.
71. J. Cirera and E. Ruiz, *Inorg. Chem.*, 2018, **57**, 702–709.
72. M. E. Switzer, R. Wang, M. F. Rettig and A. H. Maki, *J. Am. Chem. Soc.*, 1974, **96**, 7669–7674.
73. M. D. Walter, C. D. Sofield, C. H. Booth and R. A. Andersen, *Organometallics*, 2009, **28**, 2005–2019.
74. K. D. Murnaghan, C. Carbonera, L. Toupet, M. Griffin, M. M. Dîrtu, C. Desplanches, Y. Garcia, E. Collet, J. F. Létard and G. G. Morgan, *Chem. Eur. J.*, 2014, **20**, 5613–5618.
75. M. Griffin, S. Shakespeare, H. J. Shepherd, C. J. Harding, J. F. Létard, C. Desplanches, A. E. Goeta, J. A. K. Howard, A. K. Powell, V. Mereacre, Y. Garcia, A. D. Naik, H. Müller-Bunz and G. G. Morgan, *Angew. Chem. Int. Ed.*, 2011, **50**, 896–900.

76. A. J. Fitzpatrick, H. M. O'Connor and G. G. Morgan, *Dalton Trans.*, 2015, **44**, 20839–20842.
77. W. Phonsri, B. A. I. Lewis, G. N. L. Jameson and K. S. Murray, *Chem. Commun.*, 2019, **55**, 14031–14034.
78. W. Phonsri, D. S. Macedo, B. A. I. Lewis, D. F. Wain and K. S. Murray, *Magnetochemistry*, 2019, **5**, 37.
79. D. J. Harding, P. Harding and W. Phonsri, *Coord. Chem. Rev.*, 2016, **313**, 38–61.
80. S. Murata, K. Takahashi, T. Sakurai, H. Ohta, T. Yamamoto, Y. Einaga, Y. Shiota and K. Yoshizawa, *Crystals*, 2016, **6**, 49.
81. K. Takahashi, K. Kawamukai, M. Okai, T. Mochida, T. Sakurai, H. Ohta, T. Yamamoto, Y. Einaga, Y. Shiota and K. Yoshizawa, *Chem. Eur. J.*, 2016, **22**, 1253–1257.
82. C. Cook, F. Habib, T. Aharen, R. Clérac, A. Hu and M. Murugesu, *Inorg. Chem.*, 2013, **52**, 1825–1831.
83. Z. Y. Li, J. W. Dai, Y. Shiota, K. Yoshizawa, S. Kanegawa and O. Sato, *Chem. Eur. J.*, 2013, **19**, 12948–12952.
84. S. Floquet, M. L. Boillot, E. Rivière, F. Varret, K. Boukheddaden, D. Morineau and P. Négrier, *New J. Chem.*, 2003, **27**, 341–348.
85. S. Floquet, N. Guillou, P. Négrier, E. Rivière and M. L. Boillot, *New J. Chem.*, 2006, **30**, 1621–1627.
86. S. K. Karuppannan, A. Martín-Rodríguez, E. Ruiz, P. Harding, D. J. Harding, X. Yu, A. Tadich, B. Cowie, D. Qi and C. A. Nijhuis, *Chem. Sci.*, 2021, **12**, 2381–2388.
87. P. Guionneau, M. Marchivie, G. Bravic, J. F. Létard and D. Chasseau, *J. Mater. Chem.*, 2002, **12**, 2546–2551.
88. A. B. Gaspar, M. C. Muñoz, V. Niel and J. A. Real, *Inorg. Chem.*, 2001, **40**, 9–10.
89. J. Zarembowitch and O. Kahn, *Inorg. Chem.,* 1984, **23**, 589–593.
90. F. Fürmeyer, D. Münzberg, L. M. Carrella and E. Rentschler, *Molecules*, 2020, **25**, 855.
91. N. M. J. Nik Ibrahim, S. M. Said, A. Mainal, M. F. Mohd Sabri, N. Abdullah, M. M. I. Megat Hasnan, H. Che Hassan, M. F. Mohd Salleh and W. A. Wan Mohd Mahiyiddin, *Mater. Res. Bull.*, 2020, **126**, 110828.
92. D. A. Pantazis, C. A. Murillo and J. E. McGrady, *Dalton Trans.*, 2007, 608–614.
93. G. Alcover-Fortuny, C. De Graaf and R. Caballol, *Phys. Chem. Chem. Phys.*, 2015, **17**, 217–225.
94. H. Ma, J. L. Petersen, V. G. Young, G. T. Yee and M. P. Jensen, *J. Am. Chem. Soc.*, 2011, **133**, 5644–5647.

95. Y. Homma and T. Ishida, *Chem. Mater.*, 2018, **30**, 1835–1838.
96. S. Venkataramani, U. Jana, M. Dommaschk, F. D. Sönnichsen, F. Tuczek and R. Herges, *Science*, 2011, **331**, 445–448.
97. S. Thies, C. Bornholdt, F. Köhler, F. D. Sönnichsen, C. Näther, F. Tuczek and R. Herges, *Chem. Eur. J.*, 2010, **16**, 10074–10083.
98. J. Olguín, *Coord. Chem. Rev.*, 2020, **407**, 213148.
99. P. Gütlich and Y. Garcia, in *Spin Crossover in Transition Metal Compounds II. Topics in Current Chemistry*, Springer, Berlin, Heidelberg, 2004, vol. 234, pp. 49–62.
100. M. Ohba, K. Yoneda, G. Agusti, M. C. Muñoz, A. B. Gaspar, J. A. Real, M. Yamasaki, H. Ando, Y. Nakao, S. Sakaki and S. Kitagawa, *Angew. Chem. Int. Ed.*, 2009, **48**, 4767–4771.
101. S. M. Neville, G. J. Halder, K. W. Chapman, M. B. Duriska, B. Moubaraki, K. S. Murray and C. J. Kepert, *J. Am. Chem. Soc.*, 2009, **131**, 12106–12108.
102. J. Cirera, *Rev. Inorg. Chem.*, 2014, **34**, 199–216.
103. C. Bartual-Murgui, L. Salmon, A. Akou, N. A. Ortega-Villar, H. J. Shepherd, M. C. Muñoz, G. Molnár, J. A. Real and A. Bousseksou, *Chem. Eur. J.*, 2012, **18**, 507–516.
104. C. Bartual-Murgui, A. Akou, C. Thibault, G. Molnár, C. Vieu, L. Salmon and A. Bousseksou, *J. Mater. Chem. C*, 2015, **3**, 1277–1285.
105. G. J. Halder, C. J. Kepert, B. Moubaraki, K. S. Murray and J. D. Cashion, *Science*, 2002, **298**, 1762–1765.
106. S. Cobo, G. Molnár, J. A. Real and A. Bousseksou, *Angew. Chem. Int. Ed.*, 2006, **45**, 5786–5789.
107. M. A. Halcrow, *Spin-Crossover Materials: Properties and Applications*, John Wiley & Sons, Ltd., Oxford, 2013.
108. J. R. Galán Mascarós, G. Aromí and M. Darawsheh, *C. R. Chim.*, 2018, **21**, 1209–1229.
109. J. Olguín and S. Brooker, *Coord. Chem. Rev.*, 2011, **255**, 203–240.
110. Y. Sunatsuki, R. Kawamoto, K. Fujita, H. Maruyama, T. Suzuki, H. Ishida, M. Kojima, S. Iijima and N. Matsumoto, *Coord. Chem. Rev.*, 2010, **254**, 1871–1881.
111. B. Weber, *Coord. Chem. Rev.*, 2009, **253**, 2432–2449.
112. M. Nihei, T. Shiga, Y. Maeda and H. Oshio, *Coord. Chem. Rev.*, 2007, **251**, 2606–2621.
113. M. D. Darawsheh, L. A. Barrios, O. Roubeau, S. J. Teat and G. Aromí, *Chem. Commun.*, 2017, **53**, 569–572.
114. S. L. Yang, X. Zhang, Q. Wang, C. Wu, H. Liu, D. Jiang, R. Lavendomme, D. Zhang and E. Q. Gao, *JACS Au*, 2023, **3**, 2183–2191.

115. O. Sato, *Nat. Chem.*, 2016, **8**, 644–656.
116. G. Ke, C. Duan, F. Huang and X. Guo, *InfoMat.*, 2020, **2**, 92–112.
117. Z. S. Yao, Z. Tang and J. Tao, *Chem. Commun.*, 2020, **56**, 2071–2086.
118. M. Deumal, S. Vela, M. Fumanal, J. Ribas-Arino and J. J. Novoa, *J. Mater. Chem. C*, 2021, **9**, 10624–10646.
119. J. Tao, J. P. Perdew, V. N. Staroverov and G. E. Scuseria, *Phys. Rev. Lett.*, 2003, **91**, 146401.
120. V. N. Staroverov, G. E. Scuseria, J. Tao and J. P. Perdew, *J. Chem. Phys.*, 2003, **119**, 12129–12137.
121. A. Schäfer, C. Huber and R. Ahlrichs, *J. Chem. Phys.*, 1994, **100**, 5829–5835.
122. A. Schäfer, H. Horn and R. Ahlrichs, *J. Chem. Phys.*, 1992, **97**, 2571–2577.
123. M. Darawsheh, L. A. Barrios, O. Roubeau, S. J. Teat and G. Aromí, *Chem. Eur. J.*, 2016, **22**, 8635–8645.
124. L. Navarro, A. Garcia-Duran and J. Cirera, *Dalton Trans.*, 2024, **53**, 14592–14601.
125. J.-A. Real, H. Bolvin, A. Bousseksou, A. Dworkin, O. Kahn, F. Varret and J. Zarembowitch, *J. Am. Chem. Soc.*, 1992, **114**, 4650–4658.
126. C. P. Slichter and H. G. Drickamer, *J. Chem. Phys.*, 1972, **56**, 2142–2160.
127. M. Darawsheh, L. A. Barrios, O. Roubeau, S. J. Teat and G. Aromí, *Angew. Chem. Int. Ed.*, 2018, **130**, 13697–13701.
128. M. J. Frisch, G. W. Trucks, H. B. Schlegel, G. E. Scuseria, M. a. Robb, J. R. Cheeseman, G. Scalmani, V. Barone, G. a. Petersson, H. Nakatsuji, X. Li, M. Caricato, a. V. Marenich, J. Bloino, B. G. Janesko, R. Gomperts, B. Mennucci, H. P. Hratchian, J. V. Ortiz, a. F. Izmaylov, J. L. Sonnenberg, Williams, F. Ding, F. Lipparini, F. Egidi, J. Goings, B. Peng, A. Petrone, T. Henderson, D. Ranasinghe, V. G. Zakrzewski, J. Gao, N. Rega, G. Zheng, W. Liang, M. Hada, M. Ehara, K. Toyota, R. Fukuda, J. Hasegawa, M. Ishida, T. Nakajima, Y. Honda, O. Kitao, H. Nakai, T. Vreven, K. Throssell, J. a. Montgomery Jr., J. E. Peralta, F. Ogliaro, M. J. Bearpark, J. J. Heyd, E. N. Brothers, K. N. Kudin, V. N. Staroverov, T. a. Keith, R. Kobayashi, J. Normand, K. Raghavachari, a. P. Rendell, J. C. Burant, S. S. Iyengar, J. Tomasi, M. Cossi, J. M. Millam, M. Klene, C. Adamo, R. Cammi, J. W. Ochterski, R. L. Martin, K. Morokuma, O. Farkas, J. B. Foresman and D. J. Fox, *Gaussian Inc., Wallingford CT*, 2016, Revision B.01.
129. F. Weigend and R. Ahlrichs, *Phys. Chem. Chem. Phys.*, 2005, **7**, 3297–3305.
130. F. Weigend, *Phys. Chem. Chem. Phys.*, 2006, **8**, 1057–1065.
131. J. Cirera, M. Via-Nadal and E. Ruiz, *Inorg. Chem.*, 2018, **57**, 14097–14105.

132. J. Cirera and E. Ruiz, *Comments Inorg. Chem.*, 2019, **39**, 216–241.
133. J. Cirera and F. Paesani, *Inorg. Chem.*, 2012, **51**, 8194–8201.
134. F. Furche and J. P. Perdew, *J. Chem. Phys.*, 2006, **124**, 044103.
135. K. P. Jensen and J. Cirera, *J. Phys. Chem. A*, 2009, **113**, 10033–10039.
136. M. Swart, *J. Chem. Theory Comput.*, 2008, **4**, 2057–2066.
137. G. Van Rossum and F. L. Drake, *Python Software Foundation*, 2020, Version 3.8.3.
138. C. Angeli, R. Cimiraglia and J. P. Malrieu, *J. Chem. Phys.*, 2002, **117**, 9138–9153.
139. F. Neese, *Wiley Interdiscip. Rev. Comput. Mol. Sci.*, 2018, **8**, e1327.
140. S. K. Singh, J. Eng, M. Atanasov and F. Neese, *Coord. Chem. Rev.*, 2017, **344**, 2–25.
141. S. Alvarez, P. Alemany, D. Casanova, J. Cirera, M. Llunell and D. Avnir, *Coord. Chem. Rev.*, 2005, **249**, 1693–1708.
142. D. Casanova, M. Llunell, P. Alemany and S. Alvarez, *Chem. Eur. J.*, 2005, **11**, 1479–1494.
143. M. Llunell, D. Casanova, J. Cirera, P. Alemany and S. Alvarez, 2013, Version 2.1.
144. L. S. Harimanow, K. H. Sugiyarto, D. C. Craig, M. L. Scudder and H. A. Goodwin, *Aust. J. Chem*, 1999, **52**, 109–122.
145. C. R. Groom, I. J. Bruno, M. P. Lightfoot and S. C. Ward, *Acta Crystallogr. B Struct. Sci. Cryst. Eng. Mater.*, 2016, **72**, 171–179.
146. N. C. Handy and A. J. Cohen, *Mol. Phys.*, 2001, **99**, 403–412.
147. M. Swart, A. W. Ehlers and K. Lammertsma, *Mol. Phys.*, 2004, **102**, 2467–2474.
148. J. Cirera and E. Ruiz, *J. Mater. Chem. C*, 2015, **3**, 7954–7961.
149. J. Cirera and E. Ruiz, *Inorg. Chem.*, 2016, **55**, 1657–1663.
150. J. G. Park, I.-R. Jeon and T. D. Harris, *Inorg. Chem.*, 2015, **54**, 359–369.
151. K. Nakano, N. Suemura, K. Yoneda, S. Kawata and S. Kaizaki, *Dalton Trans.*, 2005, 740–743.
152. A. Kimura and T. Ishida, *Inorganics*, 2017, **5**, 52.
153. H. C. Liang, Y. Pan, H. L. Zhu, Y. S. Meng, C. H. Liu, T. Liu and Y. Y. Zhu, *Inorg. Chem. Front.*, 2022, **9**, 2343–2352.
154. L. J. Kershaw Cook, R. Kulmaczewski, R. Mohammed, S. Dudley, S. A. Barrett, M. A. Little, R. J. Deeth and M. A. Halcrow, *Angew. Chem. Int. Ed.*, 2016, **55**, 4327–4331.
155. B. Dey, A. Mondal and S. Konar, *Chem. Asian J.*, 2020, **15**, 1709–1721.
156. B. Dey, S. Mehta, A. Mondal, J. Cirera, E. Colacio and V. Chandrasekhar, *ACS Omega*, 2022, **7**, 39268–39279.
157. L. P. Hammett, *Chem. Rev.*, 1935, **17**, 125–136.

158. L. P. Hammett, *J. Am. Chem. Soc.*, 1937, **59**, 96–103.
159. C. Hansch, A. Leo and R. W. Taft, *Chem. Rev.*, 1991, **91**, 165–195.
160. A. Hauser, J. Jeftić, H. Romstedt, R. Hinek and H. Spiering, *Coord. Chem. Rev.*, 1999, **190–192**, 471–491.
161. P. Gütlich, Y. Garcia and H. Spiering, in *Magnetism: Molecules to Materials IV: Nanosized Magnetic Materials*, eds. J. S. Miller and M. Drillon, Wiley-VCH Verlag GmbH & Co. KGaA, 2001, pp. 271–344.
162. A. Bousseksou, J. Nasser, J. Linares, K. Boukheddaden and F. Varret, *J. Phys. I France*, 1992, **2**, 1381–1403.
163. J. Cirera, V. Babin and F. Paesani, *Inorg. Chem.*, 2014, **53**, 11020–11028.
164. R. A. Bilbeisi, S. Zarra, H. L. C. Feltham, G. N. L. Jameson, J. K. Clegg, S. Brooker and J. R. Nitschke, *Chem. Eur. J.*, 2013, **19**, 8058–8062.
165. J. B. Liu, W. H. E. Schwarz and J. Li, *Chem. Eur. J.*, 2013, **19**, 14758–14767.
166. M. A. Blanco, A. Costales, A. Martí N Pendá and V. Luañ, *Phys. Rev. B*, 2000, **62**, 12028–12039.
167. R. D. Shannon and C. T. Prewitt, *Acta Cryst. B*, 1969, **17**, 925–946.
168. R. D. Shannon, *Acta Cryst.*, 1976, **32**, 751–767.
169. B. Cordero, V. Gómez, A. E. Platero-Prats, M. Revés, J. Echeverría, E. Cremades, F. Barragán and S. Alvarez, *Dalton Trans.*, 2008, 2832–2838.
170. S. Alvarez, *Dalton Trans.*, 2013, **42**, 8617–8636.

CHAPTER 6

General Conclusions

This chapter compiles the findings from the investigation developed in this doctoral thesis. Several spin-crossover systems were studied and modelled using different computational methods in order to understand the insights of such phenomena and therefore help in the design of new materials with tailored properties that can operate at specific temperatures.

Let us recap the systems studied:

- [Cr($^{n\text{-Me}}$indenyl)$_2$] family with n = 0–7.[1]
- Anionic [Fe(R_1-L_1-pR_2)(L_2)$_3$]$^-$ systems, with L_1 = tris(pyridine-2-yl)R_1methane, where R_1 = CH_2-R or O-R, R = –H, –Me, –Et, –^{n}Pr and –^{n}Bu, R_2 = $–NH_2$, –OH, –OMe, –Me, –F, –H, –Cl, –Br, $–CF_3$ and $–NO_2$, and L_2 = NCO^-, NCS^-, $NCSe^-$ and $NCBH_3^-$.[2]
- [Fe(phen)$_2$(NCS)$_2$] with phen = phenantroline.
- Dinuclear Fe(II)-based [Fe_2] metal-organic cages: ([Fe_2(L_1^R)$_3$]@X)$^{3+}$ family with L_1 = 1,3-bis-(3-(pyridin-2-yl)-1*H*-pyrazol-5-yl)benzene, X = H^-, F^-, Cl^-, Br^-, I^-, and $[BF_4]^-$, R = H, F, and CH_3.[3]

6.1. Spin-State Energy Gap from Density Functional Theory Calculations

Although it is known that TPSSh performs relatively well for spin transitions and seems a reasonable starting point, it is recommended to perform a benchmark before studying systems for which little information is available. In our case, it has been observed that even for less common systems, such as Cr(II)-based systems and anionic SCO systems, TPSSh continues to provide results that surpass other DFT methods, even considering the challenges of calculating spin-state energy gaps associated with this type of calculations.

Regarding the choice of the basis set, a benchmark was performed in the first system studied in Chapter 3, and in general it is observed that TZVP or Def2-TZVP basis sets are sufficient to describe sufficiently well our coordination complexes as it happens in other systems that exhibit SCO.

As a final remark, small changes in the spin-state energy gap have a larger impact in the computed transition temperatures, thus making more important the trends than the absolute value in these types of systems.

6.2. Multiconfiguration Pair-Density Functional Theory Applied to Spin-State Energy Gap

As it remains a challenge to calculate the spin-state energy gap with DFT methods, in Chapter 4 we used the Multiconfigurational Pair-Density Functional Theory (MC-PDFT) to overcome the limitations of the DFT methods, especially in terms of the electronic correlations.

The choice of the active space plays a role in the description of the spin-state energies and with this work we cannot assure that the MC-PDFT method is better or worse than DFT as a rule of thumb, since we only have studied one system. In our case, the effort in both, setting up the calculations and the associated computational cost involved has not been worth it compared to the gain in accuracy with respect to the DFT calculations. Although it is possible to reproduce quantitatively the $T_{1/2}$ for the studied system, there is a strong dependency on the choice of tMC-PDFT and basis set, which altogether with the expensiveness of the calculation makes this option only useful if one wants to study a given system.

6.3. Tuning of the Spin-Crossover Properties *via* Ligand Design

The fine-tuning of the SCO properties by ligand design has been a redundant topic throughout this thesis, and it is not surprising given that it allows us to study and understand how certain modifications can lead to new custom-designed materials that can operate at certain temperatures.

To modify the transition temperature in the [Cr($^{n\text{-Me}}$indenyl)$_2$] family,[1] three factors need to be considered: the relative position of the indenyl rings (eclipsed or staggered configuration), the number of methyl groups added, and their position on the indenyl rings. In general, the more methyl groups the indenyl rings have, the larger the HS-LS energy differences. A model has been developed based on all the generated data, showing that certain positions amplify this effect compared to others (C4 and C7), and it determines the relative weight of methylating these positions. Although the $\Delta E_{\text{HS-LS}}$ and $\Delta H_{\text{HS-LS}}$ energy differences may be similar between eclipsed and staggered configurations, the entropy differences are affected by these configurations, which in turn impacts the $T_{1/2}$ values.

In the anionic Fe(II)-based SCO systems,[2] there are three positions where the ligand can be modified to modulate the $T_{1/2}$. The side chain appears to have no effect on $T_{1/2}$, L_2 ligands have a pronounced effect on energies and $T_{1/2}$, and the *para* position of the pyridyl rings has a much subtler effect. A “two-knob” model can be built in which modifying L_2 determines the

temperature range, while functionalizing the *para* position of the rings allows for finer degree of tuning. This can be related to the electronic structure of the system by observing the orbitals, and it can be correlated with the strength and nature of the substituents and their electron-donating or electron-withdrawing effects.

In metal-organic cages,[3] as the size of the guest increases, the transition temperatures become smaller because the expansion from the inside causes the Fe–N bonds to lengthen, reducing the ligand field around the metal centre. This can be observed by analysing the electronic structure of the Fe(II) metal centres. As seen in previous chapters, EDGs or EWGs affect the transition temperatures through modifications at the *para* position of the pyridyl rings and also through modifications at the pyrazole rings. The ρ parameter, which determines whether a single-step or two-step transition occurs, can be calculated from the obtained results, indicating a tendency for two-step transitions with smaller guests that introduce differences between the Fe(II) sites.

The effect of the EDGs and EWGs on $T_{1/2}$ depends on the type of system and the nature of the ligands.

6.4. Contributions to the Field

The studies developed in this thesis contribute to the fields of molecular magnetism and materials chemistry by offering an in-depth analysis of the factors affecting spin-crossover for some Cr(II) and Fe(II) complexes. The insights gained provide practical guidelines for designing new SCO materials with improved properties, strengthening the connection between theoretical models and experimental outcomes. Calculations can cover the lack of experimental data, and generate models.

By tackling the challenges of predicting and fine-tuning SCO behaviour, this work tries to open the door for developing next-generation materials with applications in molecular electronics, sensing technologies, and data storage, contributing to the progress of functional materials research.

6.5. Future Challenges

Although substantial progress has been achieved, several challenges and opportunities for future research persist.

Expand the computational methods to tackle larger and more intricate systems remains a key objective. This involves improving the accuracy and scalability of computational and quantum chemical methods while integrating them effectively with machine learning approaches.

In the long run computational calculations imply a high energy cost. How can we reduce the energy cost and the impact on the environment? By using machine learning models that do not have to perform those calculations. Close collaboration with experimental researchers is key to validate and improve these models effectively since translating theoretical findings into practical solutions is another significant challenge. Research should focus on developing SCO materials with tailored properties for real applications like molecular sensors and electronic devices. Emphasizing the connection between theoretical studies and practical performance requirements will promote and enhance technological advancements.

Investigations should aim to develop eco-friendly, cost-effective methods for designing and synthesizing SCO materials, reducing environmental impact while ensuring affordability for broader use. As much as computer power has increased, calculations remain resource-intensive and energy-demanding. Therefore, the use of novel computational strategies to accelerate the computer assisted study and discovery of SCO complexes should be explored. Accelerated electronic structure calculations based on Graphical Process Units (GPUs) can generate enough quantum chemical data to feed and train a neural network that links such descriptors with the molecular topology. This artificial intelligence (AI) can later screen structural datasets searching for new SCO candidates and predict their physical properties based solely on molecular topology.

By addressing these challenges and exploring new directions, the field of SCO research can progress further, leading to innovation in material science and widening the scope of potential applications for SCO materials.

6.6. Publications

1. L. Navarro, F. Rodriguez and J. Cirera, *Dalton Trans.*, 2021, **50**, 8704–8710.
   Author's contributions: The candidate performed the computational experiments, carried out the results analysis alongside with the other author, and contributed to the manuscript revisions.
2. L. Navarro and J. Cirera, *Inorg. Chem. Front.*, 2022, **10**, 250–258.
   Author's contributions: The candidate performed the computational experiments, carried out the results analysis alongside with the other author, and contributed to the manuscript revisions.
3. L. Navarro, A. Garcia-Duran and J. Cirera, *Dalton Trans.*, 2024, **53**, 14592–14601.
   Author's contributions: The candidate performed the computational experiments, carried out the results analysis alongside with the other authors, and contributed to the manuscript revisions.